AN INTEGRATED HYDRODYNAMIC AND POLLUTANT TRANSPORT MODEL FOR THE NEARSHORE AREAS OF THE GREAT LAKES AND THEIR TRIBUTARIES

Jian Wu

B. Sc. (Nanjing Meteorology College)

M. Sc. (Academia of Science of China)

A Thesis

Submitted to the School of Graduate Studies
in Partial Fulfillment of the Requirements
For the Degree

DOCTOR OF PHILOSOPHY

McMaster University

Department of Civil Engineering

HYDRODYNAMIC AND POLLUTANT TRANSPORT MODELS

Doctor of Philosophy (1993) MCMASTER UNIVERSITY

(Civil Engineering) Hamilton, Ontario

TITLE: An Integrated Hydrodynamic and Pollutant Transport Model for the Nearshore Areas of the Great Lakes and Their Tributaries

AUTHOR: Jian Wu, M. Sc. (Academia of Science of China)

SUPERVISOR: Professor I. K. Tsanis

NUMBER OF PAGES: 338, XXVI

ABSTRACT

This thesis deals with the modelling of the circulation and pollutant transport in the nearshore areas of lakes and their tributaries. An integrated hydrodynamic/pollutant transport model was developed which operates in an interactive environment and is equipped with powerful graphics. The model can predict: (a) the horizontal and vertical current structure in the lake under isothermal and stratified conditions for steady and variable wind conditions, (b) the spatial and temporal pollutant concentration distributions in the lake from multiple input pollutant sources such as creeks, sewer treatment plant outfalls (STPs) and combined sewer outfalls (CSOs) discharging in the lake, and (c) the particle trajectories released in different locations in the lake. The model was calibrated with extant laboratory data. The water level set-up and current structure in the Great Lakes were obtained under various wind conditions and in two cases, in Lake St.Clair and Lake Ontario, the model was verified with current meter and water elevation measurements, respectively. The model was successfully applied to the St. Clair River in Sarnia for a number of storm cases and was proven to be an effective tool in screening remedial options for mitigation of bacteriological pollution in the Bay. The field data collected during the 1990-1991 field season in Hamilton Harbour was analyzed and used to verify the model. The seiches of Lake Ontario and Hamilton Harbour were revealed for the first time in the water level data in the Harbour. The simulated and measured currents and drogue trajectories were in good agreement, indicating the presence of topographical eddies and mixing zones in the Harbour. Finally, a nested-grid model was developed and successfully applied in three nearshore areas of Hamilton Harbour to examine the impact of artificial islands by studying the changes in current patterns and concentration peak, exposure, and flushing time in different locations of concern.

ACKNOWLEDGEMENTS

First and foremost, I would like to thank my supervisor Dr. Ioannis K. Tsanis for his constant support and encouragement. His supervision and guidance greatly contributed much to the successful completion of the thesis. He has shown continuous interest and has worked tirelessly to help solve the problems of both technical and non-technical nature, encountered in the course of this work. His honesty, integrity, work ethic and friendly help have been a great source of motivation. I thank him greatly.

Thanks are also due to Dr. F. M. Boyce and Mr. F. Chiocchio, the National Water Research Institute (NWRI) of the Canada Centre for Inland Waters (CCIW) for their fruitful discussion and permission to use the 1990 & 1991 field data of Hamilton Harbour. Suggestions from Dr. M. Donelan and Dr. C. R. Murthy (CCIW) are appreciated. Gratitude is also extended to Dr. G. Patry and Dr. A. N. Hrymak for their interest and help throughout the course of this work, and to Dr. D. Schwab of the Great Lakes Environmental Research Laboratory (GLERL, Michigan) for his comments as the external examiner of the thesis.

Thanks also go to Todd Pfaff and Patricia Monger who helped me solve many computer related problems, thus ensuring that my computations, plots, and text could be done. Special thanks give to Debbi, Gail and Grace from the Civil Enginnering Department office, and my "co-workers" Dr. F.P. Brissette, Dr. H. Shen, P. Xu and C. Valeo.

I also have to thank numerous friends in Hamilton and family, friends and colleagues in China for their constant encouragement. Finally, I would like to express my love and gratitude to my wife Meng Yu for all she has done during my study.

CONTENTS

LIST OF FIGURES

LIST OF TABLES

LIST OF SYMBOLS

C = Chezy friction coefficient

C_D = wind drag coefficient

C_g = group wave velocity

C_T = coefficient of sensible heat transfer

C_κ = constant in the distribution of vertical eddy viscosity

D_L, D_T = the longitudinal and transverse dispersion coefficients

D_x, D_y, D_z = the dispersion coefficients in the x, y and z directions, respectively

c = pollutant concentration

f = Coriolis coefficient

g = acceleration due to the gravity

H = total water depth ($= h + \zeta$)

h = water depth

i, j, k = index of grids in x-, y- and σ axis, respectively

K_h = horizontal eddy viscosity

K_v = vertical eddy viscosity

$\vec{k}(k_x, k_y)$ = wavenumber vector

L = length of channel

M_n = Manning's coefficient

m = ratio of bottom to surface shear velocity

N_h = horizontal dispersion coefficient of temperature

N_v = vertical dispersion coefficient of temperature

n = index of time level

P = pressure

Q = flowrate

R_h = the hydraulic radius of a river

R_i = Reynolds number

R_{kw} = roughness Reynolds number

$\vec{R}\,(R_x, R_y)$ = wave ray vector

r_1, r_2 = pseudo-Gaussian random number

S_T = Stanton number

s = slope of a river bottom

T = temperature

T_r = residence time of a basin

T_s = period of seiche

t = time

t_h = smoothing factor

U, V = depth-averaged velocity in the x, y directions, respectively

u, v, w = velocity in the x, y and z directions, respectively

$\bar{u}_0$ = velocity normalized by surface shear velocity

u_{*_s} = surface shear velocity

W = wind velocity

X, Y = location of particle

x, y, z = Cartesian coordinates

Z_0 = zero velocity height

Z_{ow} = absolute roughness

z_b = bottom roughness length

z_s = surface roughness length

z_{bh} = relative bottom roughness length

z_{sh} = relative surface roughness length

$\alpha_1, \alpha_2, \alpha_3$ = ratios for the statistic comparison of current data

η = ratio of bottom to surface shear stress

$\gamma_1, \gamma_2, \gamma_3$ = ratios for the statistic comparison of drogue data

κ = von Karman constant

λ = parameter in vertical viscosity distribution

ν = kinematic viscosity

Ω = angular rotation of the Earth.

ω	= vertical velocity in σ coordinates
ϕ	= geographic latitude
ρ	= water density
ρ_a	= air density
σ	= σ coordinates
$\tau_b(\tau_{bx}, \tau_{by})$	= bottom shear stress
$\tau_s(\tau_{sx}, \tau_{sy})$	= wind stress acting on the surface
τ_u, τ_v, τ_T	= the horizontal diffusivity terms in the σ coordinates
τ_x, τ_y	= shear stress components in the x, y directions, respectively
θ	= the angle between the local flow direction and x-axis
ζ	= water elevation above the still surface
$\Delta x, \Delta y$	= horizontal grid size in the x, y directions, respectively
Δz	= vertical grid size in Cartesian coordinate
$\Delta\sigma$	= vertical grid size in σ coordinate

Superscripts

$\vec{x}$	= vector quantity
x'	= turbulent fluctuation component
$\bar{x}$	= mean component

Subscripts

a	= air
b	= bottom
h	= horizontal
n	= normal direction to the shore
s	= surface
v	= vertical
w	= water

Acronyms

CCIW	= Canada Centre for Inland Waters
FFT	= Fast Fourier Transform
LMS	= Lake Modelling System
MEDS	= Marine Environmental Data Service
NWRI	= National Water Research Institute
Q3D	= Quasi Three-Dimensional Circulation Model
SED3D	= Three-Dimensional Sediment Transport Model
VHI	= Vertical-Horizontal Integrating
VHI3D	= Three-dimensional Circulation Model Using the VHI Method
WQSP	= Water Quality Simulation Program
2DH	= Depth-Averaged Circulation Model
3D	= Multi-Layered Three-Dimensional Circulation Model

CHAPTER 1

INTRODUCTION

The Great Lakes are Canada's most precious fresh water resource. They play an important role in meeting human needs for drinking water, sources of food, energy, and places of recreation. With the rapid increase of population and development, more pollutants are introduced into the lakes causing serious problems and concerns for water quality. Eutrophication, which is defined as the enrichment of a water body from a nutrient-poor, low productivity condition, to a nutrient-rich, high productivity condition (using Phosphorus as an indicator of trophic state), and contamination in water column and sediments due to toxic chemicals loading, are considered as two major environmental concerns in lakes. There are 42 *"Areas of Concern"* in the Great Lakes where water quality, or sediment and biota contaminant content do not meet standards that have been identified by the International Joint Commission in 1989. Nearshore areas in lakes, including harbours, waterfronts and small basins are a source of major environmental concern because while they are used for recreational purposes and are a source of drinking water, they also receive the effluent from sewage treatment plants (STP), combined sewage outfalls (CSO's), storm runoff, and tributary streams.

Remedial Action Plans (RAP) are being developed for most of these environmental concern areas in the Great Lakes, such as the following areas in Ontario: Hamilton Harbour, Toronto Waterfront, the St. Catharine's Waterfront and the Collingwood Harbour in Georgian

Bay. The RAP objectives are to identify the existing environmental problems, to delineate the physical and chemical mechanisms of various processes, to study the impact of any environmental engineering plans on the water quality, and finally, to make the area a vibrant centrepiece in the local community. Detailed knowledge of the hydrological transport processes such as advection and diffusion are necessary because essential elements for life and productivity such as oxygen, heat and nutrients, and toxic chemicals are transported and dispersed through these processes. The same processes cause the dilution of pollutants that is required in order to assure safe and reliable water supply and recreation sites under quality controlled conditions.

Four properties that characterize the hydrodynamics in the Great Lakes and, by extension, lakes and bays in general cited, by Boyce (1974) are: "lakes are closed basins, the wind is the principal source of mechanical energy, the basins are vertically stratified during the summer and the sizes are large enough to be significantly influenced by the earth's rotation on their dynamics". The hydrodynamic behaviour in lakes is largely determined by their geometry. The flow is predominately turbulent since the Reynolds number usually is very high (for a typical Great Lake with the horizontal length scale of 10^5 m and the velocity scale of 10^{-1} m/s, the Reynolds number is an order of 10^9). The size of most lakes is much smaller than that of the ocean, resulting in a negligible effect of astronomical tides, but large enough for a significant Coriolis effect due to the earth's rotation to be apparent. The hydraulically-induced flow by tributaries is only significant near the mouth regions or in the whole lake for cases of small lakes with large in/outflows, i.e., Lake St. Clair. The lake circulation is mainly induced by the wind. The wind set-up is caused by the pressure gradient due to the effect of wind, resulting in a lake-wide oscillation called seiche. The thermal stratification and overturns also present significant impacts on the current structure in lakes. Dual mixing patterns are typical of temperate zone

lakes. During the summer, the mixing is limited and a vertical temperature gradient results. The *thermocline*, characterized by a steep temperature gradient, separates the warm upper layer called the *epilimnion* from the cool lower layer called the *hypolimnion*. Lake overturns occur during the spring and the autumn, when the vertical temperature gradient has vanished and the wind mixing is influential.

The pollutant transport is accomplished by two distinct physical mechanisms, advection and diffusion. The first describes the entrainment of the pollutant material in the ambient flow and its transport with velocity equal to the fluid velocity (assuming negligible resistance to the flow). The second mechanism describes, in the case of laminar flow, the Brownian motion of the pollutant's molecules, resulting in the continuous increases of the area that the pollutant occupies. In the case of turbulent flow, the motions at molecular level become negligible before the similar process of entraining pollutant masses in turbulent eddies, leading to the same result but at a much faster rate. Finally, for the non-conservative pollutant, processes such as settling, and biological and chemical reactions with the environment, will result in a decrease or increase in its initial mass.

Hydrodynamic and pollutant transport processes can be studied by both field observations and laboratory experiments and simulated by mathematical models, as illustrated in Fig. 1.1. The laboratory and field data are used for the delineation of the physical processes of transport and mixing, and parameterization of these processes. Specifically, the laboratory experiment is one of the most widely used conventional approaches in understanding the important mechanisms of air-water interaction, hydraulic and wind-induced flows, and pollutant transport. The experiments are less costly and more easily controlled compared to the field measurements. Field measurements are most desirable for monitoring climatological features of

current, temperature, water level and water quality. However, they are expensive due to the high labour cost involved, and have spatial and temporal limitations especially in large lakes. It is not an easy task to conduct an extensive field study program. In the last two decades, with the development of powerful computer sources and computational methods, numerical models have become a powerful tool for engineers to solve complex environmental problems. With the aid of numerical models, the understanding of hydraulic features in natural lakes became possible, and feasibility studies of remedial actions in the areas of environmental concern were undertaken. Before applying the model to the actual problems, the evaluation of model performance is necessary to enhance product quality and credibility. As a result, laboratory and field data are required for the calibration and verification of models.

The hydrodynamic model is the basis and main frame in any water quality modelling system. The water quality model performance is largely dependent on the description of the circulation by the hydrodynamic model. The current distributions in both the horizontal and vertical planes are needed in any physical limnological studies. The current field predicted by the hydrodynamic model is essential to the transport model of the pollutant constituents, because the pollutants, in addition to being diffused due to the turbulence, are transported through the prevailing ambient currents. The trajectory model can give us a Lagrangian frame of the paths of particles under different environmental conditions. In addition the Monte-Carlo random-walk approach can simulate the diffusion of particles.

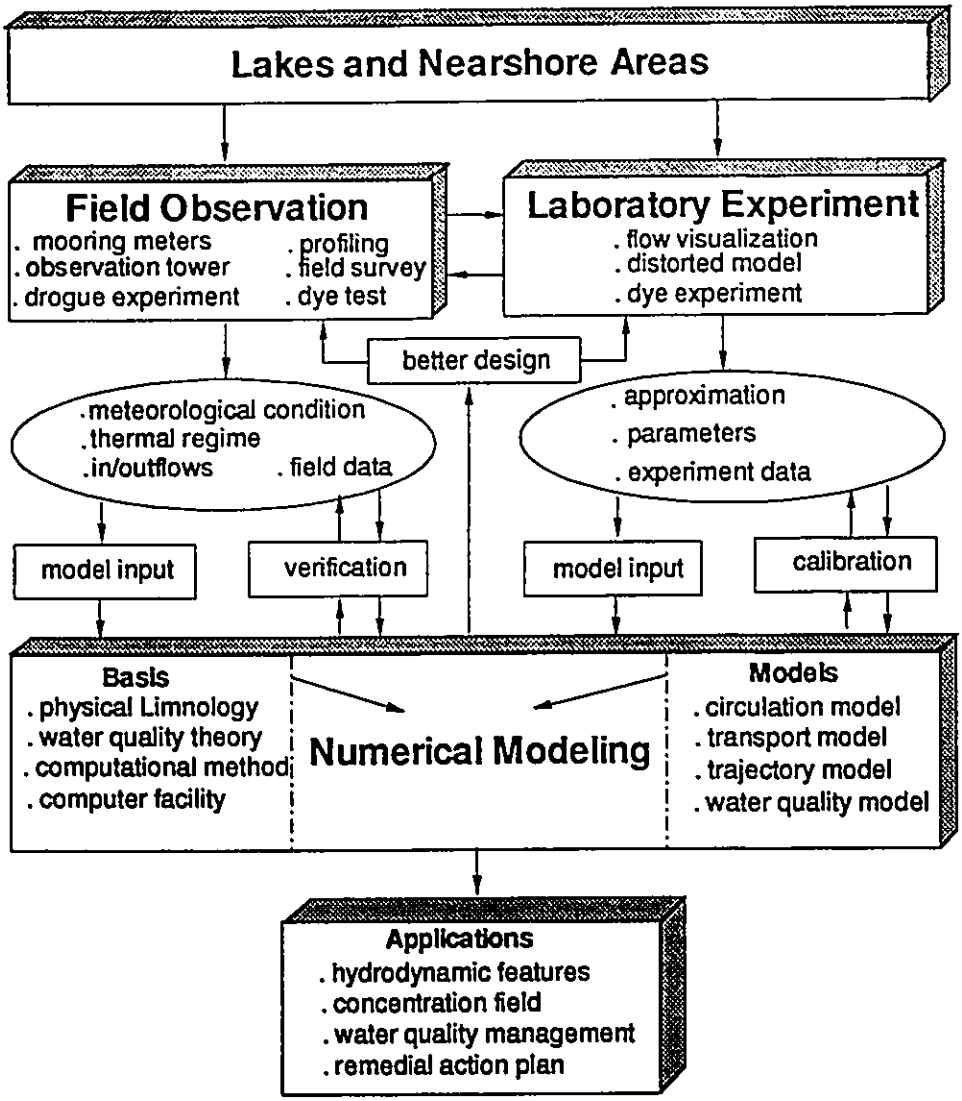

Fig 1.1 Schematic diagram of approaches for lake research, including field observation, laboratory experiment, and numerical modelling. The numerical approach is emphasised in this system.

CHAPTER 2

LITERATURE REVIEW AND SCOPE OF THE DISSERTATION

2.1 LITERATURE REVIEW

The numerical approach towards lake circulation is addressed in this dissertation. Consequently, the literature review will mainly focus on the model development for lakes. However, since laboratory results will be used in addition to field measurements for the model calibration and verification, relevant literature on laboratory experiments will also be presented.

A number of hydrodynamic models have been developed and applied to the Great Lakes over the last two decades, as shown in Table 2.1. Excellent reviews can be found in Cheng and Smith (1989), Schwab (1992). Two-dimensional models are relatively easy to use and may provide reasonable results when the detailed flow in the third dimension is relatively unimportant. The depth-averaged two-dimensional model (2DH), which is obtained by integrating the three-dimensional model equations over the depth, has been extensively used for simulating storm surges, long-term circulation and pollutant transport in lakes. In the two-dimensional model by Simons & Lam (1986), the non-linear advection and horizontal diffusivity terms were not taken into account. This assumption cannot be made for the nearshore areas in the Great Lakes. The 2D model without non-linear advective and diffusive terms, failed to reproduce the hydraulically-induced circulation patterns in the physical model of Windermere Basin. The circulation model that included advective and diffusive terms successfully obtained the pattern

Table 2.1 Existing hydrodynamic/pollutant transport models for the Great Lakes

Model	Developers	Lake Applied	Theory (1)	Method	Modeling (2)
Rigid-Lid (2D)	Schwab 1981 Schwab et al. 1983 Schwab et al. 1987 Schwab et al. 1989	 Lake Michigan Lake Erie Lake St. Clair	RL	FDM	V2 V2 V2,CC V2,TR
2D	Simons & Lam 1986 Simons et al. 1989	Test Basin Lake St. Clair	LW	FDM	V2,CC V2,ZZ
RAND (2D)	Leendertse 1969 MOE 1989	Estuaries Lake Ontario	LW	FDM	V2,TR,CC V2,ZZ,NS
3D	Ibrahim 1985	Lake St. Clair	EK	FEM	V3,CC
3D	Simons 1972,74,83 James & Eid 1978	Lake Ontario Hamilton Harbour	LW	FDM	V3,ZZ,NS V3
3D	Huang 1987	Lake Ontario	LW	FDM	V3,ZZ
CH3D	Sheng 1982,84	Lake Erie	LW	FDM	V3,ZZ,SS
LEIFS (*)	Bedford/Schwab 1990	The Great Lakes	LW	FDM	V3,ZZ

Notes: (1) RL = rigid-lid theory
LW = long-wave theory for nearly horizontal flows
EK = Ekman flow theory

(2) V2 = two-dimensional velocities (u,v)
V3 = three-dimensional velocities (u,v,w)
ZZ = water set-up
TR = particle trajectory prediction is included
CC = pollutant transport model is included
SS = sediment transport model is included
NS = capable for modelling the nearshore areas in lakes

(*) = the model system is being developed

which had been observed in the experiments (Blaisdell, 1990). The simulation of circulation in Lake Ontario supported the above finding (Wu & Tsanis, 1991). Despite the historical contribution and importance of two-dimensional models, they can only describe the global mass transport in lakes because the wind-induced circulation has a distinct vertical structure. The depth-averaged velocities can not be directly obtained from field measurements, implying a difficulty in the verification of current simulation. The verification can only be partially performed in terms of seiche periods and water elevation changes.

In recent years, researchers have noticed that the traditional two-dimensional models were not adequate in case of wind-driven circulation because of the inherent assumption of uniform depth-averaged velocity (Ramming & Kowalik, 1980; Wang & O'Connor, 1975; Koutitas, 1988). Thus, a quasi three-dimensional model using a non-uniform velocity profile (parabolic profile) in the vertical plane, incorporating the drift and return flows, has been developed and applied in the simulation of ocean tide (Koutitas, 1988) and lake circulation (Wu & Tsanis, 1991). Additional correction terms were introduced into the advection terms and bottom friction terms. The model can calculate the currents at any depth including the surface. It is also computationally efficient because it is based on a two-dimensional framework. The disadvantage of existing quasi three-dimensional models is that the vertical eddy viscosity is taken as a constant instead of the parabolic distribution which is more representative of wind-induced flow (Tsanis, 1986). A vertical-horizontal splitting (VHS) method was developed and applied in recent years to formulate an efficient quasi three-dimensional coastal circulation model (Lardner & Cekirge, 1988; AL-Rabeh & Gunay, 1992; Jin & Kranenburg, 1993). In addition to the problems with using the 2DH model, there was a lack of sound physical integration between the first module (the depth-averaged equations) and the second module (the vertical momentum

equation). Also, significant computational efficiency has not been achieved because the second module has to be solved semi-implicitly in the vertical direction.

Thermal stratification has been excluded in the two-dimensional and quasi three-dimensional models. Consequently, a multi-layer three-dimensional model including the thermal stratification effect is required for stratified lakes. The application of three-dimensional numerical models has been increased during the last decade due to faster workstations with large RAM memory that can handle large matrices, and super graphic capability. The simplest three-dimensional model is based on the Ekman's dynamic formulation (Ibrahim & McCorquodale, 1985). The spectral model, using continuous functions, is considered as an accurate method in predicting the vertical current structure in the ocean (Heaps, 1972; Davies, 1987,1991). While many simplifying assumptions are made in the spectral model, the solutions are no longer efficient for lake models in which factors such as the non-periodic wind stress, river inflow, and baroclinic forcing become important (Cheng & Smith, 1990). Some of the widely used models were the extension of the vertical averaged two-dimensional model, such as the two-layer stratified model (Koutitas, 1988) and the multi-layer models (Simons, 1980; Leendertse & Liu, 1975, 1977).

Two types of vertical grids are generally used in the finite difference models of lakes. In the first type, the vertical domain of the water body is separated by layers of constant depth, as adopted by Leendertse and Liu (1975), Simons (1972) and Eid (1981). In general, the water depth varies over a lake basin, shallow in nearshore areas and deep in the central basin. Thus, this grid is insufficient to resolve large variations of depth over the domain. The second type of grid is a vertically-stretched grid, or σ coordinate transformation, which leads to a smooth representation of the topography, and in addition, gives the same order of resolution for the shallow and deeper

parts of the water body. This transformation will introduce additional terms which require numerical treatment. In some cases, their physical significance is not apparent. However, most of the additional terms are contained in the horizontal diffusivity terms. Since the horizontal diffusion is generally small compared to the vertical diffusion and horizontal advection, only the leading terms need to be retained in general (Sheng, 1983). Tests on the different formulations of vertical and horizontal diffusivities, and pressure gradient force over steep topography in the sigma coordinate system were conducted by Mellor et al. (1985) and Haney (1990), respectively. Although there are increased calculations and uncertainties using the σ-transformation, the ability to deal with a large variation of water depth offsets other inherent disadvantages. A further refinement of this transformation is to increase the vertical resolution either near the surface or/and both surface and bottom (Swanson, 1986; Davis, 1991).

In the horizontal plane, both the finite difference and finite element methods are employed. Although the finite element method has the ability to accurately represent the complex lake basin, it has few applications in three dimensional models due to a number of elements involved and insufficient data to verify the model. Traditional finite-difference models use rectangular Cartesian grids, which resolve the geometry with "stair-steps". This grid became inefficient in representing features such as: coastal boundary layer dynamics, flow in channels, embayment, and around islands, and flows near engineering structures. To resolve the smallest spatial scales of interest for an engineering problem and at the same time maintain reasonable computational cost, a transformation has been applied by many investigators to allow increased user control of grid placement. These transformations include the change of variables from Cartesian coordinates to the orthogonal curvilinear coordinates (Blumberg et al., 1987) or the boundary fitted coordinates (Swanson, 1986; Sheng, 1990). Successful applications were mainly

found in the large bays, estuaries and wide rivers where many tributaries exist, and geometry is complicated. Examples of this include: Chesapeake Bay (Johnson et al., 1990), the James River (Sheng, Choi and Kuo, 1990) and Potomac Estuary (Hinz et al., 1990). However, due to the limited field data available for model calibration, the use of the curvilinear or boundary fitted coordinates in lake models is limited. The above transformations will provide better shoreline description by using a large number of elements that in turn increase the required computational time. An alternative efficient way is the use of a nested-grid modelling technique in which a high resolution fine grid is used for the local nearshore area of interest, and the velocity and elevation along the artificial open boundary in the fine grid are provided from the overall coarse grid for the whole lake (Murthy et al., 1986; Tsanis & Wu, 1992, 1993).

On the selection of the time step, if the explicit time integration method is used, the time step will be governed by the speed of propagation of the free surface wave (Koutitas, 1988). Also a condition will be imposed by the vertical diffusion terms which are related to the vertical eddy viscosity and the water depth. In lakes and their nearshore areas, the shallow water depth and high vertical eddy viscosity results in a small time step due to the stability requirement. It is necessary to treat the diffusion terms in implicit, at least semi-implicit scheme, such as the Crank-Nicholson implicit scheme (Koutitas et al., 1986) or the three time level Dufort-Frankel scheme (Davies, 1985).

The study of the fate and transport of the contaminants discharged from sewers, and industrial outfalls into the nearshore areas, has been one of the most active and challenging research areas of the Great Lakes for many years (Eid, 1981; Elzawahry, 1985). However, no numerical method has yet fully overcome the difficulty associated with the convection-dominated transport problems. It is not an easy task to accurately solve the advection-diffusion equation.

Physically, advection and diffusion are two distinct physical mechanisms acting on the transport processes, as discussed in the first chapter. Mathematically, this equation is a linear PDE of mixed type: the hyperbolic type - advection part, and parabolic type - diffusion part. The parabolic part can be approximated by centered finite differences, either explicit or implicit scheme. The most difficult task is the approximation of the advective hyperbolic part, i.e., the pure advection equation. Although the pure Lagrangian Method (LM) has been employed to simulate a large number of particles (Leendertse & Liu, 1975; Koutitas, 1988), the widely used numerical technique in the pollutant transport modelling in lakes is the Eulerian Method (Elzawahry, 1985; Swanson, 1986). It has been shown that explicit methods become unstable for Courant number greater than unity (CFL), while implicit methods, even when stable, tend to significantly lose accuracy above the same limit (Baptista, 1987).

The importance, scope and procedure of model performance evaluation have been highlighted several times by the American Society of Civil Engineering (ASCE) through Task Committees on hydraulics verification, and on transport prediction in partially stratified tidal water (Ditmars et al., 1987; Wang et al., 1990). They strongly recommended that no modelling study be published without a quantitative model performance evaluation. In summary, calibration and verification are the two essential parts of model performance evaluation. Calibration is the process of adjusting the model configuration, including discretization, numerical techniques, and model parameters, to achieve the best agreement of computations with observations or scientific truths such as analytical solutions and widely accepted physical laws. Calibration often involves different forcing conditions such river inflow, wind, tides (ignored in lakes model) and should at least include conditions similar to those anticipated for the applications. Verification is a process of model comparison with an independent data set (one not used for model calibration), and some

appropriate sensitivity analysis of the less certain input conditions and parameters. Measures or quantitative indices for model performance consist of parametric statistic or skill tests. Unfortunately, universally accepted procedures for how to measure and evaluate model performance have not been established (Wang et al., 1990).

In general, there are two types of laboratory experiment that can simulate the lake currents from which the circulation model calibration can benefit. The first type is conducted in either the conventional wind-water tunnels (Baines & Knapp, 1965; Goossens et al., 1982; Koutitas & O'Connor, 1980; Tsuruya et al., 1985), or the belt-type apparatus (Reichardt, 1956; Huey & Williamson, 1974), or a moving-box over a stationary plate (Tsanis, 1986). The second type is conducted in a physical model of a lake, such as the model Lake Ontario (Li et al., 1975) and the models of of Lake Brienz and Lake Murten in Switzerland (Nydegger, 1979), the model of Lake Biwa at Lake Biwa Research Institute (LBRI) of Japan, and the model of the Windermere Basin of Hamilton Harbour in Canada (Engel, 1988). In the first type of experiment, the topography effect was ignored and measurements usually focused on the mean velocity profile and turbulence characteristics of the wind-induced currents. A comprehensive review on the both analytical and experimental approaches was undertaken by Tsanis (1986, 1990). The topography of the lake, the rotation of the earth, and thermal effect were included in the distorted models (rotation and thermal effect were excluded in the model of Windermere Basin). The results from channels are useful for the formulation of vertical viscosity distribution and calibration of 3D models, while the circulation pattern and dye distribution from the distorted physical models are excellent data for calibration of two- and three-dimensional circulation models.

Field data are most desirable for the calibration and verification of models because they directly represent the physical and/or chemical processes in the lakes. However, since the field measurements are spatially and temporally limited due to the expenses involved and many times are not error-free due to uncontrollable factors, exact comparisons are rarely achieved. Trends and features in different times and space scales are usually tried between the simulated and field data. Field investigation in lakes can be traced back many years. As early as 1799, with thermal-lagged thermometers, Saussure discovered that temperature in Leman and other deep Swiss lakes in the summer was near that of maximum density (Graf & Mortimer, 1979). A drift bottle was used to track the current in lakes. Chrystal (1905) and Defant (1953) examined the seiche periods in lakes. Numerous field investigations have been undertaken in the Great Lakes and other lakes in the world. A well-known program was the International Field Year on the Great Lakes (IFYGL) of 1972, which provided a wealth of knowledge on water movements in Lake Ontario (IFYGL, 1981). More recently, extensive field studies were executed using a system approach in which data collection and numerical modelling are treated as two components of an integrated program, such as the Lake Ontario 1982/83 current study (Simons & Schertzer, 1989), the Lake Erie 1983 program (Lam et al., 1983) and the Hamilton Harbour 1990/91 physical study (Boyce & Chiocchio, 1991).

The first numerical model for Hamilton Harbour was the two-dimensional model developed in 1974 by Ontario Ministry of the Environment (MOE; 1974). The model predictions were tested to examine their sensitivity to the various input variables, and the model solutions were compared to conventional grab sampling surveys. The comparisons were only qualitative because of the insufficient field data set. The grid size and simulation time were limited due to the lack of computer resources. Eid and James (1978) applied a three-dimensional stratified

circulation model to Hamilton Harbour in a 300 m X 300 m grid. Efforts had been made to evaluate the surface wind drag coefficient for various wind conditions. This three-dimensional model is a multi-layered model with fixed layer thickness over the whole harbour. The non-linear advection and horizontal diffusivity terms were ignored which was inadequate, as discussed in the above section. The verification, which was not satisfactory, was made using only a survey of the surface velocity at several locations. The coarse grid used was unable to represent shorelines. Since then, there have been no further model developments for Hamilton Harbour. Field data are limited spatially and temporally, and are insufficient for the further study of subjects such as the horizontal mixing feature, which is essential in the modelling of water quality. Furthermore, the remedial action plan (RAP) for the harbour also requires the employment of numerical models for the feasibility study of remedial measures.

Since 1990, as the computations for 2D and 3D circulation and pollutant transport problems became routine, the modelling task was gradually shifted from equation solving to pre-processing model inputs, to post-processing model results, and to data processing to aid model calibration and verification. The model products provided to users should be user-friendly and operational. These are the major features of the fifth generation hydrodynamic model of surface water (Abbott et al., 1991). The use of computer graphic visualization and animation is an effective method in displaying large volumes of model input and output. Efforts have been made in the undergoing development of the Great Lakes Forecasting System (GLFS) project (Bedford et al., 1990; Yen et al., 1992), the operational oilspill model (Spaulding, et al., 1992), the pollutant transport modelling of the Collingwood Harbour of Lake Huron (MOE, 1992), and model development at McMaster University (Tsanis et al., 1990; Tsanis & Wu, 1991, 1992).

2.2 STATEMENT OF THE PROBLEM

It is concluded from the above literature review that a new stratified three-dimensional circulation models and techniques for modelling the circulation in the nearshore areas in lakes, and an efficient three-dimensional wind-induced circulation model is required, along with the demands of the coupled pollutant transport and dispersion model, and the drogue trajectory prediction model. The integrating model system should be operational and easy to graphically display the simulation results for model users. Performance evaluations include comparing model simulations with analytical solutions, laboratory results on hydraulically- and wind-induced flow and dye transport and dispersion, as well as with various field data such as mooring current meter data, drogue trajectories, water elevation. Given the fact that the model performance evaluations for previous models were insufficient and incomprehensive, these points will be addressed through this dissertation. Furthermore, effort will be made to establish a standard statistical criteria with solid physical mechanism for the model comparison in terms of lake currents. Many field investigations were designed independently from modelling efforts. A system approach is required in which data collection and numerical modelling are treated as two components of an integrated program. Extensive studies during the 1990 & 1991 field seasons in Hamilton Harbour were designed by the scientists at the National Water Research Institute (NWRI) of CCIW, specially for the verification of models developed in this dissertation. Consequently, a useful field data set has been obtained from this field study program.

As a result, the objective of this dissertation is to develop an integrated hydrodynamic and pollutant transport modelling system, to undertake a complete model performance evaluation using laboratory and field data, and to apply the model to the Great Lakes and their tributaries, especially to Hamilton Harbour.

2.3 COMPOSITION OF THE DISSERTATION

Following the general introduction (*Chapter 1*), literature review, and statement of the problem (*Chapter 2*), the dissertation is divided into four parts: **Part I - Model Developments**, covers the analytical background of circulation and pollutant transport models (*Chapter 3*); new model developments including the stratified three-dimensional hydrodynamic model, the highly efficient three-dimensional wind-induced model using the vertical-horizontal integration approach, the pollutant transport model and particle trajectory model, and an integrated lake modelling system (*Chapter 4*). **Part II - Model Verifications with Laboratory Data**, covers the modelling of hydraulically-induced circulation and dye transport and dispersion in the physical model of Windermere Basin (*Chapter 5*); the numerical study of wind-induced currents and comparison of various circulation models (*Chapter 6*). **Part III - Model Applications to the Great Lakes**, includes two chapters, one involving circulation modelling for the North American Great Lakes (*Chapter 7*); and another on modelling bacterial transport and feasibility study of remedial measures of the St. Clair River in Sarnia (*Chapter 8*). **Part IV - Hamilton Harbour Study**, involves analysis of field data from the 1990 & 1991 field seasons in Hamilton Harbour (*Chapter 9*); model verifications using the moored current meters data, water level data, and trajectory data from drogue experiments (*Chapter 10*); and finally, the application of nested-grid modelling technique to the feasibility study of remedial measures in three nearshore areas in Hamilton Harbour (*Chapter 11*). The last chapter (*Chapter 12*) summarizes the achievements obtained from this dissertation and points out the recommendations for further study.

PART I

MODEL DEVELOPMENTS

The development of an integrated hydrodynamic/pollutant transport modelling system for the Great Lakes and their tributaries is the essential subject of the dissertation. Because the circulation model is the core of the modelling system, the analytical background of circulation models is firstly reviewed, along with the considerations of some important terms in the model equations. Then, a multi-layered three-dimensional circulation model (3D), using the σ coordinates transformation in the vertical plane and the fractional step technique, is developed for both homogeneous and stratified lakes. Because of the inherent problems in the conventional depth-averaged wind-induced circulation model (2DH) and the weakness in the quasi three-dimensional model (Q3D), a new three-dimensional wind-induced circulation model (VHI3D) is developed, using a vertical/horizontal integrating (VHI) approach. To simulate the transport of pollutants, an advection-diffusion model is developed. Also, a second-order particle trajectory model coupled with the Monte-Carlo random-walk approach is presented to predict the movements of drogues or drifters in lakes. Based on the above model development, an integrated lake modelling system (LMS), which operates in an interactive environment and is equipped with powerful graphics, is finally developed.

CHAPTER 3

ANALYTICAL BACKGROUND OF CIRCULATION MODELS

Modelling 3D lake circulation is a mixture of art and science that requires a thorough understanding of the dynamics to allow compromises by trading off terms of secondary importance for simplicity. Although there are various formulations of models for ocean, estuaries, and lakes, basic model equations and basic assumptions are similar in most models. Therefore, it is helpful to review these basics before any new model developments. Specifically, following the description of the model equations and three basic approximations, turbulence, closure scheme, and circulation theories will be presented with the consideration of important terms in the model equations. Finally, the conventional depth-averaged circulation model and the quasi three-dimensional circulation model will be presented.

3.1 THEORETICAL BACKGROUND OF CIRCULATION MODELS

3.1.1 Model Equations

The governing system of equations for flows and transports of scalar variables in a lake includes the conservation equations of mass and momentum, the conservative equation for a

scalar variable, and the equation of state (Cheng & Smith, 1990). The lake is large enough so that the Coriolis acceleration should be included, yet small enough so that the acceleration can be treated as a constant. Lake dimension results in a quite large Reynolds number (greater than 10^8) even for a small current of 1 cm/s. Therefore the flow is always turbulent. In Cartesian coordinates (see Fig. 3.1), the governing equations, written for turbulent mean variables, include (Cheng & Smith, 1990):

the continuity equation of mass,

$$\frac{D\rho}{Dt} + \rho\left(\frac{\partial u}{\partial x} + \frac{\partial v}{\partial y} + \frac{\partial w}{\partial z}\right) = 0, \tag{3.1}$$

the momentum equation in x, y and z directions,

$$\frac{\partial u}{\partial t} + \frac{\partial uu}{\partial x} + \frac{\partial uv}{\partial y} + \frac{\partial uw}{\partial z} = fv - \frac{1}{\rho}\frac{\partial p}{\partial x} - \left[\frac{\partial \overline{u'u'}}{\partial x} + \frac{\partial \overline{u'v'}}{\partial y} + \frac{\partial \overline{u'w'}}{\partial z}\right], \tag{3.2}$$

$$\frac{\partial v}{\partial t} + \frac{\partial vu}{\partial x} + \frac{\partial vv}{\partial y} + \frac{\partial vw}{\partial z} = -fu - \frac{1}{\rho}\frac{\partial p}{\partial y} - \left[\frac{\partial \overline{u'v'}}{\partial x} + \frac{\partial \overline{v'v'}}{\partial y} + \frac{\partial \overline{w'v'}}{\partial z}\right], \tag{3.3}$$

$$\frac{\partial w}{\partial t} + \frac{\partial wu}{\partial x} + \frac{\partial wv}{\partial y} + \frac{\partial ww}{\partial z} = -\frac{1}{\rho}\frac{\partial p}{\partial z} - g - \left[\frac{\partial \overline{u'w'}}{\partial x} + \frac{\partial \overline{v'w'}}{\partial y} + \frac{\partial \overline{w'w'}}{\partial z}\right], \tag{3.4}$$

the conservation equation for a scalar variable, C_j,

$$\frac{\partial C_j}{\partial t} + \frac{\partial Cu}{\partial x} + \frac{\partial Cv}{\partial y} + \frac{\partial Cw}{\partial z} = -\left[\frac{\partial \overline{u'C'_j}}{\partial x} + \frac{\partial \overline{v'C'_j}}{\partial y} + \frac{\partial \overline{w'C'_j}}{\partial z}\right], \quad j = 0, 1, 2,... \tag{3.5}$$

and the equation of state,

$$\rho = \rho(s, T), \tag{3.6}$$

where, t is time; (x, y, z) are the Cartesian coordinates; u ,v ,w are the velocity components in the x, y, and z directions, respectively; ρ is density of water; g is the acceleration due to the gravity; s is salinity; T is temperature; C_j is a conservative scalar variable, such as s or T; (u', v', w', C'_j)

are the turbulent fluctuations of (u, v, w, C_j); p is pressure; $f = 2\,\Omega\,sin(\phi)$ is the Coriolis coefficient; ϕ the geographic latitude of the domain and Ω the angular rotation of the Earth. The turbulence correlations are indicated by over bars, $\overline{u'u'}$, $\overline{v'v'}$, $\overline{w'w'}$ are the normal turbulent stresses, and $\overline{u'v'}$, $\overline{u'w'}$, $\overline{v'w'}$ are the Reynolds turbulent stresses.

The system of equations is not closed until the the turbulent stresses are defined, and the appropriate initial and boundary conditions are given. Typically, at the water surface, a kinematic condition is that the wind stress is specified as a given function. At air-water and water-sediment interfaces, no fluxes of mass nor conservative solutes are permitted. Practically, necessary assumptions and approximations must be introduced to simulate a complex real-world system, and the resultant simplified governing equations are then solved by a chosen numerical method suitable for that particular formulation.

3.1.2 Basic Assumptions

There are three basic approximations used on most hydrodynamic models applied to oceans, estuaries, lakes and impoundments:

1 *Incompressible Flow*

For lakes or shallow estuary systems, the water can be assumed to be incompressible, and the continuity equation can be written as:

$$\frac{\partial u}{\partial x} + \frac{\partial v}{\partial y} + \frac{\partial w}{\partial z} = 0\,, \qquad \frac{D\rho}{Dt} = 0 \tag{3.7}$$

2 *Hydrostatic Approximation*

The characteristic length in the vertical direction is two to three orders of magnitude

smaller than the characteristic horizontal dimension. Therefore, the vertical pressure gradient can be balanced only by the gravitational acceleration in the z-direction, i.e.,

$$0 = -\frac{\partial p}{\partial z} - \rho g \tag{3.8}$$

By integrating the above equation from z to the free surface, $z = \zeta$ where ζ is the super water elevation above the mean water level, the horizontal pressure gradient can be separated into an atmospheric gradient term, a *barotropic* (water surface gradient) term and a *baroclinic* (density gradient) term:

$$\frac{\partial p}{\partial x} = \frac{\partial p_a}{\partial x} + \rho_s g \frac{\partial \zeta}{\partial x} + \int_z^\zeta g \frac{\partial \rho}{\partial x} dz \tag{3.9}$$

where, ρ_s is the surface water density. Atmospheric pressure gradients when compared to wind stress (both are the external forces to lake) are relatively unimportant and usually are neglected.

3 *Boussinesq Approximation*

Density variations are of order 10^{-3}, resulting in negligible effect on barotropic terms (ρ_s can be substituted by a constant reference density ρ_0). On the other hand, the effect of buoyancy arising from the differences in fluid density along horizontal surfaces are not negligible. As a result, the effect of density variation is only retained in the baroclinic terms. This is called the *Boussinesq Approximation*. The x-momentum equation (3.2) with the hydrostatic and Boussinesq approximation becomes

$$\frac{\partial u}{\partial t} + \frac{\partial uu}{\partial x} + \frac{\partial uv}{\partial y} + \frac{\partial uw}{\partial z} = fv - g\frac{\partial \zeta}{\partial x} - \frac{g}{\rho_0}\int_z^\zeta \frac{\partial \rho}{\partial x} dz - \left[\frac{\partial \overline{u'u'}}{\partial x} + \frac{\partial \overline{u'v'}}{\partial y} + \frac{\partial \overline{u'w'}}{\partial z} \right], \tag{3.10}$$

and the y-momentum equation becomes

$$\frac{\partial v}{\partial t}+\frac{\partial vu}{\partial x}+\frac{\partial vv}{\partial y}+\frac{\partial vw}{\partial z}=-fu-g\frac{\partial \zeta}{\partial y}-\frac{g}{\rho_0}\int_z^{\zeta}\frac{\partial \rho}{\partial y}dz-\left[\frac{\partial \overline{u'v'}}{\partial x}+\frac{\partial \overline{v'v'}}{\partial y}+\frac{\partial \overline{w'v'}}{\partial z}\right] \tag{3.11}$$

3.1.3 Turbulence Closure

There are two major turbulence closure approaches for lakes, namely, eddy viscosity-diffusivity and second-order closure. Virtually most lake and estuary models have adopted the viscosity-diffusivity approach. In this approach, the turbulent transport terms can be written as

$$-\left[\frac{\partial \overline{u'u'}}{\partial x}+\frac{\partial \overline{v'u'}}{\partial y}+\frac{\partial \overline{w'u'}}{\partial z}\right]=\frac{\partial}{\partial x}(K_h\frac{\partial u}{\partial x})+\frac{\partial}{\partial y}(K_h\frac{\partial u}{\partial y})+\frac{\partial}{\partial z}(K_v\frac{\partial u}{\partial z}) \tag{3.12}$$

$$-\left[\frac{\partial \overline{u'v'}}{\partial x}+\frac{\partial \overline{v'v'}}{\partial y}+\frac{\partial \overline{w'v'}}{\partial z}\right]=\frac{\partial}{\partial x}(K_h\frac{\partial v}{\partial x})+\frac{\partial}{\partial y}(K_h\frac{\partial v}{\partial y})+\frac{\partial}{\partial z}(K_v\frac{\partial v}{\partial z}) \tag{3.13}$$

$$-\left[\frac{\partial \overline{u'C'}}{\partial x}+\frac{\partial \overline{v'C'}}{\partial y}+\frac{\partial \overline{w'C'}}{\partial z}\right]=\frac{\partial}{\partial x}(N_h\frac{\partial C}{\partial x})+\frac{\partial}{\partial y}(N_h\frac{\partial C}{\partial y})+\frac{\partial}{\partial z}(N_v\frac{\partial C}{\partial z}) \tag{3.14}$$

where, K_h and N_h are the horizontal eddy viscosity and diffusivity coefficients, and K_v and N_v are the vertical eddy viscosity and diffusivity coefficients, respectively. In most lakes, because the ratio of vertical length scale to horizontal length scale is very small, the horizontal mixing terms are orders of magnitude smaller than the vertical mixing terms. As a result, the use of a sophisticated turbulence closure model for the horizontal mixing terms is generally not warranted. Most models treat the horizontal eddy viscosity coefficients as constants, or these terms are simply neglected. After this simplification, the role of the turbulent closure becomes that of determining the variation of the turbulent transport in the vertical. A semi-empirical theory of vertical mixing, assuming that the eddy viscosity is constant or using an empirical equation to relate it to other parameters, has been used in most circulation models. The effect of

stratification, as measured by the Richardson number, R_i, on the intensity of vertical turbulent mixing, is parameterized by a number of empirical stability functions (Sheng, 1983; Blumberg, 1986):

$$K_v = K_{v0}\phi_1(R_i);\quad N_v = N_{v0}\phi_2(R_i); \tag{3.15}$$

where

$$R_i = -\frac{g}{\rho}\frac{\partial\rho/\partial z}{(\partial|U|/\partial z)^2} \tag{3.16}$$

in which K_{v0} and N_{v0} are the eddy viscosity coefficients in absence of any density stratification and the ϕ_1 and ϕ_2 are stability functions (Sheng, 1983; Blumberg, 1986). More sophisticated turbulence models may be found in literature, such as one-equation, or $K-L_0$ model (Rodi , 1978; Koutitas & O'Connor, 1980) and two-equation or $K-\varepsilon$ model (Svensson, 1978; Pearce & Cooper, 1981; Mellor, 1973; Blumberg, 1987).

3.1.4 Circulation Theory

(A) Long-Wave Theory

The velocity profile develops slowly with time and uniformly in stages, having the same form as in the river channel:

$$u = \frac{u_{*_s}}{\kappa}\ln\frac{h+z}{z_0} \tag{3.17}$$

where, u_{*_s} is the shear velocity at the surface; h is the water depth relative to the mean water level; z_0 is the roughness in the bottom; and κ =0.4 is the Von Karman constant. The current intensity is almost uniform over the depth, i.e., same direction over the whole depth with steep gradients developing only near the bottom. This flow structure is similar to a hydraulically-

induced flow such as a river flow.

(B) Shear-Induced Countercurrent Flow Theory

Inherently, wind-induced currents in natural lakes, estuarines and embayments are shear-induced types of flows. The vertical mixing mechanism can be examined using steady plane Couette laminar flow (for slow wind-induced current), and turbulent flow. In these flows, the current close to the surface is in the direction of the applied shear stress, while away from the surface to the bottom, a return current develops. Required by the continuity, the integrated flow transport from the surface to the bottom is zero, i.e. zero net volume flux.

The laminar flow has a parabolic velocity distribution and a linear shear stress distribution. The bottom to surface shear stress ratio equals to -0.5, and the zero velocity occurs at $z / h = 0$ and $z / h = 2/3$ where z is measured upwards from the lake bottom. A constant viscosity over the depth leads to a parabolic velocity profile, as the exact solution of the Navier-Stokes equation, which is close to the experimentally determined profile (Tsanis, 1986). Analogous to the laminar flow theory, a constant vertical eddy viscosity evaluated by the applied wind shear stress τ_s was used in many circulation models, for example, Koutitas and O'Connor (1980) used:

$$K_v = \bar{\lambda} h \sqrt{\tau_s / \rho} \tag{3.18}$$

where, $\bar{\lambda}$ is a constant. Taking the mean value of a parabolic distribution of eddy viscosity, it was suggested that $\lambda = 0.066$.

In the case of turbulent shear-induced countercurrent flow, both viscous stresses (due to the molecular motion), and Reynolds stresses (due to turbulence), contribute to the total shear stress. Close to the water surface and bottom boundaries, the viscous stresses are predominant

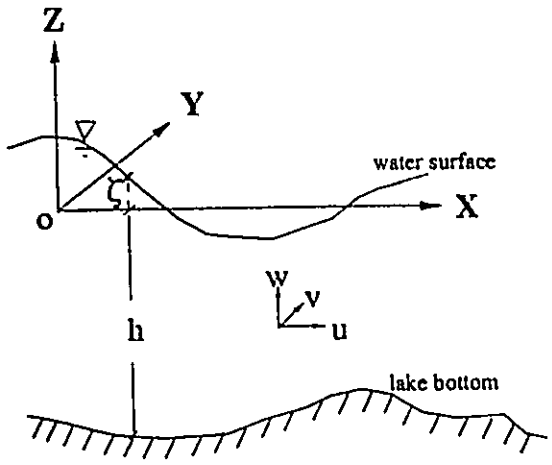

Fig. 3.1 Cartesian coordinates system for the hydrodynamic model of lakes.

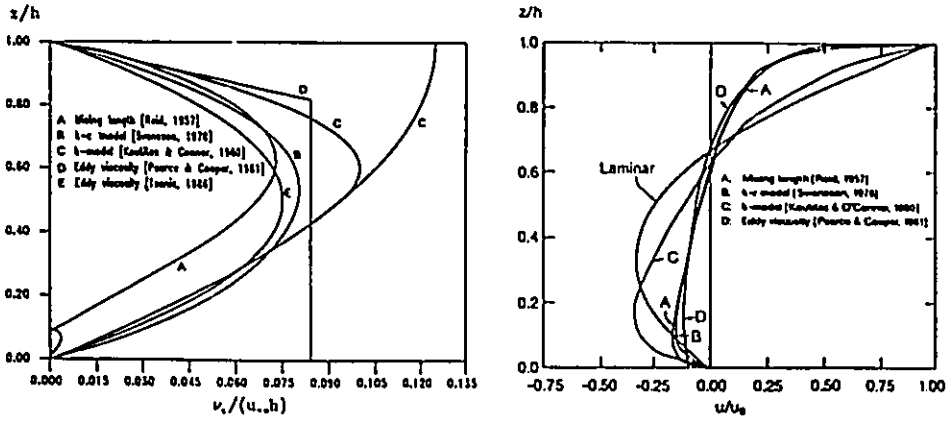

Fig. 3.2 Various distributions of eddy viscosity used in analytical models of wind-induced flows; and existing analytically predicted mean velocity distribution (adopted from Tsanis, 1989).

while in the rest of flow field the Reynolds stresses greatly exceed the viscous contribution. The thicknesses of these viscous sublayers are very small compared to the depth. The velocity changes linearly with the distance from the boundary, while steep velocity gradients exist in the sublayers. The velocity distribution then depends on the distribution of the turbulent shear stress with z, which is provided by introducing appropriate "closure" hypotheses. The calculated eddy viscosities in various models, normalized by the surface shear-stress and depth, are shown in Fig. 3.2(a) (reproduced from Tsanis, 1989). These models include the mixing length hypothesis (Reid, 1957), $K-\varepsilon$ model (Svensson, 1978), $K-L$ model (Koutitas & O'Connor, 1980) and eddy viscosity (Pearce & Copper, 1981; Tsanis, 1986). The mean velocity profile based on the above models are presented in an nondimensional term in Fig. 3.2(b) (u_s is the surface velocity). It was concluded that a proper simple parabolic distribution of eddy viscosity can produce a close velocity profile as predicted by sophisticated closure models, and use of a parabolic distribution of eddy viscosity results in a double-logarithmic velocity distribution in the vertical (Tsanis, 1989).

(C) Implication to the Model Formulation

Although the flows in lakes, estuaries and embayments are controlled by a number of factors, the effects of topography, Coriolis force, and seiches have been included in the most conventional depth-averaged two-dimensional circulation models. However, the consideration of the vertical mixing is not satisfactory due to the usage of long-wave theory. The above shear-induced flow theory provides some implications to the formulation of new types of three-dimensional wind-driven circulation model. It is noticed that in the above theory, zero net mass flux is preserved. In other words, the depth-averaged velocity is zero, while in the natural basins, depth-mean velocity is usually not equal to zero. Therefore, modification is needed to include

such a feature. In the lakes and estuaries, the wind-driven flows are turbulent shear-induced flows. The parabolic profile is not adequate enough to describe such flows, especially near the surface and bottom. Numerically, special care has to be taken in the evaluation of steep velocity gradients in the thin viscous sublayers. Only when the velocity profile is reasonably considered, the bottom shear stress terms and advective terms in the two-dimensional depth-averaged model can be correctly evaluated.

3.1.5 Model Consideration

In this section, the consideration of various terms in the circulation models is discussed.

(A) Baroclinic Terms

Baroclinic terms present the effect of thermal stratification. Great simplification can be achieved if these terms can be assumed to be small and therefore are neglected. If the density can be justifiably assumed to be constant, then the transport equation of temperature, or salinity, can be uncoupled from the continuity and momentum equations. Since the thermal stratification is usually present in the summer period, a strategy was based on the following consideration. Assumed that in the simulation period, the wind did not significantly affect the stratification and the determination of the state of stratification is not a primary modelling objective, then the density field can be treated diagnostically. The baroclinic terms in the momentum equation are not solved, but evaluated, by assuming the temperature (or salinity) field is known a *priori* from the measurements or from independent studies. However, this method can't apply to the case of rapid change of weather conditions, nor medium- and long- term simulation. In a review paper

by the ASCE Task Committee (Wang et al., 1990) pointed out that the simulation of partially stratified estuaries or lakes, is one of the most challenging areas in recent years. A completed field data base was required to provide the input initial density field and verify the simulations.

(B) Advection Terms

The non-linear advection terms are often the source of difficulties in numerical solutions since they give rise to nonlinear instabilities. As a result, in some model formulations, the advection terms are neglected (Simons, 1972; Eid, 1981). This simplification needs to be carefully justified for different applications (Blaisdell et al., 1991; Wu & Tsanis, 1991).

(C) Bottom Shear Stress Terms

The bottom stress formulation which is a specification of the rate of momentum loss at the water-sediment interface, assumes a variety of forms in different models. The bottom stress is treated to be proportional to a quadratic form of velocity in most two-dimensional models (Leendertse, 1967; Koutitas, 1986; Simons, 1972), and enters into the 3D circulation model through the bottom boundary conditions (Sheng, 1983). The proportional constant or friction coefficient can be assigned as a constant, or calculated from the roughness or Manning coefficient and water depth, or evaluated using the results from the turbulent boundary layer theory. Other models assume the bottom stress to be linearly proportional to velocity. A no-slip condition assuming a zero velocity at lake-bottom interface is also adopted by many 3D circulation models.

(D) Rigid-Lid Approximation

In the early lake circulation models, a rigid-lid approximation was used (Cheng et al., 1976; Schwab, 1981). In this approximation, the free surface deformations are ignored, i.e.,

$\partial\zeta / \partial t \approx 0$. As a result, along with the neglection of non-linear advection terms, a simplified model by solving stream function was formed for the steady circulation. However, in most cases such an approximation is not justified.

3.2 A DEPTH-AVERAGED CIRCULATION MODEL (2DH)

Based on the long-wave theory, the current intensity is almost uniform over the depth with a steep gradient near the bed. Introducing the depth-averaged velocity components U and V,

$$U = \frac{1}{H}\int_{-h}^{\zeta} u dz \quad , \quad V = \frac{1}{H}\int_{-h}^{\zeta} v dz \tag{3.19}$$

where $\zeta(x,y)$ is the water elevation above the still water level (SWL), $H = h + \zeta$ is the thickness of the water column, the depth-averaged form of the convective acceleration terms are:

$$\frac{1}{H}\int_{-h}^{\zeta} u\frac{\partial u}{\partial x}dz \approx U\frac{\partial U}{\partial x} \quad , \quad \frac{1}{H}\int_{-h}^{\zeta} v\frac{\partial u}{\partial y}dz \approx V\frac{\partial U}{\partial y} \tag{3.20}$$

$$\frac{1}{H}\int_{-h}^{\zeta} u\frac{\partial v}{\partial x}dz \approx U\frac{\partial V}{\partial x} \quad , \quad \frac{1}{H}\int_{-h}^{\zeta} v\frac{\partial v}{\partial y}dz \approx V\frac{\partial V}{\partial y} \tag{3.21}$$

Integrating the continuity and momentum equations (3.1) to (3.4) over the depth, with the hydrostatic approximation, yields to the conventional two-dimensional depth-averaged circulation model:

$$\frac{\partial U}{\partial t} + U\frac{\partial U}{\partial x} + V\frac{\partial U}{\partial y} = fV - g\frac{\partial \zeta}{\partial x} + K_h\left(\frac{\partial^2 U}{\partial x^2} + \frac{\partial^2 U}{\partial y^2}\right) + \frac{\tau_{sx} - \tau_{bx}}{\rho H} \tag{3.22}$$

$$\frac{\partial V}{\partial t} + U\frac{\partial V}{\partial x} + V\frac{\partial V}{\partial y} = -fU - g\frac{\partial \zeta}{\partial y} + K_h\left(\frac{\partial^2 V}{\partial x^2} + \frac{\partial^2 V}{\partial y^2}\right) + \frac{\tau_{sy} - \tau_{by}}{\rho H} \tag{3.23}$$

$$\frac{\partial \zeta}{\partial t} + \frac{\partial HU}{\partial x} + \frac{\partial HV}{\partial y} = 0 \tag{3.24}$$

where, τ_{sx} , τ_{sy} are the surface shear stresses:

$$\tau_{sx} = K_v \frac{\partial u}{\partial x}\Big|_{z=0}; \qquad \tau_{sy} = K_v \frac{\partial v}{\partial y}\Big|_{z=0} \tag{3.25}$$

and τ_{bx} , τ_{by} are the bottom shear stresses:

$$\tau_{bx} = K_v \frac{\partial u}{\partial x}\Big|_{z=-h}; \qquad \tau_{by} = K_v \frac{\partial v}{\partial y}\Big|_{z=-h} \tag{3.26}$$

When required, the vertical current structure can be calculated in terms of depth-averaged velocities as follows

$$u(z) = \frac{U}{\left[\frac{z_0}{h} - 1 + \ln\left(\frac{h}{z_0}\right)\right]} \ln\frac{z}{z_0}, \qquad v(z) = \frac{V}{\left[\frac{z_0}{h} - 1 + \ln\left(\frac{h}{z_0}\right)\right]} \ln\frac{z}{z_0} \tag{3.27}$$

where, $z_0 = k_s/30$ is the zero-velocity level, k_s is the absolute bed roughness or equivalent roughness ($z_0/h \ll 1$). This model gives good results in case where the vertical distribution of the velocity components U and V is close to uniform, i.e., unidirectional river flows.

3.3 A QUASI THREE-DIMENSIONAL CIRCULATION MODEL (Q3D)

In order to incorporate the effects of the non-uniform velocity in the vertical plane, Koutitas et al. (1986) developed a so-called quasi three-dimensional wind-driven circulation model (Q3D). This model is presented here with some modifications. A parabolic velocity distribution, for example in z-direction, is assumed as

$$u(z) = \alpha z^2 + \beta z + \gamma \tag{3.28}$$

where, z is measured upwards from the lake bottom for the convenience of model derivation. Then three conditions, i.e, wind shear stress at free water surface, no-slip condition at the bottom, and the definition of depth-averaged velocities are used to determine these three coefficients α, β, γ. Then the velocity profiles as a function of depth-mean velocity and wind shear stress are

obtained:

$$u = (-\frac{3}{2}U + \frac{3}{4}\frac{\tau_{sx}}{\rho}\frac{h}{K_v})(\frac{z}{h})^2 + \frac{\tau_{sx}}{\rho}\frac{h}{K_v}\frac{z}{h} + (\frac{3}{2}U + \frac{\tau_{sx}}{\rho}\frac{h}{4K_v}) \tag{3.29}$$

$$v = (-\frac{3}{2}V + \frac{3}{4}\frac{\tau_{sy}}{\rho}\frac{h}{K_v})(\frac{z}{h})^2 + \frac{\tau_{sy}}{\rho}\frac{h}{K_v}\frac{z}{h} + (\frac{3}{2}V + \frac{\tau_{sy}}{\rho}\frac{h}{4K_v}) \tag{3.30}$$

In order to be consistent with the parabolic velocity distribution a constant viscosity in the vertical direction is assumed. The depth-averaged advective terms are evaluated via Eqs. (3.29) and (3.30). For example,

$$\frac{1}{h}\int_0^h u\frac{\partial u}{\partial x}dz = U\frac{\partial U}{\partial x} + (0.2U + \frac{\tau_{sx}h}{40\rho K_v})\frac{\partial U}{\partial x} \tag{3.31}$$

The bottom friction shear stresses are evaluated as

$$\tau_{bx} = = 3\bar{\lambda}\frac{U}{h}\sqrt{\tau_{sx}/\rho} - 0.5\frac{\tau_{sx}}{\rho h} \tag{3.32}$$

$$\tau_{by} = = 3\bar{\lambda}\frac{V}{h}\sqrt{\tau_{sy}/\rho} - 0.5\frac{\tau_{sy}}{\rho h} \tag{3.33}$$

Finally, the two-dimensional model, improved with respect to the horizontal momentum dispersion and the bottom friction for wind-driven circulation, becomes,

$$\frac{\partial U}{\partial t} + (U + 0.2U + \frac{\tau_{sx}h}{40\rho K_v})\frac{\partial U}{\partial x} + (V + 0.2V + \frac{\tau_{sy}h}{40\rho K_v})\frac{\partial U}{\partial y} = fV - g\frac{\partial \zeta}{\partial x} + \frac{\tau_{sx} - \tau_{bx}}{\rho H} \tag{3.34}$$

$$\frac{\partial V}{\partial t} + (U + 0.2U + \frac{\tau_{sx}h}{40\rho K_v})\frac{\partial V}{\partial x} + (V + 0.2V + \frac{\tau_{sy}h}{40\rho K_v})\frac{\partial V}{\partial y} = -fU - g\frac{\partial \zeta}{\partial y} + \frac{\tau_{sy} - \tau_{by}}{\rho H} \tag{3.35}$$

$$\frac{\partial \zeta}{\partial t} + \frac{\partial HU}{\partial x} + \frac{\partial HV}{\partial y} = Q \tag{3.36}$$

The model permits the computation of the current patterns at different depths. The surface velocity is calculated via Eqs. (3.29) and (3.30) by setting $z = 0$:

$$u_s = 1.5U + \frac{\tau_{sx} h}{4\rho K_v}; \qquad v_s = 1.5V + \frac{\tau_{sy} h}{4\rho K_v} \tag{3.37}$$

This model takes account the variation of the velocity components U and V in the vertical direction and is suitable for predictions of wind-induced circulation in lakes.

3.4 SUMMARY

In this chapter, the theoretical background for the lake circulation models has been reviewed. Considerations on several important terms such as barotropic and baroclinic terms, horizontal diffusivity terms, and bottom shear stress terms are discussed. Finally, the conventional depth-averaged circulation model and a quasi three-dimensional circulation model are presented.

CHAPTER 4

NEW MODEL DEVELOPMENTS

This chapter presents new model developments, including a multi-layered three-dimensional circulation model (3D), a computationally efficient three-dimensional wind-induced circulation model (VHI3D) using the vertical/horizontal integrating (VHI) approach, a pollutant transport model, and a second-order particle trajectory model coupling with a random-walk approach. Finally, an integrated lake modelling system (LMS) including various developed models along with the pre-processing, post-processing and graphics package is presented.

4.1 A MULTI-LAYERED THREE-DIMENSIONAL HYDRODYNAMIC MODEL (3D)

4.1.1 Model Equations

The flow in lakes is three-dimensional, time-dependent and turbulent. It can be simulated by the 3D hydrodynamic model, knowing the wind and in/outflow conditions. For the simulation of large-scaled circulation, the flow domain is comprised of horizontal dimensions usually several orders of magnitude larger than the vertical dimension. Therefore, the *incompressible*, *hydrostatic* and *boussinesq* approximations can be soundly made. The lake system is assumed to be large enough so that the Coriolis acceleration must be included, yet small enough so that the acceleration can be treated as a constant. The equation for temperature along with the equation of state is included to consider the effect of thermal stratification in lakes.

The model equations can be expressed as follows:

Conservation of momentum - x direction

$$\frac{\partial u}{\partial t}+\frac{\partial uu}{\partial x}+\frac{\partial uv}{\partial y}+\frac{\partial uw}{\partial z}=fv-g\frac{\partial \zeta}{\partial x}-\frac{g}{\rho_0}\int_z^{\zeta}\frac{\partial \rho}{\partial x}dz+\frac{\partial}{\partial x}(K_h\frac{\partial u}{\partial x})+\frac{\partial}{\partial y}(K_h\frac{\partial u}{\partial y})+\frac{\partial}{\partial z}(K_v\frac{\partial u}{\partial z}) \quad (4.1)$$

Conservation of momentum - y direction

$$\frac{\partial v}{\partial t}+\frac{\partial vu}{\partial x}+\frac{\partial vv}{\partial y}+\frac{\partial vw}{\partial z}=-fu-g\frac{\partial \zeta}{\partial y}-\frac{g}{\rho_0}\int_z^{\zeta}\frac{\partial \rho}{\partial y}dz+\frac{\partial}{\partial x}(K_h\frac{\partial v}{\partial x})+\frac{\partial}{\partial y}(K_h\frac{\partial v}{\partial y})+\frac{\partial}{\partial z}(K_v\frac{\partial v}{\partial z}) \quad (4.2)$$

Conservation of momentum - z direction

$$\frac{\partial p}{\partial z}=-\rho g \quad (4.3)$$

Conservation of mass (continuity equation)

$$\frac{\partial u}{\partial x}+\frac{\partial v}{\partial y}+\frac{\partial w}{\partial z}=0 \quad (4.4)$$

Conservation of energy

$$\frac{\partial T}{\partial t}+\frac{\partial uT}{\partial x}+\frac{\partial vT}{\partial y}+\frac{\partial wT}{\partial z}=\frac{\partial}{\partial x}(N_h\frac{\partial T}{\partial x})+\frac{\partial}{\partial y}(N_h\frac{\partial T}{\partial y})+\frac{\partial}{\partial z}(N_v\frac{\partial T}{\partial z}) \quad (4.5)$$

The equation of state for lake fresh water, relating temperature to density, is given as

$$\rho=\rho_4(1-a\ \delta T^2) \quad (4.6)$$

where, $a=6.8X10^{-6}\ {}^0C^{-2}$ is the constant; ρ_4 is the water density at 4^oC; and $\delta T=T-T_4$ is the temperature deviation from 4^oC.

4.1.2 Boundary and Initial Conditions

Obtaining solutions for the above model equations requires the specification of appropriate boundary and initial conditions. In this section, the vertical boundary conditions at

the free water surface and lake bottom will be described, along with the lateral boundary conditions and the initial conditions.

(A) Boundary Conditions at the Surface

The kinematic boundary condition is imposed at the free water surface:

$$w = \frac{\partial \zeta}{\partial t} + u \frac{\partial \zeta}{\partial x} + v \frac{\partial \zeta}{\partial y} \tag{4.7}$$

The momentum and heat across the air-water interface are the primary causes of circulation. The momentum flux described as wind shear stress can be evaluated by the wind velocity,

$$(\tau_{sx}, \tau_{sy}) = \rho_a C_D \sqrt{W_x^2 + W_y^2}\,(W_x, W_y) \tag{4.8}$$

where $W = (W_x, W_y)$ is the wind velocity measured at 10 m above the still water surface; ρ_a is the air density; and C_D is a surface wind drag coefficient which is typically of order of $0[10^{-3}]$. According to Wu (1969), the drag coefficient for neutral stratification is given by

$$C_D = (0.8 + 0.065W) * 10^{-3} \tag{4.9}$$

Similar to the wind-wave model by Donelan et al. (1974), Eid (1981) proposed a formula relating the drag coefficient to the wind speed at distance z (usually 10 m) as well as wave height (H_s) and wave velocity (c):

$$C_D = \left[\frac{k}{\ln(z/\beta H_s)}\right]^2 (1.0 - \frac{c}{W})^2 \tag{4.10}$$

After evaluation using wind and wave data in Hamilton Harbour, a formula similar to Eq. (4.9) was presented:

$$C_D = (0.75 + 0.075W) * 10^{-3} \tag{4.11}$$

Usually, the heat exchange rate at the surface is taken as zero during the short-term simulation. However, this assumption may not be justified. In general, there are two approaches

to determine heat exchange flux. The first approach is a simple but efficient one which is similar to the momentum flux formula, i.e., an empirical function with environmental parameters (Large & Pond 1981; Smith & Anderson, 1984; Wu, 1992). Ignoring the molecular transfer term, the heat flux across air-water interface can be expressed as (Wu, 1992):

$$H_0 = \rho C_P \overline{w'T'} = \rho C_P C_T U_Z (T_0 - T_Z) \tag{4.12}$$

where, H_0 is the sensible heat flux; T' and w' are the temperature and the vertical velocity fluctuations, respectively; T_Z is the potential air temperature at the elevation Z above the mean water surface; T_0 is the potential air temperature at the surface, i.e., water temperature at the surface; ρ is the density of air; C_p is the specific heat of air at a constant pressure; C_T is the coefficient of sensible heat transfer and is also called the Stanton number (S_T). Based on the direct measurement of $\overline{w'T'}$ from field studies, an empirical formula of the heat transfer coefficient, varying with wind and atmospheric stability conditions and temperature difference, is:

$$C_T = (0.72 + 0.0175 W \Delta T) \times 10^{-3} \quad , \quad W < 8\, m/s \tag{4.13}$$

$$C_T = (1.000 + 0.0015 W \Delta T) \times 10^{-3} \quad , \quad W > 8\, m/s \tag{4.14}$$

where W is wind velocity at 10 m above the mean water surface, expressed in meters per second, $\Delta T = T_0 - T_{10}$ is the temperature difference between the water surface and at 10 m above the water surface, expressed in degrees Celsius (Wu, 1992).

The second approach is based on the energy budget calculation: the net heat exchange is the difference between absorbed solar radiation and heat losses due to the evaporation, conduction and reverse radiation (Ryan, 1971; Shen, 1991).

(B) Boundary Conditions at the Bottom

The kinematic boundary condition at the bottom is:

$$w_b = u_b \frac{\partial h}{\partial x} + v_b \frac{\partial h}{\partial y} \tag{4.15}$$

where subscript b refers to bottom; h is the water depth. For the shear stress condition, there are two kinds of boundary conditions:

(1) no-slip condition, i.e., the velocity at the bottom is equal to zero

$$u = v = w = 0 \tag{4.16}$$

Then, the bottom shear is evaluated from the velocity and vertical eddy viscosity near the bottom directly in the model;

(2) a quadratic law similar to that at the surface:

$$(\tau_{bx}, \tau_{by}) = r\sqrt{u_b^2 + v_b^2}\,(u_b, v_b) \tag{4.17}$$

where (τ_{bx}, τ_{by}) are the shear stresses at the bottom in the x and y directions respectively; r is the bottom friction coefficient; (u_b, v_b) are the bottom velocity components (usually at the layer close to the bottom) in the x and y directions, respectively. There is no heat allowed to transfer through the bottom, or at least, the flux is assumed negligible.

(C) Lateral Boundary Conditions

Along the shoreline where river inflow or outflow may occur, the variables generally take a prior known value:

$$u = u_r(x, y, z, t) \tag{4.18}$$

$$v = v_r(x, y, z, t) \tag{4.19}$$

$$w = 0.0 \tag{4.20}$$

$$T = T_r(x, y, z, t) \tag{4.21}$$

while along the land shoreline, no normal fluxes of momentum and heat are allowed:

$$\vec{V}_n = 0 \; ; \qquad N_h \frac{\partial T}{\partial n} = 0 \tag{4.22}$$

where n is the outward directed normal.

(D) Open Boundary Conditions

At the open boundary, i.e., computational or artificial boundary, the surface elevation or mass flux is required, as is the flux of energy into the system. In the nested-grid model system, the velocity, elevation and temperature may be interpolated from the coarse grid model. Otherwise, free radiation or open boundary condition should be used (Miller et al., 1981). In the free radiation condition, no perturbation is incoming through that boundary. Outgoing signals are allowed to cross without back reflection. The condition applied is

$$h\, U_n = \zeta \sqrt{gh} \tag{4.23}$$

where U_n is the depth-averaged normal velocity. Because only the depth-averaged velocity is provided in this open boundary condition, in order to provide three-dimensional velocity, a profile at the open boundary must be adopted, for example, using a 2nd order parabola as described by Eq. (3.29) and (3.30). This profile is valid for a laminar type of flow and is an approximation for the turbulent flow.

(E) Initial Conditions

The initial spatial distribution of velocities and temperature distribution must be specified for the simulation. The velocities are taken to be zero, unless the initial velocity field is given. A step-growth wind is used in the simulation for a smooth start purpose, and a warm-up period is introduced for the variable wind process. In the case of thermal stratification, the initial temperature field is needed.

4.1.3 σ Coordinates Transformation

The σ coordinate transformation, as shown in Fig. 4.1, leads to a smooth representation of the topography. Additionally, the same order of resolution for the shallow and deeper parts of the water body will be applied to the model equation. The model equations are transformed from (x, y, z, t) to (x', y', σ, t') coordinates (Swanson, 1986), where,

$$x' = x \quad y' = y \quad \sigma = \frac{z - \zeta(x,y,t)}{h(x,y) + \zeta(x,y,t)} \quad t' = t \tag{4.24}$$

The differential operator transformation can be derived from the following relationships based on the chain rule (see Appendix 1):

$$\frac{\partial}{\partial x} = \frac{\partial}{\partial x'} - \frac{1}{H}\left[(1+\sigma)\frac{\partial \zeta}{\partial x'} + \sigma\frac{\partial h}{\partial x'}\right]\frac{\partial}{\partial \sigma} \tag{4.25}$$

$$\frac{\partial}{\partial y} = \frac{\partial}{\partial y'} - \frac{1}{H}\left[(1+\sigma)\frac{\partial \zeta}{\partial y'} + \sigma\frac{\partial h}{\partial y'}\right]\frac{\partial}{\partial \sigma} \tag{4.26}$$

$$\frac{\partial}{\partial z} = \frac{1}{H}\frac{\partial}{\partial \sigma} \tag{4.27}$$

$$\frac{\partial}{\partial t} = \frac{\partial}{\partial t'} - \frac{1}{H}\left[(1+\sigma)\frac{\partial \zeta}{\partial t}\right]\frac{\partial}{\partial \sigma} \tag{4.28}$$

Therefore, model equations (4.1) to (4.5) in sigma co-ordinates are now written as (all ′ sign will be dropped for notational convenience):

$$\frac{\partial u}{\partial t} + u\frac{\partial u}{\partial x} + v\frac{\partial u}{\partial y} + \omega\frac{\partial u}{\partial \sigma} = fv - g\frac{\partial \zeta}{\partial x} + B_x + \tau_u + \frac{1}{H}\frac{\partial}{\partial \sigma}\left(\frac{K_v}{H}\frac{\partial u}{\partial \sigma}\right) \tag{4.29}$$

$$\frac{\partial v}{\partial t} + u\frac{\partial v}{\partial x} + v\frac{\partial v}{\partial y} + \omega\frac{\partial v}{\partial \sigma} = -fu - g\frac{\partial \zeta}{\partial y} + B_y + \tau_v + \frac{1}{H}\frac{\partial}{\partial \sigma}\left(\frac{K_v}{H}\frac{\partial v}{\partial \sigma}\right) \tag{4.30}$$

$$\frac{\partial P}{\partial \sigma} = -\frac{1}{H}\rho g \tag{4.31}$$

$$\frac{\partial \zeta}{\partial t} + \frac{\partial Hu}{\partial x} + \frac{\partial Hv}{\partial y} + \frac{\partial H\omega}{\partial \sigma} = 0 \tag{4.32}$$

$$\frac{\partial T}{\partial t} + u\frac{\partial T}{\partial x} + v\frac{\partial T}{\partial y} + \omega\frac{\partial T}{\partial \sigma} = \tau_T + \frac{1}{H}\frac{\partial}{\partial \sigma}(\frac{N_v}{H}\frac{\partial T}{\partial \sigma}) \tag{4.33}$$

where ω is the vertical velocity component in the σ coordinates, as

$$\omega = \frac{w}{H} - \frac{u}{H}(\sigma\frac{\partial H}{\partial x} + \frac{\partial \zeta}{\partial x}) - \frac{v}{H}(\sigma\frac{\partial H}{\partial y} + \frac{\partial \zeta}{\partial y}) - \frac{1}{H}(\sigma\frac{\partial H}{\partial t} + \frac{\partial \zeta}{\partial t}) \tag{4.34}$$

τ_u, τ_v and τ_T are the horizontal eddy diffusivity terms in the σ coordinates (see Appendix 1).

$$\tau_u = \frac{1}{H}\frac{\partial H\tau_x}{\partial x} - \frac{1}{H}\frac{\partial}{\partial \sigma}\left[(\sigma\frac{\partial H}{\partial x} + \frac{\partial \zeta}{\partial x})\tau_x\right] + \frac{1}{H}\frac{\partial H\tau_y}{\partial y} - \frac{1}{H}\frac{\partial}{\partial \sigma}\left[(\sigma\frac{\partial H}{\partial y} + \frac{\partial \zeta}{\partial y})\tau_y\right] \tag{4.35}$$

where,

$$\tau_x = K_h\left[\frac{\partial u}{\partial x} - \frac{\partial u}{\partial \sigma}(\frac{\sigma}{H}\frac{\partial H}{\partial x} + \frac{1}{H}\frac{\partial \zeta}{\partial x})\right] \tag{4.36}$$

$$\tau_y = K_h\left[\frac{\partial u}{\partial y} - \frac{\partial u}{\partial \sigma}(\frac{\sigma}{H}\frac{\partial H}{\partial y} + \frac{1}{H}\frac{\partial \zeta}{\partial y})\right] \tag{4.37}$$

and similar formula can be derived for the τ_v and τ_T.

B_x and B_y are atmospheric pressure gradients (neglected), baroclinic density gradients due to the temperature difference, and coordinates transformation, as follows:

$$B_x = -\frac{gH}{\rho_0}\frac{\partial}{\partial x}\int_\sigma^0 \rho d\sigma + \frac{g}{\rho_0}\frac{\partial H}{\partial x}\int_\sigma^0 \sigma\frac{\partial \rho}{\partial \sigma}d\sigma \tag{4.38}$$

$$B_y = -\frac{gH}{\rho_0}\frac{\partial}{\partial y}\int_\sigma^0 \rho d\sigma + \frac{g}{\rho_0}\frac{\partial H}{\partial y}\int_\sigma^0 \sigma\frac{\partial \rho}{\partial \sigma}d\sigma \tag{4.39}$$

All the boundary conditions can be easily transformed into the forms in σ coordinates using the appropriate operator transformation described in Eqs. (4.25) to (4.28).

4.1.5 Turbulence Parameterization

Because the ratio of vertical length scale to horizontal length scale is very small for most lakes, the horizontal mixing terms are orders of magnitude smaller that the vertical mixing terms. The usage of a sophisticated turbulence closure model for the horizontal mixing terms are generally not warranted. The effect of stratification on the intensity of vertical turbulent mixing is parameterized by the empirical stability functions, see Eq. (3.15). The stability function ϕ_1 and ϕ_2 are taken as (Blumberg, 1986):

$$\phi_1 = (1 + \sigma_1 R_i)^{m_1}, \quad \phi_2 = (1 + \sigma_2 R_i)^{m_2} \tag{4.40}$$

where the constants $\sigma_1, m_1, \sigma_2, m_2$ are empirical constants:

$$\phi_1 = (1.0 + R_i)\,(1.0 - 0.1\,R_i)^{1/2} \tag{4.41}$$

$$\phi_2 = (1.0 - 0.1\,R_i)^{1/2} \tag{4.42}$$

$$\phi_1 = 0.0; \quad \phi_2 = 0.0; \quad \text{for } R_i > 10 \tag{4.43}$$

For wind generated circulation a parabolic distribution is used (Koutitas & O'Connor, 1980).

$$K_{v0} = \sigma\,(1 + \sigma)\,\sqrt{\tau_s/\rho}\,C_\kappa\,h \tag{4.44}$$

where, τ_s is the wind shear stress at water surface. $C_\kappa = 0.2 - 0.4$ is the constant.

It is obvious from Eq. (3.14) that in the case of stable thermal stratification (positive high Richardson number), the vertical transport of momentum and heat are suppressed, while in the unstable case (negative Richardson number) the transport is enhanced. Finally it should be pointed out that the above formula is not universal and further investigation is needed.

4.1.6 Numerical Schemes for the 3D Model

(A) Fractional Step Method for the 3D Model

The fractional step method (time-splitting) was first developed by Yanenko (1971). A consistency analysis has been done for the linear equations. Although the analysis has not yet been made for the full non-linear Navier-Stokes equations, it has been used successfully in a number of hydrodynamic models and advection-diffusion transport models. The key point is that the equation to be solved is broken into a series of intermediate steps, for example, advection and diffusion, so that the most suitable scheme can be employed for a specific step according to the mathematical and physical features of each step equation. Splitting momentum equations into two steps, that is, advection step and propagation + diffusion + source step, Eqs. (4.29), (4.30), give,

$$\frac{\partial u^*}{\partial t} = -u\frac{\partial u}{\partial x} - v\frac{\partial u}{\partial y} - \omega\frac{\partial u}{\partial \sigma} + fv - g\frac{\partial \zeta}{\partial x} + B_x + \tau_u \tag{4.45}$$

$$\frac{\partial v^*}{\partial t} = -u\frac{\partial v}{\partial x} - v\frac{\partial v}{\partial y} - \omega\frac{\partial v}{\partial \sigma} - fu - g\frac{\partial \zeta}{\partial y} + B_y + \tau_v \tag{4.46}$$

$$\frac{\partial u}{\partial t} = \frac{1}{H}\frac{\partial}{\partial \sigma}\left(\frac{K_u}{H}\frac{\partial u^*}{\partial \sigma}\right) \tag{4.47}$$

$$\frac{\partial v}{\partial t} = \frac{1}{H}\frac{\partial}{\partial \sigma}\left(\frac{K_v}{H}\frac{\partial v^*}{\partial \sigma}\right) \tag{4.48}$$

(B) Grid Discretization and Finite Difference Representation

As shown in Fig. 4.2, a staggered finite difference grid system is used. Horizontally, ζ and T are computed at the centre of mesh with u at left and right faces and v at the up and down faces of the mesh. This arrangement is convenient for derivatives and boundary conditions. Vertically, the horizontal velocity components are calculated at the level surface, therefore, the boundary conditions at the bottom, i.e., no-slip conditions $u = v = 0$, can be accurately satisfied. The vertical velocity w is calculated at the middle of each layer. A 3D view of discretization is

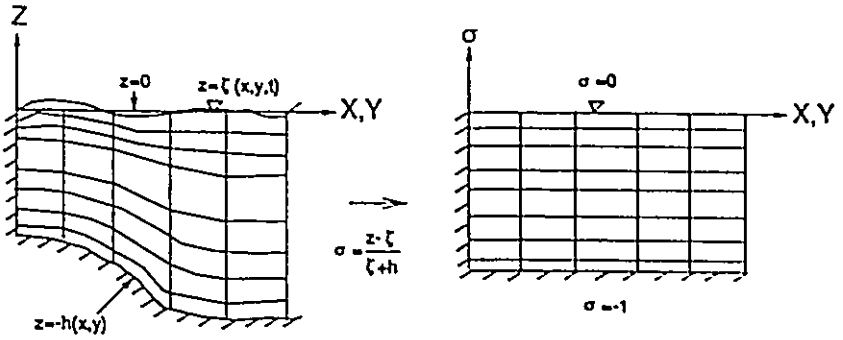

Fig. 4.1 σ coordinates transformation in the vertical plane, from layer discretization in the Cartesian coordinates (left) to the one in σ coordinates (right).

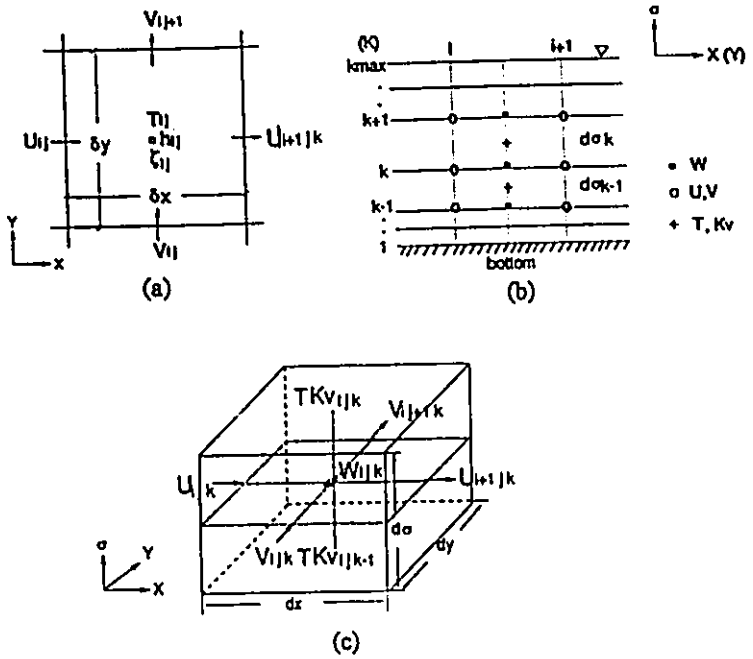

Fig. 4.2 Variable arrangements in a staggered finite difference grid system for the 3D hydrodynamic model. (a) view of a horizontal grid, (b) view of a vertical mesh, and (c) a 3D view.

also shown in the figure. In order to increase resolution both in the free surface and bottom layers, a mesh of varying thickness $\Delta\sigma$ can be used. The finite difference representation of a variable can be written as:

$$\phi(x, y, \sigma, t) = \phi(i\Delta x, j\Delta y, k\Delta\sigma, n\Delta t) = \phi^{n}_{ijk} \tag{4.49}$$

where, $i = 1, 2, \ldots, imax$; $j = 1, 2, \ldots, jmax$; $k = 1, 2, \ldots, kmax$; $imax$, $jmax$ and $kmax$ are the maximum grid number in the x, y, and σ directions, respectively; n refers to the time level of integration. Let the following expressions

$$\delta_t\phi = (\phi_{ijk}{}^{n+1} - \phi_{ijk}{}^{n}) / \Delta t \tag{4.50}$$

$$\delta_x\phi = (\phi_{i+1jk} - \phi_{i-1jk}) / (2\Delta x) \tag{4.51}$$

$$\delta_x{}^2\phi = (\phi_{i+1jk} - 2\phi_{ijk} + \phi_{i-1jk}) / \Delta x^2 \tag{4.52}$$

$$\bar{\phi}^{x} = (\phi_{i+1jk} + \phi_{i-1jk}) / 2 \tag{4.53}$$

represent the first derivative in the time and x directions, the second derivative in the x direction, and average value of ϕ in the x direction. Similar expressions are straightforward in the y and z directions. In addition, one can define

$$\delta_\sigma{}^2\phi^{n}{}_{ijk} = (K_v{}^{n}{}_{ijk}\,\frac{\phi^{n}{}_{ijk+1} - \phi^{n}{}_{ijk}}{\Delta\sigma_k} - K_v{}^{n}{}_{ijk-1}\,\frac{\phi^{n}{}_{ijk} - \phi^{n}{}_{ijk-1}}{\Delta\sigma_{k-1}}) / \left[(\Delta\sigma_k + \Delta\sigma_{k-1}) / 2\right] \tag{4.54}$$

as the finite difference of the vertical diffusivity term, where ϕ is a horizontal velocity component.

(C) Numerical Scheme for the Advection Step

An explicit scheme is applied for the advection step:

$$\delta_t u = -u\delta_x u - \bar{v}^{xy}\delta_y u - \bar{\omega}^{x}\delta_\sigma u + f\bar{v}^{xy} - g\delta_x\zeta + \overline{B_x}^{x\sigma} + \tau_u \tag{4.55}$$

$$\delta_t v = -\bar{u}^{yx}\delta_x v - v\delta_y v - \bar{\omega}^{y}\delta_\sigma v - f\bar{u}^{xy} - g\delta_y\zeta + \overline{B_y}^{y\sigma} + \tau_v \tag{4.56}$$

$$\delta_t\zeta = -\delta_x(HU) - \delta_y(HV) \tag{4.57}$$

The baroclinic terms at layer k can be expressed as:

$$B_x = -\frac{g}{\rho_0}\delta_x\left(H\sum_{m=k}^{kmax-1}\rho_m\Delta\sigma_m\right) + \frac{g}{\rho_0}\frac{\partial H}{\partial x}\sum_{m=k}^{kmax-1}(\rho_{m+1}-\rho_m)\sigma_m \tag{4.58}$$

$$B_y = -\frac{g}{\rho_0}\delta_y\left(H\sum_{m=k}^{kmax-1}\rho_m\Delta\sigma_m\right) + \frac{g}{\rho_0}\frac{\partial H}{\partial y}\sum_{m=k}^{kmax-1}(\rho_{m+1}-\rho_m)\sigma_m \tag{4.59}$$

(D) Implicit Scheme for the Vertical Eddy Diffusion Step

As pointed out in Chapter 3, the explicit scheme is very constrained on the time step due to the stability requirement, therefore, the implicit scheme has to be used. A Crank-Nickolson semi-implicit scheme is used here. Equations for the vertical eddy viscosity step become

$$u^{n+1}{}_{ijk} = u^{*n}{}_{ijk} + \frac{\Delta t}{\bar{H}^2}(\delta_\sigma{}^2 u^{*n}{}_{ijk} + \delta_\sigma{}^2 u^{n+1}{}_{ijk})/2 \tag{4.60}$$

$$v^{n+1}{}_{ijk} = v^{*n}{}_{ijk} + \frac{\Delta t}{\bar{H}^2}(\delta_\sigma{}^2 v^{*n}{}_{ijk} + \delta_\sigma{}^2 v^{n+1}{}_{ijk})/2 \tag{4.61}$$

Rearranging Eqs. (4.60) and (4.61), the following equations can be obtained.

$$au^{n+1}{}_{ijk+1} + bu^{n+1}{}_{ijk} + cu^{n+1}{}_{ijk-1} = f \tag{4.62}$$

$$av^{n+1}{}_{ijk+1} + bv^{n+1}{}_{ijk} + cv^{n+1}{}_{ijk-1} = g \tag{4.63}$$

where the coefficients a, b, c, f, g are

$$b = 1 + \frac{\Delta t}{\bar{H}^2}\left(\frac{K^n{}_{vijk}}{\Delta\sigma_k} + \frac{K^n{}_{vijk-1}}{\Delta\sigma_{k-1}}\right)\frac{1}{\Delta\sigma_k + \Delta\sigma_{k-1}} \tag{4.64}$$

$$a = -\frac{\Delta t}{\bar{H}^2}\left(\frac{K^n{}_{vijk}}{\Delta\sigma_k}\right)\frac{1}{\Delta\sigma_k + \Delta\sigma_{k-1}} \tag{4.65}$$

$$c = -\frac{\Delta t}{\bar{H}^2}\left(\frac{K^n{}_{vijk-1}}{\Delta\sigma_{k-1}}\right)\frac{1}{\Delta\sigma_k + \Delta\sigma_{k-1}} \tag{4.66}$$

$$f = u^n{}_{ijk} + \frac{\Delta t}{\bar{H}^2}\delta_\sigma{}^2 u^{*n}{}_{ijk} / 2 \tag{4.67}$$

$$g = v^n{}_{ijk} + \frac{\Delta t}{\bar{H}^2}\delta_\sigma{}^2 v^{*n}{}_{ijk} / 2 \tag{4.68}$$

It should be pointed out that the vertical eddy viscosity coefficients in a, b and c at the new time level are approximated by the one at previous time level. Then a tridiagonal set of equations for the velocity components u and v can be obtained and solved using the Thomas algorithm. The depth-averaged velocities can be obtained from the calculated multi-layered velocities

$$U = \sum_{k=1}^{k=kmax-1} \bar{u}^k \Delta\sigma_k \tag{4.69}$$

$$V = \sum_{k=1}^{k=kmax-1} \bar{v}^k \Delta\sigma_k \tag{4.70}$$

The vertical velocity component in σ coordinates can be calculated from

$$\omega^{n+1}{}_{ijk+1} = \omega^{n+1}{}_{ijk} - \frac{\Delta\sigma_k}{H}(\delta_t \zeta + \delta_x(\bar{H}^x \bar{u}^x) + \delta_y(\bar{H}^y \bar{v}^y)) \tag{4.71}$$

(E) Numerical Scheme for the Temperature Equation

The propagation of surface gravity wave is excluded in the temperature equation. Therefore, the constraints for the time step are related only to the advection and diffusion, especially the vertical diffusion terms. Similar to the hydrodynamic model scheme, the fractional step method is employed. For the first step, an explicit scheme is used,

$$\delta_t T = -\bar{u}^x \delta_x T - \bar{v}^y \delta_y T - \omega\delta_\sigma T + \tau_T \tag{4.72}$$

A similar implicit scheme for the momentum is applied for the vertical diffusivity term:

$$T^{n+1}_{ijk} = T^{*n}_{ijk} + \frac{\Delta t}{\bar{H}^2}(\delta_\sigma{}^2 T^{*n}_{ijk} + \delta_\sigma{}^2 T^{n+1}_{ijk})/2 \qquad (4.73)$$

Fig. 4.3 summarizes the order of operations for the multi-layered three-dimensional circulation model.

4.2 A NEW 3D WIND-INDUCED CIRCULATION MODEL (VH13D)

4.2.1 Discussion on the 2D and 3D Circulation Models

There exists a long tradition (over two decades) that for large scale water bodies, a two-dimensional modelling approach has been used to describe the depth-averaged mass transport and changes of water elevations (Schwab, 1981; Simons & Lam, 1986; Leendertse et al., 1970, 1975). Problems have been noticed by many researchers when the conventional two-dimensional models were used for the simulation of wind-driven circulation. Koutitas (1986) pointed out that velocity profiles develop in an entirely different way for the two cases of tidal and wind-induced circulation. Simons and Schertzer (1989) pointed out that the conventional 2DH circulation models underestimated the observed current speeds and wind-induced water set-up, partially during strong wind conditions. From the practical viewpoint, the simulation results may be adjusted by increasing the wind drag coefficient or decreasing the bottom friction coefficient. From a physical viewpoint, however, it is highly significant. They realized the physically unrealistic formulation of bottom friction terms in the 2DH model. However, no solution to this problem was proposed in their works.

In fact, the conventional depth-averaged two-dimensional model (2DH) was based on the long-wave circulation theory. The depth-averaged nonlinear advective terms in the 2DH

model are only valid when the vertical velocity distribution is nearly uniform. That is, the depth-averaged velocity does not differ much from the velocity at an arbitrary depth. This distribution is met only in special situations, such as in the storm surge phenomena, and, as a general rule, in tidal long waves. Moreover, the formulation of bottom shear stress, either using quadratic law or linear relation of the depth-averaged velocity, is unrealistic in the case of wind-induced circulation, where bottom return flow may have the opposite sign to the depth-averaged velocities. When depth-averaged velocities are zero or very small, the bottom shear stress disappears.

Efforts have been undertaken to improve the formulation of bottom friction stress and depth-averaged advective terms by introducing momentum dispersion into advective terms, and relating the bottom friction stress to the wind shear stress (Wang & O'Connor, 1975; Ramming & Kowalik, 1980). These works were not entirely satisfactory, due to the lack of sound physical mechanism. Koutitas (1988) first developed the "quasi depth-varying" (Q3D) model to account for the variety of horizontal velocity in the vertical plane (see Chapter 3). However, since the parabolic profile (see Eq.(3.29)) is only consistent with a laminar type of flow, the model was unable to accurately simulate surface drift currents and currents near the bottom, where steep velocity gradients are presented in the wind-driven flows in natural water bodies.

Optimizing the conventional depth-averaged circulation model for the simulation of wind-driven circulation is an urgent task because it is still widely-used for many engineering applications, and was used either as an external model in the external-internal mode-splitting 3D models (Simons, 1980; Sheng, 1983; Swanson, 1986), or used as the first module in the vertical-horizontal splitting 3D model (Lardner & Cekirge, 1988). Inherent problems were not realized when the conventional 2DH mode was used in these 3D models. Multi-layered three-

dimensional models are considered as the final solution to the above problem. However, the multi-layered 3D model is expensive in computation time, and furthermore, very high resolution grids are needed near the water surface and at the bottom, in order to predict the steep velocity gradients in these boundary layers.

An efficient three-dimensional wind-induced model can be developed based on the previous theoretical analysis, as well as field and laboratory measurements on the turbulent shear-induced flows. In contrast to the vertical-horizontal splitting (VHS) method which was developed in recent years, the vertical-horizontal intergrating (VHI) method is named in the consideration of integration of depth-averaged velocities and vertical velocity structure.

4.2.2 Formulation of the VHI3D Model

It is concluded from the discussion on the shear-induced currents, that for the turbulent flow, a double-logarithmic profile can be used to describe the vertical structure of the horizontal velocity, while the vertical eddy viscosity has a parabolic distribution. Including the viscous sublayer thickness, this parabolic eddy viscosity distribution can be expressed as

$$K_v = \frac{\lambda u_{*_s}}{h}(z + z_b)(z_s + h - z) \tag{4.74}$$

where, λ = numerical parameter; and z_b and z_s are characteristic lengths determined at $z = 0$ and $z = h$, respectively; z_b and z_s are a relative measure of the thickness of the viscous sublayer and are very small compared to h; $u_{*_s} = \sqrt{\tau_s/\rho}$ is the surface shear velocity which can be evaluated from the wind.

In fact, as shown in Fig. 4.4, the parabolic distribution of the vertical eddy viscosity is very similar to that widely used in coastal three-dimensional circulation models (Davis, 1980;

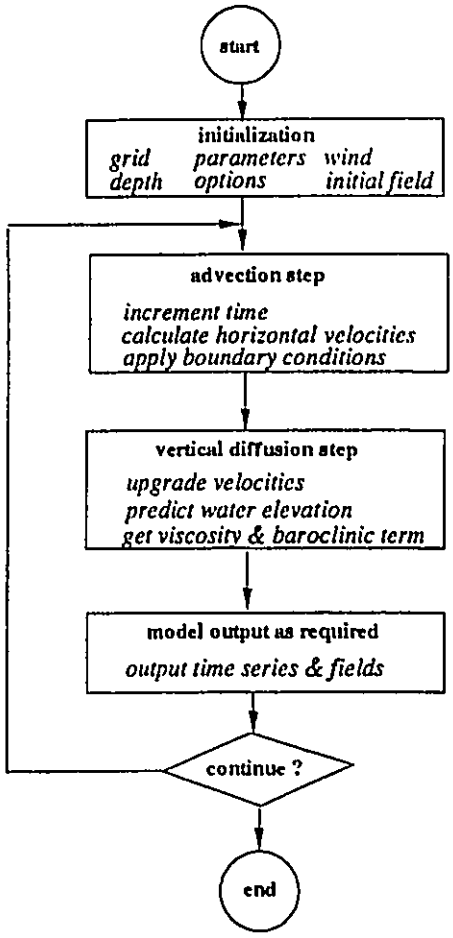

Fig. 4.3 Diagram of major steps of numerical scheme for the multi-layered three-dimensional hydrodynamic model.

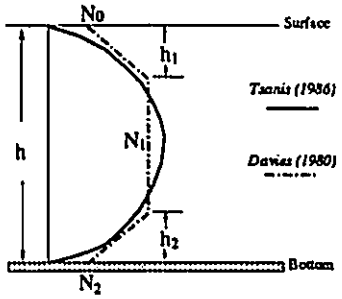

Fig. 4.4 Distributions of vertical eddy viscosity used in VHI3D (Tsanis, 1986) and one in coastal 3D circulation models (Davis, 1980). The latter has a top layer and a bottom layer where the viscosity changes linearly, and a middle layer with a uniform over depth.

Heaps, 1987; Al-Rabeh and Gunay, 1992). The latter has a top layer of depth h_1 in which viscosity N increases from N_0 to N_1 and a bottom layer of depth h_2 in which N decreases from N_1 to N_2. In between the two layers N is uniform over the depth. Numerical values of h_1, h_2, N_0, N_1 and N_2 can be found in Davies (1980).

Let's first consider only the x-direction. The velocity profile takes a double-logarithmic profile as

$$u(z) = a \ln(1 + \frac{z}{z_s}) + b \ln(1 - \frac{z}{z_b + h}) + c \tag{4.75}$$

For the convenience of model derivation, the vertical coordinates are taken in such way that the bottom is zero. The following conditions are used to determine the above coefficients a, b, c.

Condition 1: at the free surface, the shear-stress is evaluated by the wind velocity

$$K_v \frac{\partial u}{\partial z}\Big|_{z=h} = \tau_s ; \qquad \tau_s = \rho_a C_D W |W| \tag{4.76}$$

Condition 2: at the bottom, velocity equals to zero

$$u|_{z=0} = 0 \tag{4.77}$$

Condition 3: depth-averaged velocity definition

$$\frac{1}{H}\int_0^h u dz = U \tag{4.78}$$

These three conditions form an algebraic system with three unknown coefficients solution of which yield:

$$c = 0 \tag{4.78}$$

$$a = a_1 U + a_2 u_{*_s} \tag{4.79}$$

$$b = b_1 U + b_2 u_{*_s} \tag{4.80}$$

where, a_1, a_2, b_1 and b_2 are calculated from the following equations

$$a_1 = -\frac{p_2}{pq}, \quad a_2 = \frac{q_2}{pq}, \quad b_1 = \frac{p_1}{pq}, \quad b_2 = -\frac{q_1}{pq} \tag{4.81}$$

in which, p_1 and p_2 are related to the $z_{sh} = z_s/h$ and $z_{bh} = z_b/h$, and, $pq = p_1q_2 - q_1p_2$, q_1 and q_2 are derived from the integrations.

$$p_1 = \lambda z_{sh} \tag{4.82}$$

$$p_2 = \lambda z_{sh}/z_{bh} \tag{4.83}$$

$$q_1 = (1 + z_{sh})\left[\ln(1 + 1/z_{sh}) - 1\right] + z_{sh} \tag{4.84}$$

$$q_2 = -z_{bh}\left[ln(z_{bh}) - \ln(1 + z_{bh}) - 1\right] - (1 + z_{bh}) \tag{4.85}$$

Therefore, the velocity at any depth can be expressed in terms of the depth-averaged velocities and wind stress acting on the surface.

$$u(z) = (a_1U + a_2u_{*s})\ln(1 + \frac{z}{z_s}) + (b_1U + b_2u_{*s})\ln(1 - \frac{z}{z_b + h}) \tag{4.86}$$

Suppose the wind shear stress at surface can be divided into two components in x and y directions as

$$\tau_{sx} = \rho_a C_D W_x \sqrt{W_x^2 + W_y^2}, \quad \tau_{sy} = \rho_a C_D W_y \sqrt{W_x^2 + W_y^2}, \quad \tau_s = \sqrt{\tau_{sx}^2 + \tau_{sy}^2} \tag{4.87}$$

Define

$$\tau_x = \tau_{sx}/\tau_s, \quad \tau_y = \tau_{sy}/\tau_s \tag{4.88}$$

Then the general profiles for both velocity components u and v are written as

$$u = (a_1U + a_2\tau_x)\ln(1 + \frac{z}{z_s}) + (b_1U + b_2\tau_x)\ln(1 - \frac{z}{z_b + h}) \tag{4.89}$$

$$v = (a_1V + a_2\tau_y)\ln(1 + \frac{z}{z_s}) + (b_1V + b_2\tau_y)\ln(1 - \frac{z}{z_b + h}) \tag{4.90}$$

The bottom shear stresses then can be evaluated using these velocity profiles:

$$\tau_{bx} = K_v \frac{\partial u}{\partial z}\Big|_{z=0} = \lambda\sqrt{\tau_s/\rho}\, z_{bh}(z_{sh}+1)\left[(a_1U + a_2\tau_x)/z_{sh} - (b_1U + b_2\tau_x)/(z_{bh}+1)\right] \tag{4.91}$$

$$\tau_{by} = K_v \frac{\partial v}{\partial z}\Big|_{z=0} = \lambda\sqrt{\tau_s/\rho}\, z_{bh}(z_{sh}+1)\left[(a_1V + a_2\tau_y)/z_{sh} - (b_1V + b_2\tau_y)/(z_{bh}+1)\right] \tag{4.92}$$

Substitution of the above velocity profile in the convective terms and depth-averaging lead to

$$\frac{1}{h}\int_0^h u\frac{\partial u}{\partial x}dz = (X_1U + X_2\tau_x)\frac{\partial U}{\partial x} \tag{4.93}$$

$$\frac{1}{h}\int_0^h v\frac{\partial u}{\partial y}dz = (X_1V + X_2\tau_y)\frac{\partial U}{\partial y} \tag{4.94}$$

$$\frac{1}{h}\int_0^h u\frac{\partial v}{\partial x}dz = (X_1U + X_2\tau_x)\cdot\frac{\partial V}{\partial x} \tag{4.95}$$

$$\frac{1}{h}\int_0^h v\frac{\partial v}{\partial y}dz = (X_1V + X_2\tau_y)\frac{\partial V}{\partial y} \tag{4.96}$$

where,

$$X_1 = a_1^2 I_1 + 2a_1b_1I_2 + b_1^2 I_3 \tag{4.97}$$

$$X_2 = a_1a_2I_1 + (a_2b_1 + a_1b_2)I_2 + b_1b_2I_3 \tag{4.98}$$

and

$$I_1 = (1+z_{sh})\left[\ln^2(1+\frac{1}{z_{sh}}) - 2\ln(1+\frac{1}{z_{sh}}) + 2\right] - 2z_{sh} \tag{4.99}$$

$$I_2 = \frac{1}{2}(\ln z_{sh} + \frac{1}{2}) - z_{sh}(\ln z_{sh} + 1) + \frac{3}{4}z_{sh}^2 \tag{4.100}$$

$$I_3 = -z_{bh}\left[\ln^2\frac{z_{bh}}{1+z_{bh}} - 2\ln\frac{z_{bh}}{1+z_{bh}} + 2\right] + 2 \tag{4.101}$$

Based on the above expressions (see Appendix I for the detail derivations), the new two-dimensional circulation model for wind-driven flows is described as follows:

$$\frac{\partial U}{\partial t} + (X_1 U + X_2 \tau_x)\frac{\partial U}{\partial x} + (X_1 V + X_2 \tau_y)\frac{\partial U}{\partial y} = fV - g\frac{\partial \zeta}{\partial x} + K_h\left(\frac{\partial^2 U}{\partial x^2} + \frac{\partial^2 U}{\partial y^2}\right) + \frac{\tau_{sx} - \tau_{bx}}{\rho H} \qquad (4.102)$$

$$\frac{\partial V}{\partial t} + (X_1 U + X_2 \tau_x)\frac{\partial V}{\partial x} + (X_1 V + X_2 \tau_y)\frac{\partial V}{\partial y} = -fU - g\frac{\partial \zeta}{\partial y} + K_h\left(\frac{\partial^2 V}{\partial x^2} + \frac{\partial^2 V}{\partial y^2}\right) + \frac{\tau_{sy} - \tau_{by}}{\rho H} \qquad (4.103)$$

$$\frac{\partial \zeta}{\partial t} + \frac{\partial HU}{\partial x} + \frac{\partial HV}{\partial y} = 0 \qquad (4.104)$$

4.2.3 Characteristics of the VH13D Model

The model equation seems lengthy and complicated. However, the model equation only involves several sets of constants and coefficients and has no significant difference from the 2DH model. The vertical current structure can be easily calculated. As a result, the model is much more efficient than the multi-layered three-dimensional model. Due to the inherent integration of the vertical and horizontal current structure, the model has some advantages over the 2DH model and even over the complicated multi-layered 3D model. The calculation can follow these steps:

(1) specify the viscous sublayer thicknesses z_{sh} and z_{bh} and λ in the eddy viscosity distribution; input wind velocity components and depth data and all model parameters, such as wind drag coefficient, time step, grid size, Coriolis parameters.

(2) calculate the coefficients p_1, p_2, q_1 and q_2, a_1, a_2, b_1 and b_2 for the determination of profile and bottom shear stress terms, and, I_1, I_2, I_3, X_1, X_2 for the evaluation of advective terms.

(3) employ a finite difference scheme to numerically solve the model equations in a staggered-grid system; the predicted variables are the two depth-averaged velocity components U, V, and water elevation ζ.

(4) calculate the horizontal velocities at different depths, if required at a time, by simply employing the velocity profile given by Eqs. (4.89) and (4.90), using the depth-averaged velocity, wind shear stress and coefficients a_1, a_2, b_1 and b_2. The surface velocities can be calculated via

$$u_s = (a_1 U + a_2 \tau_x) \ln(1 + \frac{h}{z_s}) + (b_1 U + b_2 \tau_x) \ln(1 - \frac{h}{z_b + h}) \tag{4.105}$$

$$v_s = (a_1 V + a_2 \tau_y) \ln(1 + \frac{h}{z_s}) + (b_1 V + b_2 \tau_y) \ln(1 - \frac{h}{z_b + h}) \tag{4.106}$$

The vertical velocity component w can be calculate from the original continuity equation, i.e.,

$$w(z) = -\int_0^z (\frac{\partial u}{\partial x} + \frac{\partial v}{\partial y}) dz \tag{4.107}$$

4.2.4 Numerical Schemes for the 2DH, Q3D and VH13D Models

The same numerical scheme will be applied for the 2D, Q3D and VH13D models, because these models can be written in the same form of equations as follows:

$$\frac{\partial U}{\partial t} + U^* \frac{\partial U}{\partial x} + V^* \frac{\partial U}{\partial y} = fV - g\frac{\partial \zeta}{\partial x} + K_h(\frac{\partial^2 U}{\partial x^2} + \frac{\partial^2 U}{\partial y^2}) + \frac{\tau_{sx} - \tau_{bx}}{\rho H} \tag{4.108}$$

$$\frac{\partial V}{\partial t} + U^* \frac{\partial V}{\partial x} + V^* \frac{\partial V}{\partial y} = -fU - g\frac{\partial \zeta}{\partial y} + K_h(\frac{\partial^2 V}{\partial x^2} + \frac{\partial^2 V}{\partial y^2}) + \frac{\tau_{sy} - \tau_{by}}{\rho H} \tag{4.109}$$

$$\frac{\partial \zeta}{\partial t} + \frac{\partial HU}{\partial x} + \frac{\partial HV}{\partial y} = 0 \tag{4.110}$$

where U^* and V^* are the equivalent horizontal velocity components in x and y directions, respectively. For the 2DH model,

$$U^* = U \tag{4.111}$$

$$V^* = V \tag{4.112}$$

for the Q3D model,

$$U^* = 1.2U + \frac{\tau_{sx} h}{40\rho K_v} \tag{4.113}$$

$$V^* = 1.2V + \frac{\tau_{sy} h}{40\rho K_v} \tag{4.114}$$

and for the VHI3D model,

$$U^* = X_1 U + X_2 \tau_x \tag{4.115}$$

$$V^* = X_1 V + X_2 \tau_y \tag{4.116}$$

where X_1, X_2, τ_x and τ_y are given in Eqs. (4.97), (4.98) and (4.91), (4.92), respectively. The bottom shear stresses are evaluated by Eq. (3.10) or (3.11) for the 2DH model, Eqs. (3.32) and (3.33) for the Q3D model, Eqs. (4.91) and (4.92) for the VHI3D model.

Basically, there are three types of discretization methods for circulation models: finite difference method (FDM), finite element method (FEM) and control volume method (CVM). The FDM is mostly used in the coastal and lake circulation models because of its direct and simple formulation. The explicit scheme is computationally simple, but the time step must be small so that the Courant number is less than 1 in order to attain numerical stability. The implicit scheme does not have this limitation, but it requires the matrix equations. In fact, based on the Neumann's stability analysis, the Courant - Friedrichs - Lewy (CFL) condition for explicit scheme is

$$(\sqrt{gh_{max}} + U)\frac{\Delta t}{\Delta X} \le [1 - (f\,\Delta T)^2]^{1/2} \tag{4.117}$$

where, H_{max} is the maximum depth in the domain. Because the time step is small fraction of the inertial period $2\pi/f$ and the advective velocity U is much smaller that the speed of surface gravity wave $\sqrt{gh_{max}}$, therefore, Eq. (4.117) reduces to

$$\Delta t \le \frac{\Delta x}{\sqrt{g h_{max}}} \tag{4.118}$$

This equation indicates that the time step constraint mainly results from the horizontal pressure gradient terms. If we want to get a stable solution with the time step beyond the above constraint, the horizontal pressure gradient terms must be implicitly treated in the scheme. In the following section, an explicit scheme and a semi-implicit scheme are developed for the general model equations.

(A) Explicit Scheme

The same staggered horizontal grid used in the 3D model (see Fig. 4.2) will be employed. A forward scheme for time derivative and central difference scheme for advection terms are used in the following explicit scheme.

$$\frac{U_{ij}^{n+1} - U_{ij}^{n}}{\Delta t} = -U^{*}_{ij} \frac{U_{i+1j}^{n} - U_{i-1j}^{n}}{2\Delta x} - V^{*}_{ij} \frac{U_{ij+1}^{n} - U_{ij-1}^{n}}{2\Delta x} + f\,\bar{V}_{ij}^{xy} - g\frac{\zeta_{i+1j}^{n} - \zeta_{ij}^{n}}{\Delta x} + \left(\frac{\tau_{sx} - \tau_{bx}}{H}\right)_{ij}^{n} \tag{4.119}$$

$$\frac{V_{ij}^{n+1} - V_{ij}^{n}}{\Delta t} = -U^{*}_{ij} \frac{V_{i+1j}^{n} - V_{i-1j}^{n}}{2\Delta x} - V^{*}_{ij} \frac{V_{ij+1}^{n} - V_{ij-1}^{n}}{2\Delta x} - f\,\bar{U}_{ij}^{yx} - g\frac{\zeta_{ij+1}^{n} - \zeta_{ij}^{n}}{\Delta x} + \left(\frac{\tau_{sx} - \tau_{bx}}{H}\right)_{ij}^{n} \tag{4.120}$$

$$\frac{\zeta_{ij}^{n+1} - \zeta_{ij}^{n}}{\Delta t} = -\frac{H_{i+1j}^{n} U_{i+1j}^{n+1} - H_{ij}^{n} U_{ij}^{n+1}}{\Delta x} - \frac{H_{ij+1}^{n} V_{i+1j}^{n+1} - H_{ij}^{n} V_{ij}^{n+1}}{\Delta x} \tag{4.121}$$

in which,

$$\bar{U}_{ij}^{yx} = (U_{ij}^{n} + U_{ij-1}^{n} + U_{i+1j}^{n} + U_{i+1j-1}^{n})/4 \tag{4.122}$$

$$\bar{V}_{ij}^{xy} = (V_{ij}^{n} + V_{ij+1}^{n} + V_{i-1j}^{n} + V_{i-1j+1}^{n})/4 \tag{4.123}$$

Notice that the horizontal diffusivity terms are included in this scheme through a spatial

smoothing algorithm

$$\phi_{ij} = t_h \ \phi_{ij} + (1 - t_h) \frac{\phi_{i-1j} + \phi_{i+1j} + \phi_{ij-1} + \phi_{ij+1}}{4} \tag{4.124}$$

where ϕ refers to either U or V; t_h is the smoothing factor which can be determined by the horizontal coefficient of eddy viscosity K_h, grid size Δx and time step Δt,

$$t_h = 1 - \frac{4 \Delta t \ K_h}{(\Delta x)^2} \tag{4.125}$$

The computational step for the above scheme is very simple: after solving ${U_{ij}}^{n+1}$ and ${V_{ij}}^{n+1}$, the water elevation at new time level ${\zeta_{ij}}^{n+1}$ can be directly obtained from Eq. (4.121). All the boundary conditions can be easily implemented in the staggered grid system.

(B) Semi-Implicit Scheme

In the semi-implicit scheme, the horizontal pressure gradient terms in the momentum equations and the velocities in the continuity equation are treated implicitly using a Crank-Nickolson scheme. The finite difference equations for the models are:

$${U_{ij}}^{n+1} = {U^{**}}_{ij} - \frac{g \Delta t}{\Delta x} ({\zeta_{ij}}^{n+1} - {\zeta_{i-1j}}^{n+1}) \tag{4.126}$$

$${V_{ij}}^{n+1} = {V^{**}}_{ij} - \frac{g \Delta t}{\Delta x} ({\zeta_{ij}}^{n+1} - {\zeta_{ij-1}}^{n+1}) \tag{4.127}$$

$${\zeta_{ij}}^{n+1} = {\zeta_{ij}}^{n} - \frac{\Delta t}{2\Delta x} ({H_{i+1j}}^{n} {U_{i+1j}}^{n} - {H_{ij}}^{n} {U_{ij}}^{n} + {H_{ij+1}}^{n} {V_{i+1j}}^{n} - {H_{ij}}^{n} {V_{ij}}^{n}) \tag{4.128}$$

$$- \frac{\Delta t}{2\Delta x} ({H_{i+1j}}^{n} {U_{i+1j}}^{n+1} - {H_{ij}}^{n} {U_{ij}}^{n+1} + {H_{ij+1}}^{n} {V_{i+1j}}^{n+1} - {H_{ij}}^{n} {V_{ij}}^{n+1})$$

where

$${U^{**}}_{ij} = {U_{ij}}^{n} - \Delta t \ {U^{*}}_{ij} \frac{{U_{i+1j}}^{n} - {U_{i-1j}}^{n}}{2\Delta x} - \Delta t \ {V^{*}}_{ij} \frac{{U_{ij+1}}^{n} - {U_{ij-1}}^{n}}{2\Delta x} \tag{4.129}$$

$$+\Delta t\, f\, \bar{V}_{ij}^{xy} - g\,\Delta t\,\frac{\zeta_{i+1j}^{n}-\zeta_{ij}^{n}}{\Delta x}+\Delta t\,(\frac{\tau_{sx}-\tau_{bx}}{H})_{ij}^{n}$$

$$V^{**}_{ij} = V_{ij}^{n} - \Delta t\, U^{*}_{ij}\,\frac{V_{i+1j}^{n}-V_{i-1j}^{n}}{2\Delta x} - \Delta t\, V^{*}_{ij}\,\frac{V_{ij+1}^{n}-V_{ij-1}^{n}}{2\Delta x} \tag{4.130}$$

$$-\Delta t\, f\, \bar{U}_{ij}^{yx} - g\Delta t\,\frac{\zeta_{ij+1}^{n}-\zeta_{ij}^{n}}{\Delta x}+\Delta t\,(\frac{\tau_{sy}-\tau_{by}}{H})_{ij}^{n}$$

Substituting Eqs. (4.128) and (4.129) into Eq. (4.130), the following equation for water elevation can be obtained:

$$\zeta_{ij}^{n+1} = a\,\zeta_{i+1j}^{n+1} + b\,\zeta_{i-1j}^{n+1} + c\,\zeta_{ij+1}^{n+1} + d\,\zeta_{ij-1}^{n+1} + e \tag{4.131}$$

Let's define

$$q = (\frac{\Delta t}{2\Delta x})^2 g\ ; \quad p = 1 + q\,(H_{i+1j}^{n} + 2H_{ij}^{n} + H_{ij+1}^{n}) \tag{4.132}$$

then the coefficients in Eq. (4.132) can be expressed as

$$a = qH_{i+1j}^{n}/p\ ; \quad b = d = qH_{i}j^{n}/p\ ; \quad c = qH_{ij+1}^{n}/p \tag{4.133}$$

and

$$\frac{e}{p} = \zeta_{ij}^{n} - -\frac{\Delta t}{2\Delta x}[H_{i+1j}^{n}(U_{i+1j}^{n} + U^{**}_{i+1j}) - H_{ij}^{n}(U_{ij}^{n} + U^{**}_{ij} + V_{ij}^{n} + V^{**}_{ij}) \tag{4.134}$$

$$+ H_{ij+1}^{n}(U_{ij+1}^{n} + U^{**}_{ij+1})]$$

Equation (4.134) constitutes the single Helmholtz equation to be solved by successive over relaxation (SOR). Once the solution for the surface elevation is determined, Eqs. (4.126) and (4.127) are used to directly calculate the depth-averaged velocities. Compared to the other semi-implicit schemes (Backhau, 1983; Casulli, 1990), this scheme is more easily programmable, due to the introduction of U^{**}_{ij} and V^{**}_{ij}, which is similar to the solution obtained by the explicit scheme, except only using half of the horizontal pressure gradient terms. In summary, the procedures for the 2DH, Q3D, VHI3D models are shown in Fig. 4.5.

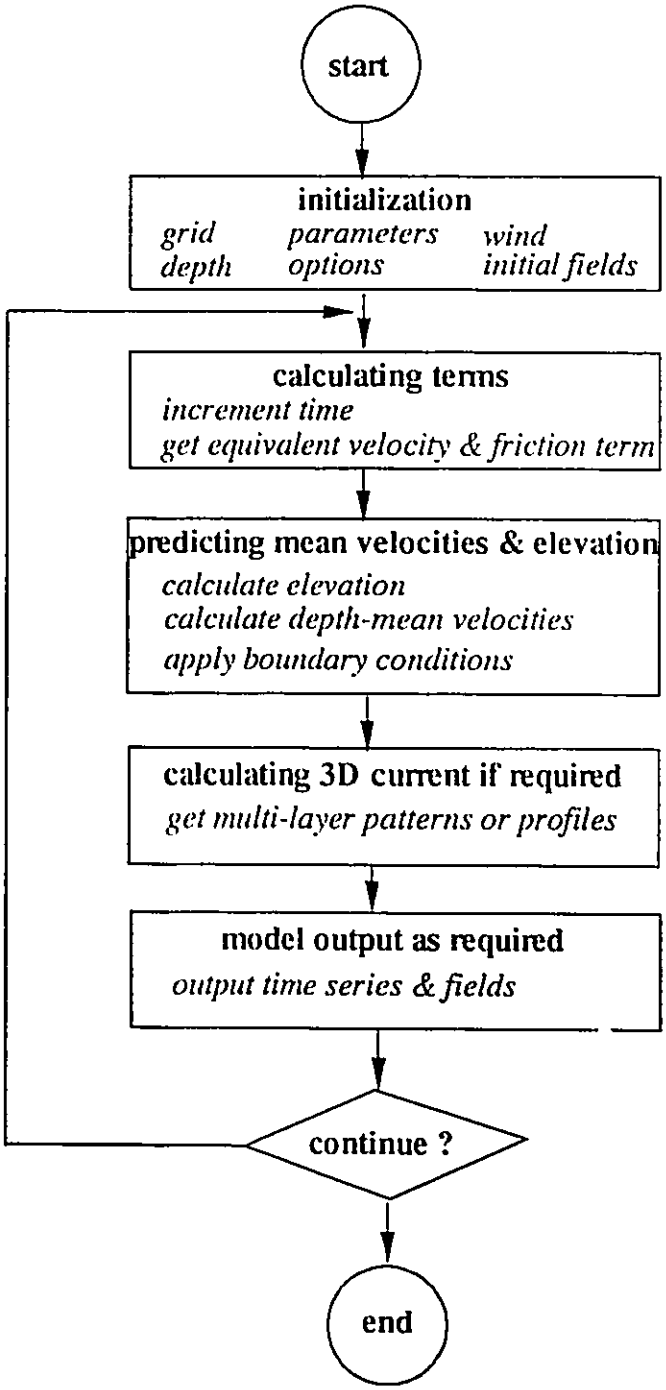

Fig. 4.5 Major steps of the numerical scheme for the 2DH, Q3D and VHI3D models.

4.3 A PARTICLE TRAJECTORY MODEL

Determination of oil or powerless vessel movement is required in the case of an oilspill or vessel rescue emergency in the marine and Great Lakes environment. Experiments using drogue and satellite drifters have been employed recently, to determine the current structure in lakes (Murthy et al., 1986; Wu et al., 1987; Tsanis et al., 1989; Boyce et al., 1991). After the current field has been obtained by the circulation model, it is a straightforward process to formulate a particle trajectory prediction model.

4.3.1 A Second-Order Lagrangian Trajectory Model

The equations governing the current-induced particle motions are

$$\frac{\partial X}{\partial t} = U(x,y); \qquad \frac{\partial Y}{\partial t} = V(x,y) \tag{4.135}$$

where X, Y are the particle's coordinates and U, and V are the depth-averaged velocity components. A second-order finite difference scheme can be applied to numerically integrate the above equations (Bennett et al., 1987). This scheme is given by

$$X^{n+1} = X^n + U(X^n, Y^n)\Delta t + \frac{1}{2}\frac{\partial U}{\partial x}(X^{n+1} - X^n)\Delta t + \frac{1}{2}\frac{\partial U}{\partial y}(Y^{n+1} - Y^n)\Delta t \tag{4.136}$$

$$Y^{n+1} = Y^n + V(X^n, Y^n)\Delta t + \frac{1}{2}\frac{\partial V}{\partial x}(X^{n+1} - X^n)\Delta t + \frac{1}{2}\frac{\partial V}{\partial y}(Y^{n+1} - Y^n)\Delta t \tag{4.137}$$

The values of the velocities U, V and their derivatives at time level n are computed using a bilinear interpolation scheme, as shown in Fig. 4.6, in each mesh from the values of u and v at the four corner points of the grid square in which the particle begins the time step. The slipping factor (resistance to the water) and/or windage factor (resistance to the wind) may be considered in the individual application.

4.3.2 A Random-Walk Approach

It should be mentioned that in the above trajectory prediction model, an assumption is obviously made, that is, that the particle follows the current, and its trajectory is determined uniquely by the current velocity. However, the particle trajectories are not uniquely defined by the local velocity field and may be affected by the turbulence and diffusion, as in the case of pollutant dispersion, due to the sub-grid scale processes, which are not simulated in the circulation model. The simulated trajectories in the above section can be considered as the centroid of a diffusive path or cloud. The dispersion can be simulated by a Monte-Carlo random-walk approach. The random displacement evaluated by random number and horizontal dispersion coefficients was added to the movement computed from the flow field (Leendertse, 1977; Koutitas, 1986). Assume that in lakes, the diffusive field is homogeneous. Therefore, trajectory prediction equations can be modified as:

$$X^{n+1} = X^{*} + r_1 \sqrt{6 \Delta t D_x} \tag{4.138}$$

$$Y^{n+1} = Y^{*} + r_2 \sqrt{6 \Delta t D_y} \tag{4.139}$$

where, X^{*} and Y^{*} are the predictions from the Lagrangian model (Eqs. 4.136 and 4.137); r_1 and r_2 is a pseudo-Gaussian random number with mean zero, and a standard derivation of unity; D_x and D_y are dispersion coefficients in the x and y directions, respectively. See Appendix 1 for the detail derivation. According to the drogue-cloud experiments in Lake Tai, the horizontal dispersion coefficients are about 0.1 to 1.0 m^2/s (Wu et al., 1987). The values in Lake Erie are about 1 to 10 m^2/s (Elzawahry, 1985).

4.4 A POLLUTANT TRANSPORT MODEL

4.4.1 Model Equation

Given a definition of the current field from the hydrodynamic model, and estimates of the source and sinks and interaction of the pollutant of interest with other pollutant or organisms present in the receiving water, a pollutant transport and fate model (water quality model) can predict the spatial and temporal distributions of the pollutant in the water column. The pollutant transport model is based on the conservation of the constituent mass equation expressed in three dimensions as

$$\frac{\partial C}{\partial t} + u\frac{\partial C}{\partial x} + v\frac{\partial C}{\partial y} + w\frac{\partial C}{\partial z} = \frac{\partial}{\partial x}(D_x\frac{\partial C}{\partial x}) + \frac{\partial}{\partial y}(D_y\frac{\partial C}{\partial y}) + \frac{\partial}{\partial z}(D_z\frac{\partial C}{\partial z}) + S + \left[R\right]C \qquad (4.140)$$

where C represents the concentration of the dissolved constituent; u, v and w are velocity components in the x, y and z directions, respectively; D_x, D_y, and D_z are turbulent dispersion coefficients (they are usually taken as constants); S represents sources and sinks of material; and $\left[R\right]$ is a reaction matrix. In most cases, a two-dimensional transport model is used:

$$\frac{\partial C}{\partial t} + U\frac{\partial C}{\partial x} + V\frac{\partial C}{\partial y} = D_x\frac{\partial^2 c}{\partial x^2} + D_y\frac{\partial^2 c}{\partial y^2} + S + \left[R\right]C \qquad (4.141)$$

The boundary conditions completing the model are (a) solid boundaries - zero normal flux, (b) free transmission boundaries - uniform flux and (c) pollutant sources - concentration is known.

4.4.2 Numerical Schemes

The above equation is solved by the finite difference method, and the same staggered grid, as in the circulation model, is used (the concentration is set at the centre of the mesh, see Fig. 4.2(a)). The finite difference representation of concentration can be written as:

$$C(x, y, t) = C(i\Delta x, j\Delta y, n\Delta t) = C^n{}_{ij} \qquad (4.142)$$

and define

$$CX_{ij} = u_{ij}\frac{\Delta t}{\Delta x}, \quad CY_{ij} = v_{ij}\frac{\Delta t}{\Delta y} \tag{4.143}$$

as the Courant number, and set

$$DX = \frac{D_x \Delta t}{\Delta x^2}, \quad DY = \frac{D_y \Delta t}{\Delta y^2} \tag{4.144}$$

The explicit central finite difference scheme

$$\delta D^n{}_{ij} = (D_x\frac{\partial^2 C}{\partial x^2} + D_y\frac{\partial^2 C}{\partial y^2})\Delta t = DX(C^n{}_{i+1j} - 2C^n{}_{ij} + C^n{}_{i-1j}) + DY(C^n{}_{ij+1} - 2C^n{}_{ij} + C^n{}_{ij-1}) \tag{4.145}$$

is used for the diffusion terms. Five numerical schemes are usually applied for the advection terms. The source term or simple decay term is not included in the following scheme, since it can be directly included.

(A) Explicit Scheme

$$C^{n+1}{}_{ij} = C^n{}_{ij} - CX_{ij}(C^n{}_{i+1j} - C^n{}_{i-1j}) - CY_{ij}(C^n{}_{ij+1} - C^n{}_{ij-1}) + \delta D^n{}_{ij} \tag{4.146}$$

(B) First-Order Upwind Scheme

$$\begin{aligned} C^{n+1}{}_{ij} &= C^n{}_{ij} - CX_{ij}(C^n{}_{ij} - C^n{}_{i-1j}) - CY_{ij}(C^n{}_{ij} - C^n{}_{ij-1}) + \delta D^n{}_{ij} \quad \text{for } u>0,\ v>0; \\ &= -CX_{ij}(C^n{}_{i+1j} - C^n{}_{ij}) - CY_{ij}(C^n{}_{ij+1} - C^n{}_{ij}) + \delta D^n{}_{ij} \quad \text{for } u<0,\ v<0 \end{aligned} \tag{4.147}$$

(C) McCormack Two-Step Scheme

$$C^{*n+1}{}_{ij} = C^n{}_{ij} - CX_{ij}(C^n{}_{i+1j} - C^n{}_{ij}) - CY_{ij}(C^n{}_{ij+1} - C^n{}_{ij}) + \delta D^n{}_{ij} \tag{4.148}$$

$$C^{**n+1}{}_{ij} = C^{*n}{}_{ij} - CX_{ij}(C^{*n+1}{}_{ij} - C^{*n}{}_{i-1j}) - CY_{ij}(C^{*n+1}{}_{ij} - C^{*n}{}_{ij-1}) + \delta D^{*n}{}_{ij} \tag{4.149}$$

$$C^{n+1}{}_{ij} = \frac{1}{2}(C^n{}_{ij} + C^{**n+1}{}_{ij}) \tag{4.150}$$

(D) QUICK Scheme

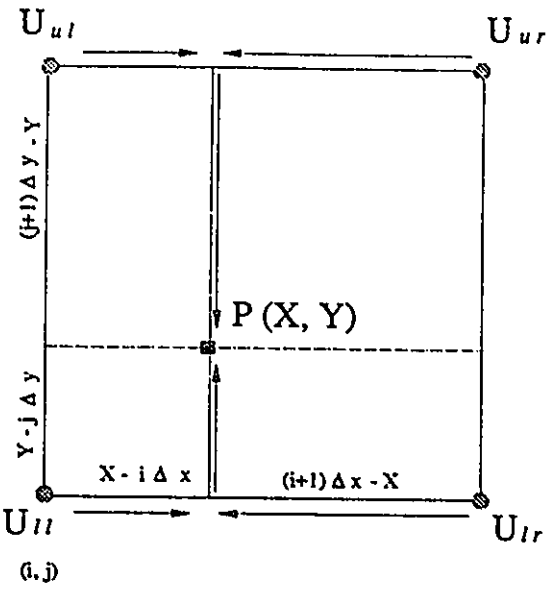

Fig. 4.6 A bilinear interpolation scheme for the particle trajectory prediction model.

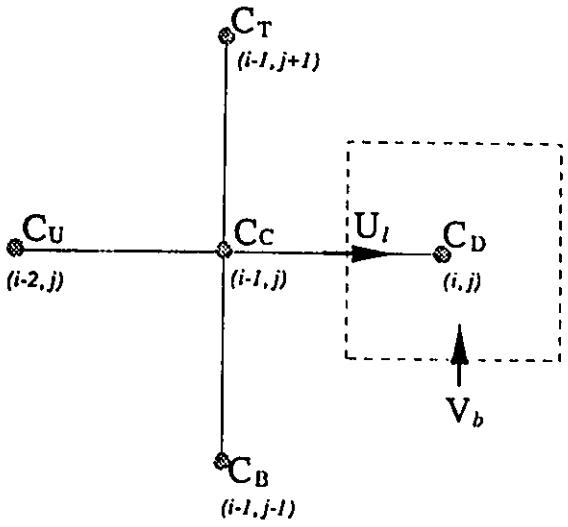

Fig. 4.7 Two-dimensional control volume showing nodes involved in estimating the left-face value for u_l >0 in QUICK or SHARP scheme.

The quadratic upstream interpolation for convective kinematics (QUICK) is a third-order upwinding scheme (Leonard, 1979). Fig. 4.7 shows a control volume centered at node (i,j), focusing on the convection across the left face for velocity $U_l > 0$. The downstream (D), central (C), upstream (U) and transverse (T, B) nodes in such cases are presented in the figure. For the basic QUICK scheme, the convected value averaged at the left face is

$$C_l = \frac{1}{2}(C_D + C_C) - \frac{1}{8}(C_D - 2C_C + C_U) + \frac{1}{24}(C_T - 2C_C + C_B) \tag{4.151}$$

which includes the linear interpolation term, the upstream normal curvature term and a small term representing the effect of upstream-biased transverse curvature in computing the face average. A similar formula is used for calculating the convected value C_b at the bottom faces. As a result, the left-face fluxes (convective plus diffusive) is

$$FLUXL_{ij} = CX_{ij}\, C_l - DX\,(C_{ij} - C_{i-1j}) \tag{4.152}$$

and bottom -face fluxes

$$FLUXB_{ij} = CY_{ij}\, C_b - DX\,(C_{ij} - C_{i-1j}) \tag{4.153}$$

The explicit algorithm is then written as

$$C^{n+1}{}_{ij} = C^{n}{}_{ij} + FLUXL_{ij} - FLUXL_{i+1j} + FLUXB_{ij} - FLUXB_{ij+1} \tag{4.154}$$

(D) SHARP Scheme

The same procedure is used in the Simple High-Accuracy Resolution Program (SHARP). The normal curvature factor (CF) is a constant in the QUICK algorithm (1 / 8 in Eq. 4.151). According to the range of normalized variable $\bar{C}_C = (C_C - C_U)/(C_D - C_U)$, the different approximations (third-order upwinding, quadratic formula, exact exponential upwinding formula) for the factor CF are employed in the SHARP method (Leonard, 1988).

In order to examine the behaviour of the above schemes, a one-dimensional advection-diffusion problem was used. The grid size was 1.0 m and the velocity u was 1.0 m/s. The horizontal dispersion coefficient D_x was taken as 0.002, 0.01, 0.1 and 1.0 m^2/s which corresponds to the Peclet number P_e of 500, 100, 10 and 1, respectively. The simulations by the upwind, McCormack, QUICK, and SHARP schemes were compared with the corresponding exact solutions (see Appendix 1). The conclusion can be clearly made from the comparisons in Fig. 4.8. For high advection case (Figs. 4.8(a), (b)), an oscillational solution is produced by the McCormack scheme, with slight overshoots by the QUICK scheme. The first upwind scheme does not produce overshoots, but the artificial (or numerical) diffusion makes the results distorted. The SHARP scheme produces good results without any oscillations or overshoots. When the diffusion is close to the advection, all schemes produce similar results, as shown in Figs. 4.8(c) and (d).

4.5 LMS - AN INTEGRATED LAKE MODELLING SYSTEM

The structure of the operational modelling system is of importance to the model evaluation and application. All sub-models should be integrally coupled, so that the system is capable of solving various complicated engineering problems. It includes pre-processing (model inputs and various options), processing (simulation and evaluation) and post-processing (outputs and application). Based on the above new model development, an integrated Lake Modelling System (LMS) is designed for the Great Lakes and its tributaries, as shown in Fig. 4.9. The system operates under steady or variable wind conditions using the 2DH, Q3D, VHI3D or 3D hydrodynamic models and permits usage of a nested-grid modelling system (which will be presented in Chapter 11). The output from the hydrodynamic model is then used as the input for

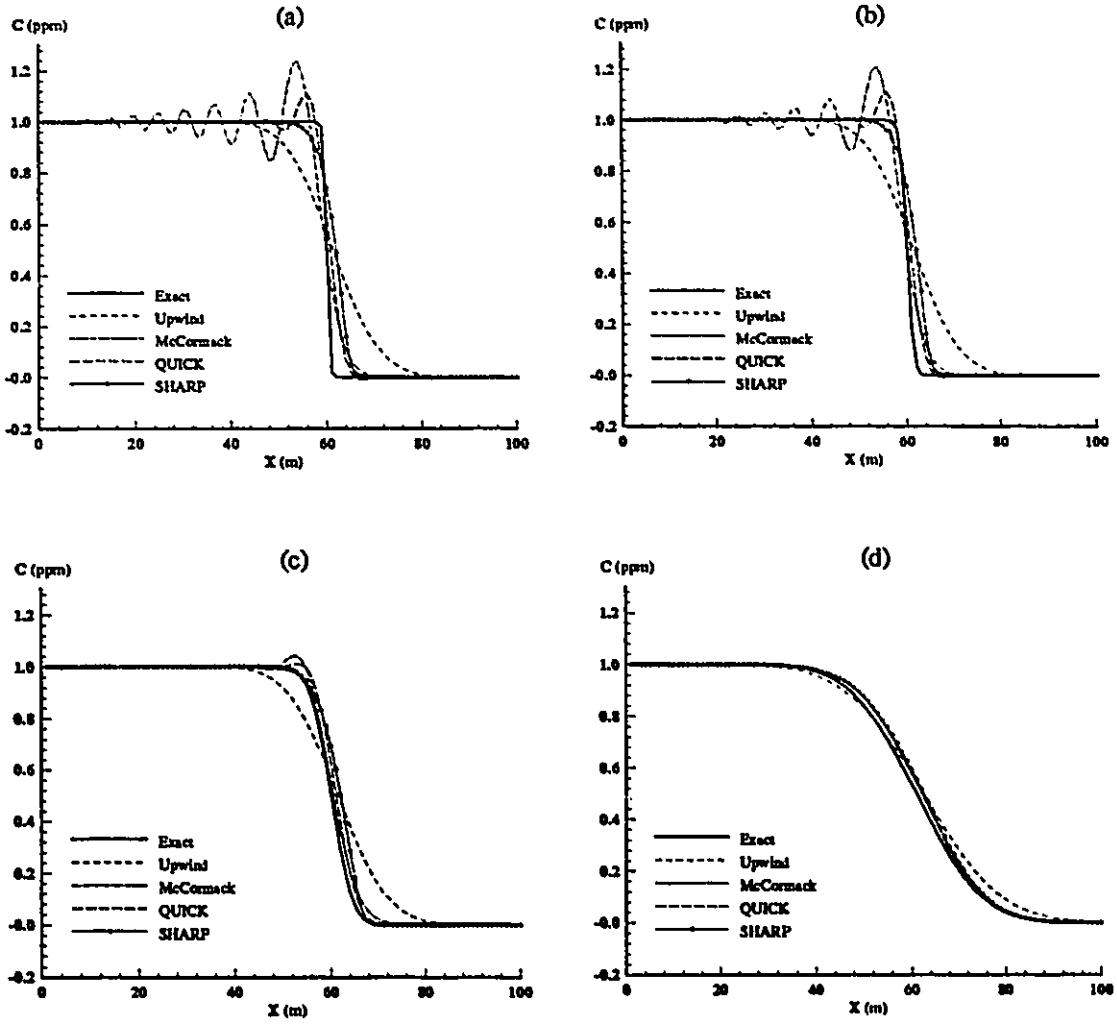

Fig. 4.8 Comparison of simulations by *Upwind*, *McCormack*, *QUICK*, and *SHARP* scheme with analytical solutions under various Peclet number ($P_e = u\Delta x / D_x$): (a) P_e=500, (b) P_e =100, (c) P_e =10, (d) P_e=1.

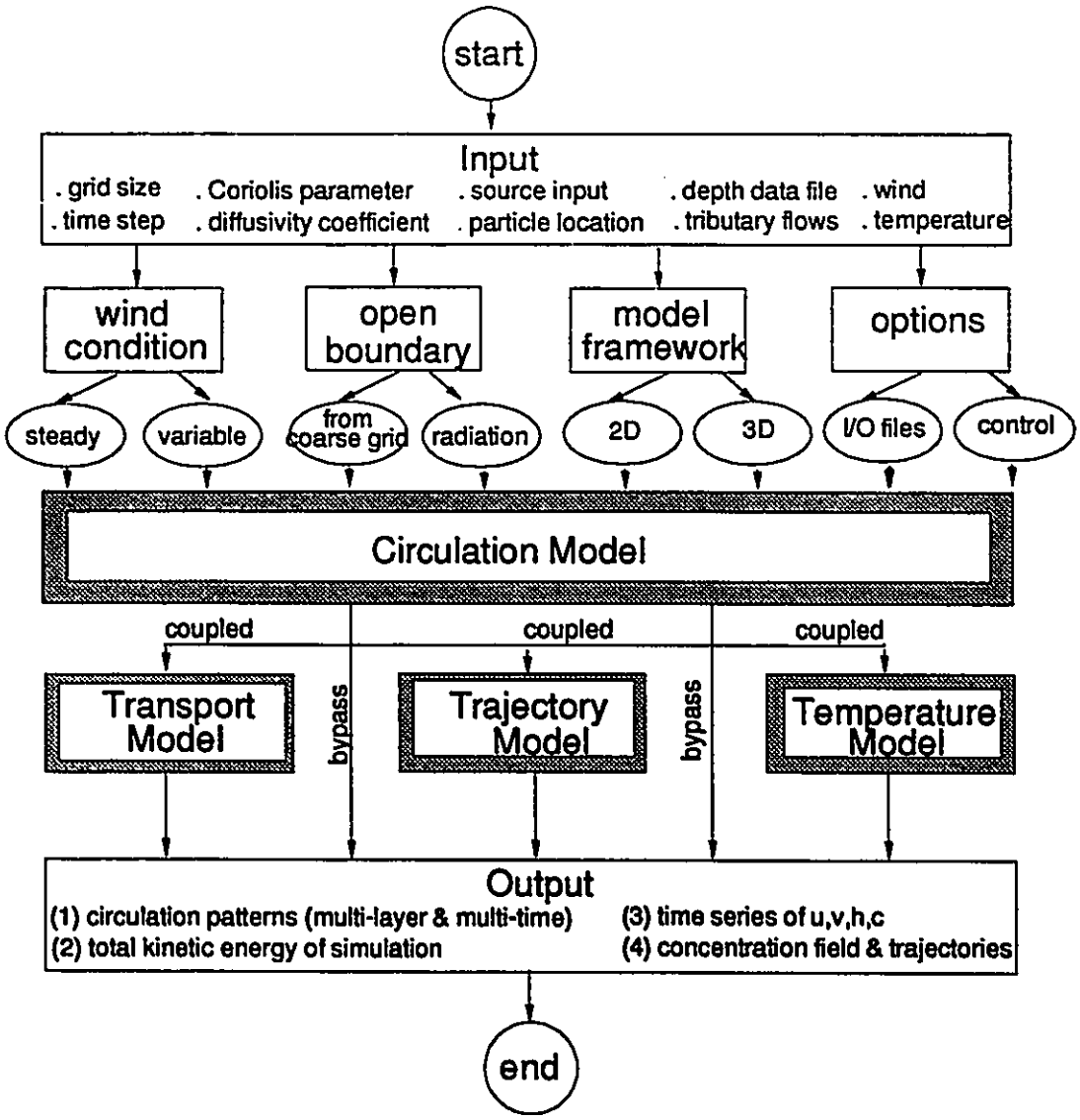

Fig. 4.9 An integrated lake modelling system (LMS) for the Great Lakes and tributaries.

the pollutant transport and trajectory prediction model. The transport model can accept inputs from various point sources such as creeks, sewer treatment plants (STP's) and combined sewer outfalls (CSO's), while in the trajectory model the movement of more than 5000 particles can be predicted. The temperature model is applied when the basin is thermally stratified.

LMS was developed in the Workstation - SunSparc 10/30, which has 100 Mb RAM, a DOS window and equipped with 3.4 Gb hard disk. There are 24 subroutines called by the main program, and 20 small programs (for preparing depth data, boundary of the lake and data analysis). In total, over 5000 lines of FORTRAN code have been written for this system.

LMS operates in an interactive environment, and has powerful computer graphics making use of the tools of the commercial packages TECPLOT and MATLAB. Fig. 4.10 shows the graphic capabilities including *X-Y Plot* - for time series of any variables such as wind, current, water elevation; *Vector Plot* - for depth-averaged or multi-layered circulation patterns; *Contours Plot* - for pollutant concentration field and spatial distribution of any variables; *Trajectory Plot* - for particle trajectories; *3D-Mesh Plot* - for a 3D view of any variables. By using zooming, rotating, and overlapping techniques, comprehensive plots are made from the above basic plots. For example, by overlapping a vector plot of a circulation pattern into a flooding contour plot of a pollutant concentration field, or a scattered plot of particle trajectories, the effect of current on the pollutant transport or particle movement should be clearly presented and easily analyzed. A batch mode allows non-expert users to run the modelling system and display the simulation results. Animation of these plots has also been developed for LMS, which provides a colourful and dynamic visualization of simulation results. It is also a good tool for public education on environmental issues.

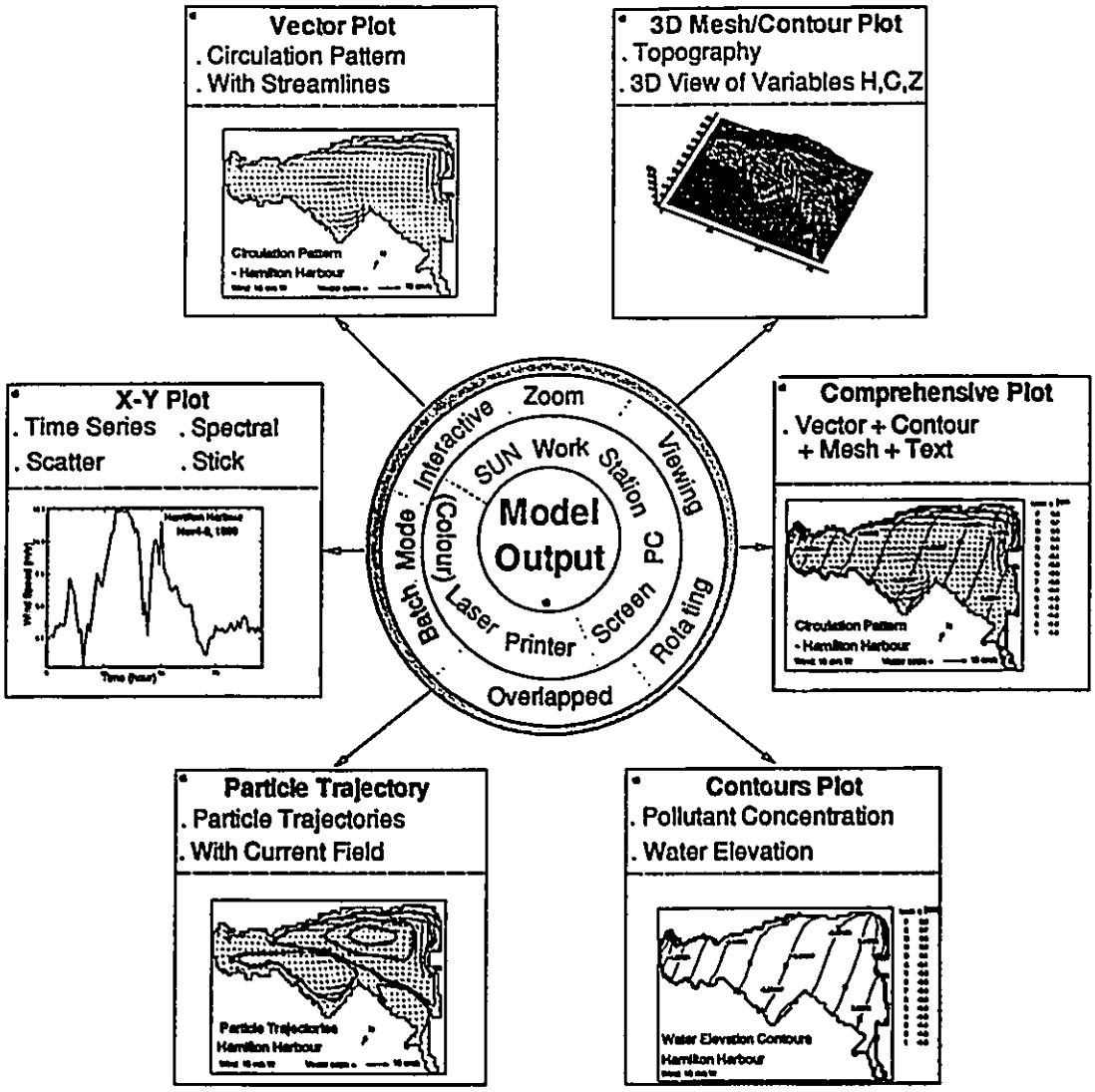

Fig. 4.10 The graphics capability for the outputs of LMS.

4.6 SUMMARY

In summary, a multi-layered three-dimensional circulation model (3D) is developed for both homogeneous and stratified lakes. The σ coordinate is used in the vertical direction to keep the same vertical resolution for shallow and deep parts of the basin. This leads to a smooth representation of the topography. The fractional step method is employed to split the vertical diffusion terms from the horizontal advective mode, so that a semi-implicit scheme can be applied for the vertical diffusion equation to offset the restriction on the time step. An efficient three-dimensional wind-induced model (VHI3D) is developed using a vertical-horizontal integrating (VHI) approach. A double-logarithmic velocity profile and parabolic distribution of eddy viscosity including both surface and bottom sublayer characteristic lengths are employed to accurately evaluate the bottom shear stress and depth-integrated advective terms. After solving the new two-dimensional circulation model, the vertical structure of the current can be directly calculated using the obtained depth-averaged velocity, known wind shear stress, and depth and sublayer thicknesses. Various schemes have been proposed for the pollutant transport model, and a second-order particle trajectory model with a random-walk approach is presented to predict the movement of drogues or drifters in lakes. Finally, an integrated lake modelling system - LMS is developed.

PART II

MODEL VERIFICATIONS WITH LABORATORY DATA

In order to test coding problems in computer programs, and determine model response in the numerical sense to the expected forcing mechanisms, an important step in model development is the comparison of model simulations with analytical solutions, experimental results, and field observation data. In the following two chapters, efforts will focus on the model evaluation, using analytical solutions and extant laboratory data.

The first study is to apply the depth-averaged circulation model (2DH), and dye transport model for the physical model of the Windermere Basin. The circulation model is verified with the measured hydraulically-induced flow pattern. The advection-diffusion model is employed to simulate the dye transport in the basin, and the simulations are used to study the residence time in the basin. In the second study, the laboratory data from the experiments on wind-induced countercurrents is used to verify the three-dimensional circulation models, i.e., 3D, Q3D and VHI3D. Then, these models are compared, for the simulation of wind-induced circulation patterns, in a simplified basin. Finally, a numerical experiment is undertaken to examine the wind-induced current in a stratified basin.

CHAPTER 5

DYE TRANSPORT AND RESIDENCE TIME IN A MODEL BASIN

In this chapter, the depth-averaged circulation model (2DH) will be calibrated in the physical model (with a 4:1 distortion in the length scale) of the Windermere Basin, using the measured hydraulically-induced flow pattern. The experimental validated velocity pattern is used as an input to a two-dimensional advection-diffusion model, to simulate the dye transport in the basin. Based on the simulations, the residence time and effects of wind, zone distribution and dikes on it will be examined.

5.1 INTRODUCTION

A collection of data from the prototype basin is most desirable. However, it is expensive, time-consuming and sometimes impossible (in the case of a new basin design). The effects of various factors cannot be isolated in the field study. As a result, aside from direct measurements in the field, two types of hydraulic models - the physical model and the numerical model, are often employed to reproduce the physical phenomenon observed in natural water bodies, and to examine the impact of proposed engineering projects on the body. A physical model is the scaled down version of a portion of the actual object, where the object may be an

existing or proposed water body. Physical modelling has a long tradition, and has been a great success in the design of hydroelectric engineering in rivers and reservoirs. However, it was not as popular for large-scale water bodies such as lakes, harbours and estuaries. This is because there are more complicated factors involved. The objective is mainly related to the environmental problems, which were not emphasised until recent years. A numerical model, on the other hand, is a set of equations, which are thought to represent the characteristics of the process being studied. The dimension and topography in the model could be the same as those in the prototype or physical model. Certain numerical methods have to be employed to solve these equations at all grid points.

The physical model is appealing because the results may be easily visualized. The model may be expensive to build, but once constructed, may be used for a variety of studies. A numerical model may be used in connection with a physical model, or directly for natural basins. A numerical model has several advantages over a physical model. For instance, it may be quicker to apply, and less costly with the aid of less expensive computers. Coriolis forces and heat exchanges may be more easily incorporated in the numerical model than in the physical model. The physical model requires that the entire model basin be rotated (Nydegger, 1979), which in turn increases the difficulty of flow measurements. Another advantage is that extreme conditions, such as very large winds or inflows, and impacts of various engineering designs on the receiving water can be studied at a lower cost. However, boundary conditions for the numerical model are often provided by the physical model or field measurements.

Similarity is the essential issue to be considered in the physical model. Geometric similarity requires that every dimension in the prototype be related to the model by a fixed ratio. The equivalence of force ratios between the model and prototype is referred to as dynamic

similarity, expressed as the Reynolds number (ratio of inertial to viscous forces), and the Froude number (ratio of inertial to gravitational forces). Because lakes, bays and basins are much larger in the horizontal direction than they are in the vertical (about 10^5 to 10^6 : 1 for the Great Lakes and 10^3 to 10^4 : 1 for bays, harbours and basins in the Great Lakes), physical models are often distorted in the vertical dimension in order to minimize the surface tension effect, and to facilitate the flow visualization. In the case of distortion in scale (with a vertical scale larger than the horizontal scale), it is necessary to make the model surface rougher in order to simulate the flow conditions in the prototype. It is impossible by using the same fluid, i.e., water in both the prototype and model to obtain Froude and Reynolds scaling. Since most geophysical flows are fully developed turbulent flows due to large length scales and small fluid viscosity, most hydraulic models simulating these flows use Froude scaling as the primary criterion for dynamic similarity. For the numerical model, geometric similarity is easily maintained, except for the inaccuracy in presenting the basin shape and depth, due to the grid discretization. Coriolis forces are easily included in the numerical model. Consequently, the Rossby number (ratio of rotational to inertial forces) can be maintained. The turbulence is described in the numerical model by various turbulence models, Therefore, calibration is required to justify these models.

A number of numerical models have been developed in the last decade to simulate large-scale circulation. Good calibration with physical models is rare, mainly due to lack of well-designed physical experiments, and the lack of integration of both models. However, such evaluation for numerical models is imperative. The flow visualization and dye transport experiments in the physical model of the Windermere Basin provide an unique opportunity to bridge such a gap.

5.2 A PHYSICAL MODEL OF THE WINDERMERE BASIN

The Windermere Basin lies at the south corner of Hamilton Harbour. It receives inflows from creeks, sewage treatment plants, and several sewer overflows. Contaminations in this basin became serious, and a cleanup of the basin is to be undertaken by dredging a portion of the basin. The physical model study was conducted at the National Water Research Institute (NWRI) to determine the hydraulic properties of the proposed basin design. Many basin configurations and flowrates have been tested (Engel, 1988) and only the standard case is presented in this study. In summary, the physical model, as shown in Fig. 5.1(a), is a fixed bed model (horizontal scale ratio of 1:60 and a vertical ratio of 1:15) with a 4:1 distortion. The depth in the model was 175 mm with a central trap of 350 mm, and a flowrate 11.4 *L/s*. Flow patterns were visualized by using Potassium Permangenate. In addition to the dye, 22 weighted ping-pong balls were released at the entrance of the basin at various times as an additional aid to visualize their trajectories; and to calculate the surface velocities in the model basin. Several flow conditioning schemes were examined, including the effects of spur dikes, a weir at the outflow of the basin, a flow deflector at the entrance of the basin, and a sediment trap. Detailed analysis of the experimental data can be found in Engel (1988) and Blaisdell (1990).

Numerical models were applied for modelling the circulation in the physical model of the Windermere Basin (Blaisdell et al., 1991). It was demonstrated that the nonlinear advective terms, and the horizontal viscosity terms in the two-dimensional circulation model are necessary to predict the zones of recirculation observed in the physical model. However, this work is limited in modelling hydraulically-driven currents. Further studies are required on the effect of flow patterns on the residence time distribution and dye transport, based on the current modelling.

(a)

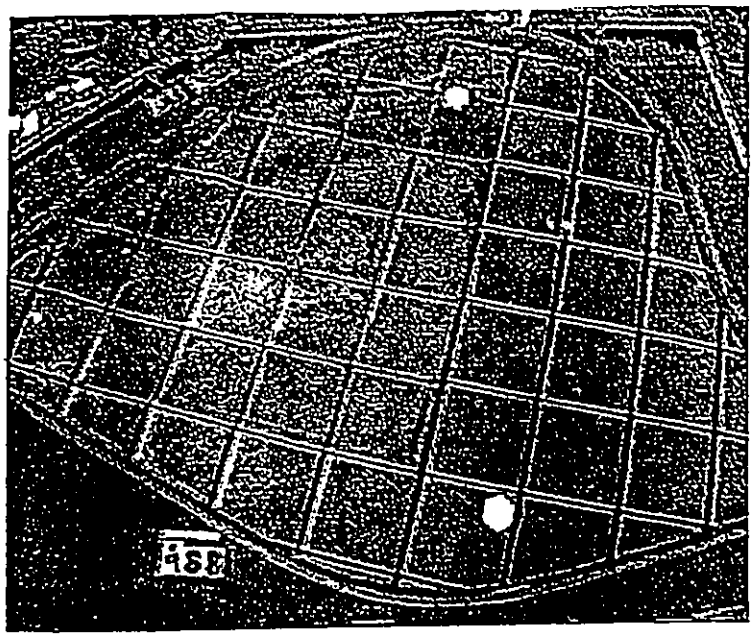

(b)

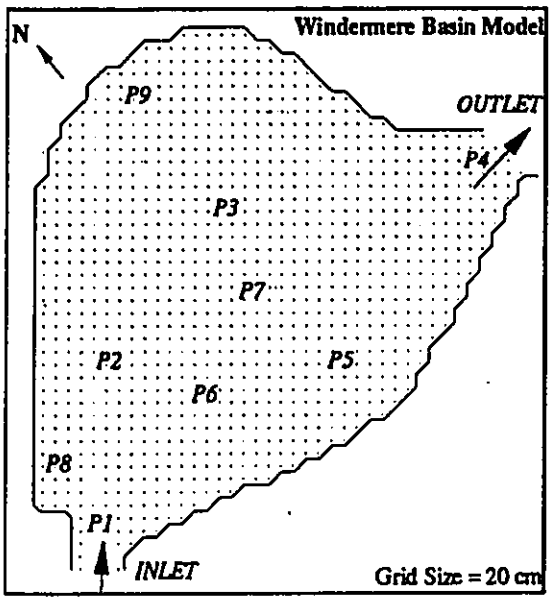

Fig. 5.1 Model of Windermere Basin: (a) the physical model in National Water Research Institute (NWRI) of Canada Centre for Inland Waters (CCIW) during testing as shown by VHS tape (the grid size is 1 meter and the white spots are the ping-pong balls); (b) the mathematical model, the grid is rotated counter - clockwise 45^0 with a size of 20 cm.

5.3 NUMERICAL MODELLING OF CIRCULATION PATTERN

The two-dimensional horizontal circulation model (2DH) is used to simulate the hydraulic circulation in the Windermere Basin model. A 44 by 47 square grid system with the grid size of $\Delta x = 0.2\,m$ is used, as shown in Fig. 5.1(b). The grid is rotated 45^0 counter-clockwise from north, to better represent the north shorelines. The points $P1$ to $P9$ are the locations where dye concentration will be displayed. Using an inflow $Q = 0.0114\,m^3/s$, and a Manning coefficient $n = 0.0115$ as in the standard case of the physical model of the Windermere Basin, the equations of motion are solved for a time step of $\Delta t = 0.04$ sec, and a value of smoothing factor $t_h = 0.995$ (eddy viscosity $A_h = 0.00125\,m^2/s$). The inlet Reynolds number $R_j = U_j h / \nu = 1.415\times10^4$, where U_j is the velocity at inlet, h is the depth at inlet, and ν is the kinematic viscosity of the water. The inlet Froude number is given as $Fr_j = U_j / \sqrt{gh} = 6.21\times10^{-2}$. The resulting hydraulic circulation of the above simulation is shown in Fig. 5.2, where the black arrows show the velocity vectors for the standard case derived from the drifter results in the experiments (Blaisdell, 1990). The magnitude and direction of the velocity vectors and the size of the recirculation zones from the simulation are in good agreement with those determined experimentally. It clearly indicates three zones of recirculation including the left hand eddy at the inlet, the central eddy, and the dead zone at the top of the basin. The advective flow path with strong current is deflected towards the left upon leaving the inlet areas. This is due to the squeezing of the advective flow between the two opposing eddies. As the central eddy develops, it forces the flow to the left, which results in a deflection and squeezing of the flow. At the top left hand side of the basin, a weak counterclockwise eddy is present. Although none of the ping-pong balls were recirculated in it, some of them show signs of being affected by it. For instance, the velocity of the ping-pong ball would drop suddenly in this region, or would be deflected to the right or left. In addition, the

advective path avoided the top of the basin, as if it was deflected by a weak eddy. In conclusion, the two-dimensional circulation model (2DH) was successful in simulating depth-averaged hydraulically-induced flow.

Horizontal eddy viscosity terms were ignored by most numerical hydrodynamic models, based on the assumption that they were very small compared with other terms. However, recent studies of the Windermere Basin (Blaisdell et al., 1991) and Lake Ontario (Wu and Tsanis, 1991) revealed that the horizontal eddy viscosity terms can not be ignored, especially for the hydraulically-induced flow in lakes. Their effects on the flow pattern were significant. Actually, there are no direct measurements on the horizontal eddy viscosity coefficient. In the present 2DH model, they are included through a spatial smoothing scheme. The eddy viscosity coefficient was then calculated from the corresponding smoothing factor, along with the time step and grid size. The bottom friction coefficient or Manning's coefficient, and horizontal eddy viscosity coefficient or smoothing factor, are the two important parameters in the model. A test using different values of these parameters has been undertaken. Fig. 5.3 shows the circulation patterns for eddy viscosity coefficients of 0.005, 0.0025, 0.00125 m^2/s. It is clearly indicated that a smaller size of eddies is obtained for a larger coefficient: a plug type of flow is presented for the large eddy viscosity. The simulation with a value of 0.00125 m^2/s (smoothing factor $t_h = 0.995$) gives most close result to the measured one. The Manning's coefficient has a similar effect on the flow simulation. Fig. 5.4 shows the circulation patterns for Manning's coefficient n=0.115 ($C_b = 0.0168$, for $h = 0.175\ m$), 0.0345 ($C_b = 0.01512$) and 0.0115 ($C_b = 0.00168$). The smaller size of eddies is presented for a larger Manning's coefficient, which corresponds to a rougher bottom and more resistance to the flow. A plug type flow appears for a value of 0.115. A value of $n = 0.0115$ gives the closest result to the measured one.

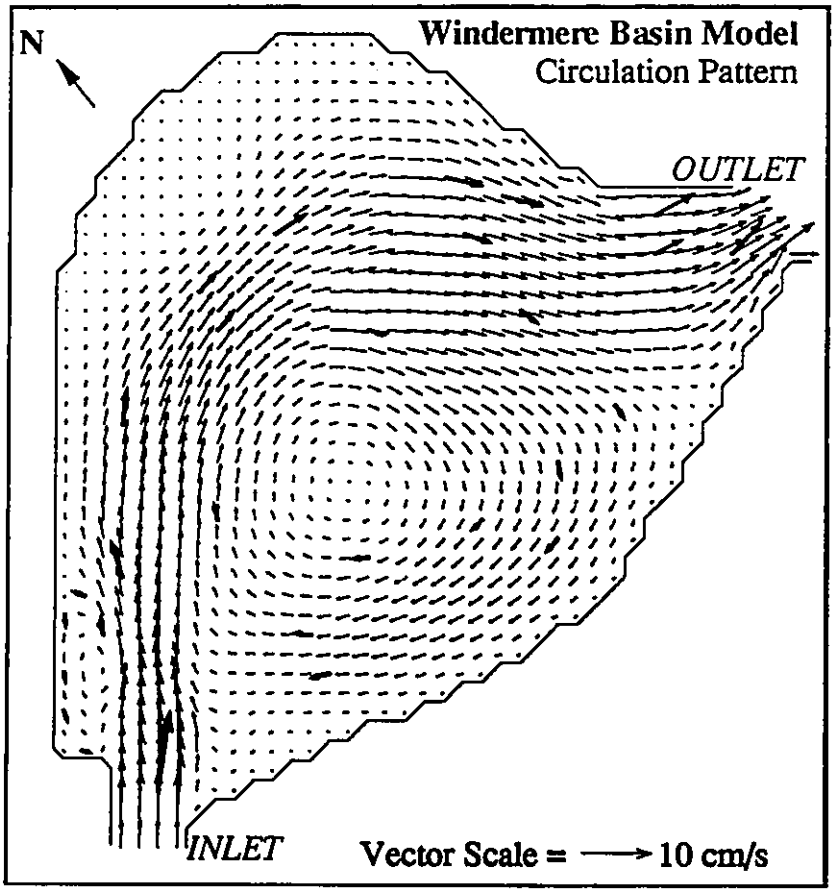

Fig. 5.2 The simulated depth-averaged circulation pattern in the physical model of Windermere Basin by the numerical model in the standard case. The black arrows show the velocities for the standard case, derived from the drifter experimental results (Blaisdell, 1990).

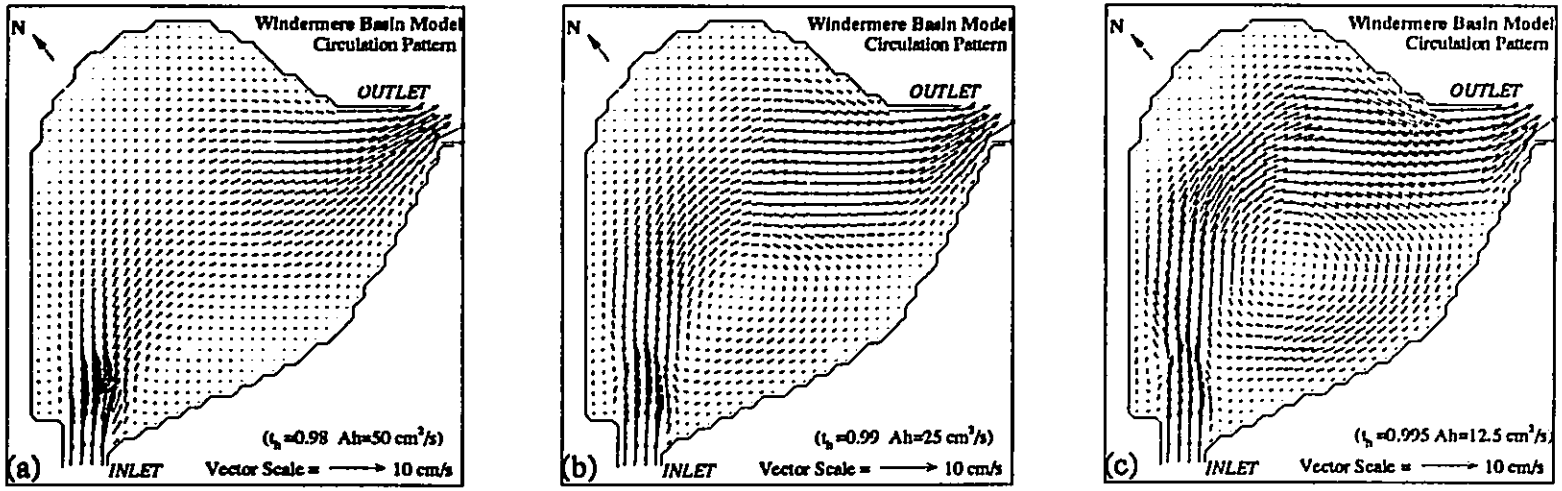

Fig. 5.3 Sensitivity of horizontal eddy viscosity A_h or smoothing factor t_h on the simulated circulation pattern in Windermere Basin (standard case): (a) $A_h = 50.0\ cm^2/s$ ($t_h = 0.98$). (b) $A_h = 25.0\ cm^2/s$ ($t_h = 0.99$). (c) $A_h = 12.5\ cm^2/s$ ($t_h = 0.995$).

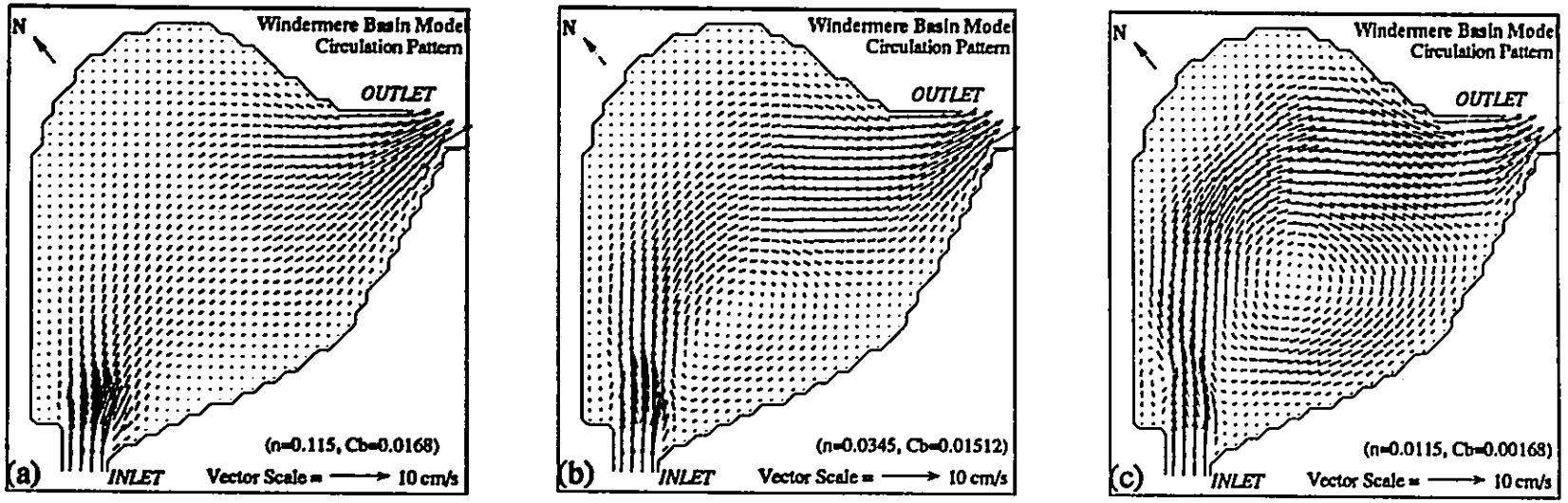

Fig. 5.4 Sensitivity of Manning's Coefficient n or bottom friction coefficient C_b on the simulated circulation pattern in Windermere Basin (standard case): with (a) n = 0.1150 (C_b = 0.01680), (b) n = 0.0345 (C_b = 0.01512), (c) n = 0.0115 (C_b = 0.00163).

5.4 NUMERICAL MODELLING OF DYE TRANSPORT

The hydraulically-induced circulation pattern (see Fig. 5.2) was used as an input in the two-dimensional advection-diffusion model to simulate the transport of the continuous injected dye in the basin. The location of the dye injection was in a channel, a few meters upstream from the inlet. The dye was fully mixed both in the vertical and horizontal planes, as it was entering the basin.

Initially, the first-order upwind scheme was applied for the advection-diffusion model. It is noticed that in the Windermere Basin, the Peclet number $P_e = U_j \Delta x / D$ at inlet ($U_j = 0.08\, m/s$, $\Delta x = 0.2\, m$, $D = 0.0005\, m^2/s$) is as high as 80. Therefore, the SHARP scheme, was applied for an accurate simulation. Fig. 5.5 shows the simulation results from the upwind scheme, the SHARP scheme and the random-walk tracking approach, for the dye (with the concentration of 1000 ppm) emitted from the central point of the inlet only at the first time step. The horizontal dispersion coefficient was taken as a constant of 0.0005 m^2/s in all methods. The equal concentration contours at 30, 60, and 120 seconds from the emission of the dye are presented in Fig. 5.5. In the random-walk tracking approach, the 1000 particles were released at the same point as in the advection-diffusion model. Then, the trajectories of the particles were tracked. The "concentration" field was constructed by counting the number of particles fallen in each grid. The results clearly indicate that the first-order upwind scheme introduced some numerical diffusivity, resulting in a larger dispersion than the SHARP scheme and the random-walk tracking approach. The random-walk tracking approach is able to simulate the transport and dispersion in the case of the impulsive input, but not in the case of the continuous input. The SHARP scheme will be employed in the following simulations.

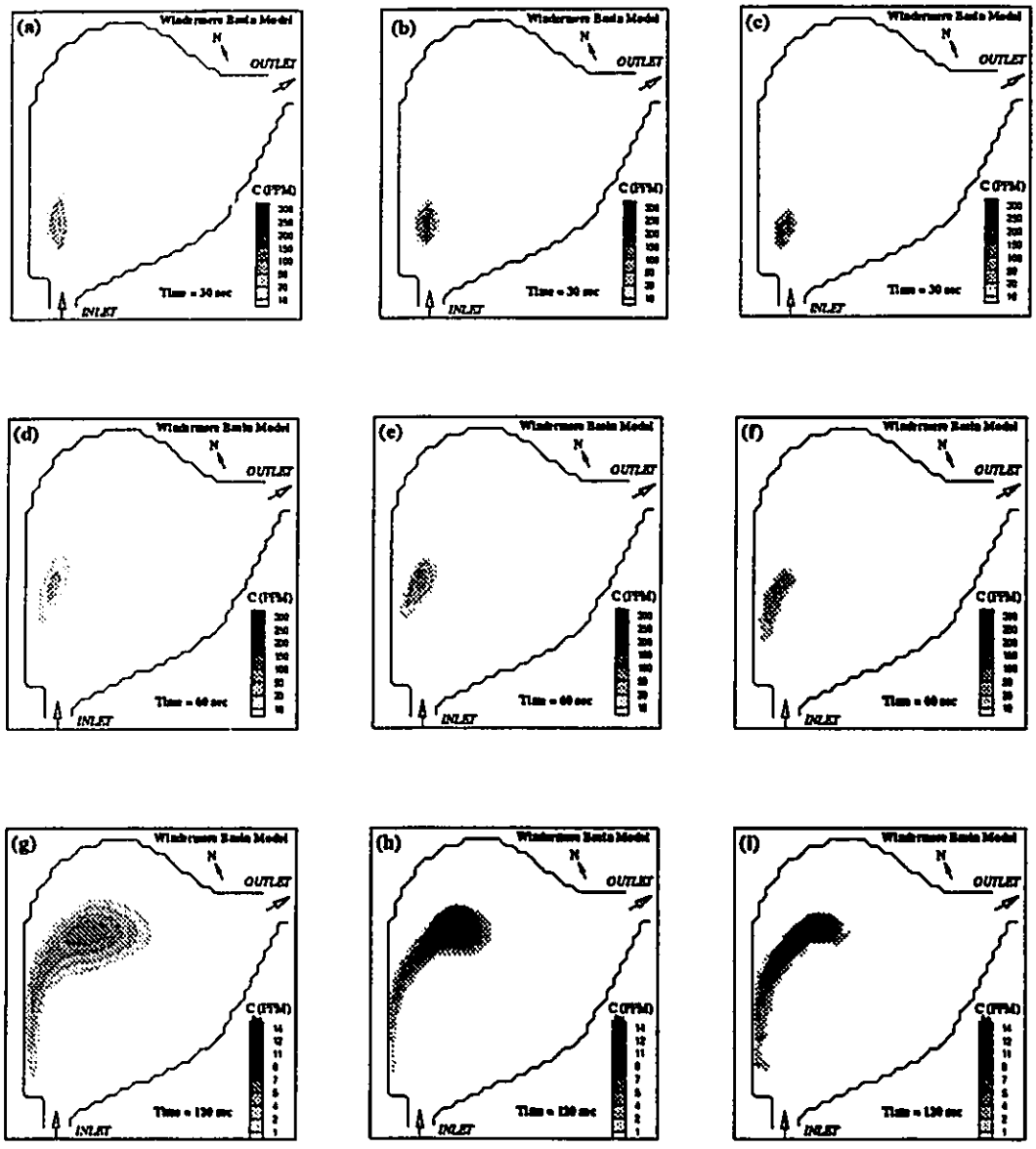

Fig. 5.5 Comparison of first-order upwinding scheme, SHARP scheme, and random-walk tracking approach for the simulation of a dye emitted into the basin. The simulations at 30, 60, 120 seconds are presented for the three methods: (a),(d),(g) for the first upwind scheme, (b), (e), (h) for the SHARP scheme, and, (c), (f), (i) for random-walk tracking approach.

A test was performed for a continuous dye released into the basin using different values of the dispersion coefficient, i.e., D = 0.1, 0.01, 0.001 and 0.0005 m^2/s. The inlet Peclet number had values of 0.16, 1.6, 16 and 80, respectively. Fig. 5.6 shows the equal dye concentration contours at six minutes after the dye release. In Fig. 5.6(a), the dye entering the basin is diffused faster than it is advected, resulting in the dye front covering the whole basin while moving towards the basin's outlet. In Figs. 5.6(c) and (d), the advection dominates the diffusion. The effects of the left hand side eddy at the inlet, the central eddy, and the dead zone are evident. The latter results are similar, indicating that the diffusion in both cases is insignificant. As we know, the dispersion coefficient varies with the plume width, as denoted by L (m). A formula with the power 4/3 of L was recommended for use by Lam, et al. (1984). To avoid the non-linear problem, as well as the difficulty in implicitly determining the dispersion coefficient, a variable but explicit coefficient was used, i.e., $D = 0.001\, L^{(4/3)}\ (m^2/s)$, where L was measured from the simulation result in Fig. 5.6(c). The concentration field for the variable coefficient is shown in Fig. 5.6(e). As observed from Figs. 5.6(c) and (e), the change of the concentration field is not significant. When the dye tends to be fully mixed in the basin, it is reasonable to use a constant coefficient in the numerical model.

Comparison of the above results, given in Fig. 5.6, with the experimental results, revealed that the best agreement between the simulation and the experiment will be achieved by using a value of dispersion coefficient of 0.001 m^2/s, which is of the same order as the eddy viscosity ($A_h = 0.00125\ m^2/s$) used in the hydrodynamic model.

Using the dispersion coefficient of 0.001 m^2/s, a simulation in the standard case for a continuous dye release is undertaken. Then these simulations are compared with the corresponding images reproduced from the VHS video tape of the experiment. Figs. 5.7(a), (b),

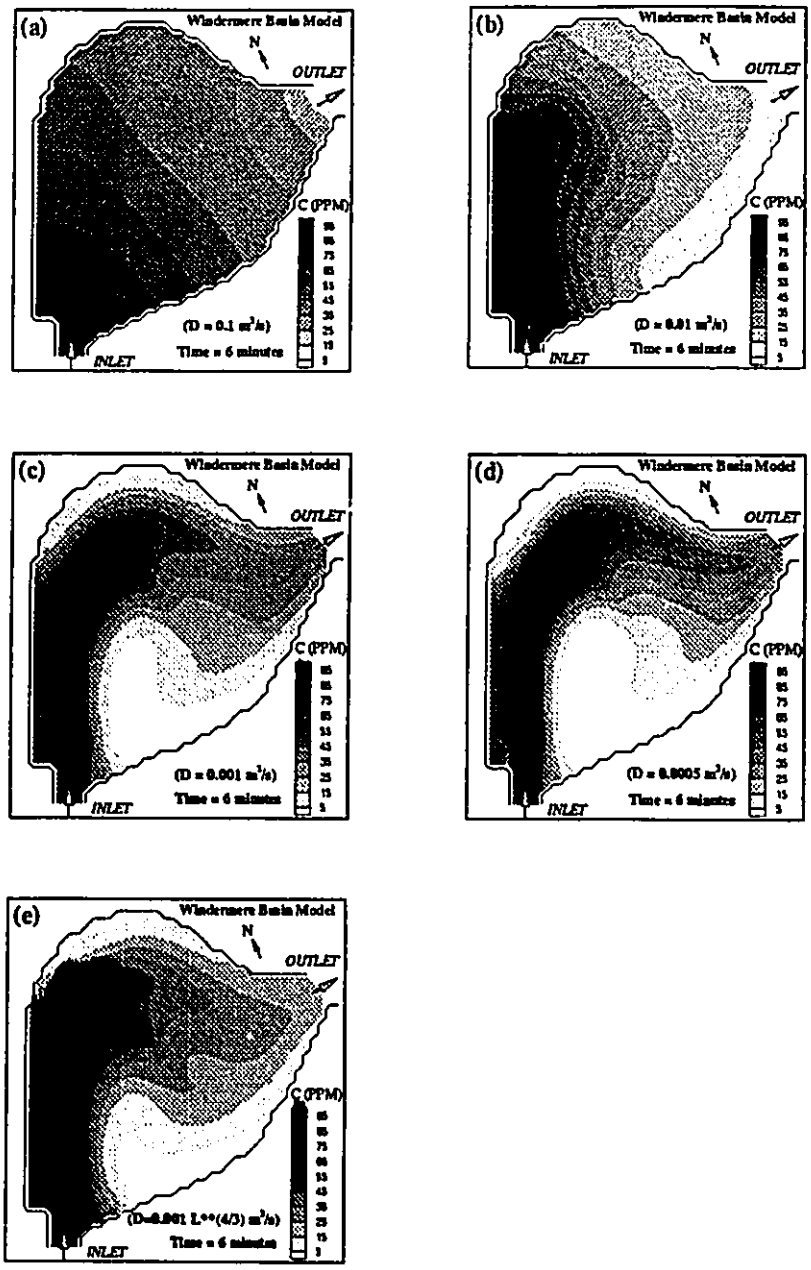

Fig. 5.6 *Advection-Diffusion Modelling*: simulated equal dye concentration contours for a continuous dye introduction at the inlet to the Windermere Basin model, 6 minutes after the dye release with dispersion coefficient of (a) D = 0.1 m^2/s, (b) D = 0.01 m^2/s, (c) D = 0.001 m^2/s, (d) D = 0.0005 m^2/s, and, (e) D = 0.001 $L^{(4/3)}$ m^2/s.

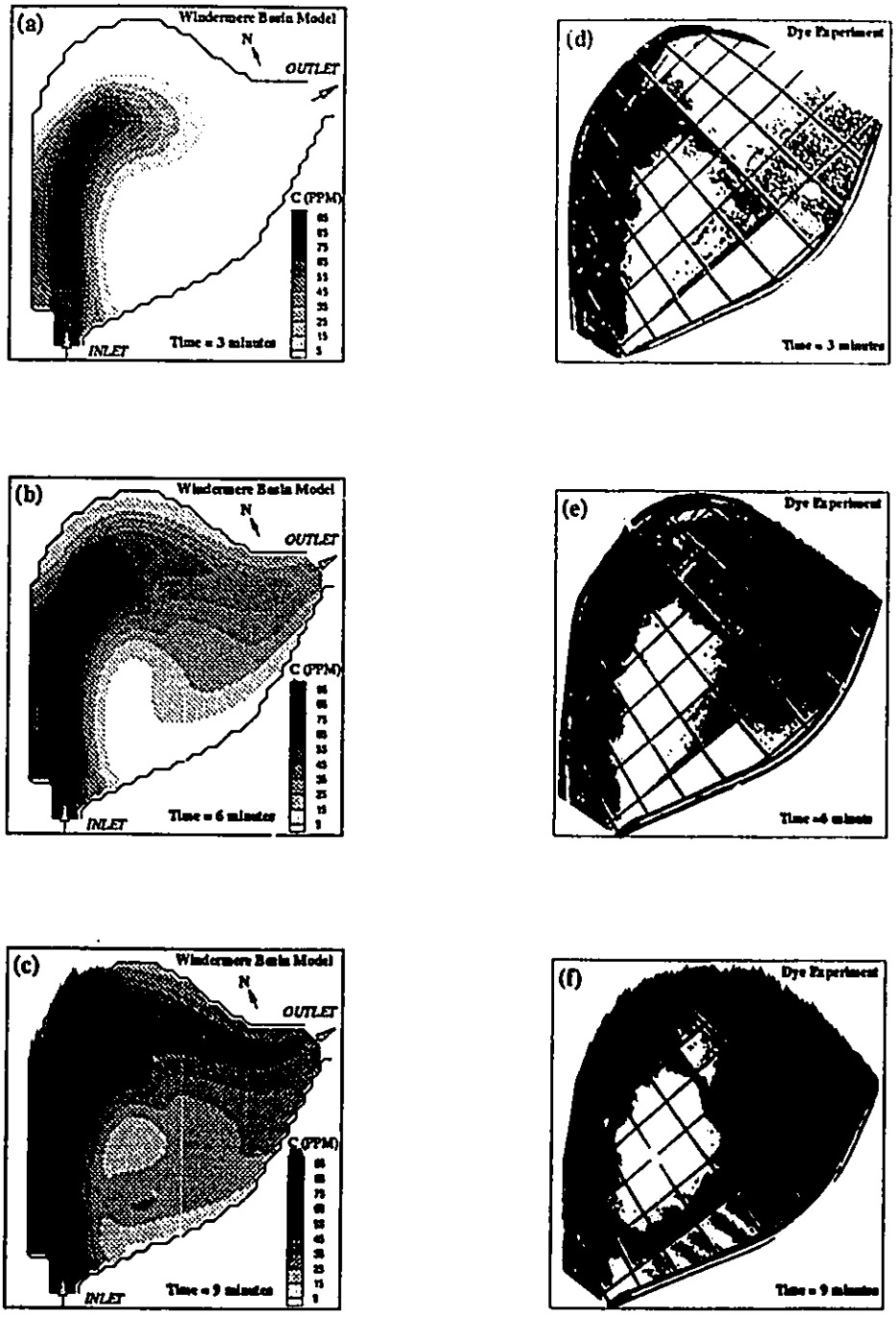

Fig. 5.7 Simulated equal dye concentration contours at (a) 3 minutes; (b) 6 minutes and (c) 9 minutes and images from the dye experiment in the laboratory model at (a) 3 minutes; (b) 6 minutes and (c) 9 minutes after a continuous emission of dye into the basin.

(c) present the simulated contours for the case under consideration for 3, 6, and 9 minutes after the dye release. Figs. 5.7(d), (e), (f) show the images from the experiment for 3, 6, and 9 minutes after the dye release. It is observed that the fronts and outlines in the simulation are close to that in the experiment (the images from the experiment are slightly distorted in brightness when they are copied). No attempt is made to compare dye concentration distribution inside the visual outline because of the lack of laboratory measurements.

Typical flow patterns that occur in a shallow sedimentation basin, as given by Thackston et al. (1987), include the advective, mixed and dead zones. The advective zone is the regime where currents are highly advective and advance directly from inlet to outlet. The dead zone is the regime where velocities are very small, and very weak recirculating currents exist. The mixed zone consists of large strong gyres, where the exchange between the mixed zone and the main advective flow zone is higher than the dead zone. The effect of zone distribution on the trace movement was discussed (Thackston et al., 1987; Engel, 1988). However, so far no examples are available to clearly demonstrate such an effect.

By using the numerical model, an excellent numerical experiment can be designed to demonstrate the effect of zones of circulation on the dye transport, and distribution in a large shallow sedimentation basin such as the Windermere Basin. In this test, a dye with a concentration of 100 ppm is continuously released for 1.5 minutes. The standard circulation case (see Fig. 5.2) with the calibrated set of parameters ($A_h = 12.5\, m^2/s$, $n = 0.0115$, and $D = 0.001\, m^2/s$) is employed in the experiment. Figs. 5.8(a) - (f) and Figs. 5.9(a) - (f) show the simulated flooding contours of dye concentration at 1, 2, 3, 4, 5, 6, 9, 15, 30, 60, 90, 120 minutes after the initial emission of the dye, respectively.

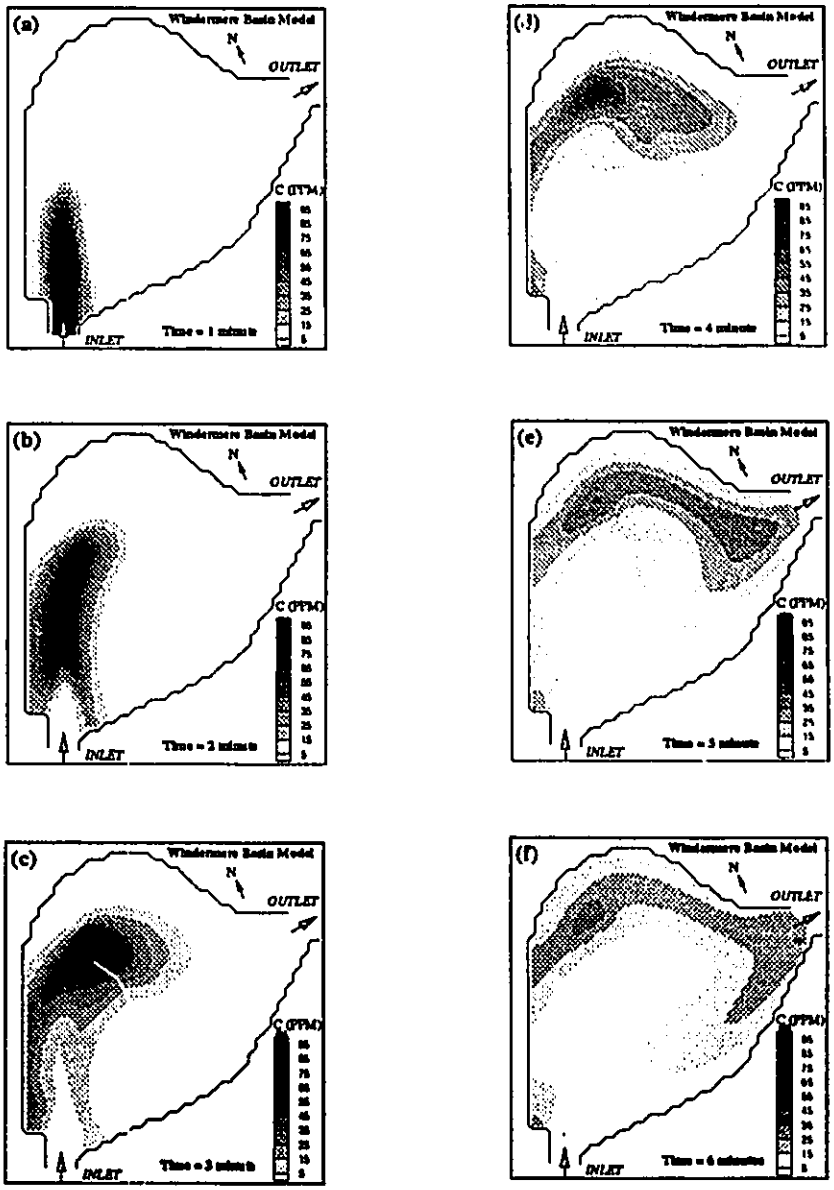

Fig. 5.8 Simulated equal dye concentration contours in the Windermere Basin model for a 1.5 minutes emission of dye at (a) 1, (b) 2, (c) 3, (d) 4, (e) 5, (f) 6 minutes after the initial emission of the dye.

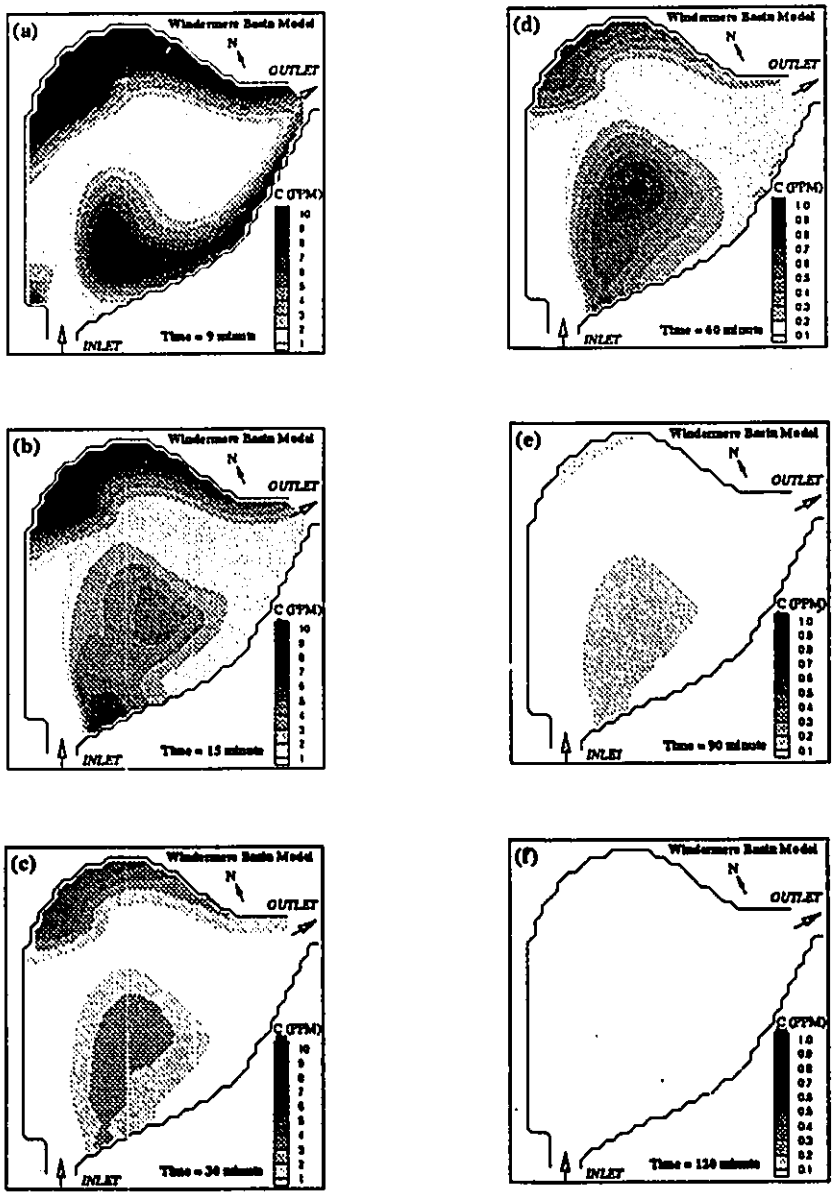

Fig. 5.9 Simulated equal dye concentration contours in the Windermere Basin model for a 1.5 minutes emission of dye at (a) 9, (b) 15, (c) 30, (d) 60, (e) 90, (f) 120 minutes after the initial emission of the dye.

The dye reaches the outlet in about 4.5 minutes. Before arriving at the outlet (1 to 4 minutes), this cloud of dye follows the strong current in the main advective flow zone. Part of the dye enters the small counterclockwise eddy (mixed zone) in the left hand side of the inlet. No dye enters the dead zone at the top of the basin and the central large eddy. After the dye front arrives at the outlet (5 to 9 minutes), part of the dye leaves the basin, part of dye follows the return flow entering the central large clockwise eddy (mixed zone), and part of the dye enters the dead zone at the top, as shown in Figs. 5.8(e), (f), and Fig. 5.9(a). The dye didn't reach the centre of the central mixed zone at this stage. The concentration fields after 15 minutes (Figs. 5.9(b)-(f)) clearly display the evolution of dye distribution in the different zones. In the advective zone, the strong currents force the dye to leave this zone. The dye that entered the mixed zone in the left hand side of inlet eventually leaves this area because the scale of this eddy is small and the exchange between this zone and the main advective flow zone is expected to be high, see Fig. 5.2. However, for the dead zone in the top of the basin, due to the slow exchange with the main advective flow zone, the dye stays in the zone for a much longer time than in other areas (1 ppm dye remains in the zone after one hour). It is interesting to observe the dye distribution in the central mixed zone. The dye accumulates gradually into the central area of the eddy in less than 30 minutes (Figs. 5.9(a) and (b)), then leaves this zone from the outer regime to the inner regime (see Figs. 5.9(c), (d), (e), (f)) through the exchange with the main advective flow. Even after one and a half hour, about 0.1 ppm dye remains at the centre of the zone (see Fig. 5.9(e)). Finally, all dye leaves the basin, see Fig. 5.9(f).

5.5 NUMERICAL STUDY OF RESIDENCE TIME

In an ideal sedimentation basin, every part of the fluid entering the basin is evenly distributed in the vertical cross section of the entrance, and the flow advances at a uniform and constant velocity to the outlet. In such a case, the flow regime consists of a plug flow only, and each part resides in the system for a period equal to the theoretical residence time given as $T_r = V / Q$, where T_r = the theoretical residence time, V = volume of water in the basin, and Q = the discharge. However, in a real basin, the flow pattern deviates from plug flow, due to the existence of dead zones, lateral dispersion and mixing. The more a basin deviates from the ideal, the lower the trapping efficiency will be (Thackston et al., 1987). The hydraulic efficiency E_h is defined as $E_h = \bar{t} / T_r$, where $\bar{t}$ is the actual mean residence time. For the standard case of the Windermere Basin model, the theoretical residence time is 0.2414 hours ($Q = 0.0114\, m^3/s$, $V = 9.907\, m^3$). The effect of various zones on the dye transport has been clearly demonstrated in the above section. For a sedimentation basin such as the Windermere Basin model, the degree of treatment depends in some ways on the actual residence time. As a result, the estimation of mean residence time and its distribution is important.

5.5.1 Numerical Tracer Test

The flow regime and residence time for a sedimentation basin are usually determined by a tracer test. The flow curve (trace concentration at outlet as a function of time) then can be used to determine the hydraulic efficiency. However, as pointed out by Thackston, et al. (1987), literature contains little information about the hydraulics of large, shallow basins due to the difficulty of performing tracer tests in remote locations on large facilities with long residence times. It is also not an easy task to analyze the experimental results from a physical model.

Furthermore, factors can not be isolated when performing such tests both in the field and in physical models. It is feasible and convenient to perform such tests using the numerical model. An example of residence time calculations can be found for Lake St. Clair (Schwab et al., 1989).

The parameters used in this test are same as those used in the test described in Figs. 5.8 and 5.9. The dye is released for 4 minutes, which is the time needed for the dye to first reach the outlet. Fig. 5.10 shows the simulated results on the residence time tracer (dye) test. The time series of dye concentrations at 9 locations, as labelled in Fig. 5.1(b), are presented in Figs. 5.10(a) and (b), where *P1* to *P4* are located in the main advective flow zone, and *P5* to *P9* in the mixed zones and dead zones. The dye arrives at points in the advective zone in a very short time, for example, at *P3* in $0.15T_r$ and at *P4* in $0.28\ T_r$ (T_r =0.2414 hour is the theoretical residence time for the basin). The delay of the peak concentration is obvious, and the peak concentrations are decreased with the increase of its distance from the inlet (95 ppm at *P2*, 45 ppm at *P3*, 40 ppm at *P4*). The *short-circuiting* exists for the advective flow zone, in which the large portion of dye exits the basin in much less time than T_r (below than $0.5T_r$). In contrast, the dye leaves these points at mixed zones and dead zones in a much longer time than T_r (about $2T_r$ to $4T_r$). A useful index *A (%)* can be constructed according to the dye occupying (over 1 ppm concentration) volume relative to the whole volume. As shown in Fig. 5.10(c), about 55% of the whole volume was occupied when the dye first arrived at the outlet, and 95% within the residence time T_r.

The feature of zones can also be reflected when one examines the dye history at the outlet. Fig. 5.10(d) shows the accumulated dye mass at the outlet normalized by the total mass emitted from the inlet as the function of time normalized by the theoretical residence time. Fig. 5.10(e) shows the transient dye mass at the outlet. It is observed that about 70% of the dye leaves the basin within T_r or 0.2414 hour; 99 % of the dye leaves the basin in $6T_r$. Fig. 5.10(f) shows the

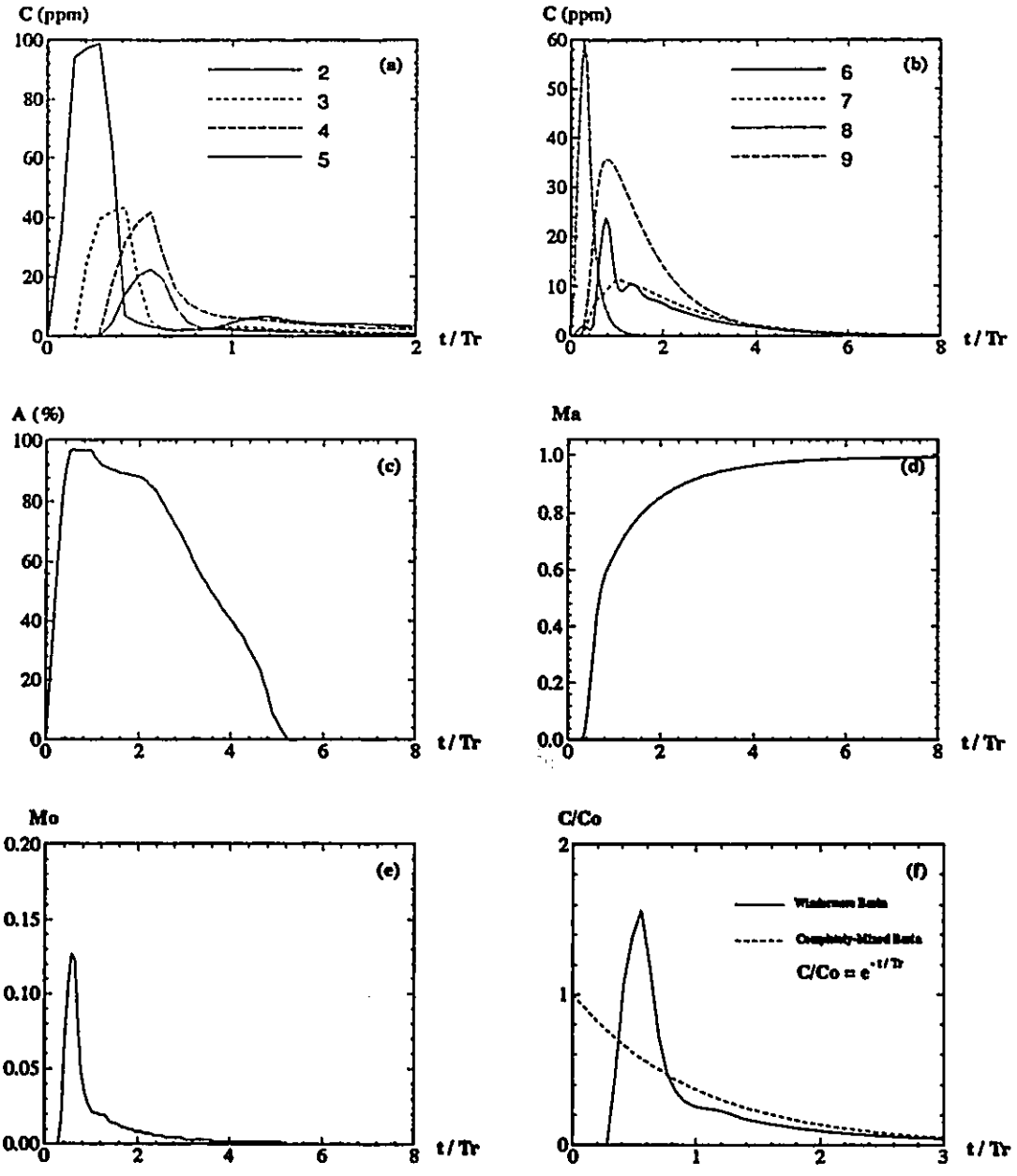

Fig. 5.10 Study of the residence time: (a) the dye concentrations at points in advective flow zone, (b) the dye concentrations at points in mixing and dead zone, (c) the effective volume as the function of relative time, (d) the ratio of accumulated dye quantity at outlet to the total emissioned dye quantity, (e) the ratio of dye quantity at outlet to the total emissioned dye quantity, and (f) the dye curve from the Windermere Basin and the theoretical curve from a completely-mixed basin (The relative time is the ratio of time to the theoretical residence time ,i.e. volume / inflow).

dye curve in the above test (solid line) and theoretical curve from a completely-mixed basin (dashed line). The theoretical curve is obtained from $C/C_o = e^{-t/T_r}$. The shape of the curve in the Windermere Basin resembles that of a completely-mixed basin, except that there is a lag time of $0.2T_r$ before dye occurs at the outlet, a slight peak (C/C_o = 1.6) in dye concentration at $0.6T_r$, and a decay climb slightly below the completely-mixed curve after $0.8T_r$. In summary, in the physical model of the Windermere Basin, the advective flow zone results in a short-circuiting for the large portion of dye, and the mixed zone and dead zones result in a very long flow-through time for the small portion of dye.

5.5.2 Methods of Increasing Residence Time

Hydraulic residence time is directly influenced by such physical variables as depth, shape, side slope, shoaling, as well as hydraulic characteristics such as the degree of mixing, stratification, and flow zone distribution. Increasing the residence time implies an increase in the hydraulic efficiency of the settling basin. No attempt is made in this study to examine all factors affecting the residence time. It is assumed that the depth and basin configuration remain unchangeable. For the Windermere Basin, the standard case is implied. The objective of increasing residence time is to increase the path length of the advective flow, and the area of the dead zone or weakly mixed zone.

The first test is to examine the wind effect on the residence time distribution, which is very difficult to study in the field or with the physical model. In the test, the dye is continuously emitted for four minutes. The depth-averaged circulation pattern under a 10 m/s NE (against the inflow) and a SW wind (in the same direction as the inflow) are shown in Figs. 5.11 (a) and (b), respectively. The northeast wind causes the size decrease of both the central eddy, and the dead

zone at the top of basin, and the increase of the size of the left hand side eddy at inlet. The advective flow path is deflected more to the right when compared with the hydraulic case. The southwest wind causes the disappearance of the dead zone, the decrease of the size of the left hand side eddy at the inlet, and splits the central eddy in two counterclockwise and clockwise eddies. The advective flow path is deflected slightly to the right, parallel to the top shore of the basin to the outlet. The dye curve at the outlet for these two wind conditions, and for the hydraulic case is presented in Fig. 5.11 (c). The time that the dye takes to reach the outlet from the inlet are very close in all cases. The curve under a NE wind is flatter than the curve of a SE, and no wind conditions, indicating a larger mean residence time in the NE wind than in the other two cases. The peak in NE wind condition is lower than other cases. These findings are attributable to the two large central eddies in the NE wind condition, see Fig. 5.11(a).

Site conditions which promote unevenly distributed flow tend to degrade the residence time away from ideal plug flow. Spur dikes are by far the most effective and reliable devices which can be used to increase residence time (Thackston, et al., 1987). Three dike configurations and other devices were tested in the physical model study of the Windermere Basin. The configuration *DIKE #3* was considered as the best case (Engel, 1988). In this configuration, as shown in Fig. 5.12(a), two parallel spur dikes are constructed in the basin, one at the right side of the inlet, and another at the central basin. The same test condition is used as in the test of residence time. (Fig. 5.10). Fig. 5.12(a), (b), (c) present the simulated circulation patterns under this dike configuration, equal dye concentration contours at nine minutes, and the dye curve at the outlet with and without dikes, respectively. It is observed from Fig. 5.12 (a) that the effect of the dikes is evident, causing the advective flow to meander through the whole basin along the dikes, and dead zones behind the dikes. This has the effect of increasing the advective flow path

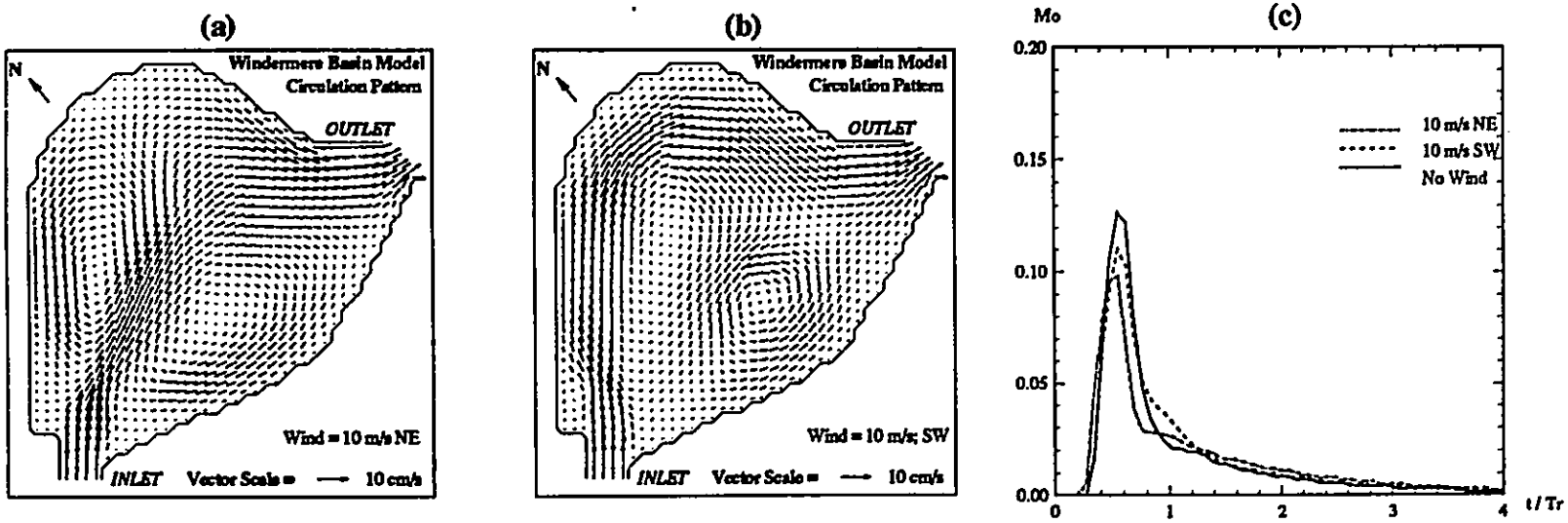

Fig. 5.11 Effect of wind conditions: (a) circulation pattern with a 10 m/s NE wind, (b) circulation pattern with a 10 m/s SW wind, (c) dye quantity at outlet to the total emissioned dye quantity as function of relative time (The relative time is the ratio of time to the theoretical residence time ,i.e, volume / inflow).

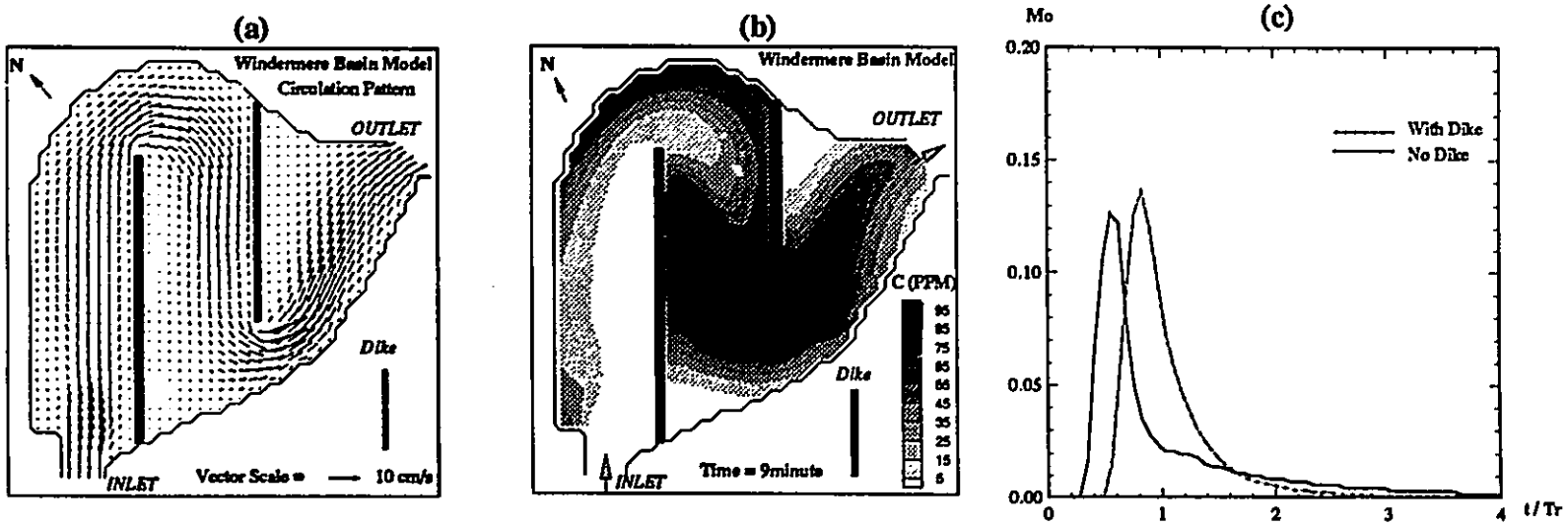

Fig. 5.12 Effect of dike: (a) circulation pattern with a dike, (b) equal dye concentration contours at 9 minutes, (c) dye quantity at outlet to the total emissioned dye quantity as function of relative time (The relative time is the ratio of time to the theoretical residence time ,i.e, volume / inflow).

length and breaking up the large eddies. As expected, under such flow patterns, the dye's arriving time and peak time are longer, compared with the case without the dike. As a result, the mean residence time is significantly increased. The goal of increasing the mean residence time has been achieved.

5.6 PARTICLE TRAJECTORY PREDICTION

The Lagrangian trajectory prediction model, as described in Chapter 4, is used to simulate the path of drifters released in current field in the Windermere Basin as a complementary calibration of the circulation model. In the trajectory model, the particle trajectory is uniquely determined by the current field. The simulated circulation pattern under the standard case for the Windermere Basin (see Fig. 5.2) is used to predict the drifter's trajectories. The simulated trajectories for several drifters are given in Fig. 5.13. The simulated trajectories closely resemble those observed in the experiment, referring to Blaisdell (1990) and Fig. 5.2. As expected, the particles follow the streamlines in the current field.

When viewing the dye experiment on a video tape, one can observe that the movement of the dye front is somehow random and a clear outline is hard to identify. This may be attributed to the turbulent movement in the current field. The Lagrangian prediction should be modified to couple such the random movement. The advection-diffusion (AD) model which is used in modelling dye transport and dispersion was not able to present such a random movement, though it was successful in modelling the dye distribution in the basin. The trajectory prediction model with, the coupling of the random-walk approach (see Chapter 4), is applied in the standard case of the Windermere Basin. The diffusion coefficient takes the same value as in the advection-diffusion model. 1000 particles are released at the center of the inlet, and their trajectories at 30

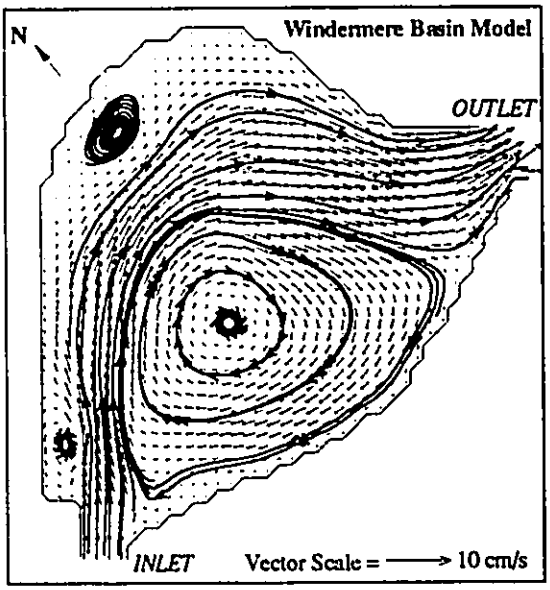

Fig. 5.13 *Lagrangian Simulation*: the trajectories of particles released in the different regime of zones in the Windermere Basin in the standard case. The trajectories are predicted by the trajectory model in which the drifter follows the flow without diffusion

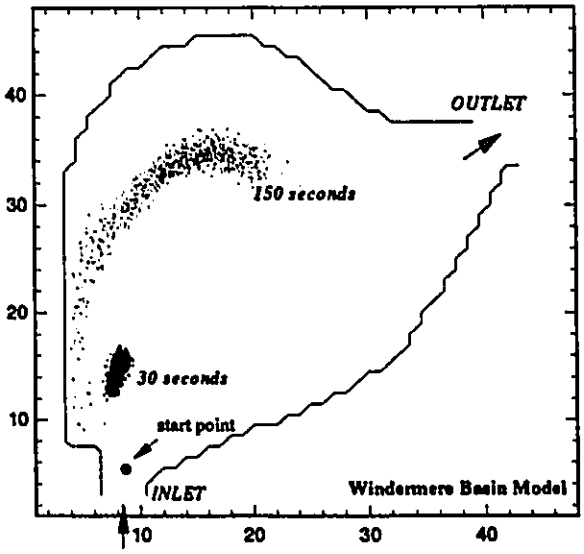

Fig. 5.14 *Random-Walk Simulation*: the trajectories of a cloud of particles (1000 particles) released in the inlet in Windermere Basin in the standard case, at 30 and 150 seconds.

and 150 seconds are outputted and presented in Fig. 5.14. The effect of turbulence on the movement of particles is evident. The last comment is that Figs. 5.13 and 5.14 only demonstrate the two methods of predicting trajectories of particles, no attempt was made to compare the two methods.

5.7 SUMMARY

In summary, the following conclusions can be drawn from the above numerical study of the current and dye transport in the physical model of the Windermere Basin:

(1). The conventional two-dimensional circulation model (2DH) is successful in simulating the depth-averaged hydraulically-induced flow. The simulation was calibrated in the physical model of the Windermere Basin using the experimentally-determined circulation pattern derived from the drifter trajectories. The model, with the horizontal viscosity coefficient of 0.00125 m^2/s and the Manning's coefficient of 0.0115, can obtain the best simulation as compared with the experimental result.

(2). The two-dimensional advection-dispersion model is successful in modelling the transport of a dye emitted into the basin, and an excellent numerical experiment was executed to demonstrate how the various zones such as the advective flow zone, mixed zone and dead zone affect the dye transport and distribution.

(3). The numerical study of residence time in the standard case indicates that for the large portion of flow, a very short residence time exists due to the advective flow (short-circuiting). Also for a small portion of flow, a much longer time than the theoretical residence time is needed due to the mixing and dead zones. The numerical tests of winds and spur dikes on

the flow zone distributions, and, the residence time has been demonstrated.

(4). A Lagrangian trajectory model and a random-walk approach were employed to predict the trajectories of particles released in the physical model of Windermere Basin.

CHAPTER 6

STUDY OF WIND-INDUCED FLOWS

Wind-induced current is the most important type of flows in geophysical water basins. Turbulent mixing in lakes and small ocean bays is primarily caused by wind action. The wind-induced drift current in the upper layer plays an important role in the mutually interacting air-water system. Any hydrodynamic models for natural water bodies must properly include this forcing mechanism in order to successfully simulate the wind-induced current structure. The countercurrent flow in a closed channel is the simplest yet the most important type of wind-induced flows, because this flow includes the turbulent mixing mechanism for the geophysical wind-driven flow, and, other factors affecting currents are excluded. Consequently, the countercurrent has been widely studied by conventional laboratory experiments. However, only limited numerical studies have been undertaken. The countercurrent flows were used to calibrate the wind-induced coastal circulation models (Pearce & Cooper, 1981; Sheng, 1983; Swanson, 1986), but the features of surface drift current and bottom boundary current haven't been well simulated in these calibrations.

In this chapter, the general multi-layer three-dimensional circulation model (3D) is employed to study the wind-induced countercurrent flows. The simulations are first compared with newly developed analytical solutions, then calibrated with the experimental results obtained by Baines and Knapp (1965), and verified using the experimental results from Tsuruya, et al.

(1985). The sensitivity study of model parameters, such as eddy viscosity, and vertical layer discretization, will be performed. The Q3D, VHI3D and 3D circulation models are evaluated using the experimental results from Tsuruya et al. (1985), and compared in a simplified basin. Finally, a numerical experiment is undertaken to examine the wind-induced current in a stratified basin.

6.1 WIND-INDUCED COUNTERCURRENT FLOWS

A wind acting on the water surface causes a drift current in the direction it is blowing, with a bottom return flow in the opposite direction. It produces a windward lowering of the water level, and a leeward rise, which is called *wind set-up*. The boundaries of the channel cause free gravity waves to combine and form standing waves, or seiches. For fully developed conditions, and one-dimensional shearing, mass conservation requires zero net flow over the depth. This type of countercurrent flow is a generalized Couette flow in a closed channel.

A series of experiments have been conducted for the study of wind-induced flow by using conventional laboratory air-water tunnels (Baines & Knapp, 1965; Wu, 1975; Tsuruya et al., 1985), and air volume in a moving bottomless box (Tsanis, 1986). The mean flows and turbulence properties were measured and analyzed. However, because of the limited length of the channel used (longitudinal aspect ratio was usually lower than 50) and the effect of side walls, a precise countercurrent flow with zero net flux in the centre of the box was difficult to obtain in the majority of the experiments due to the side wall friction. This was confirmed from undeveloped inner-law plots relative to the bottom and the non-linearity of shear stress distributions for extant experimental data (Tsanis, 1986, 1989; Andreasson, 1991). The numerical modelling approach shows great potential in the study of shear-induced countercurrent flow. It is less costly, as well

as being easily controlled and executed. Some of the features can be explored by the numerical model. For example, the wind set-up and seiche in the channel are readily predicted, while surprisingly they are rarely reported in the experiments.

6.2 ANALYTICAL APPROACH FOR STEADY SHEAR-INDUCED FLOWS

The wind-induced current in a closed basin may be either a laminar or turbulent flow, depending on the Reynolds number over which the flow changes from laminar flow to turbulent flow. Exact solutions exist for steady cases.

6.2.1 An Analytical Solution for Steady Laminar Flow

Assuming that the convective acceleration, Coriolis forces, horizontal diffusivity and cross (y direction) terms are negligible when compared to the vertical shear gradient. The solution for no-slip bottom condition, given by Heaps (1984), for constant vertical eddy viscosity is

$$u(z) = \frac{\tau_s}{4\rho K_v h}(h - z)(h - 3z) \tag{6.1}$$

where $u(z)$ is the velocity at any depth z, h is the depth, τ_s is the wind stress acting on the surface.

6.2.2 A New Analytical Solution for Steady Turbulent Flow

It is recognized from a number of experimental results that the velocity profile for a wind-driven countercurrent flow is well approximated by a double-logarithmic structure, one for the surface region and one for the bottom part of return flow (Spillane & Hess, 1978). Tsuruya et

al. (1985) presented a solution as

$$u(z) = \frac{u_{*_s}}{\kappa}\left(\ln\frac{z_s + h}{z_s - z} - m \ln\frac{z_b + h + z}{z_b}\right) \tag{6.2}$$

where, $u_{*_s} = \sqrt{\tau_s/\rho}$ is the surface shear velocity which can be evaluated by wind. κ is the von Karman constant usually taken to be 0.4. z_s and z_b are the roughness lengths in the water at the surface and the bottom, respectively. They are the relative measures of the thicknesses of the viscous sublayers, and are very small compared to the depth. $m = u_{*_b}/u_{*_s}$ is the ratio of the bottom to surface shear velocity. Knowing the wind condition, therefore the surface shear velocity, the solution relies on the values of z_s, z_b and m. Using a parabolic eddy viscosity distribution and the linearity of the shear stress distribution, Tsanis (1989) derived a analytical solution for the velocity profile. Similar to Tsuruya's solution, this solution depends on z_s, z_b and the ratio of bottom shear stress to surface shear stress $\eta = \tau_{*_b}/\tau_{*_s} = m^2$. The parameters m and η were empirically determined from previous experiments.

A new analytical solution may be derived which is independent of either ratio of shear velocity (m) or ratio of shear stress (η).

Including the viscous sublayer thicknesses and numerical parameter λ, the parabolic eddy viscosity distribution can be expressed as (Tsanis, 1989):

$$K_v = \frac{\lambda u_{*_s}}{h}(z + z_b)(z_s + h - z) \tag{6.3}$$

The velocity profile takes a double-logarithmic profile as

$$u(z) = A\, u_{*_s} \ln\left(1 + \frac{z}{z_s}\right) + B\, u_{*_s} \ln\left(1 - \frac{z}{z_b + h}\right) + C \tag{6.4}$$

The following conditions are used to determine the above coefficients A, B, C.

At the free surface, the shear-stress is evaluated by wind velocity

$$K_v \frac{\partial u}{\partial z}\Big|_{z=h} = \tau_s = \rho_a C_D W |W| \tag{6.5}$$

At the bottom, the velocity equals zero

$$u|_{z=0} = 0 \tag{6.6}$$

The depth-averaged velocity equals zero

$$\frac{1}{H}\int_0^z u dz = U = 0 \tag{6.7}$$

Using the non-dimensional variables, $z_{bh} = z_b/h$, $z_{sh} = z_s/h$, three conditions form an algebraic system of the three coefficients having as their solution:

$$C = 0 \tag{6.8}$$

$$A = q_2/(p_1 q_2 - q_1 p_2) \tag{6.9}$$

$$B = -q_1/(p_1 q_2 - q_1 p_2) \tag{6.10}$$

in which,

$$p_1 = \lambda z_{sh} \tag{6.11}$$

$$p_2 = \lambda z_{sh}/z_{bh} \tag{6.12}$$

$$q_1 = (1 + z_{sh})\left[\ln(1 + z_{sh}) - \ln(z_{sh}) - 1\right] + z_{sh} \tag{6.13}$$

$$q_2 = z_{bh}\left[ln(1 + z_{bh}) - \ln(z_{bh}) + 1\right] - (1 + z_{bh}) \tag{6.14}$$

Therefore, the velocities at any depths, normalized by the surface shear velocity, i.e., $\bar{u}_0(z) = u(z)/u_{*_s}$, can be obtained:

$$\bar{u}_0(z) = A\ \ln(1 + \frac{z}{z_s}) + B\ \ln(1 - \frac{z}{z_b + h}) \tag{6.15}$$

It is determined by z_s, z_b and λ, and independent of any ratios.

6.3 NUMERICAL STUDY USING THE 3D MODEL

6.3.1 Comparison with Analytical Solutions

A constant viscosity leads to a parabolic velocity profile as in the case of laminar flow. The simulated result from the 3D model using the same constant vertical viscosity coefficient is in good agreement with the analytical solution, as shown in Fig. 6.1(a). The zero velocity occurs at 1/3 of the depth, below the water surface. The horizontal eddy viscosity has some effect on the profile. In the case of turbulent flow, a parabolic eddy viscosity distribution is used for the model. Fig. 6.1(b) shows the predictions by 3D model, along with the analytical solution. The model predictions are in good agreement with the analytical solutions.

6.3.2 Calibration and Verification with Experimental Data

Baines and Knapp's experimental apparatus was a wind channel with a uniform depth of 0.3048 meters. As shown in Table 6.1, two wind conditions were employed, i.e., 3.901 m/s and 6.096 m/s. Thirty-one velocity measurements were made at various depths including the surface in both cases. The surface shear velocities were evaluated from the wind velocities applied (Baines & Knapp, 1965). The Reynolds numbers $R = u_s h / \nu$, where u_s is the surface velocity and $\nu = 1.0 X\ 10^{-6}\ m^2/s$ were 32700 and 46500, respectively. The same conditions are used in the 3D model. The velocity profiles normalized by the surface shear velocity by the model are presented in Fig. 6.2, together with the experimental results. It is observed from this figure that the model simulation was in good agreement with the experimental data. The normalized surface velocities from the model are 17.11 and 16.08 for case 1 and case 2, respectively. These velocities are close to the experimental data, 17.2 and 16.2, respectively. Logarithmic structures

were found both near the surface and the bottom. The return flow in the experiment exhibited a distinct peak near the bottom, due to short length of the channel and the presence of the sloping beach (Baines & Knapp, 1965). The detailed currents had not been measured close to the bottom (lower than 10 % of the whole depth).

A better presentation of the velocity profile is in terms of the coordinates of the "smooth" inner law of the velocity distribution, relative to either the surface or the bottom (Tsanis, 1986; Andreasson, 1991). In Fig. 6.3(a), curve (A) represents the viscous sublayer portion of the velocity profile,

$$\frac{u_s - u}{u_{*s}} = \frac{(h - z)\, u_{*s}}{\nu} \tag{6.16}$$

and curve (B), corresponding to the logarithmic portion of the velocity profile for hydrodynamically smooth conditions, is described by

$$\frac{u_s - u}{u_{*s}} = 5.75 \log \frac{(h - z)\, u_{*s}}{\nu} + 6.0 \tag{6.17}$$

The curves labelled (C_i) (i=1,2,3,4) represent the curves for experimental results with various Reynolds numbers. These curves, described by

$$\frac{u_s - u}{u_{*s}} = 5.75 \log(h - z) \frac{u_{*s}}{\nu} + 8.5 - 5.75 \log R_{kw} \tag{6.18}$$

are parallel to curve (B), and lie lower to curve (B) by the amount of the roughness-induced velocity reduction. This value is proportional to the roughness Reynolds number, or von Karman number $R_{kw} = u_{*s} Z_{ow}/\nu$, where Z_{ow} is the absolute roughness of the wall. The roughness length Z_{ow} can then be calculated from R_{ow} (Schlichting, 1968). The experimental data from Baines and Knapp (1965), and the simulations by the 3D model are presented in Fig. 6.3(a), together

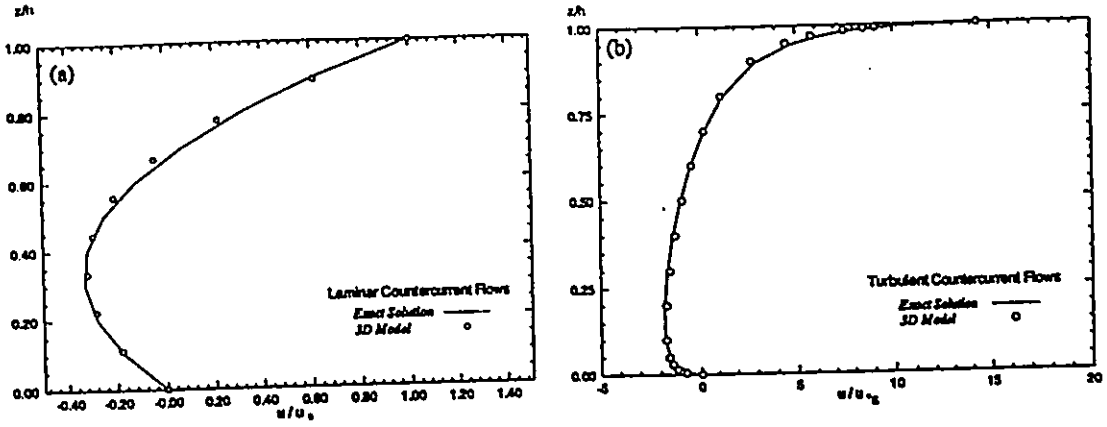

Fig. 6.1 Comparison of model simulation by 3D model with analytical solution, (a) for laminar flow, (b) for turbulent flow.

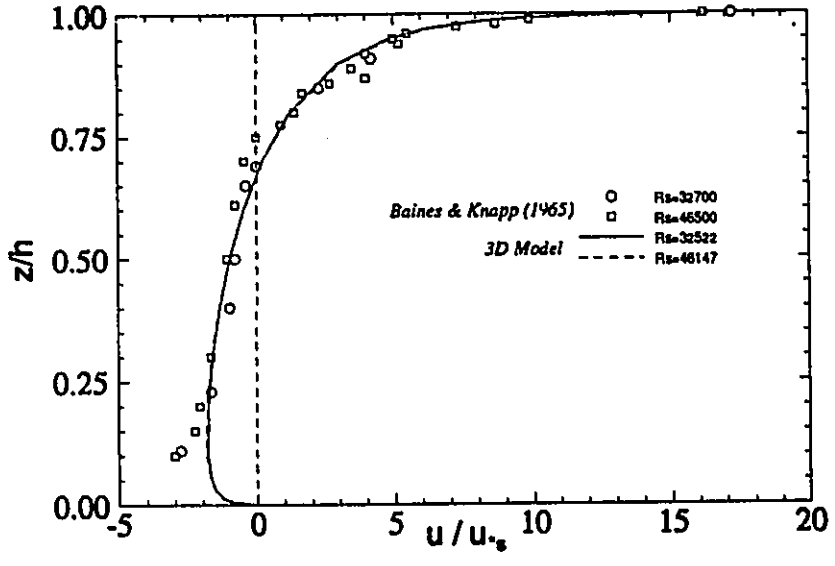

Fig. 6.2 Normalized velocity profile - calibration of 3D model with the experimental data by Baines and Knapp (1965).

with experimental data from Goossens, et al., (1982) and Tsanis (1989). Both data and simulations are seen to be in very good agreement with the firmly established law for hydrodynamically 'smooth' conditions in fully developed turbulence. The simulations are in good agreement with the experimental data in both wind conditions.

Fig. 6.3(b) shows the same model and experimental data plotted in inner-law coordinates relative to the bottom. It is inspected from this figure that, in contrast to the conditions prevailing in the surface, the turbulence in the bottom return flow is quite undeveloped in the experiments. However, a good linearity in the semi-log coordinates are observed from the simulation, showing a well developed return flow has been achieved in the numerical model.

The above conclusion could be supported from the vertical distributions of shear stresses. Fig. 6.4 presents the shear stress distributions for existing experimental data, model simulations, and theoretically linear distributions for laminar and high-Reynolds-number turbulent flow ($\eta = \tau_b/\tau_s = -0.10$). It can be seen that all of the available experimentally deduced Reynolds stresses, differ significantly from a linear distribution. As pointed out by Tsanis (1986), the reason is that the limited longitudinal channel and an immature state of the structure of turbulence at a relatively low Reynolds number was used in the majority of experiments. While in the numerical model, the channel is long enough; the mass continuity is satisfied; and the simulation is controlled by the total kinematic energy (KE), i.e., the steady state is reached when the ratio $|KE^{n+1} - KE^n|/KE^{n+1}$ becomes less than a test convergence value (10^{-8}). Therefore, as shown in Fig. 6.4, a good linearity is observed for the simulation.

Another experiment done by Tsuruya et al., (1985) is used for verification. A wind-

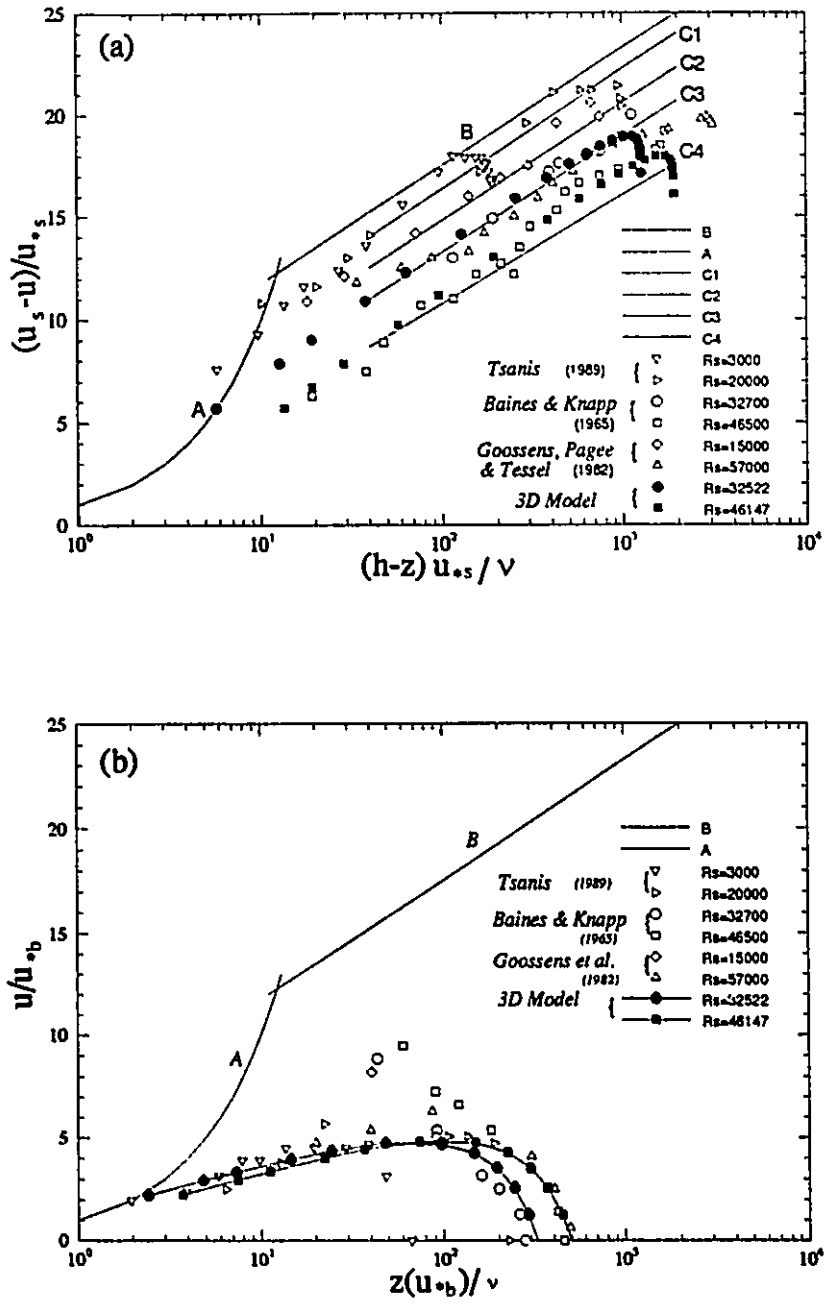

Fig. 6.3 "Smooth" Inner-law of velocity distribution of the experimental data by Baines and Knapp (1965) and the 3D model simulations, relative to (a) the surface interface, and (b) the bottom interface.

wave tank was used in the experiments. The flow visualizations were undertaken under two wind conditions, i.e., 6.73 m/s and 6.90 m/s, as shown in Table 6.2. In the numerical 3D model, the same depth was used, and the wind velocity was equal to 6.8 m/s which is between two wind conditions used in the experiments. It is observed from Fig. 6.5 and Table 6.2, that the model simulations are in good agreement with the experimental data. The surface velocity is well predicted, and the simulations fall between the two sets of experimental data. Comparisons are made in terms of the coordinates of the "smooth" inner law of the velocity distribution, relative both to the surface and the bottom, as shown in Figs. 6.6(a) and (b), respectively. It is observed that both the simulation results and experimental data are in good agreement with the law for hydrodynamically 'smooth' conditions, and the simulation results fall in the range of the experimental data.

6.3.3 Several Numerical Experiments

(A) Effect of Eddy Viscosity

Physically, when the coefficient of vertical eddy viscosity increases, the internal shear stress, and consequently turbulence increase, and the mean currents decrease. Fig. 6.7(a) shows a test using various horizontal eddy viscosity coefficients, ranging from 125 cm^2/s to 2500 cm^2/s. The simulations indicate that the effect of horizontal eddy viscosity is insignificant, because the horizontal dimension is several orders of magnitude larger than the vertical dimension. As expected, the vertical eddy viscosity significantly affects the predictions. Fig. 6.7(b) shows a test for different values of λ in the parabolic vertical eddy viscosity distribution, where two sets of experimental data from Tsuruya et al. (1985) are presented for the comparison. The normalized surface velocity reaches as high as 24.9 when $\lambda = 0.2$, while only 10.05 when $\lambda = 0.5$. In overall,

Table 6.1 Experimental results (Baines & Knapp, 1965) and simulations by the 3D model.

Quantity		Test 1	3D	Test 2	3D
Depth	h (m)	0.3048	0.3048	0.3048	0.3048
Wind Velocity	W (m/s)	3.901	3.901	6.096	6.096
Surface Shear Velocity	u_{*_s} (cm/s)	0.6233	0.6233	0.9416	0.9416
Surface Velocity	u_s (cm/s)	10.72	10.67	15.25	15.14
Reynolds Number	$R_s = u_s h/\nu$	32700	32522	46500	46147
Normalized Surface Velocity	u_s/u_{*_s}	17.20	17.11	16.20	16.08
Absolute Roughness	Z_{ow} (mm)	0.3521	0.3521	0.4795	0.4795
Zero Velocity Height	Z_0	0.69	0.68	0.75	0.68

Table 6.2 Experimental results (Tsuruya et al., 1985) and model simulations.

Quantity		Test 1	Test 2	3D
Depth	h (m)	0.15	0.15	0.15
Wind Velocity	W (m/s)	6.73	6.90	6.80
Surface Shear Velocity	u_{*_s} (cm/s)	0.815	0.835	0.823
Surface Velocity	u_s (cm/s)	10.70	12.15	11.79
Reynolds Number	$R_s = u_s h/\nu$	16050	18225	17685
Normalized Surface Velocity	u_s/u_{*_s}	12.74	14.55	14.32
Absolute Roughness	Z_{ow} (mm)	0.21	0.36	0.31

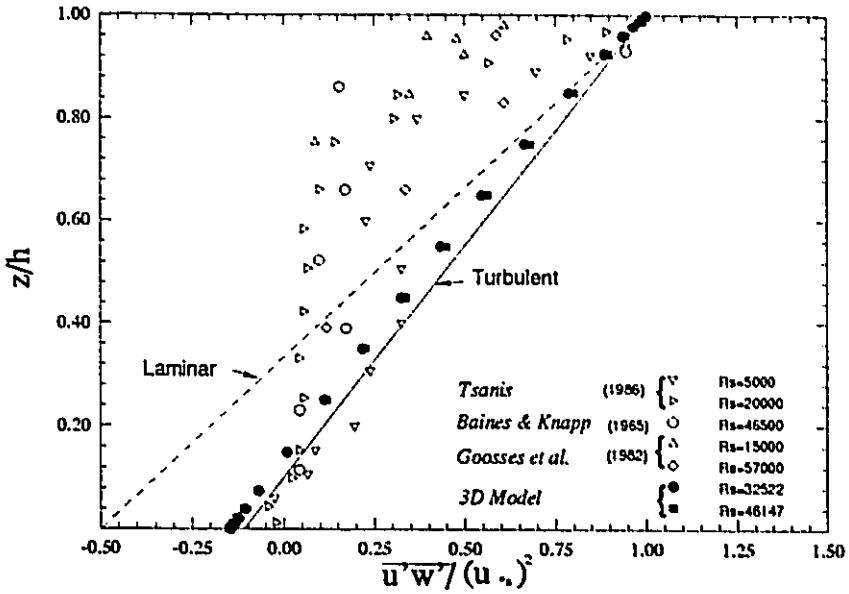

Fig. 6.4 Reynolds stress as a function of transverse position, comparison between the experimental and model results.

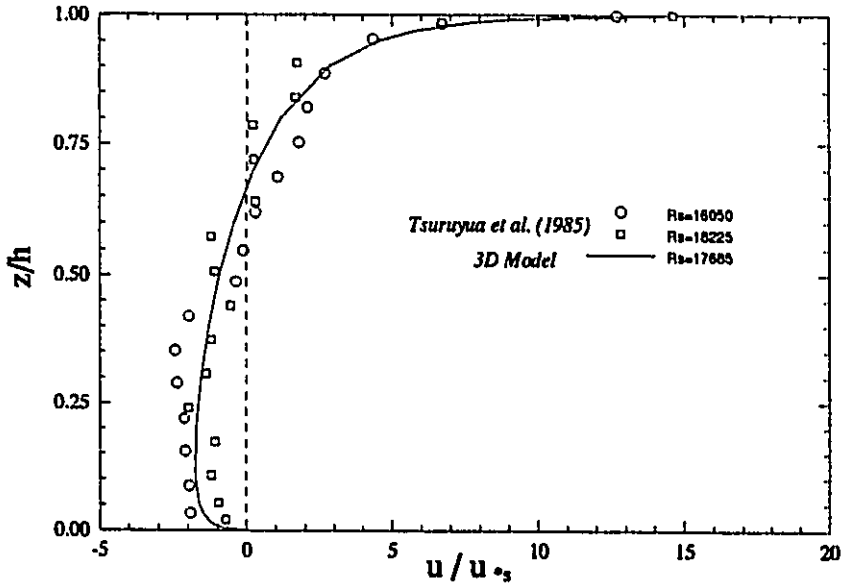

Fig. 6.5 Normalized velocity profile - verification of the 3D model with the experimental data by Tsuruya, Nakano and Kato (1985).

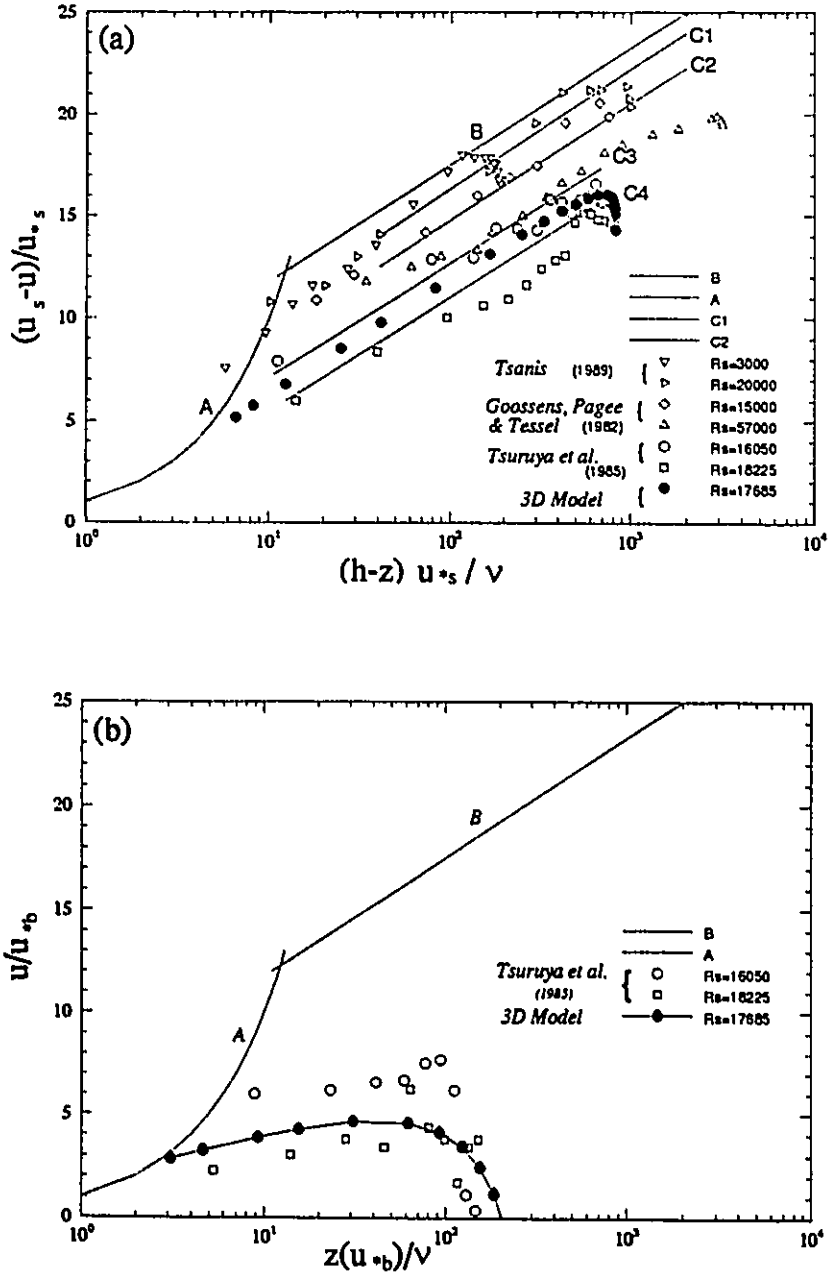

Fig. 6.6 "Smooth" inner-law of velocity distributions of the experimental data by Tsuruya, Nakano and Kato (1985) and the model simulations, relative to (a) the surface interface, and (b) the bottom interface.

a value of λ around 0.35 presents good simulation when compared with the experimental data.

(B) Effect of Vertical Discretization

Determining surface velocity is very important for the prediction of surface particle trajectories or oil spill movement, and for the study of wave-current interaction. Determining of the velocity field near the bottom is critical for the determination of the resuspension of bottom sediments. It is indicated from tests that except for the formulation of boundary conditions, the vertical layer discretization has significant effect on the prediction of surface drift and near bottom return currents. Fig. 6.8 shows the model predictions with different vertical layer discretizations, i.e., equal layers (5, 15, 30 layers), unequal layers (7, 9 layers), and unequal layers enhanced both near the surface and the bottom (30 layers). By inspecting this figure, it is found that the layer discretization has an insignificant effect on the velocities in the middle ranging from 0.2 to 0.8 of whole depth. However, high resolutions are needed to predict the surface and bottom velocity field, especially near the surface. Using the same model parameters, if the vertical grid size $\Delta\sigma$ near the surface is greater than 0.06, the surface velocity normalized surface shear velocity is lower than 8. However, when the grid size is about 0.001, a normalized surface velocity can reach 16 to 20, which compares well with the experimental results.

(C) Developing Shear-Induced Turbulent Flow

The development of shear-induced turbulent flow can be examined from the evolution of the velocity distribution, as depicted in Fig. 6.9. At the beginning (see profiles at 5 and 10 minutes), currents at all layers follow the wind direction, and there is no return flow near the bottom. Then, a strong return flow is extended to the most region except near surface (see profile at 15 minutes). Afterward (after 120 minutes in this test) the surface drift flow is balanced with

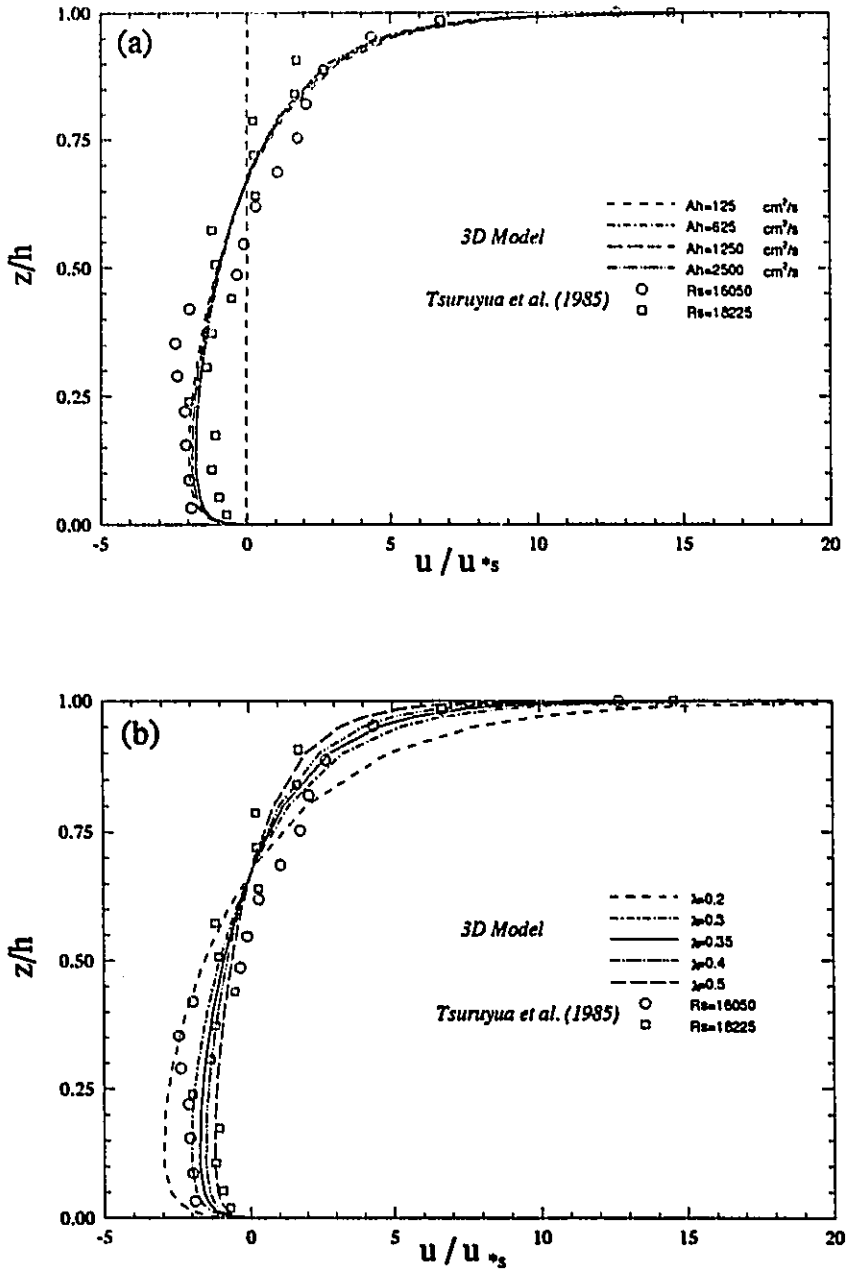

Fig. 6.7 Sensitivities of model parameters: (a) horizontal eddy viscosity and (b) λ (the constant in the vertical eddy viscosity distribution) on the simulated velocity profile. Symbols refer to the experimental data by Tsuruya, Nakano and Kato (1985).

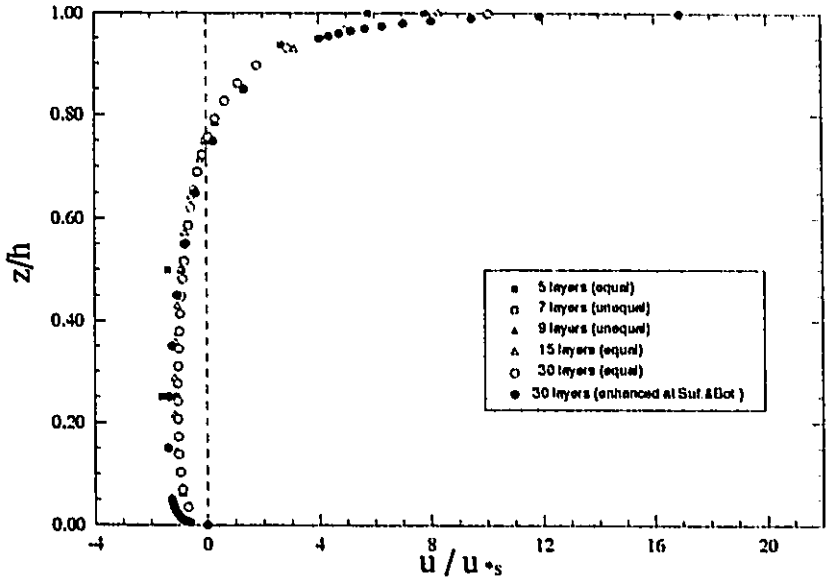

Fig. 6.8 Effect of the vertical layer discretization on the simulated velocity profile.

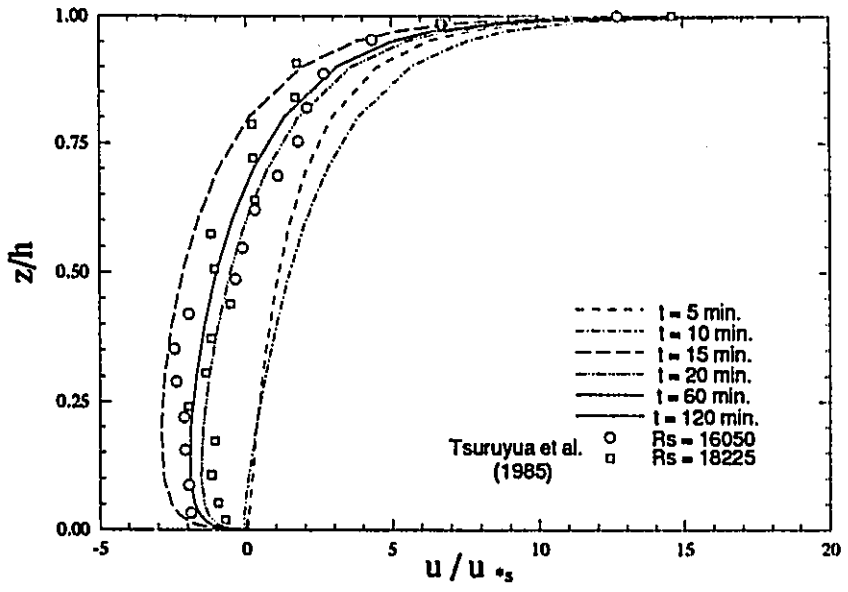

Fig. 6.9 Development of a shear-induced turbulent flow. Symbols refer to the experimental data by Tsuruya, Nakano and Kato (1985).

the return flow, and a steady state is reached.

(D) Wind-Induced Set-Up

The wind-induced set-up is a by-product of the simulation. Fig. 6.10 shows a typical wind-induced set-up, in which the total set-up is about 0.6 cm. Equal area for the water gain region (leeward) and water loss region (upwind) confirms a mass conservation in the simulation. Theoretically, the total set-up can be evaluated from the momentum equation as

$$\Delta\zeta = \frac{L}{gh} u_{*_s}^{\,2}(1-\eta) \tag{6.19}$$

where η is ratio of bottom shear stress to surface shear stress. The calculated set-up using Eq. (6.19) was 0.59 cm and is in good agreement with the simulated set-up.

(E) Seiche

Due to the boundaries of the channel, free gravity waves combine and form a standing wave or seiche. The theoretical period of seiche T_s is calculated by

$$T_s = 2\,L/\sqrt{gh} \tag{6.20}$$

where, L is the length of the channel. A 5 m/s west wind is applied in a 925 m long by 10 m deep channel, that produces, according to Eq. (6.20), a 1836.5 sec seiche. From the time series of water elevation at leeward end, as shown in Figs. 6.11(a), a period of 1828 sec is observed. The relative error to the theoretical period is 0.4 %. It is observed, from the total kinetic energy of the simulation as shown in Fig. 6.11(b), that there is an oscillation with a period of 925 seconds, which has a bigger amplitude at the beginning, and zero amplitude when approaching the steady state. The period in the kinetic energy, is half of the one in the standing wave. Therefore, the simulated period of seiche is 1850 sec. The relative error is 0.7 %. Finally, the time series of

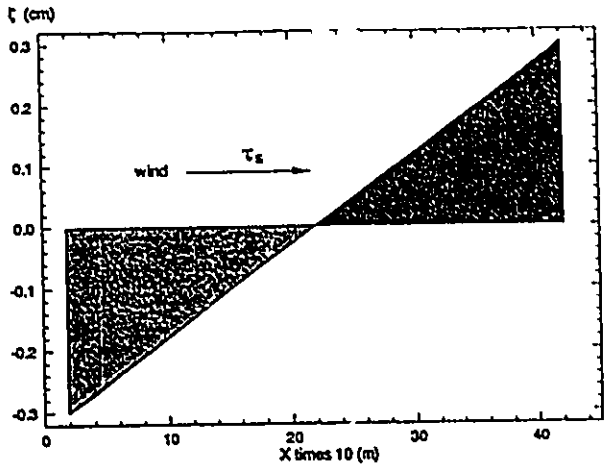

Fig. 6.10 Wind-induced set-up in a closed channel.

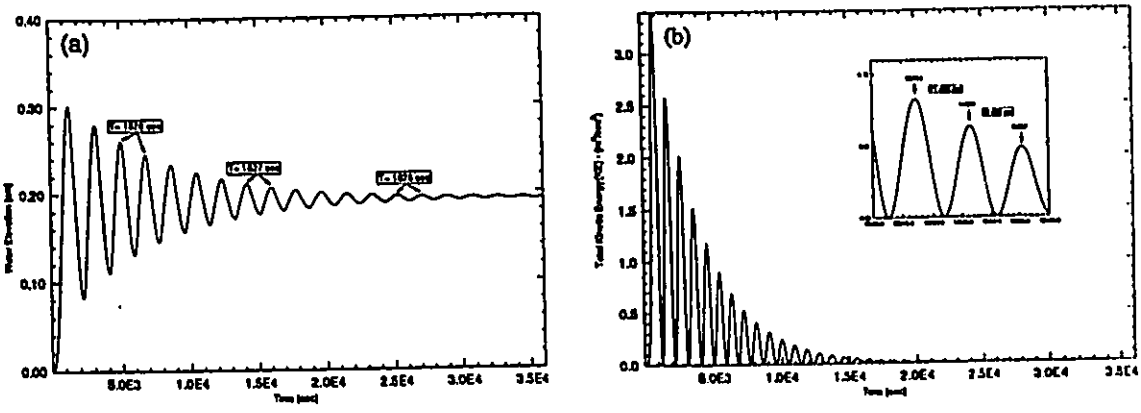

Fig. 6.11 Time series of (a) the water elevation at the leeward end of the channel and (b) the total kinematic energy evaluated by the depth-averaged velocity in the model simulation.

total kinetic energy reveals that a zero net mass flux in the vertical plane is preserved.

6.4 COMPARISONS AMONG THE 3D, Q3D AND VHI3D MODELS

6.4.1 Comparisons Using Analytical Solutions and Experimental Results

The simulated results from the Q3D and 3D models using the same constant vertical viscosity coefficient are in good agreement with the analytical solution, as shown in Fig. 6.12(a). Fig. 12(b) shows the predictions by the 3D and VHI3D models in case of turbulent flow, together with the analytical solution. It is observed that the model predictions are in good agreement with the analytical solutions, and the VHI3D model is as capable as the 3D model in simulating the current structure.

The experimental results by Tsuruya et al. (1985) are used for the model comparison between the 3D and VHI3D models. As listed in Table 6.3, the channel depth was 0.15 meter. The wind velocity was 6.8 m/s, which was between the two wind conditions (6.73 m/s and 6.9 m/s) in the experiments. The surface velocity, normalized surface velocity, and absolute roughness, both from the experiment and model simulations by the VHI3D and 3D models, are presented in Table 6.3. The simulated velocity profiles by the 3D and VHI3D models normalized by the surface shear velocity, are presented in Fig. 6.13, together with the experimental results and the prediction by the Q3D model. It is observed that the model simulations results were close to the experimental range, indicating a good agreement between model and experimental result. The logarithmic structure is found both near the surface and the bottom.

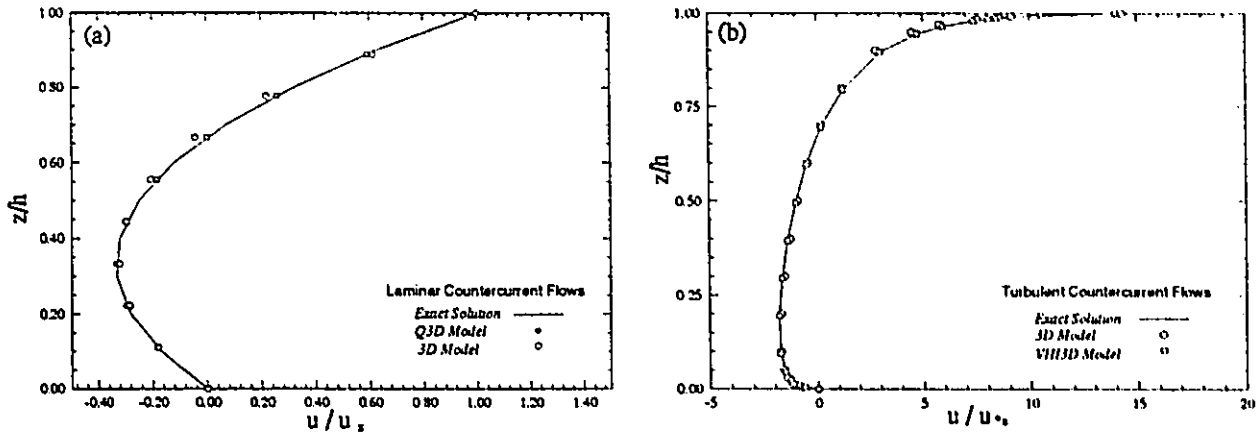

Fig. 6.12 Comparisons of simulations with the analytical solutions: (a) for the laminar flow by the 3D and Q3D models, (b) for the turbulent flow by the 3D and VHI3D models.

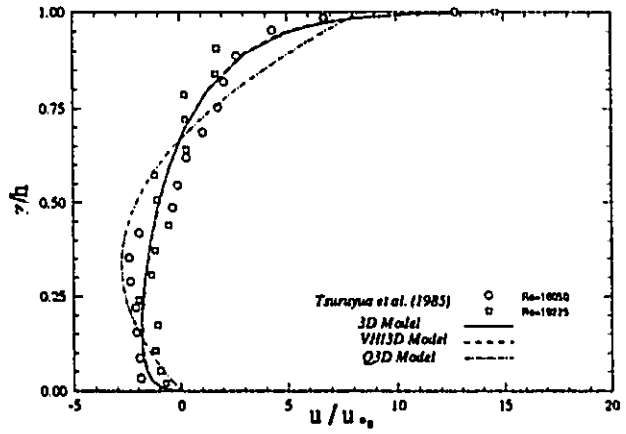

Fig. 6.13 Normalized velocity profile - calibration of the VHI3D, Q3D and 3D models with the experimental data by Tsuruya, Nakano and Kato (1985).

Table 6.3 Experimental results (Tsuruya et al., 1985) and simulations by the 3D and VHI3D models.

Quantity		Test 1	Test 2	3D	VHI3D
Depth	h (m)	0.15	0.15	0.15	0.15
Wind Velocity	W (m/s)	6.73	6.90	6.80	6.80
Surface Shear Velocity	u_{*_s} (cm/s)	0.815	0.835	0.823	0.823
Surface Velocity	u_s (cm/s)	10.70	12.15	11.79	11.55
Reynolds Number	$R_s = u_s h / \nu$	16050	18225	17685	17325
Normalized Surface Velocity	u_s / u_{*_s}	12.74	14.55	14.32	14.32
Absolute Roughness	Z_{ow} (mm)	0.21	0.36	0.31	0.33

The above comparison can be presented in terms of coordinates of the "smooth" inner law of the velocity distribution, relative to either surface or bottom interface, as shown in Fig. 6.14. The curves (A), (B), (C1) and (C2) are described by Eqs. (6.15) to (6.18), respectively. It is clearly indicated that the solid symbols representing model simulation results are located in the regime between lines C1 and C2. The absolute roughness Z_{ow} calculated from the von Karman number R_{kw} is 0.31 mm for the 3D model and 0.33 mm for the VHI3D model. Both are between 0.21 mm and 0.36 mm for the experiment. The model results are fully developed in contrast to the experimental ones, due to finite length of the channel that limits the boundary layer development. These differences are evident in Figs. 14(a) and (b). The model results are in good overall agreement in both surface and bottom layers.

6.4.2 Model Comparison in a Basin

A rectangular basin is employed to examine the model response in the presence of the wind forcing. The basin is square with a side of 10 km, is shallow near both the north and south

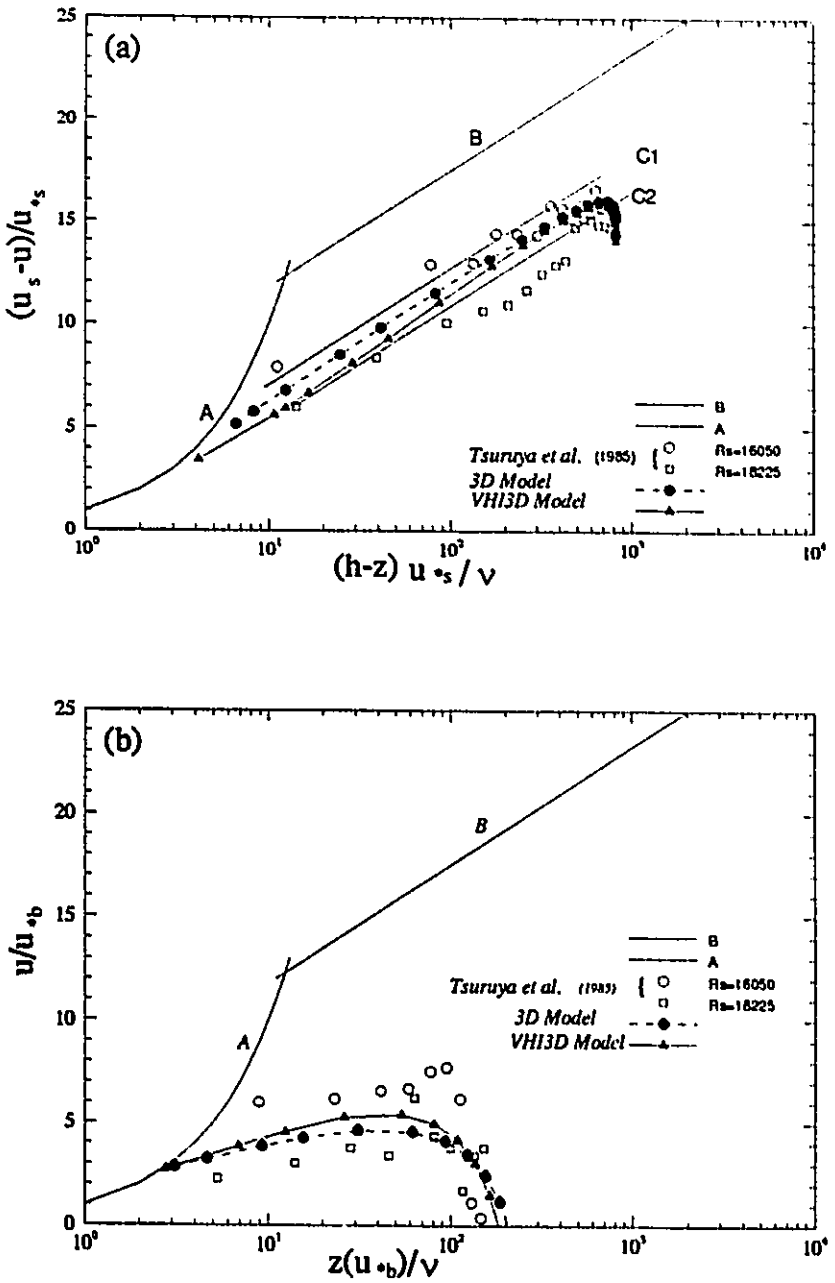

Fig. 6.14 "Smooth" inner-law of velocity distributions of the experimental data by Tsuruya, Nakano and Kato (1985) and the model simulations by the VHI3D and 3D models, relative to (a) the surface interface, (b) the bottom.

shores and gradually increased from 5 m to 15 m in the central regime. The depth is uniform in the x-direction, as shown in Fig. 6.15. A uniform 10 m/s west wind is applied in the test. The grid size of 500 m, and time step of 20 sec are used in all models. Twelve layers with enhanced resolution both near the surface and the bottom are used in the multi-layered three-dimensional model, in order to obtain good velocity profile in the vertical plane.

The steady depth-averaged circulation patterns, as shown in Fig. 6.16, predicted by the 2DH model, Q3D, VHI3D and 3D models are similar. The strong currents (about 10 cm/s) are along the wind direction in the shallow shores, while in the central deep basin, the currents are in the opposite direction. It produces two symmetric gyres in the basin, one clockwise and another counterclockwise. This is due to the topography of the basin, and is a typical feature of the wind-driven circulation in lakes, as revealed by many investigators in the numerical study. The physical mechanism, illustrated by Csanady (1982), is that at initial stage, in the shallow water the wind shear stress is greater than the pressure gradient due to the water elevation. Therefore, the water accelerates downwind, while in the deep water the pressure gradient is greater than the wind shear stress, and consequently a return flow against the wind develops. The velocity grows with time, and reaches a steady state when the pressure terms are balanced with the wind shear stress, bottom shear stress, advection and Coriolis terms.

The surface drift velocity is important for the study of surface oil spill and wave-current interaction. Although it is very difficult to measure the surface drift velocity in lakes or oceans, many laboratory experiments have been conducted to measure this velocity. The commonly accepted value of the ratio of water surface velocity to wind velocity is about 0.03 (Wu, 1975). A 10 m/s wind will produce, according to Wu (1975), a surface drift velocity of 30 cm/s. Fig. 6.17 shows the surface velocity predicted by the models. Obviously, no solution can be

obtained from the 2D model. The current predicted by the VHI3D and 3D models are almost exactly the same, about 27 to 30 cm/s in the same direction with the wind. The currents prediction by the Q3D model are about 15 to 17 cm/s in the shallow shore, while only 1 - 3 cm/s in the central deep basin.

The near bottom velocity becomes very crucial in the suspended solid transport model, because the resuspension rate is largely dependent on the near bottom shear stress, and thus the bottom velocity. The circulation patterns at the first layer near bottom (e.g., σ = 0.02) are illustrated in Fig. 6.18. The circulation patterns are similar in the Q3D, VHI3D and 3D models. However, the magnitude in the Q3D model is smaller than those in the VHI3D and 3D models. The bottom current has the same direction as the wind in the shallow shores, except in the corners, which is due to the lateral boundaries. It has an opposite direction to the wind in the central deep basin.

The vertical current structure is illustrated in Fig. 6.19. The velocity components u and v at two locations A and B (see Fig. 6.10) are included. The v component is uniform because the west wind is applied. In the shallow shores, presented by point A, there is no return flow in the low layers, and the current is along the wind direction in the whole depth. In the deep basin, presented by point B, a return flow opposite to the wind currents. The prediction by the Q3D model is of a parabolic profile, linearly decreasing from the surface to the bottom in shallow shore. The prediction by the VHI3D model is very close to the one by the 3D model. Both models have a double-logarithmic profile. The velocity distributions near the surface and bottom are well simulated.

It should be pointed out, however, that although the VHI3D and 3D models well simulate the detailed current structure, compared to the experiment and in this simplified basin, a

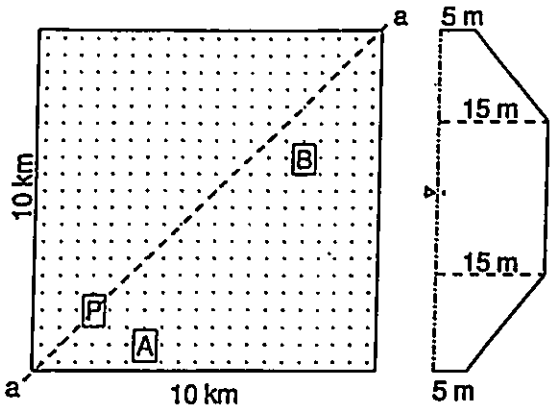

Fig. 6.15 A simplified test basin and its topography used for model comparison. The basin is uniform along x-direction and varied in y-direction.

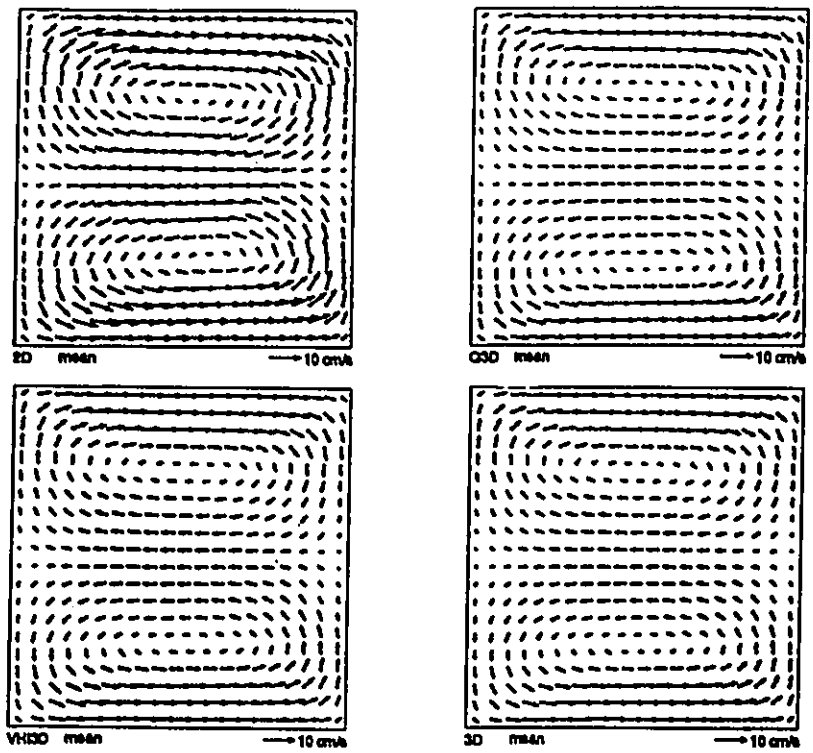

Fig. 6.16 Depth-averaged circulation patterns simulated by the 2D, Q3D, VHI3D and 3D models. A 10 m/s west wind is applied and steady state of current is presented.

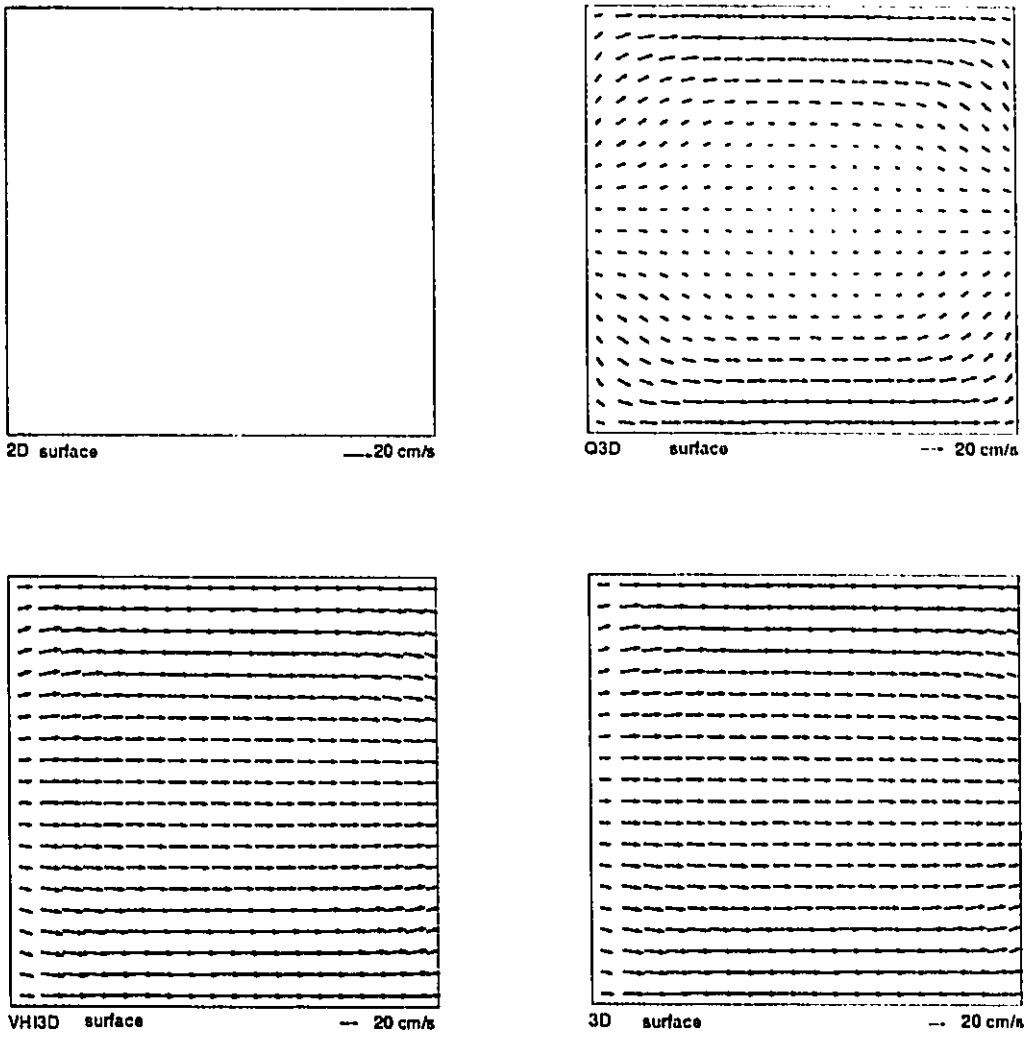

Fig. 6.17 Surface circulation patterns simulated by the 2D, Q3D, VHI3D and 3D models. A 10 m/s west wind is applied and steady state of current is presented.

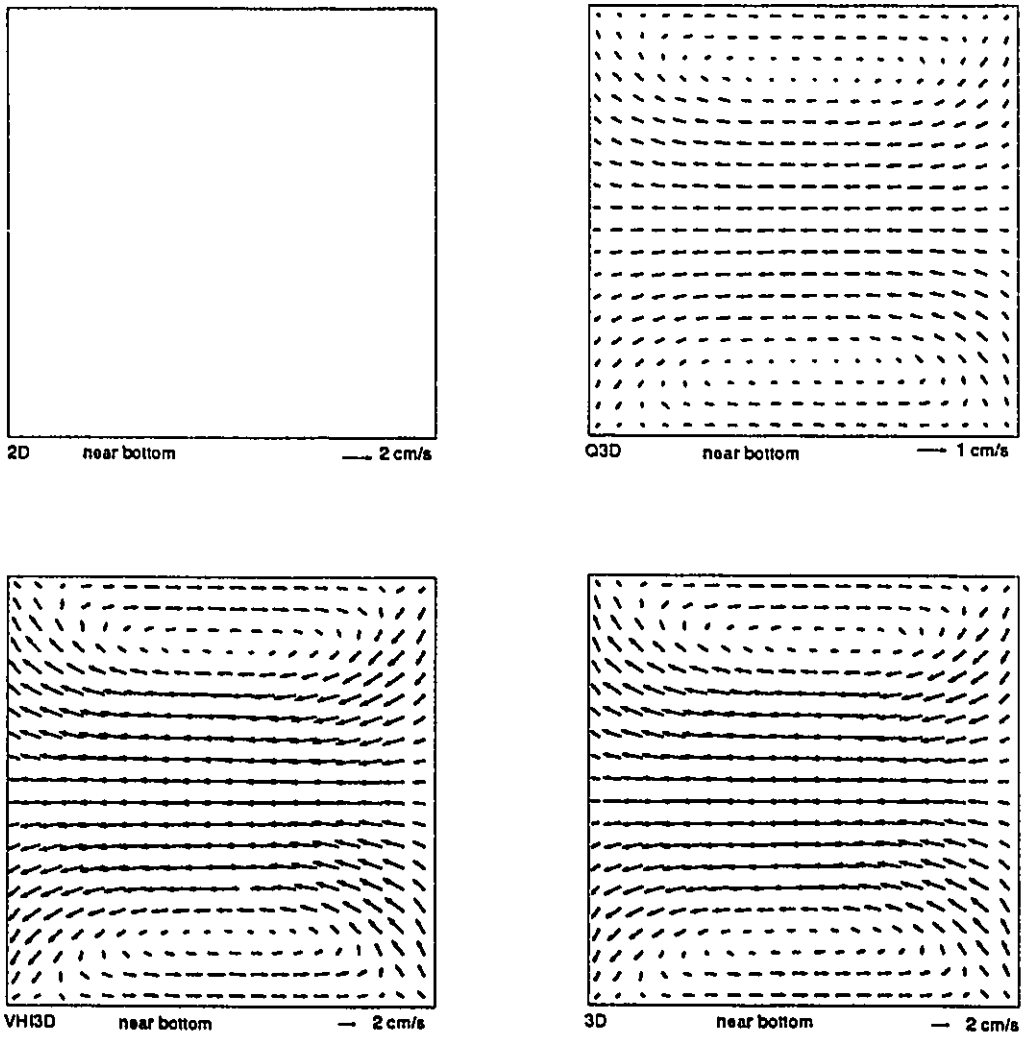

Fig. 6.18 Near bottom circulation patterns simulated by the 2D, Q3D, Q3D and 3D models. A 10 m/s west wind is applied and steady state of current is presented.

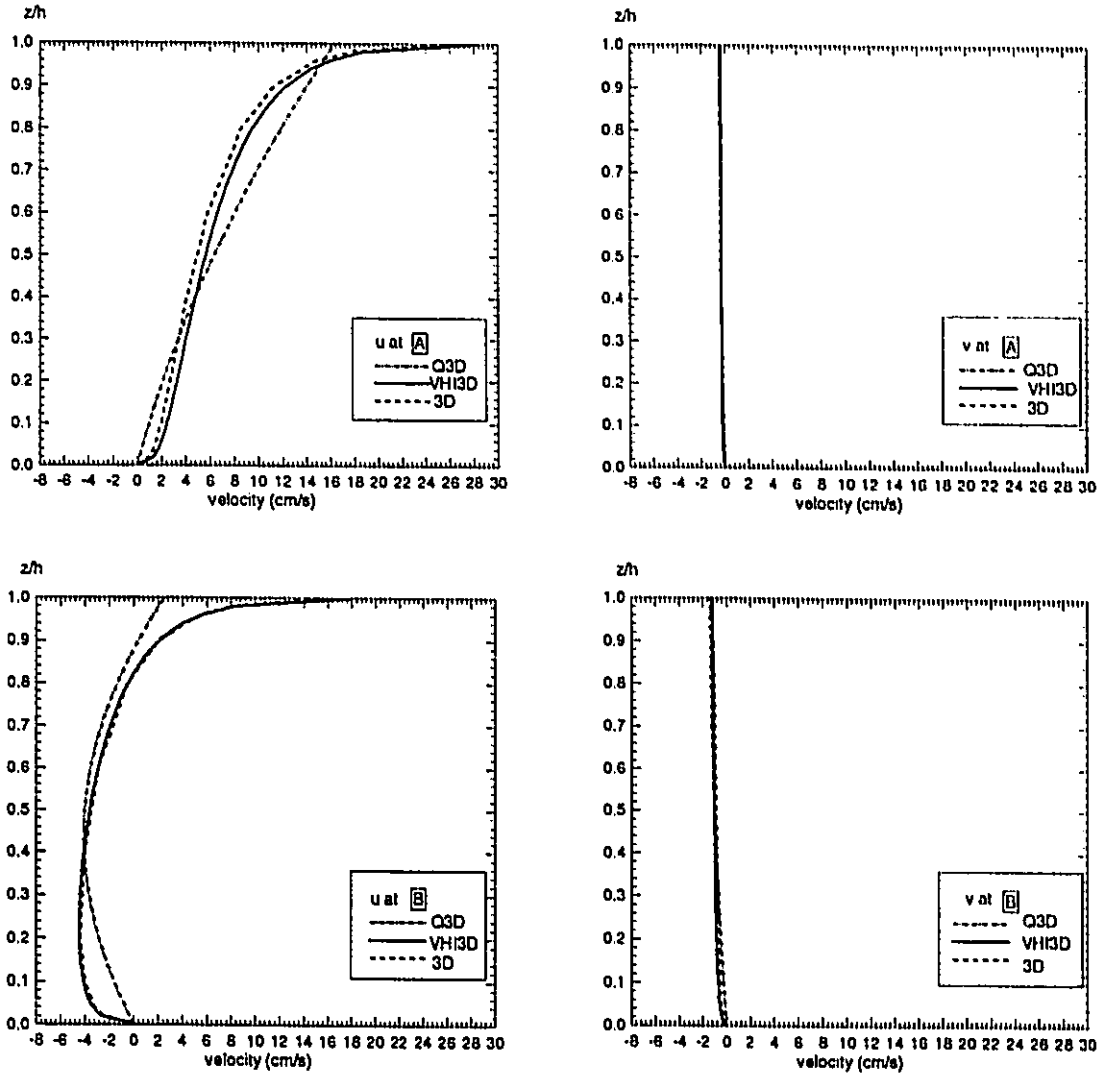

Fig. 6.19 Vertical profiles of horizontal velocity at point A and B simulated by the Q3D, VHI3D and 3D models. A 10 m/s west wind is applied and steady state of current is presented.

high resolution grid in the vertical in the 3D model must be used (see Fig. 6.8), while there are no such restrictions for the VHI3D model. The current at any depths at any location can be directly calculated with little computational work. In contrast, in the 3D model, the outputs of vertical currents are only made at those depths where the vertical layer is assigned.

Fig. 6.20 shows the simulated water elevation fields. The water goes down about 1 cm in the upwind west shore, and rises about 1 cm in the downwind east shore. The set-up predicted by the 2D model is smaller than those by the other three models. However, the set-up predicted by the Q3D model is larger than those by the VHI3D and 3D models. This is more clear to be observed from the set-up in section a-a (see Fig. 6.10), as shown in Fig. 6.21(b). From a practical or numerical viewpoint, these differences may be adjusted. For example, by decreasing bottom friction coefficient, the set-up becomes higher. From a physical viewpoint, however, the differences are highly significant, and depend largely on the different formulations of the bottom shear stress.

If the Coriolis force and advective terms are ignored under steady state conditions, the external stress is balanced by the pressure gradient, produced by the difference in water elevations. The momentum equation in x-direction becomes,

$$g\frac{\partial \zeta}{\partial x} = \frac{\tau_{sx} - \tau_{bx}}{H} \tag{6.20}$$

After integrated between two locations (separated by a length L), the set-up can be calculated by

$$\Delta\zeta = \frac{L}{g\bar{H}}(\tau_{sx} - \tau_{bx}) \tag{6.21}$$

where the $\bar{H}$ is the effective depth in the set-up line determined by the topography. Therefore, for a given surface stress which is determined by the wind velocity and wind drag coefficient, the

set-up only depends on the formulation of bottom shear stress τ_{bx}. Underestimation of bottom stress will result in overestimation of the wind set-up, and vice versa. The bottom shear stress is evaluated by the near bottom current,

$$\tau_{bx} = \nu \frac{\partial u}{\partial z} |_{z=z_a} \tag{6.22}$$

In the Q3D and VHI3D models, it is evaluated using the above formula based on the velocity profile, while in the 3D model, it is calculated from the velocity at the first layer from the bottom. The conventional 2D model, however, computes the bottom stress based on the depth-averaged velocity, by either using the quadratic law (Leentedertse, 1967) or the linear relationship (Simons, 1980, 1985; Schwab, 1983). The directions of the depth-averaged currents are not always in the same direction as the currents near the bottom. The depth-averaged velocity is usually larger than the bottom velocity. As a result, the bottom shear stress is overestimated, and, the set-up is underestimated. In the Q3D model, the bottom shear stress is underestimated because the steep velocity gradient could not be well simulated due to the parabolic velocity profile used. Therefore, the wind set-up predicted by this model is higher than the one by the VHI3D model or the 3D model.

The total kinetic energy of simulation calculated from the depth-averaged velocities is shown in Fig. 6.21. It is observed that the total kinetic energy in the 2D model is higher than those from other three models. The physical mechanism behind it is that the pressure gradient is smaller, so that, the larger portion of wind shear stress is transformed to the momentum of water, compared with the Q3D, VHI3D and 3D models.

Let's examine the computational efficiency. Assuming the computational time (CPU) for the 2D model (2.1 minutes for a 24 hours simulation in SPARC station 10) as one unit, then

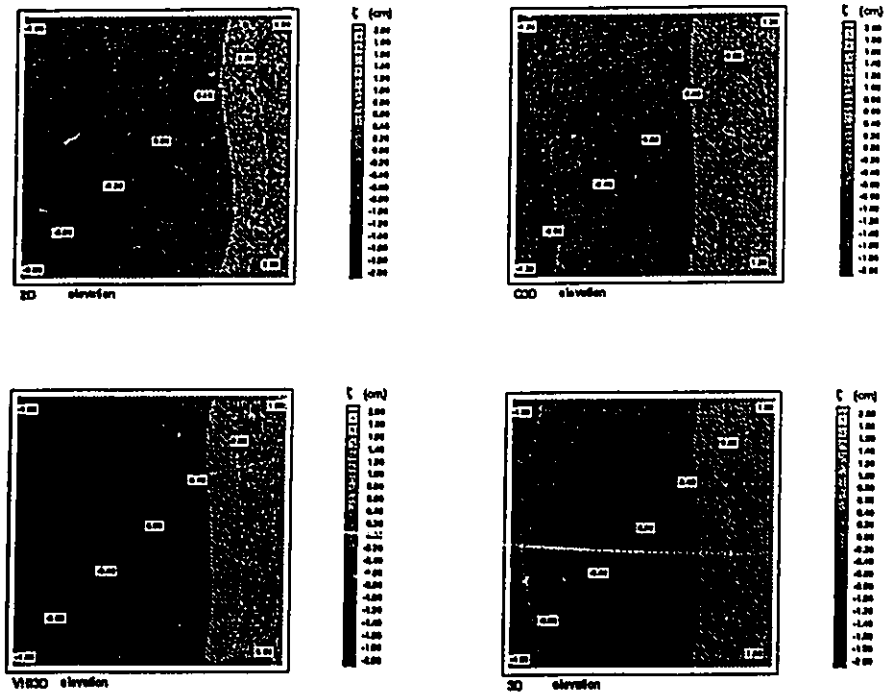

Fig. 6.20 Water elevation distributions simulated by the 2D, Q3D, VHI3D, and 3D models. A 10 m/s west wind is applied and steady state of current is presented.

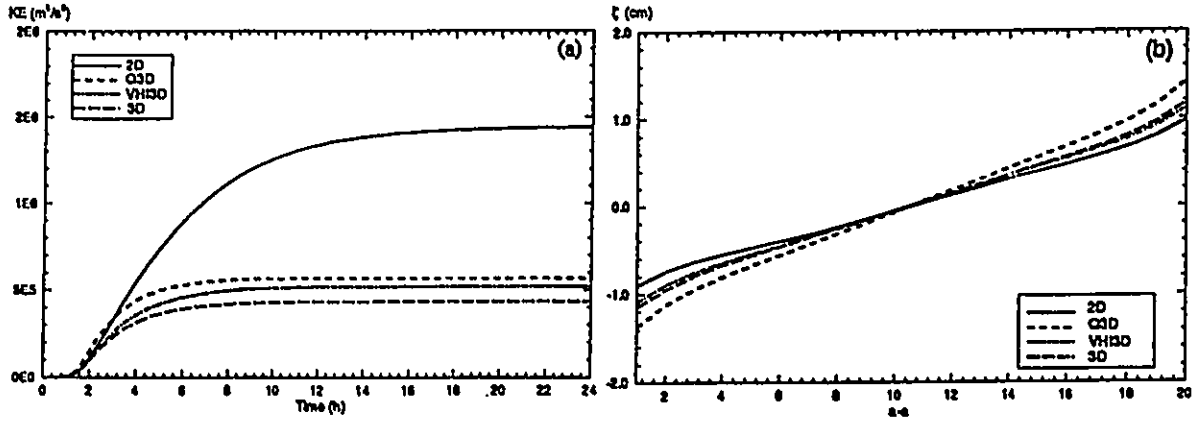

Fig. 6.21 Model comparison: (a) total kinematic energy of simulations by the 2D, Q3D, VHI3D and 3D models, (b) wind set-up along a-a section simulated by the 2D, Q3D, VHI3D and 3D models. A 10 m/s west wind is applied and steady state of current is presented.

the time for the Q3D, VHI3D and 3D models are 1.5, 1.8 and 12, respectively. The quasi-three dimensional model takes the same order of time as the 2D model. The time for the 3D model may be reduced if less layers are in the vertical plane. However, the prediction then will be less accurate.

6.5 EXPERIMENT ON THE EFFECT OF THERMAL STRATIFICATION

Although the VHI3D or Q3D model can be used as an alternative model to the general multi-layered 3D model for the simulation of wind-induced currents, the 3D model must be used when the thermal stratification is included because it is excluded in the Q3D and VHI3D models. To illustrate the application of the stratified 3D circulation model and examine the effect of thermal stratification, a numerical experiment on upwelling and downwelling is designed in this section. This will help to establish model credibility, and also provides a framework for extending the model to real stratified lakes where situations can be complicated.

6.5.1 Computational Conditions

Consider the response of a stratified lake to the onset of an upwelling favorable wind. As shown in Fig. 6.22(a), the simplified basin is a square with a scale of 10 km, having a uniform depth along the y direction, and having a depth of 15 m in the western shore which gradually increases to 5 m in the eastern shore. The initial temperature is horizontally homogeneous with a vertical profile similar to that observed in Hamilton Harbour during the summer, as shown in Fig. 6.22(b). The temperature is approximately 24^o C within 5 m below the water surface, and 12^o C below 11 m. There is a thermocline between 6 to 10 m, with a temperature difference of 12^o C. A western wind ($W_x = -10$ m/s and $W_y = -1.0$ m/s) was applied.

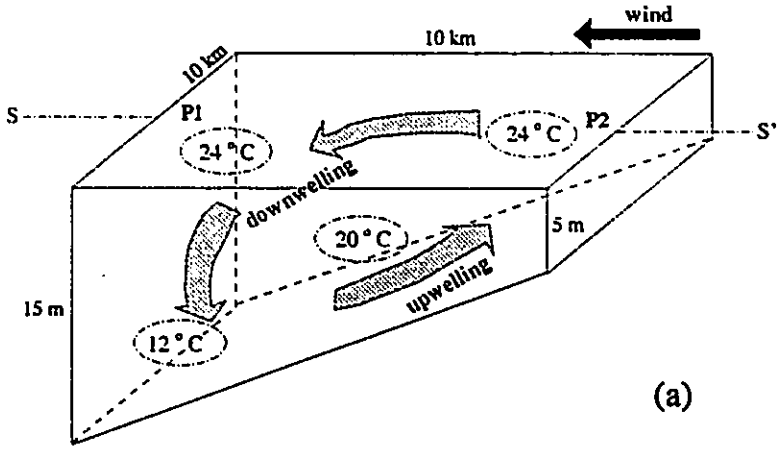

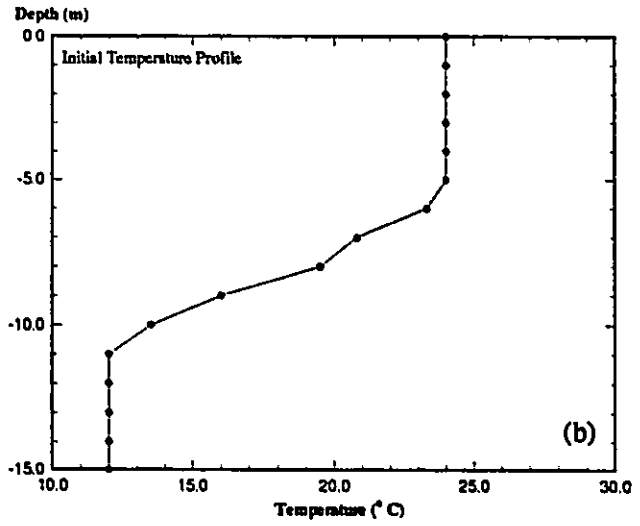

Fig. 6.22 Experiment on the effect of thermal stratification: (a) a simplified basin, (b) the initial vertical temperature profile used in the test (homogeneous in the horizontal plane).

The 3D model consists of 12 σ levels. The time step of 12 seconds and the horizontal grid size of 500 m are used in the model. Multi-layered velocities and temperatures are outputted at various simulation times. The profiles of velocities and temperature are displayed at two points, P1 and P2, and a typical cross section S-S' (see Fig. 6.22(b)).

6.5.2 Simulation Results

The depth-averaged circulation pattern and the horizontal circulation patterns at various layers (in σ layer) after 40 hours are presented in Figs. 6.23 (a)-(e). Under the action of the above western wind, about 20 cm/s western surface drift current and 3 cm/s eastern bottom return flow are obtained from the simulation (see Figs. 6.23(b)-(e)). The resulting depth-averaged velocities are very weak, only about 2 cm/s (see Fig. 6.23(a)). In the view of the section along S-S', the vertical current structure is evident. The strong current follows the wind in the upper layer forming a surface drift current, while a return flow exists around the thermocline regime. The latter flow is stronger at 10 hours (the beginning stage) than at 40 hours (after a long simulation), when the water mass with different temperatures have been fully mixed. It should be mentioned that the wind-induced currents are nearly horizontal in the test lake. The magnitude of the vertical velocity component w (less than 0.01 cm/s as shown in Figs. 6.24(c) and (d)) is much smaller than the magnitude of the horizontal velocity component u and v (1 to 20 cm/s). As a result, the vertical gyre can not be observed in the vector plot in Figs. 6.24(a) and (b), where the same scale is used for the horizontal and vertical velocity components. The scale used in the vertical (depth) is much larger than the scale used for the horizontal (x-direction). Based on this concern, one can examine the vertical gyres from the contour plot of the vertical velocity component in the cross section as shown in Figs. 6.24 (c) and (d). At 10 hours (beginning stage), a clear vertical gyre exists. The positive values, or upward velocities, are found in the eastern

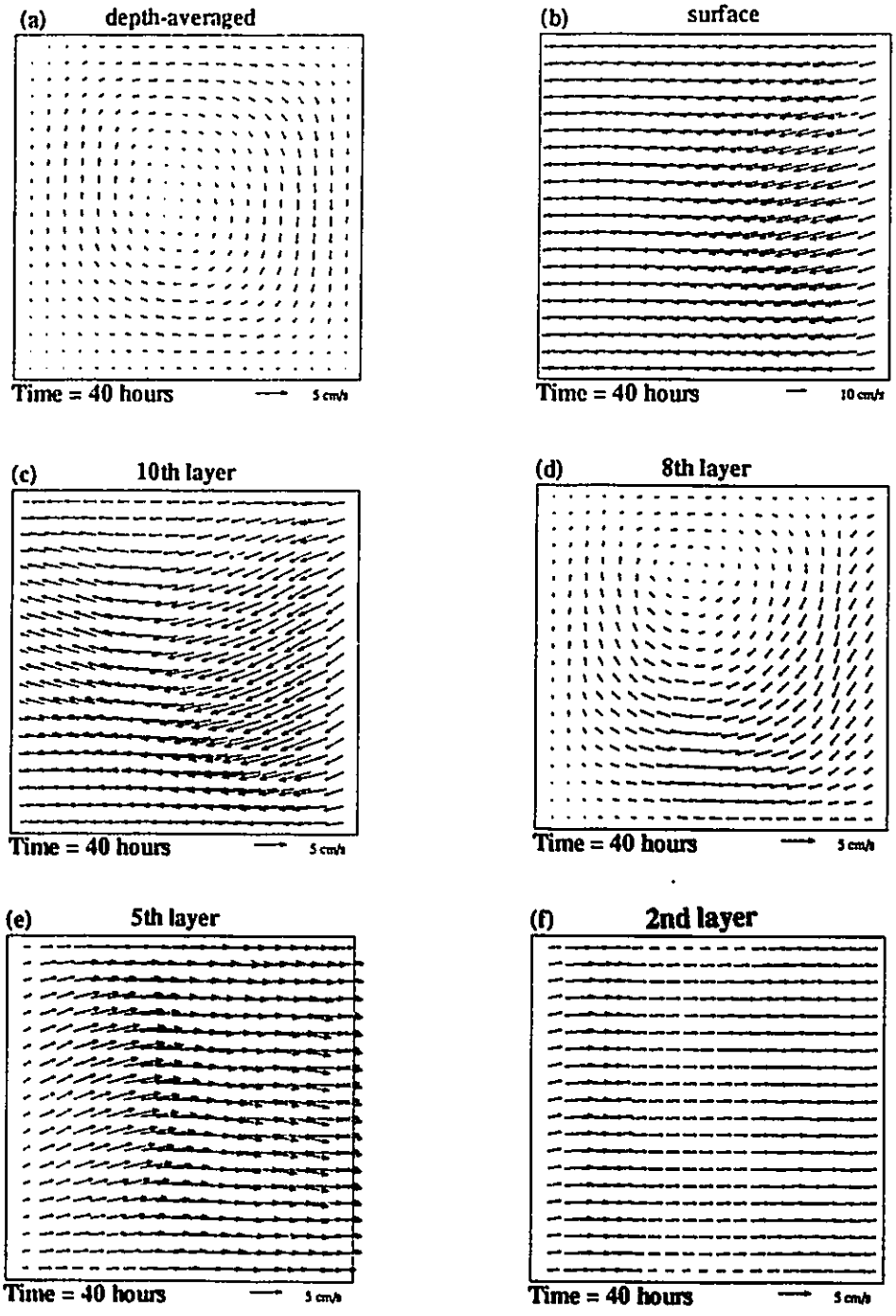

Fig. 6.23 Horizontal circulation patterns after 40 simulation hours in the test: (a) depth-averaged, (b) at surface, (c) at 10th layer ($\sigma = -0.15$), (d) at 8th layer ($\sigma = -0.3$), (e) at 5th layer ($\sigma = -0.6$) (f) at 2nd layer ($\sigma = -0.95$).

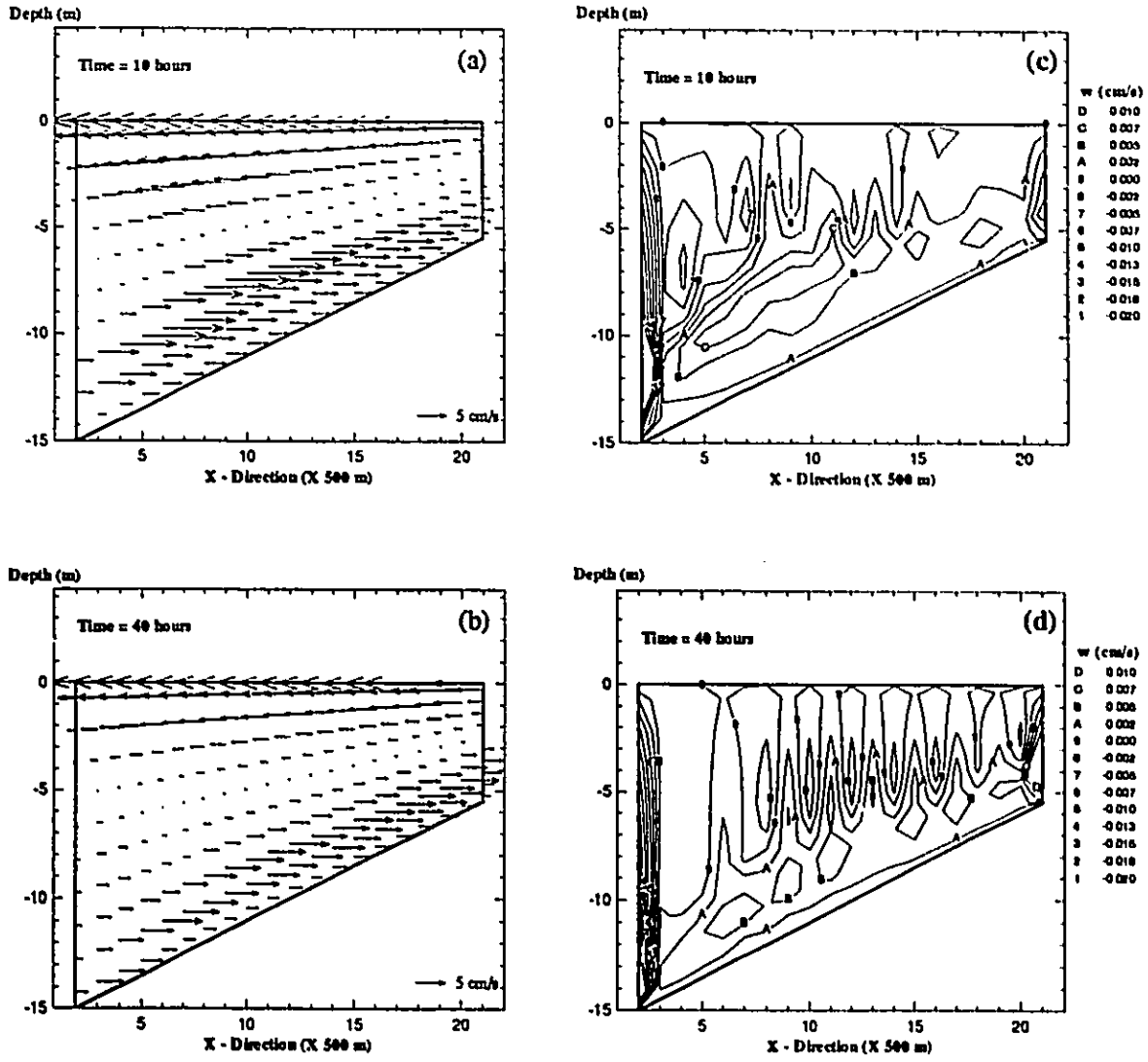

Fig. 6.24 Circulation patterns along the vertical section S-S' in the simulation:(a) velocity vectors after 10 simulation hours, (b) velocity vectors after 40 simulation hours, (the vertical velocity component W may enlarged to show the undistoted pattern) (c) contours of vertical velocity component after 10 simulation hours, (d) contours of vertical velocity component after 40 simulation hours.

shore and near bottom. A strong current was climbing along the slope of the bottom from the deep part in the west shore to the shallow part in the east shore. The sinking flow is found in the western regime. As we know, the wind-induced circulation in a lake under the action of a steady wind will eventually be stabilized and reach a steady state. However, it was found that the simulation in a stratified lake has difficulty reaching a steady state due to the effect of internal waves (it is induced by the difference of density between layers). After 40 hours, the flow is close to the steady state; upward currents are still found along the bottom. However, several weak gyres are found in the middle depth regime, reflecting the internal wave, which is due to the existence of thermocline in the regime.

The upwelling and downwelling of water mass with different temperatures are expected under the above current structure. Fig. 6.25 presents the sequential patterns of temperature along the vertical section S-S' from the simulation at the initial time and at 10, 20, 40 simulation hours, respectively. The darker of the flooding contours corresponds to the lower temperature. At the start, the temperature is horizontally uniform, see Fig. 6.25(a). Then, the cold water in the bottom gradually moves from the bottom to the upper layer along the slope of the bottom, and at the same time, warm water enters the lower layers in the western regime, see Figs. 6.25(b) and (c). Finally, after 40 simulation hours, the water mass with different temperatures are well mixed, see Fig. 6.25(d).

The effect of thermal stratification on the current structure may be examined also from the vertical distribution of the horizontal velocity component. Fig. 6.26 shows the sequential velocity profiles at displaying points P1 and P2 (see Fig. 6.22(a)) at 10, 20, and 40 simulation hours, and at 20 hours without the thermal stratification for comparison. Strong currents were developed around the thermocline regime. The profiles at P1 and P2 are very close in the non-

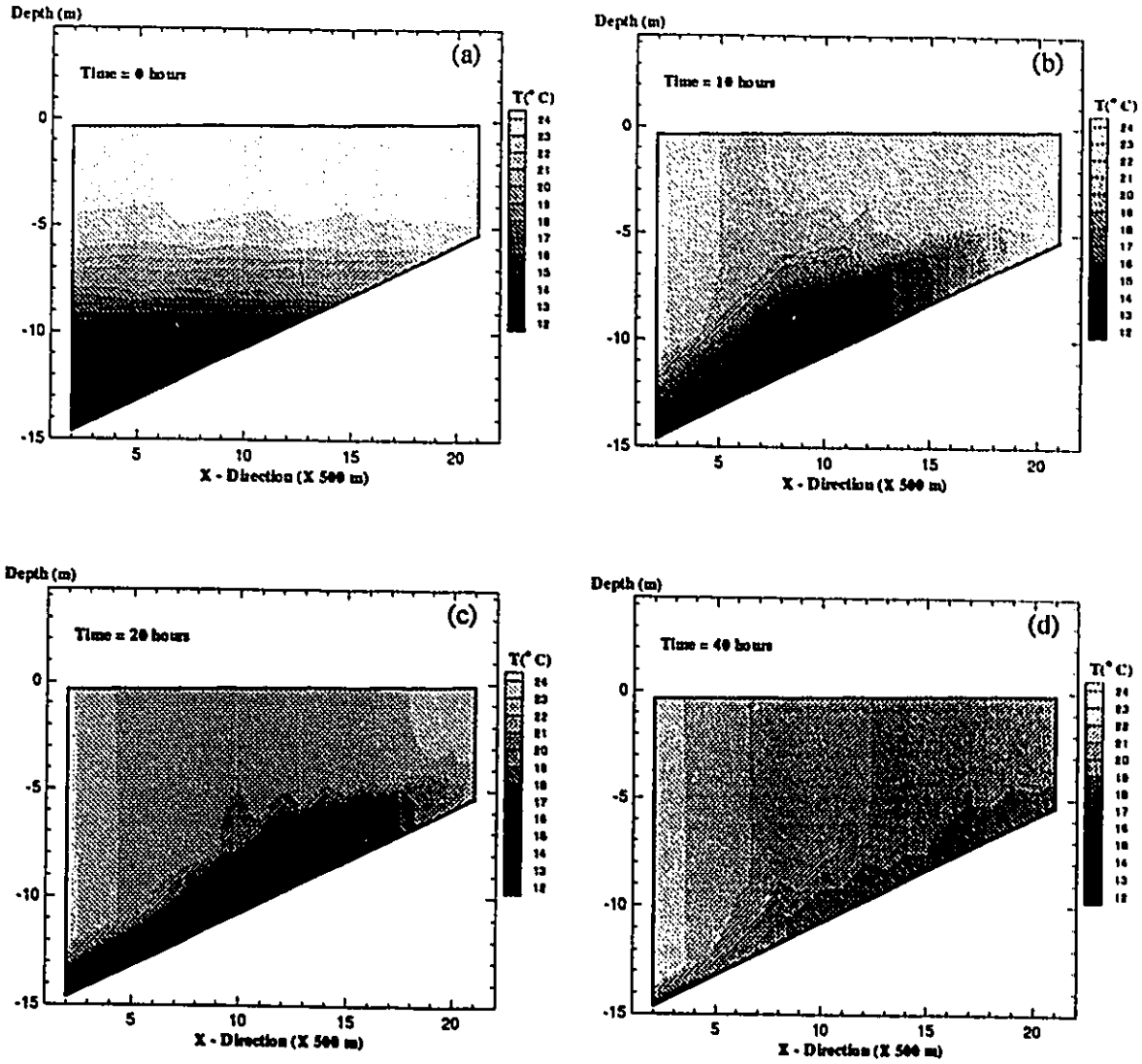

Fig. 6.25 Sequential patterns of temperature along the vertical section S-S' fromthe simulation: (a) initial, (b) 10 simulation hours, (c) 20 simulation hours, (d) 40 simulation hours.

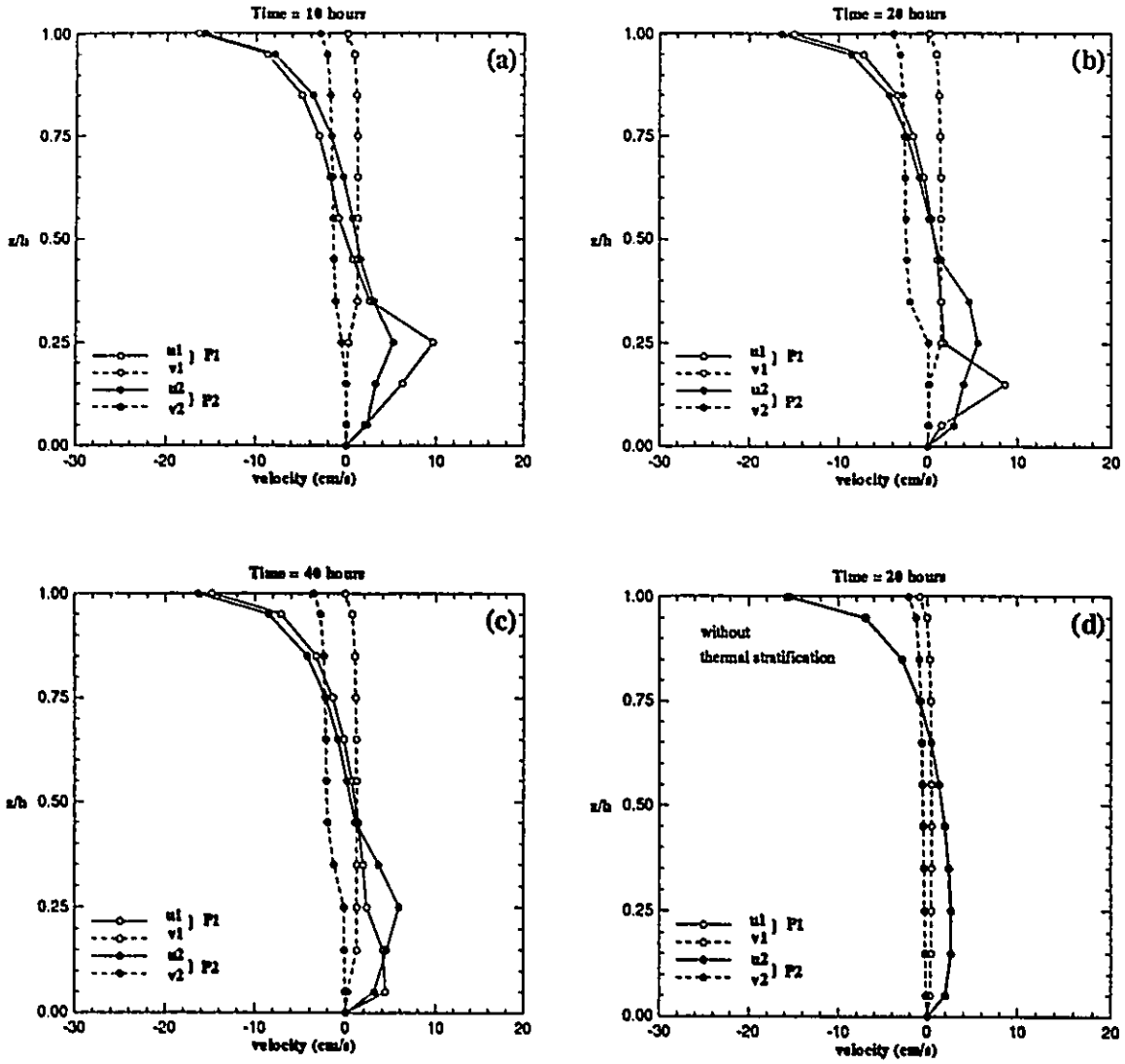

Fig. 6.26 Sequential velocity profiles at displaying point P1 and P2 (see Fig. 6.23(a)): (a) 10 simulation hours, (b) 20 simulation hours, (c) 40 simulation hours, and (d) 20 simulation hours in the case of without thermal stratification for the comparison.

stratified case, while the current structure became more complicated in the stratified case.

The internal wave is indeed complicated. Quantitative analysis can be found in the literature. The above simple numerical experiment provides us some insight into the interaction of current and temperature structure.

6.6 SUMMARY

From the above extensive study of wind-induced currents, the response of various models to the wind forcing mechanism, in a numerical sense, is clearly demonstrated. It is found that the distribution of vertical eddy viscosity plays a very important role in the simulation of wind-induced currents. A parabolic velocity profile is derived when a constant vertical viscosity is used, as in the case of laminar flow, while a double-logarithmic velocity profile with the usage of parabolic eddy viscosity distribution is derived as in the case of turbulent flow. The quasi-three dimensional model (Q3D) is excellent in modelling the laminar flow, but failed to work for the turbulent flow, especially for the currents in both the surface and bottom boundary layers. The multi-layered three-dimensional model (3D) was calibrated and verified with the newly-developed analytical solutions and the extant experimental results. However, it should be pointed out that a high resolution of vertical layer discretization must be adopted to precisely predict the surface drift current and near bottom boundary current. This finding is of significance in coupling the 3D model to the oil-spill prediction model, or air-water interaction study in which the drift current and the velocity gradient are the essential factors. It is also of significance to the sediment transport model, in which the near bottom velocity gradient is used to determine the bottom shear stress, and in turn, the sediment resuspension or settling flux.

It is concluded from the comparison among the Q3D, 3D and VHI3D models that the VHI3D model can successfully simulate the three-dimensional wind-induced currents similar to the multi-layered 3D model, while significantly less computational time is needed. The detailed structure of surface drift and near bottom currents are easily obtained with almost no computational effect in the VHI3D model, while in the 3D model, a high resolution vertical discretization must be used with a much higher computational cost. The VHI3D model developed in this thesis should have great significance for the various applications in lakes in the case of isothermal conditions.

The numerical experiment using the fully multi-layered 3D circulation model in a stratified basin provide us some insight into the current, in the stratified basin. A strong current is found in the thermocline regime, and the thermal stratification makes the current structure more complicated and non-uniform.

PART III

MODEL APPLICATIONS TO THE GREAT LAKES

To this point, the circulation models have been verified with the laboratory data. Although the verification of the models with field data is necessary (it will be done in PART IV), confidence and knowledge on the behaviour of various models have been obtained through the evaluations using the laboratory data. In this part of the thesis, the first application is to apply the Q3D and VHI3D models to efficiently predict the three-dimensional circulation patterns in the Great Lakes, which were used as a database for the Atmospheric Environment Service (AES) of Environment Canada, in order to predict spill movement in the event of a marine oil-spill emergency. The second application is to apply the integrated two-dimensional hydrodynamic and pollutant transport model in the St. Clair River in Sarnia, to study the bacterial pollution and feasibility of various remedial measures. This study provides a general approach to the environmentally concern areas of the Great Lakes, where remedial measures are required.

CHAPTER 7

MODELLING CURRENTS IN THE GREAT LAKES

Atmospheric Environment Service (AES) of Environment Canada requested an available database of water currents in the Great Lakes in order to predict spill movement in the event of a marine oil-spill emergency. The quasi-three dimensional circulation model was applied for such a purpose (Tsanis and Wu, 1991), with a total of 100 Mbytes simulation data for each lake under 3, 5, 7, 10, 15, and 20 m/s winds at 22.5 degree intervals. For the same purpose and wave-current interaction study, a similar simulation extended to Lake St. Clair (Tsanis and Wu, 1990; Wu and Tsanis, 1991). The results from these two projects will constitute this chapter. Comparisons with field results in Lake St. Clair and Lake Ontario from the existing publications will be presented.

7.1 INTRODUCTION

The Great Lakes of the St. Lawrence River system (Fig. 7.1), shared by Canada and the United States, constitute one of the largest masses of fresh water on the earth. The lakes themselves - Superior, Michigan, Huron, Erie, Ontario, and the relatively small St. Clair - have a total water area of 246,000 km^2, and a volume of 23888 km^3. The maximum depths are 406, 281, 229, 64, 224 and 6 meters, and, the average depths are 149, 85, 59, 19, 86, and 3 meters,

respectively. They provide good transportation, relatively inexpensive hydroelectric power, valuable fisheries, an abundance of water for industrial purposes, and increasingly popular recreation facilities. In addition, the lakes are fresh water supply, while at same time they act as a sewage disposal system for the population. In the event of a marine oil spill emergency in the Great Lakes, the Atmospheric Environment Service (AES) of Environment Canada is responsible for providing real-time predictions of spill movement. In addition to winds, the oil spill movement is directly affected by water currents. Therefore, there is a requirement to have available a database of water currents in the Great Lakes. This database should be easily accessible and usable in an emergency environment.

The Great Lakes are interconnected by a system of channels and rivers. As a result, the circulation patterns in these lakes are both wind and hydraulically driven. With the exception of Lake St. Clair, the hydraulically-induced current is negligible compared to the wind-induced one. Thermal stratification during the summer season must be also included, as well as spatial distribution of wind field and radiation. However, these factors are complicated and need a lot of measured or forecasted meteorological and hydrological data, along with a complicated numerical circulation model. For the purpose of establishing an easily accessible database, it's economic to exclude these factors. A depth-averaged circulation model can only simulate depth-averaged currents and obviously cannot provide currents in different layers. A fully three-dimensional circulation model requires a large amount of computational time, because the database should involve not only various wind speeds (3, 5, 7, 10, 15, 20 m/s) and directions (at intervals of 45 degree) but also different layers for all six lakes. Therefore, an efficient circulation model should be helpful and feasible for such circumstances. The Q3D and VHI3D are the appropriate models to be used, the same capability and accuracy will be maintained. The

Table 7.1 Parameters used in the circulation modelling of the Great Lakes

Parameters/Lakes	Superior	Michigan	Huron	Erie	Ontario	St. Clair
$dx\ (m)$	4000	4000	4000	4000	4000	1200
imax	152	66	102	104	77	38
jmax	71	127	94	30	30	39
C_D	0.000002	0.000002	0.000002	0.000002	0.000002	0.000002
t_h	0.9991	0.9991	0.9991	0.9991	0.9991	0.9996
$K_h\ (m^2/s)$	60	60	60	60	60	15
$dt\ (s)$	60	60	60	60	60	10
$Q\ (m^3/s)$	0.0	0.0	0.0	5500	6500	5700

Notes:

imax, jmax = maximum value of i, j grid index, respectively.
K_h, t_h = horizontal eddy viscosity and smooth factor.
C_D = wind drag coefficient (relative to 10 m wind).
dx, dt = spatial grid size and time step.
Q = average total inflow or outflow

Fig. 7.1 Geographic locations of the Great Lakes including Lake Superior, Lake Michigan, Lake Huron, Lake St. Clair, Lake Erie and Lake Ontario.

advantage over the multi-layered 3D model is that the currents at any depths can be obtained using the depth-averaged currents and the related wind conditions at almost no cost (in the fully-3D model vertical layers are discretized before any simulations, and the number of layers is limited). The Q3D and VHI3D models are applied in a 4 km grid for the Great Lakes except for Lake St. Clair where a 1.2 km grid was used. The parameters used in the model for each lake are listed in Table 7.1.

7.2 CIRCULATION AND WAVE-CURRENT INTERACTION IN LAKE ST. CLAIR

7.2.1 Introduction

Lake St. Clair is located between Lake Huron and Lake Erie, and connected with Lake Huron Via the St. Clair River and with Lake Erie via the Detroit River. It is a small shallow lake with a mean depth of 4 m and a maximum depth of 6 m (Fig. 7.2a). It has the St. Clair River as an inflow and the Detroit River as an outflow with an average flow rate of 5700 m^3. Its shallowness and high in/outflow results in a strong hydraulically-induced current aligned roughly north to south, which is the direction of the St. Clair River to the Detroit River (Schwab et al., 1989). The hydraulic residence time is only about 9 days (100 to 500 days for the other Great Lakes).

Analysis of wave data collected during the 1985 field study on Lake St. Clair revealed significant differences in certain cases between the wind and wave directions (Donelan, 1980). These differences may be due to the interaction between the waves and the currents in the St. Clair-Detroit River system flowing through Lake St. Clair. Thus, there is a need to establish the water current structure in the lake under different wind conditions so that the problem of wave-current interaction can be studied (Brissette, 1992). The simulated current field is also useful in

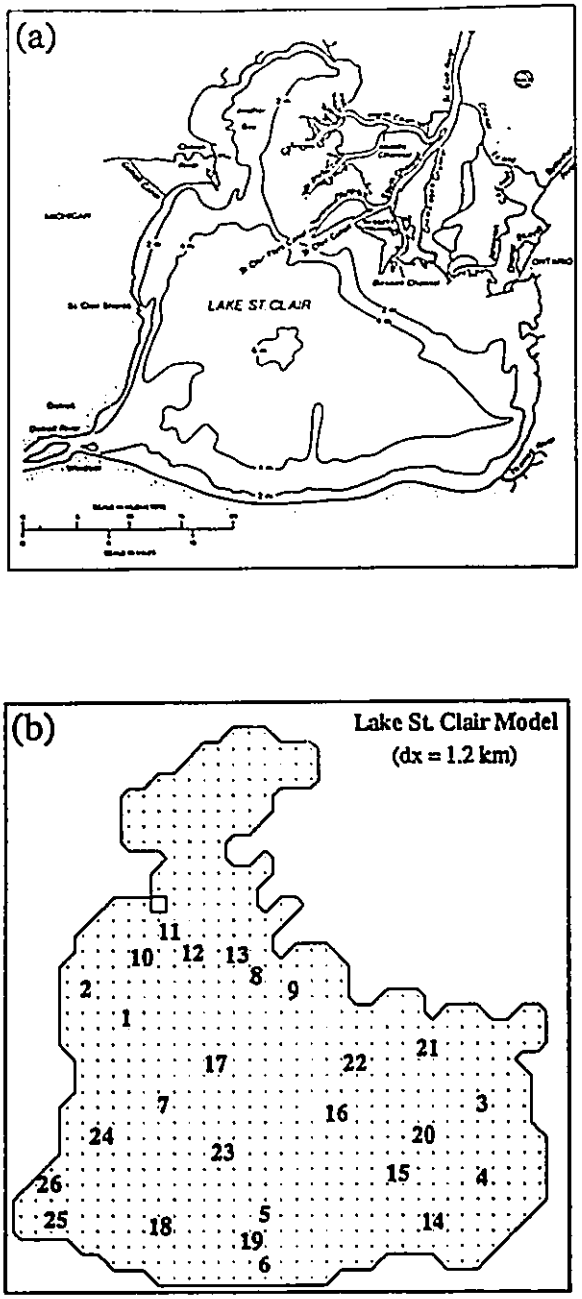

Fig. 7.2 (a) Bathymetric and location map of Lake St. Clair (Schwab et. al., 1989); (b) 1.2 km grid discretization of Lake St. Clair. The numbers show location of lake current measurements (Ibrahim and McCorqudale, 1985).

the water quality modelling in Lake St. Clair.

Three types of models have been employed for the simulations of circulation and wind set-up in Lake St. Clair. These are: a time-dependent rigid-lid model (Schwab et al., 1989), a two-dimensional depth-averaged hydrodynamic model (Simons & Schertzer, 1989; Halfon et al., 1990), and a finite element circulation model (Ibrahim & McCorquodale, 1985). All the above mentioned models ignore the nonlinear advection and horizontal diffusivity terms. The first two models are unable to simulate the three-dimensional current structure, while the third one can only estimate the steady state three-dimensional velocity field. Bottom friction was physically unrealistic in the conventional depth-averaged model for such a shallow lake, and no improvement can be made in such a 2DH model (Simons & Schertzer, 1989). The coarse grid used in the third model makes it difficult to obtain a detailed current field. As discussed in Chapter 4, the Q3D model can simulate the 3D current field in an economical and efficient way. In this section, the typical circulation patterns will be simulated and, based on that a wave ray analysis will be performed to examine the wave-current interaction in the lake.

7.2.2 Typical Circulation Patterns

The Q3D hydrodynamic model is used with a 1.2 km grid to simulate the combined hydraulically and wind-induced circulation in Lake St. Clair (Fig. 7.2b). In this simulation the wind drag coefficient C_D = 1.8 X 10^{-3}, and the mean hydraulic inflow/outflow = 5700 m^3/sec (Schwab et al., 1989). The wind speeds and directions used in the simulation were selected to meet the requirement of the wave-current interaction study. The total kinetic energy evaluated in the simulations reaches the steady state condition in a very short period, within 2 hours, since the lake is shallow and the bottom frictional damping is very large (Fig. 7.3). The 3D-mesh of a

typical wind set-up (under 10 m/s SWW wind) in Lake St. Clair is shown in Fig. 7.4. It indicates a high water level in north shore and a low level in the south.

The pure hydraulically-induced depth-mean circulation simulated by the Q3D model is shown in Fig. 7.5. An advective hydraulic pattern is evident between the inflow and outflow rivers, along with a large counterclockwise eddy covering the eastern basin. The magnitude of the current is about 20.0 - 60.0 cm/s in the advective hydraulic flow, while below 2 cm/s in the eastern basin. This result is in agreement with the observation findings under no wind condition (Schwab et al., 1989). The combined (hydraulically- and wind-induced) circulation patterns for 10 m/s winds at four directions (east, west, north, south) are presented in Fig. 7.6. The common feature in all of these patterns is that the hydraulic flow along the NE - SW direction is dominant in the central and western parts of the lake, while a wind-induced flow is dominant in the eastern part of the lake. In the eastern basin, under east and west wind conditions, the currents follow the wind in the north and south shorelines and form a return flow in the central region; while under north and south winds, the currents along the east shoreline follows the wind.

A typical multi-layer circulation pattern is shown in Fig 7.7 for the case of a 12.3 m/s wind blowing from the SWW direction (87°). At the upper layer (5th layer), the current follows the wind except in the advective hydraulic flow, where the flow is forced to turn in the wind direction. At the middle and bottom layers (3th and 2nd layers), the currents in the eastern part of the lake are 180° out of phase with the wind direction, while the central and western parts are dominated by the hydraulically-induced currents. It is interesting to examine how the wind affects the advective hydraulic flow in the upper layer. Fig. 7.8 shows the surface currents for SWW winds at four speeds, i.e., 3, 7, 10 and 20 m/s opposite to the hydraulic flow. In the eastern parts and near-shore areas of the lake, the surface currents are aligned with the wind, while in the

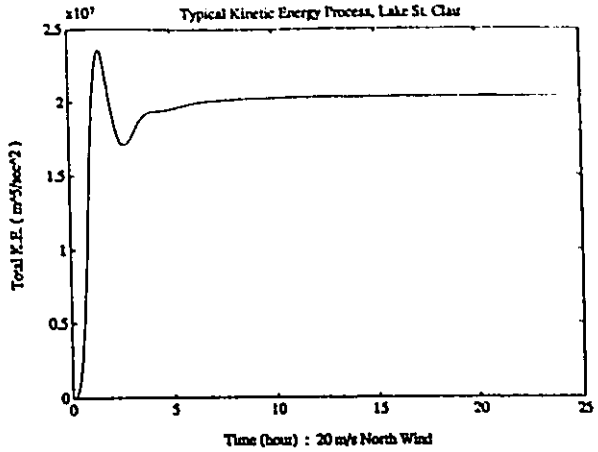

Fig. 7.3 Typical total kinetic energy process of simulation in Lake St. Clair.

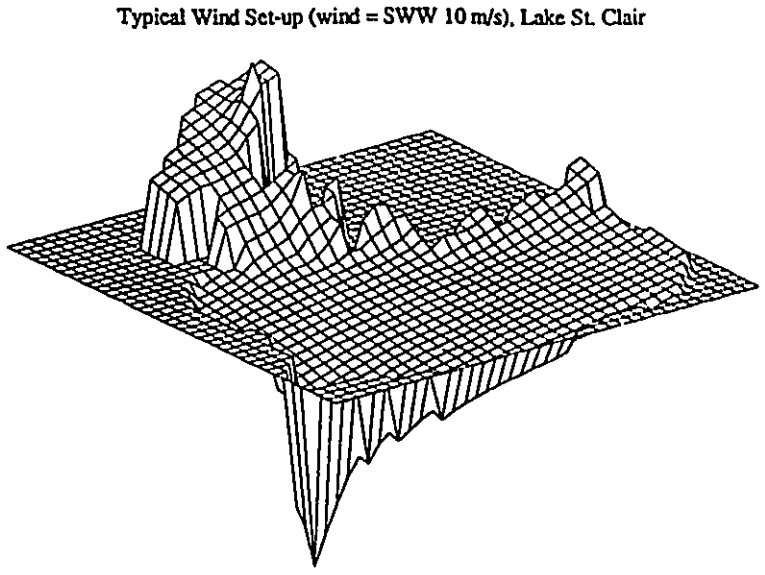

Fig. 7.4 Typical wind set-up in Lake St. Clair (wind : SWW 10 m/s)

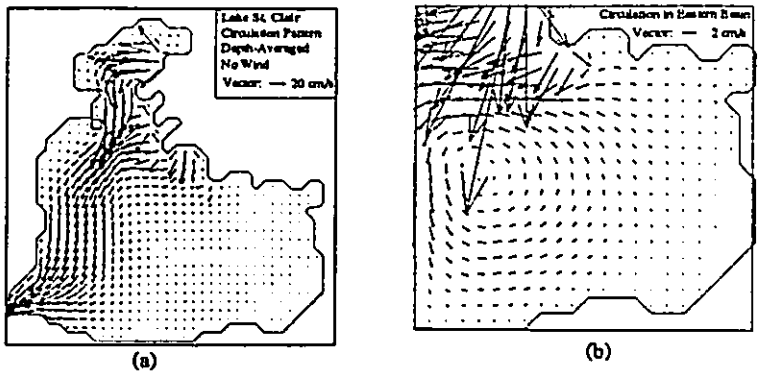

Fig. 7.5 Depth-averaged hydraulically induced circulation in Lake St. Clair. (a) in the whole lake (vector scale = 10 cm/s); (b) in the eastern basin (vector scale = 2 cm/s).

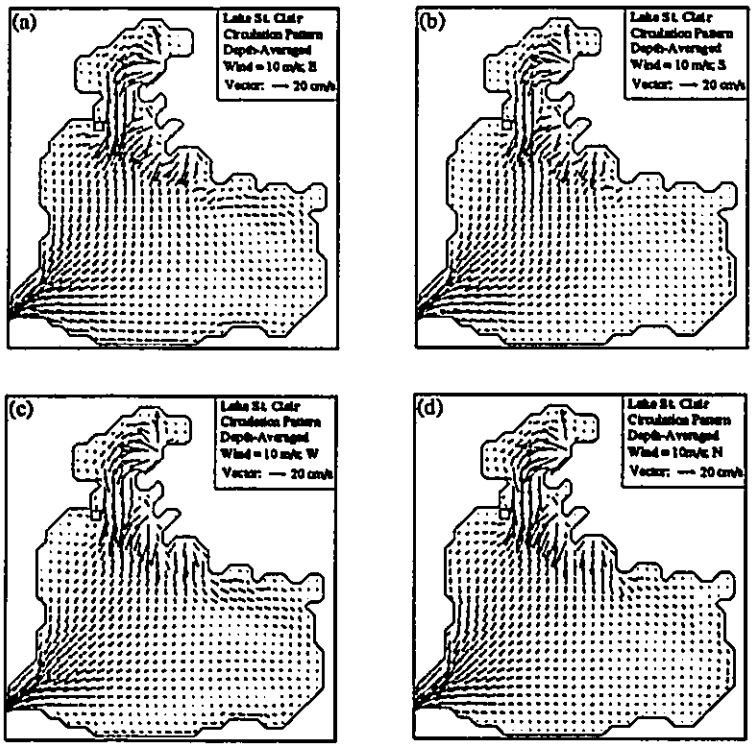

Fig. 7.6 Depth-mean circulation patterns in Lake St. Clair for a 10 m/s wind speed at four different directions (a) East; (b) South; (c) West; (d) North.

parts and near-shore areas of the lake, the surface currents are aligned with the wind, while in the hydraulically dominated flow area the lake currents are weak because the wind-induced current is acting against the hydraulic flow. This effect becomes more significant with the increase of the wind speed. With a 20 m/s wind, the hydraulic flow is totally destroyed except in river mouths (see Fig. 7.7d).

Water current data collected at two depths $z1$ and $z2$ of 26 stations, as shown in Table 7.2 and Fig. 7.2(b), on 4 days under various wind conditions (Ibrahim & McCorquodale, 1985) are used to verify the currents obtained from the Q3D model. Fig. 7.9 presents the observed and calculated current vectors for these stations. It clearly indicates a general agreement in terms of current magnitudes and directions (the ratio of the variance of difference between the observed velocities and the computed currents to the variance of the observed velocities is 0.4127).

Table 7.2 Four episodes of current measurements in Lake St. Clair (Ibrahim & McCorquodale, 1985).

Data Date	Sep. 29, 1983	June 23, 1983	July 26, 1984	July 31, 1984
Wind (m/s)	-1.18, -1.18	1.49, 3.60	0.50, -0.98	2.35, 2.35
Station#	1 2 3 4 5 6 7	8 9 10 11 12 13	14 15 16 17	18 19 20 21 22 23 24 25 26
Depth z1 (ft)	4 3 2 2 2 2 1	1 0 x x x x	x x x x	3 1 3 3 2 4 1 3 3 3
Depth z2 (ft)	7 6 6 7 5 5 5	5 x 15 5 5 5	7 4 4 1	11 12 10 8 8 12 12 8 8

Notes: x means that no measurement was made in the station.

7.2.3 Current-Induced Wave Refraction

Analysis of wave data obtained from a three-wave staff array and collected during the 1985 field study on Lake St. Clair revealed, in some cases, significant differences between the

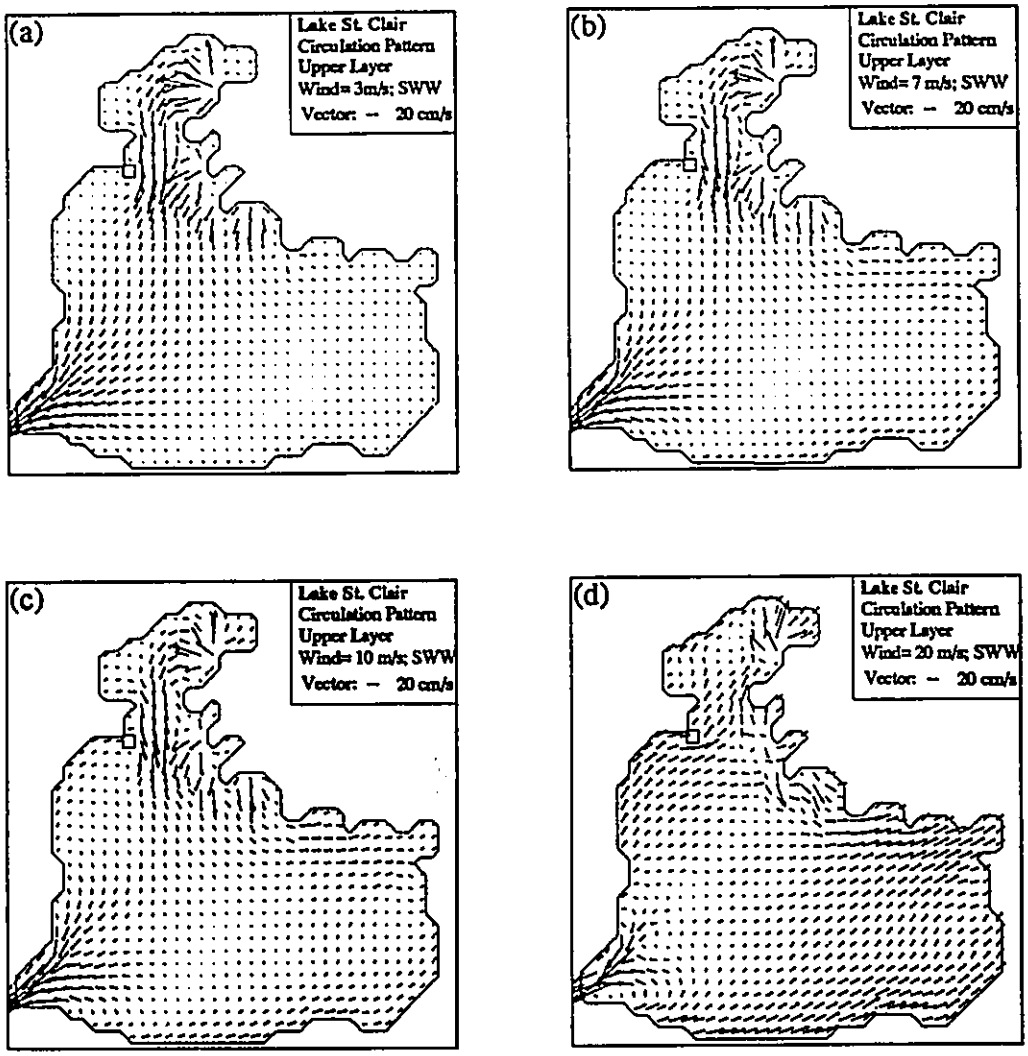

Fig. 7.7 Surface circulation patterns in Lake St. Clair for a SWW wind at four wind speeds (a) 3 m/s; (b) 7 m/s; (c) 10 m/s; (d) 20 m/s.

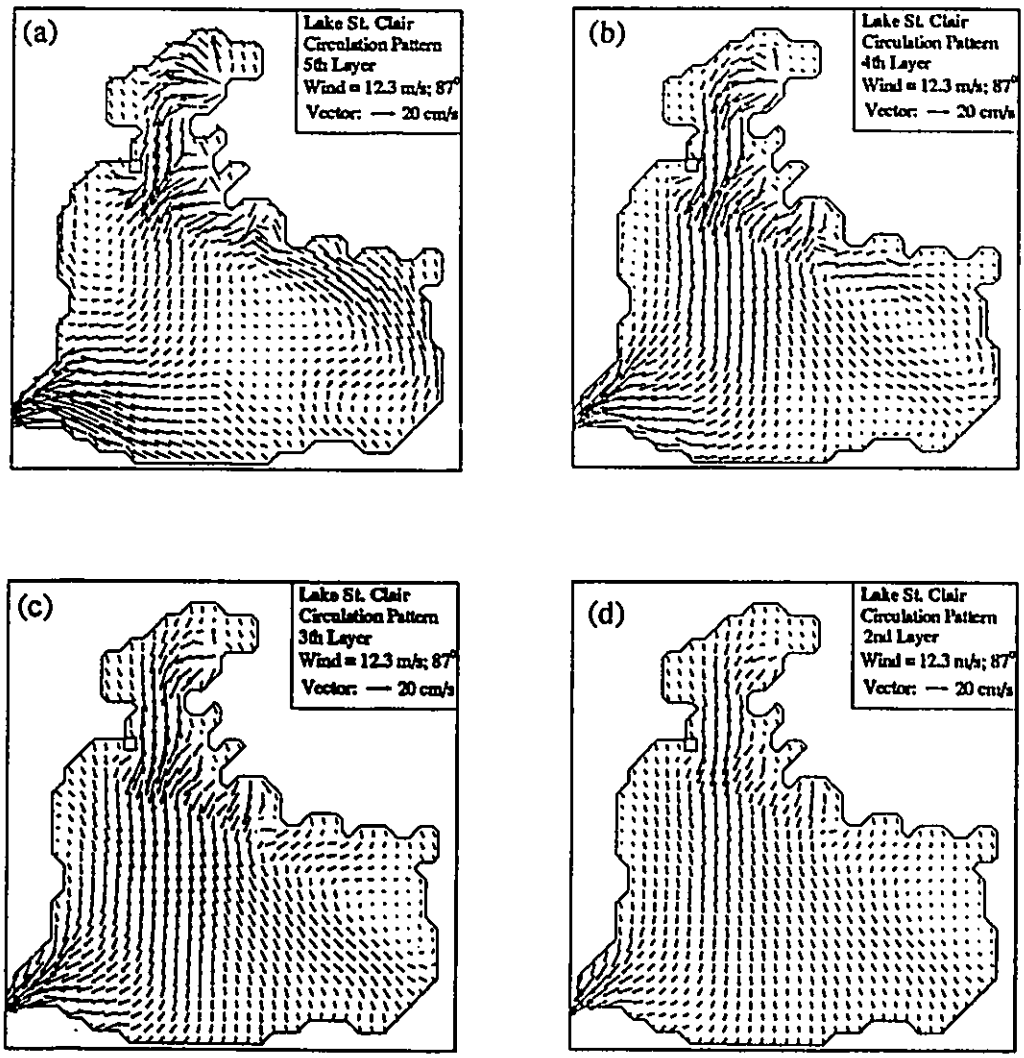

Fig. 7.8 Three-dimensional circulation pattern in Lake St. Clair. Wind = 12.3 m/s, 87 degree. (a) 5th layer - 1/5 depth below the surface, (b) 4th layer - 2/5 depth,(c) 3th layer - 3/5 depth, (d) 2nd layer - 4/5 depth.

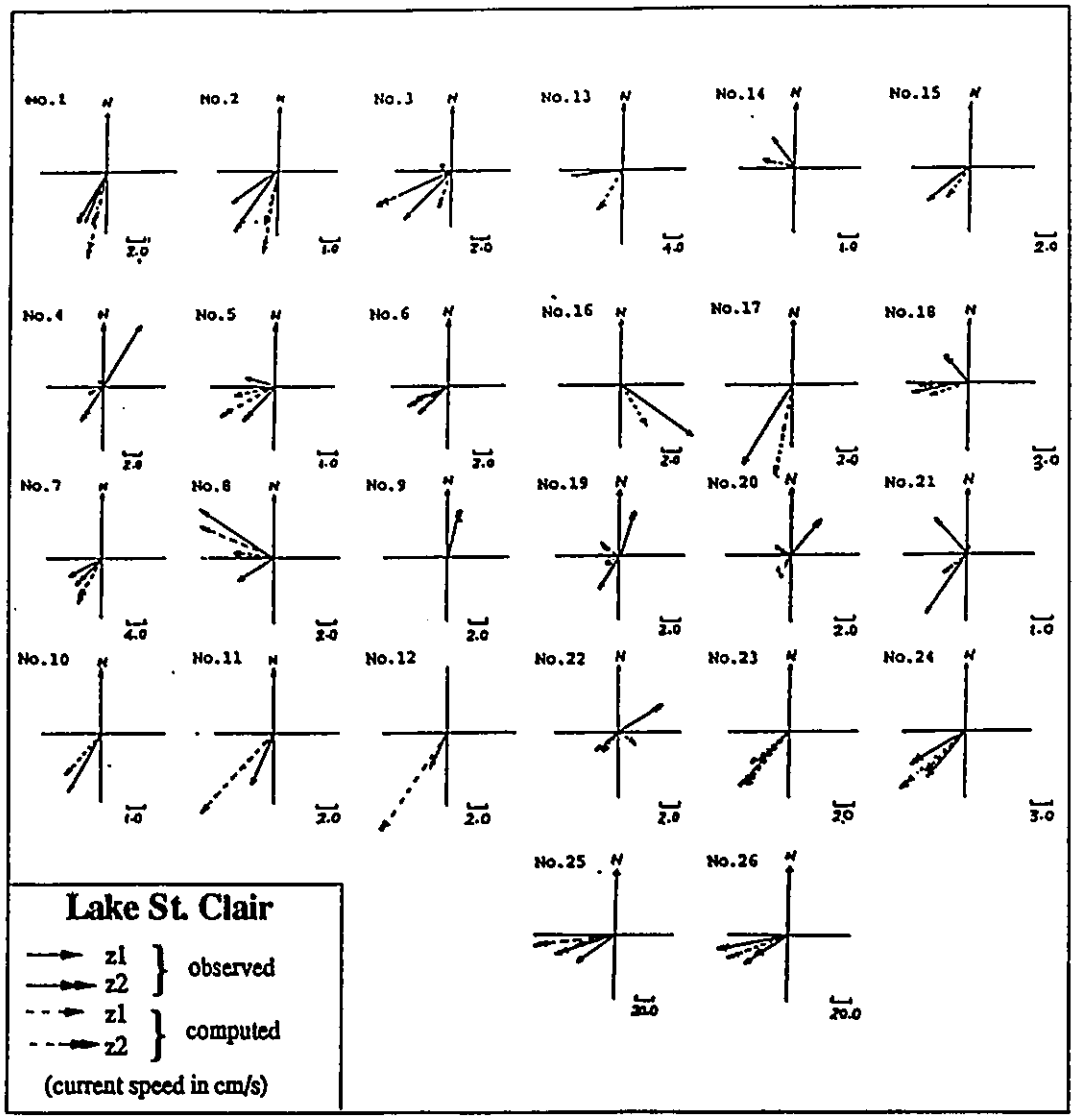

Fig. 7.9 Comparison between computed (dotted line) and observed (solid line) currents for four episodes during the Lake St. Clair field study (Ibrahim and McCorquodale, 1985).

wind directions were found at the central location on the lake (C3, closed circle in Fig. 7.10), especially for south winds. The derivations could be explained by the presence of a strong hydraulic current aligned roughly north to south, which would tend to deflect the waves toward the south if they travel with the current, or against the current if they are opposite to it. The high-resolution directional spectrum estimations displayed significant directional effects; and the wave refraction model, which includes the various possible effects on the wave refraction, revealed that the effect of fetch-gradient and refraction due to the bottom topography were insignificant while the current-induced refraction prevailed (Brissette, Tsanis and Wu, 1993).

In this study, the wave ray analysis method developed by Irvine (1987) is employed to examine the wave-current interaction in Lake St. Clair. The ray equations for waves propagating over a spatially varying current are as follows (Irvine, 1987):

$$\frac{dk_x}{dt} = -k_y \frac{\partial V}{\partial x}; \qquad \frac{dk_y}{dt} = -k_x \frac{\partial V}{\partial y} \tag{7.1}$$

and

$$\frac{dR_x}{dt} = (C_g)_x + U; \qquad \frac{dR_y}{dt} = (C_g)_y + V \tag{7.2}$$

where, U and V are the depth-averaged velocity components in x, y directions, respectively. $\vec{k}(k_x, k_y)$ is the wavenumber vector. C_g is the group velocity. $\vec{R}(R_x, R_y)$ maps out the wave rays. Eq. (7.2) indicates that the turning of waves caused by the current is due to both the advection and the dispersive nature of the waves (Phillips, 1981). In the following analysis, wave rays were computed using Eqs. (7.1) and (7.2) using a calculated current structure in Lake St. Clair. The analysis was performed using 0.4 H_s waves which are typical peak waves in Lake St. Clair for medium to strong wind conditions. The above analysis is clearly an approximation as it assumes wave components with fixed frequencies traveling without dissipation or wind input of energy.

However, the analysis should reveal some aspects of wave-current interaction in Lake St. Clair and at least indicate if such interaction is compatible with the field observation.

Fig. 7.10(a) presents the results of a wave ray analysis for the case of an easterly wind. It can be seen that the wave rays are clearly refracted by the shear current at the east end of the lake with the result that the main wave direction becomes about 50^0; an observation consistent with the field data. Waves generated further away from the WNW flowing current will show a direction more consistent with the wind. It should be noted that this analysis neglects the tendency of the waves to realign with the wind once the action of the shear current decreases. In this case, this force would be counteracted by the presence of the SE current; the waves tend to be the direction normal to it.

Fig. 7.10(b) presents results of the wave ray analysis for the case of a south-westerly blowing wind, where the waves were observed to come from either side of the current but not directly against it. The ray analysis indicates that there is very little effect from the current on the wave direction. Some insights into the problem can be gained by considering the work of Irvine (1987) in which he showed that wave patterns on a current are strongly influenced by the curvature. He also demonstrated that very small changes in the current structure can have large effects on wave rays. The circulation patterns calculated in this work should adequately represent the general features of the circulation pattern in Lake St. Clair. However, they are computed for steady cases and are obviously subject to parametrization for various factors such as horizontal diffusivity, bottom friction and wind stress. As such, the finer details of the circulation pattern such as the curvature of the main current cannot be considered exactly, especially when trying to apply a "steady state numerical circulation pattern" to wave data in unsteady wind conditions.

In order to look more closely at the effect of the curvature of the main current on the wave refraction pattern, the circulation pattern was idealized by slightly increasing the curvature of the main current. Wave rays for south-westerly winds were then traced as shown in Fig. 7.10(c). The results now indicate the significant refraction of the waves. The main effect of the refraction is the turning of the waves to the west, by up to 30^0, which is compatible with field data. This model is a simplification of the real phenomenon in Lake St. Clair but it certainly outlines the fact that currents of magnitude similar to the one observed in Lake St. Clair are sufficient to create significant refraction, and are compatible with field observations. It should be noted that the choice of 0.4 Hz waves is probably a conservative one since it implicitly assumes that the shear currents had no effect on the growth of the waves (the waves direction of propagation is not affected by the currents until they reach a period of 2.5 sec). In most cases, the depth-averaged current velocities should be considered as minimum velocities since it is to be expected that the current close to the surface is the one that affects the waves. Simply considering a logarithmic velocity profile, the average velocity of the upper 2 meters could be 20% higher than the velocity averaged over a 6 meter depth.

To our knowledge, no similar wave-interaction cases have been observed elsewhere. This can be partly explained by the fact that Lake St. Clair is characterized by an unusually low residence time, causing strong currents and especially steep horizontal velocity gradients. The horizontal velocity gradients are fundamental in controlling wave refraction, and the gradients observed in Lake St. Clair ($0-10$ *cm / sec / km*) are as high as the ones observed in the major currents such as the Gulf Stream or Kuroshio off Japan. In fact, the problem of swell refraction by such major currents (as discussed by Irvine, 1987) can be almost exactly scaled down to Lake St. Clair when considering 0.4 Hz waves. Additionally, few studies of waves make use of high-

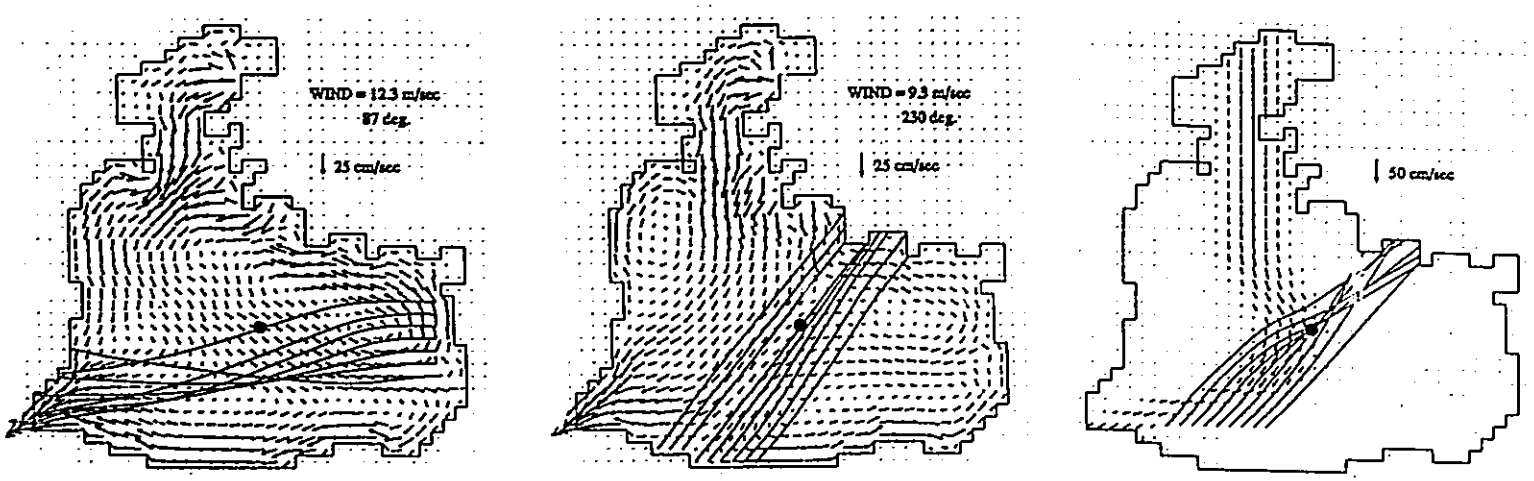

Fig. 7.10 Current-induced refraction as obtained from wave ray analysis and calculated circulation pattern in Lake St. Clair: (a) for a wind blowing from the east, refraction in excess of 20° is observed; (b) for a wind blowing from the south-west, little refraction is observed as the waves propagate directly against the shear current with a 0° angle of incidence; (c) for an idealized circulation pattern for a south-westerly wind, curvatures in the shear-current can have a dramatic effect on the wave rays, refraction of 30° is observed (the closed circle represents the location of Tower C3 during 1985 wave observation in Lake St. Clair).

resolution directional spectrum estimates which are needed to observe the complex energy structure of wave fields in strong shear currents.

7.3 MODELLING CIRCULATION AND WIND-INDUCED SET-UP IN LAKE ONTARIO

Many hydrodynamic models have been applied in Lake Ontario (Simons, 1972; Simons & Lam, 1984; Huang, 1977; Murthy et al., 1986). The most valuable model is the multi-layered three-dimensional model, which was verified using field data from the 1972 International Field Year on Lake Ontario in both homogeneous and summer stratified cases (Simons, 1980). However, the fully three-dimensional model is time-consuming to run and usually provides too much information for management problems (Simons, 1976). The multi-layered circulation patterns can be efficiently provided by the Q3D model or VHI3D model for engineering applications.

7.3.1 Wind-Induced Circulation Patterns

The Q3D and VHI3D models are applied in the 4 km grid of Lake Ontario to efficiently predict the three-dimensional current structure in the case of non-stratified seasons. Fig. 7.11 presents the depth-averaged circulation patterns under a 10 m/s west wind by the Q3D and VHI3D models, as well as the 2D model without horizontal viscosity and advective terms (Simons & Lam, 1986) and the 2DH model. It is observed that the circulation patterns are similar in all models, the current follows the wind in the shallow north and south shorelines, and the return flow is formed in the deep central basin, resulting in two lake-wide counter-clockwise and clockwise gyres. The magnitudes of currents predicted by the 2D and 2DH models are very close to each other. The horizontal eddy viscosity has an insignificant effect on the current when this

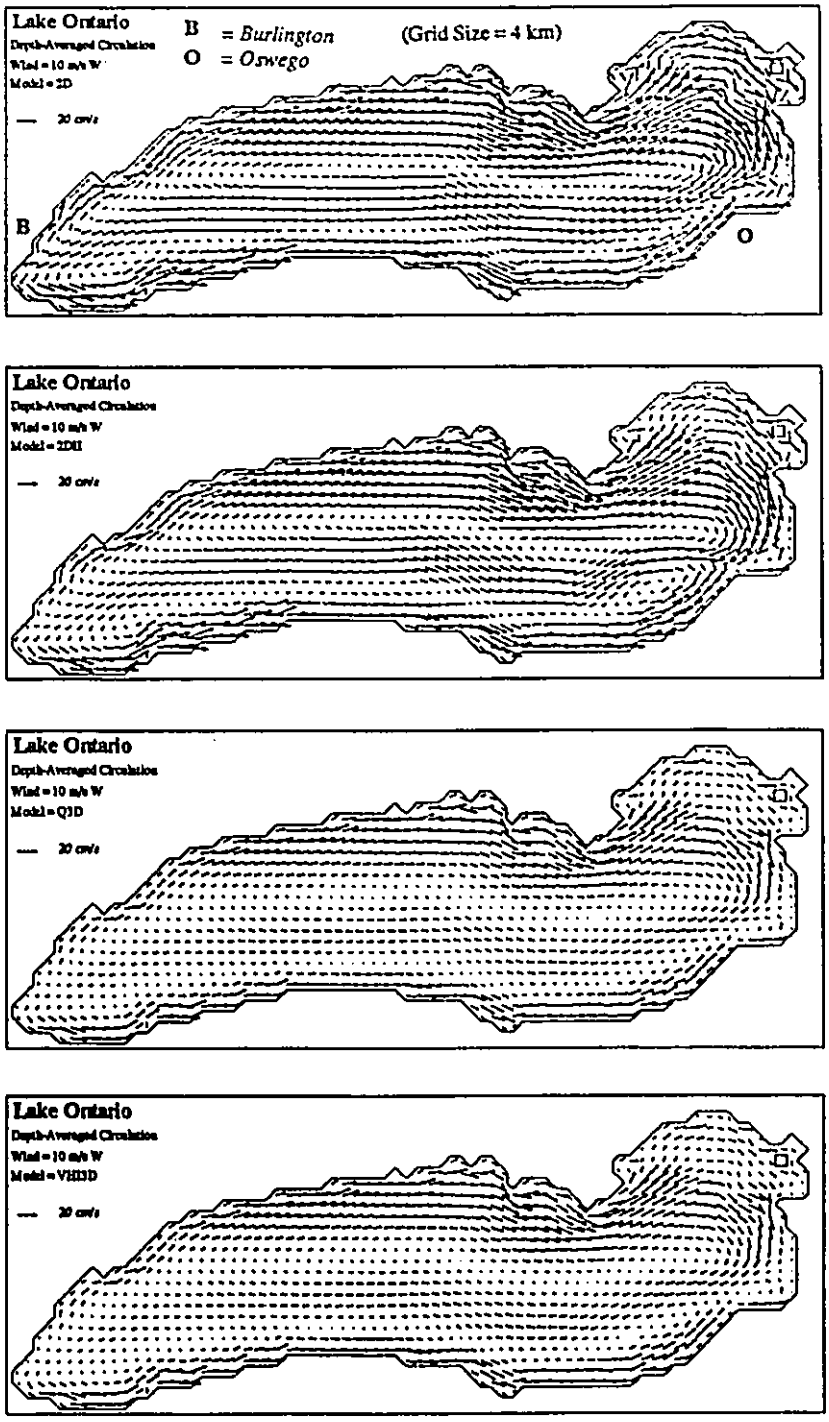

Fig. 7.11 Simulated depth-averaged circulation pattern under a 10 m/s west wind in Lake Ontario. Four different circulation models are employed.

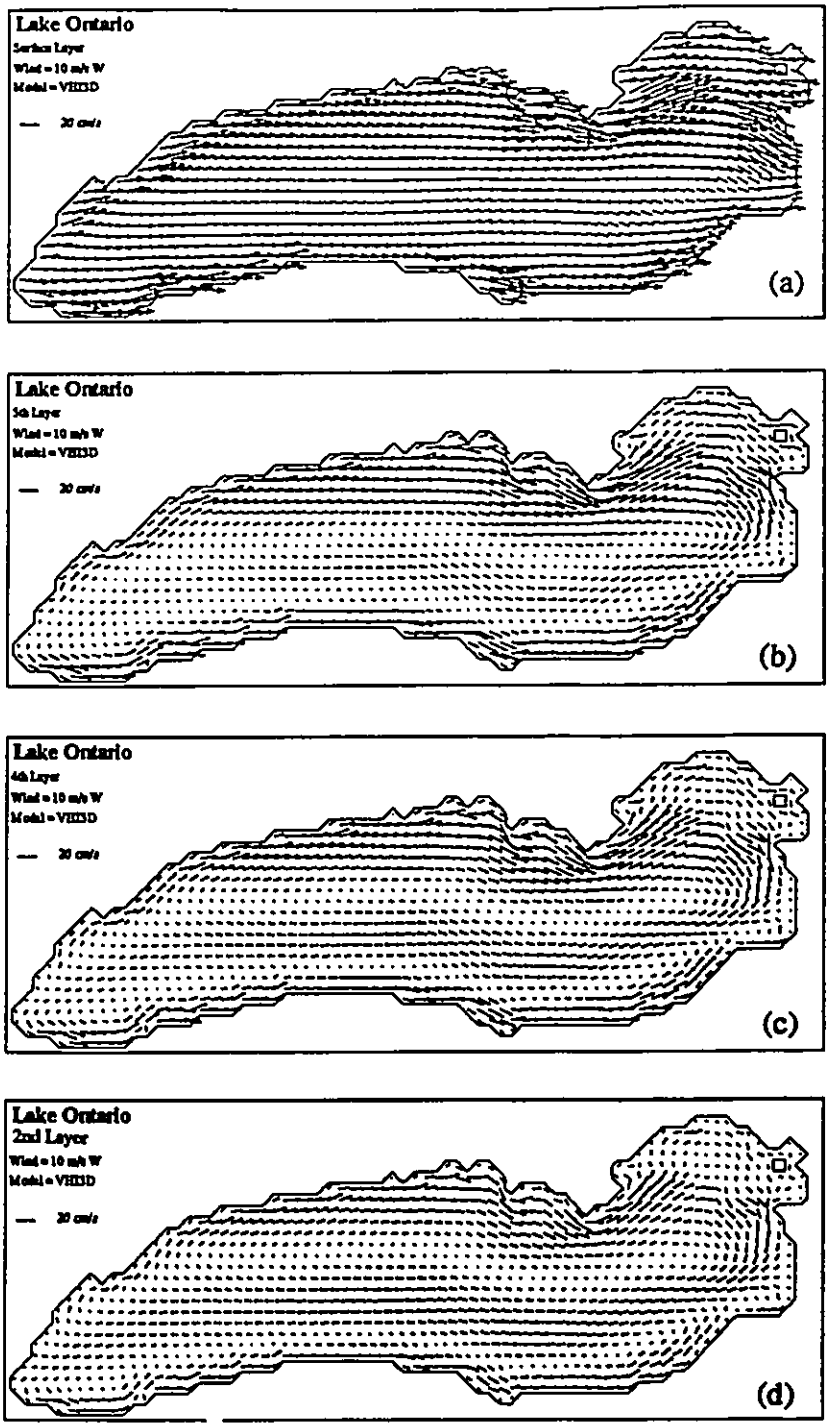

Fig. 7.12 Simulated multi-layered circulation pattern under a 10 m/s west wind in Lake Ontario. (a) surface layer, (b) 5th layer - 1/5 depth below the surface, (c) 4th layer - 2/5 depth, (d) 2nd layer - 4/5 depth.

coefficient is taken below a certain value; they are slightly larger than those of the Q3D and VHI3D models. The constants in the vertical eddy viscosity distribution in the Q3D and VHI3D models are values that are calibrated in the numerical study of countercurrent flow as described in Chapter 6, and the magnitude of simulated current can be adjusted by changing this constant. The simulated circulation patterns under a 10 m/s west wind from the VHI3D model at four typical depths (equal σ layer), i.e., surface, 5th layer (1/5 depth below water surface), 4th layer (2/5 depth), 2nd layer (4/5 depth) are presented in Fig. 7.12. The patterns indicate that the wind-induced flow in the shallow shorelines follows the wind over the whole depth, while in the deep part of the lake, except close to the surface, a return flow against the wind dominates.

7.3.2 Wind-Induced Set-Up

Fig. 7.13 shows the water elevation field under a uniform 10 m/s west wind in Lake Ontario. The maximum water level difference is about 8 cm over the whole basin. The field data of water level difference between Burlington and Oswego from the IFYGL - International Field Year for the Great Lakes (Donelan et al., 1974) is used to calibrate the model simulation. In Fig. 7.14, the small solid dots represent the field data and the straight line represents the empirical relationship between wind shear stress ($DYNES / cm^2$) and the water level difference (cm). The open circles represent the model simulations under four wind conditions (see Table 7.3). The comparison indicates a good agreement between field data and model simulations. According to Donelan et al. (1974), the best estimate of the overall 4 m wind drag coefficient is 1.35×10^{-3}; that for unstable conditions is 1.59×10^{-3}; and for neutral conditions is 1.31×10^{-3}. Using these values used in the lake circulation model, a sensitivity test (a 10 m/s wind is applied) is undertaken. The results are presented in Table 7.4. It is indicated that the simulated wind set-up significantly

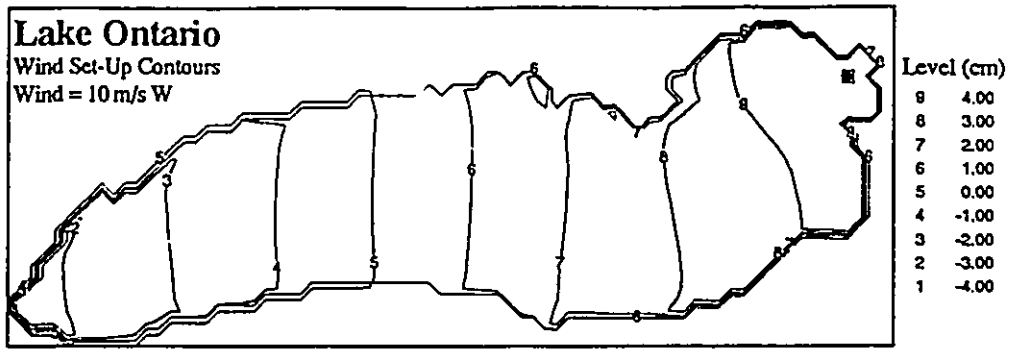

Fig. 7.13 Wind set-up under a 10 m/s west wind in Lake Ontario, simulated by the Q3D model.

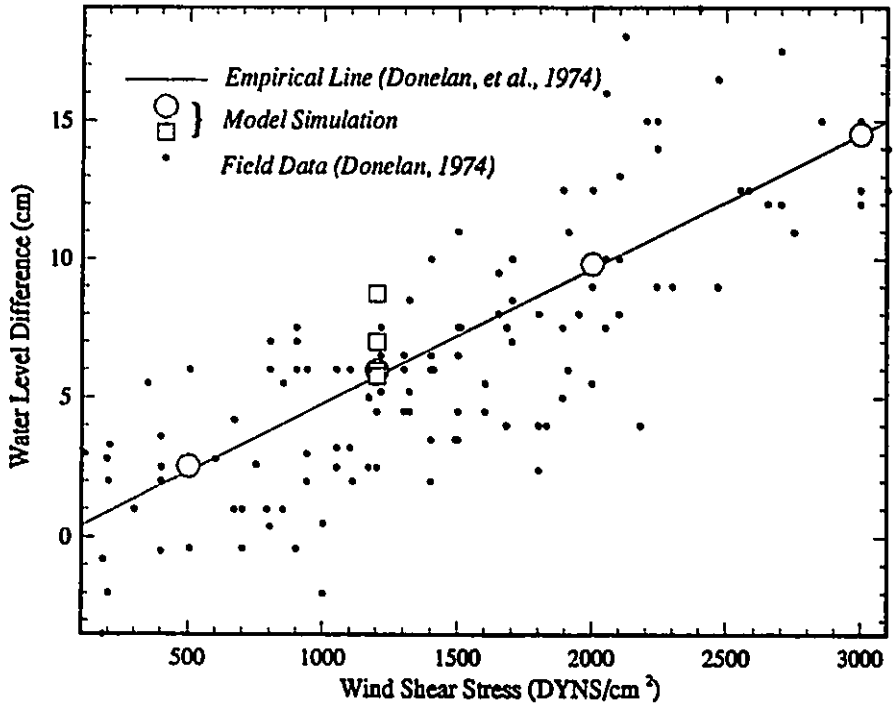

Fig. 7.14 Comparison of the simulated wind set-up along Burlington and Oswego with the empirical data (Donelan et al., 1974) in Lake Ontario.

Table 7.3 Wind-induced set-up along Burlington-Oswego for various winds

wind (m/s)	ζ_B (cm)	ζ_O (cm)	$\Delta\zeta$ (cm) from model	$\Delta\zeta$ (cm) from data *)
15.81	-5.01	9.52	14.53	14.00
12.91	-3.29	6.53	9.82	9.00
10.00	-1.95	4.01	5.96	6.00
6.455	-0.87	1.67	2.54	1.50

*Notes: *) data = the empirical value from the field data (Donelan et al., 1974).*

Table 7.4 Wind-induced set-up along Burlington-Oswego for various wind drag coefficients

C_D ($\times 10^{-3}$)	ζ_B (cm)	ζ_O (cm)	$\Delta\zeta$ (cm) from model	$\Delta\zeta$ (cm) from data *)
2.00	-2.90	5.85	8.75	6.0
1.59	-2.30	4.69	6.99	6.2
1.35	-1.95	4.01	5.96	6.0
1.31	-1.88	3.89	5.77	5.5

*Notes: *) data = the empirical value from the field data (Donelan et al., 1974).*

depends on the wind drag coefficient used in the model; about 3 cm increase can be induced by increasing the drag coefficient from 1.31×10^{-3} to 2.00×10^{-3}. As a result, a universal value of wind drag coefficient is not available. For different lakes and different field data sets, and different wind and wave conditions, the calibrated coefficients may slightly change.

7.4 MODELLING CURRENTS IN LAKE SUPERIOR, MICHIGAN, HURON AND ERIE

The VHI3D model is applied to Lake Superior, Lake Michigan, Lake Huron and Lake Erie with a grid size of 4 km. The circulation pattern under a 10 m/s west wind is presented as a demonstration. The depth-averaged circulation patterns for these lakes are shown in Figs. 7.15, 7.16, 7.17 and 7.18, respectively. In general, the patterns in Lake Superior, Michigan and Huron are very complicated. The currents follow the wind in most near-shore areas, and many gyres can be found in the central areas. For these large lakes, spatial variation of wind speed and direction must be included in order to provide a more realistic circulation pattern which requires a large data set and is not considered in this study.

7.5 SUMMARY

By applying the Q3D and VHI3D hydrodynamic models to the Great Lakes, the circulation patterns under various wind conditions have been simulated. The vertical structure or multi-layered current patterns can be easily obtained from the depth-averaged current, wind stress and related parameters. In two cases, in Lake St. Clair and Lake Ontario, the model was verified with the current and water elevation measurements, respectively.

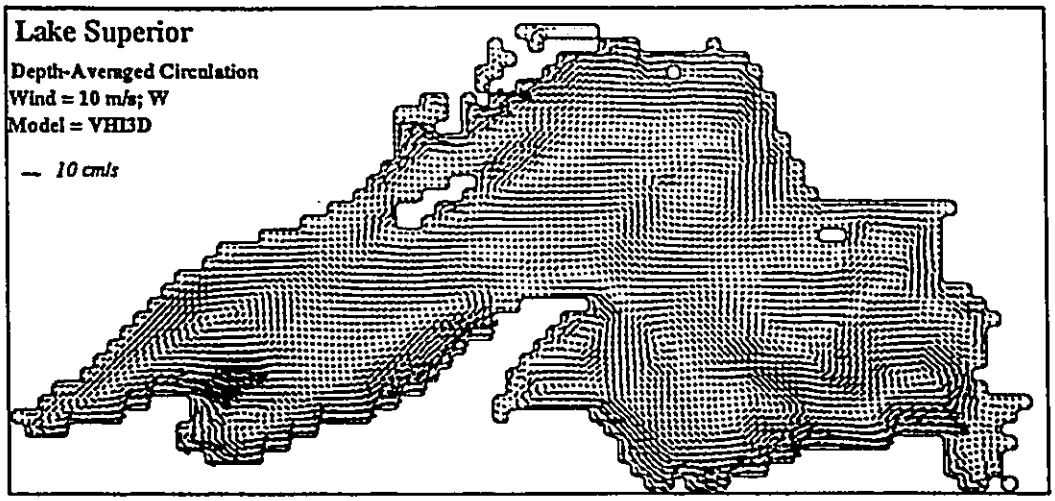

Fig. 7.15 Simulated depth-averaged circulation pattern under a 10 m/s west wind in Lake Superior.

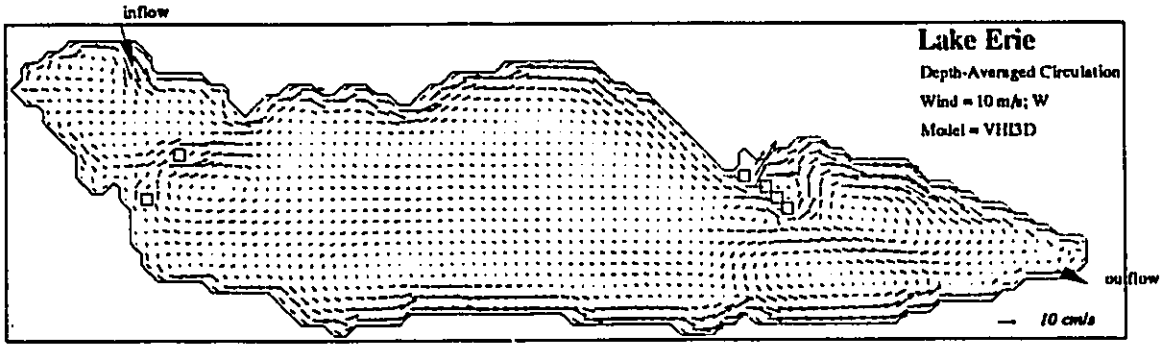

Fig. 7.16 Simulated depth-averaged circulation pattern under a 10 m/s west wind in Lake Erie.

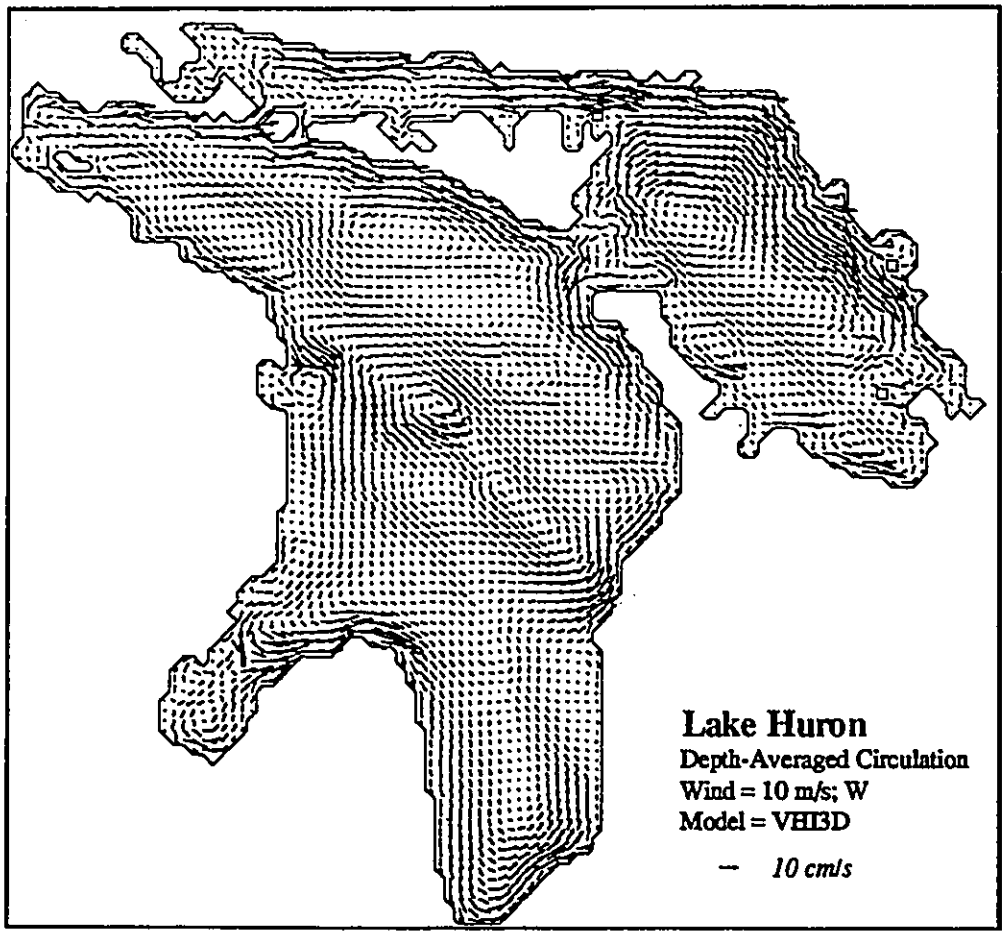

Fig. 7.17 Simulated depth-averaged circulation pattern under a 10 m/s west wind in Lake Huron.

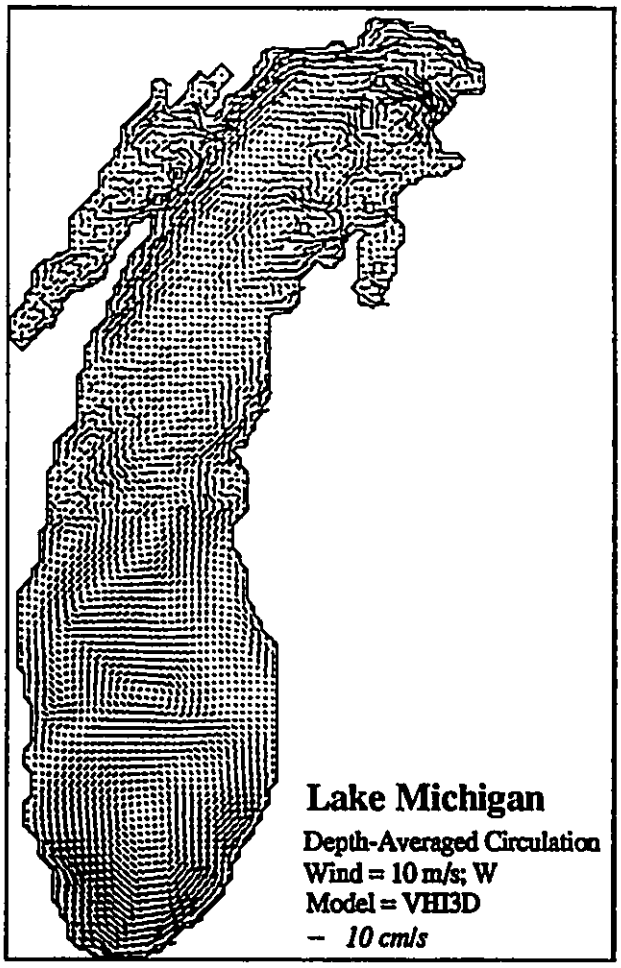

Fig. 7.18 Simulated depth-averaged circulation pattern under a 10 m/s west wind in Lake Michigan.

CHAPTER 8

BACTERIAL TRANSPORT OF THE ST. CLAIR RIVER IN SARNIA

Near-shore bacteriological pollution of the St. Clair River in Sarnia, see Fig. 8.1(a), was assessed by field surveys of general indicator bacteria (including fecal coliform, fecal streptococci, E.coli and Pseudomonas aeruginosa), originating from upstream sources (outflow from Lake Huron), dry weather sources (effluents from two sewage treatment plants in Point Edward and Sarnia), and wet-weather sources including combined sewer overflows and storm sewer discharges (Marsalek et al., 1992). The results of such surveys indicated that these sources of fecal bacteria impact adversely on recreational water use in this area and cause closing of swimming beaches. In view of the high costs of field programs, it was further recommended to examine the feasibility of extending the relatively short field data records to longer periods by mathematical modelling, and, finally, to use such calibrated models in a preliminary assessment of remedial measures. The Environmental Hydraulics Computational Laboratory at McMaster was one of the co-operating parties, in charge of the mathematical modelling (Tsanis and Wu, 1991, 1992). The results from this project will be described this chapter with additional sensitivity tests.

8.1 MODEL CONSIDERATION

The modelling of bacteria in receiving waters is impeded by the complexity of the

processes occurring in nature. Even after simplification, the processes should often include mixing and dilution, bacteria die-off or growth, and bacteria removal by sedimentation. In the case at hand, extensive simplifications are possible because of the special features of the receiving water body. In particular, the residence times in the main river channel are rather short, in the range from 45 to 90 minutes, and fast flows in the study area preclude significant sedimentation. The changes in bacterial densities caused by dieoff, growth and sedimentation are insignificant. Consequently, it is safe to assume that in the river area, the growth and sedimentation can be neglected, and the die-off can be included using a first-order decay term. The same assumptions, however, may not be fully applicable in the water bodies connected to the main river channel, and characterized by limited circulation. Such bodies include the Government Harbour and Sarnia Bay, but only the latter one is of interest in connection with water-based recreation. A detailed modelling of these water bodies would require extensive calibration data which were not available at this stage of the study. However, the parameters and sources inputs, which are important factors in the simulations will be taken from the previous field studies. Consequently, the main objective of the modelling work was to establish the feasibility of bacteria modelling in the study area with emphasis on recreational water uses and the relevant water quality guidelines. Finally, the effectiveness of various remedial measures in mitigating pollution problems in Sarnia Bay was also simulated. These simulations provide some guidance in planning controls of bacterial contamination under the general pollution control plan for the area of concern. The detail procedures of simulations are presented in Fig. 8.2.

The St. Clair River section around Sarnia Bay was discretized in 142 by 71 square grids with grid size Δx of 25 m, see Fig. 8.1(b). The two-dimensional hydrodynamic model (2DH) is used to simulate the depth-averaged current structure in the St. Clair River in Sarnia.

Coupled with the circulation model, the two-dimensional pollutant transport and fate model is used to predict the spatial and temporal distribution of the coliform bacteria. The SHARP scheme, as presented in Chapter 4, is employed for the transport model. The model system allows the time dependent inflow/outflow and bacteria discharges from storm sewers, combined sewer overflows and tributaries. The averaged in/outflow river discharge is 6,000 m^3/s. The bottom friction coefficient C_b = 0.0025, corresponding to a range of Manning's coefficient between 0.016 to 0.028 for river depths of 1 m to 25 m, respectively. This range of Manning's coefficient values is appropriate for the characteristics of the St. Clair River (Chow, 1959). The time step used in the simulation was selected as 1 second. The horizontal eddy viscosity was assumed equal to 1.5 m^2/s (similar circulation features were obtained for the viscosity of 0.5 to 3 m^2/s). Bacteria were considered as non-conservative contaminants, with a decay coefficient equal to 0.5 /day or $5.8 X\ 10^{-6}$ /s (Chamberlain and Mitchell, 1978).

The horizontal dispersion coefficients of bacteria, D_x and D_y, in Sarnia Bay and Government Harbour are taken as a constant 0.8 m^2/s (McCorquodale et al., 1986), while in the St. Clair River they are calculated by (Vepsa et al., 1992)

$$D_x = D_L \cos^2\theta + D_T \sin^2\theta \tag{8.1}$$

$$D_y = D_L \sin^2\theta + D_T \cos^2\theta \tag{8.2}$$

where,

$$\theta = arctan\ (V / U) \tag{8.3}$$

is the angle between the local flow direction and the x-axis. The D_L and D_T are the longitudinal and transverse dispersion coefficients in flow aligned local coordinate system. According to Fischer et al. (1979), they are evaluated by the following empirical formula:

$$D_T = 0.9\, h\, u_* \tag{8.4}$$

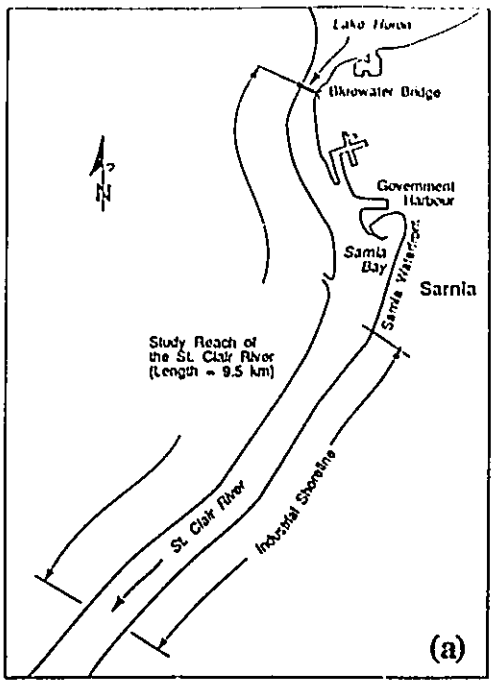

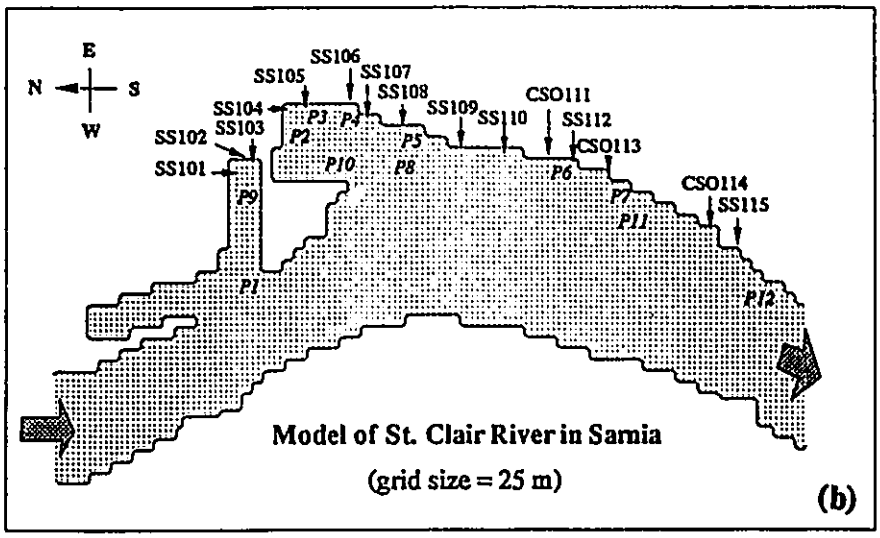

Fig. 8.1 The St. Clair River in Sarnia: (a) the study area of the bacteriological pollution, (b) the finite difference model (the grid size is 25 m, and the system is rotated 90^0 anti-clockwisely from the North. SS101 to SS115 indicted the locations of storm sewer (SS) and combined sewer overflows (CSO) and *P1* to *P12* the locations of concern).

$$D_L = 5.93\, h\, u_* \tag{8.5}$$

where, h is the water depth; u_* is the shear velocity.

$$u_* = \sqrt{g\, h\, s} \tag{8.6}$$

where, s is the slope of the river; s can be calculated from the velocity of river flow V, Manning's coefficient n, and hydraulic radius R_h (Roberson and Crowe, 1990):

$$s = \left(\frac{V\, n}{R_h^{2/3}}\right)^2 \tag{8.7}$$

For the St. Clair River in Sarnia, the averaged slope is about 0.0000176 and the shear velocity is 0.051 m/s. From the above formula, when the depth vary from 10 m to 20 m, the transverse and longitudinal dispersion coefficients are 0.45 to 0.90 m^2/s, and 2.9 to 5.8 m^2/s, respectively. The range of transverse dispersion coefficient is close to that by McCorquodale et al. (1986).

8.2 MODELLING THE CIRCULATION

The typical circulation pattern simulated by the 2DH circulation model for the St. Clair River in Sarnia is shown in Fig. 8.3. It is observed that strong advective currents about 0.5 to 1.5 m/s are passing through the main river stream, while very weak currents below 1 cm/s are found in the Government Harbour and Sarnia Bay. These two different types of flow regimes result in sharp velocity gradients, consequently, forming a counter-clockwise eddy in the mouth area in both basins. In the main river channel, the model produced current magnitudes similar to those measured by the U.S. Army Corps of Engineers (1983). The circulation pattern in Sarnia Bay has important implications for the transport of contaminants discharged into the bay. On one hand, the counterclockwise eddy will bring the bacteria from the outside of the bay into the bay, near the east shoreline. Thus, contaminants released in the bay will remain in the bay, at relatively

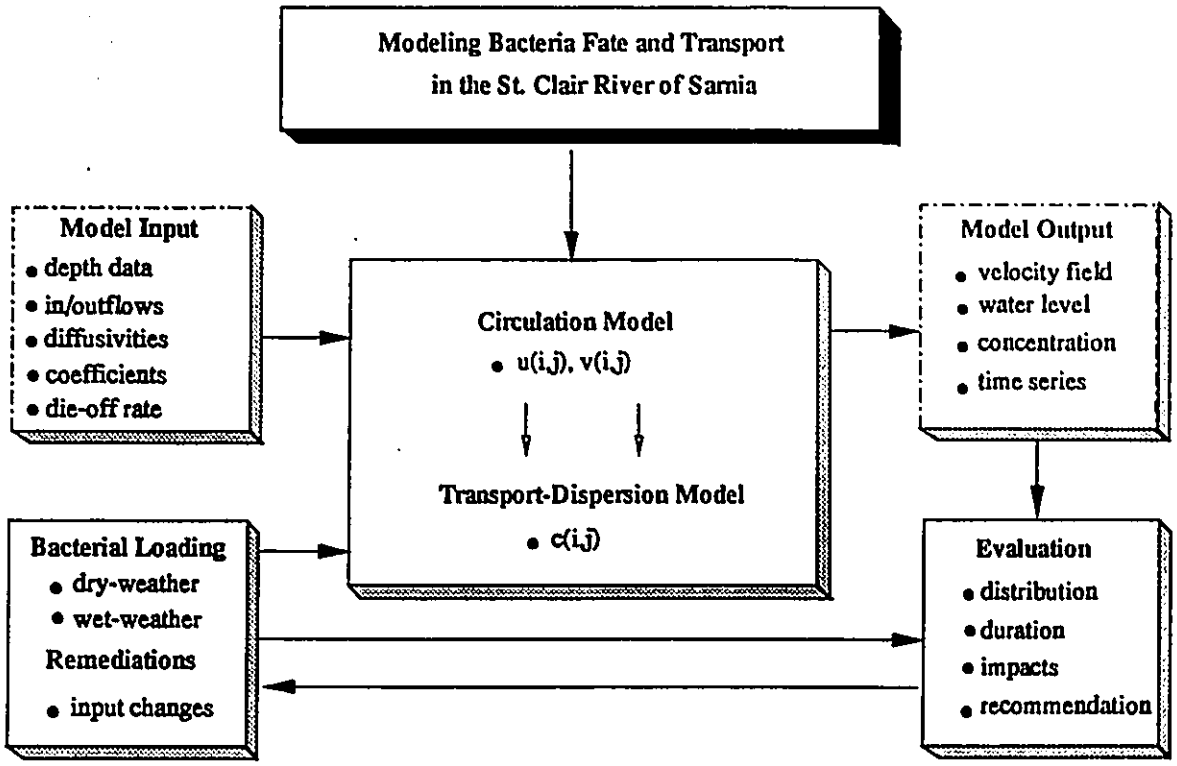

Fig. 8.2 Diagram of procedure on the modelling bacteria of the St. Clair River in Sarnia

high levels, for a long time after the release. On the other hand, the eddy helps to flush away the bacteria from the bay near the west shoreline. These findings also apply to the Government Harbour.

8.3 MODELLING THE BACTERIAL TRANSPORT

Twenty-five storm events were simulated, 22 events for the fecal coliform (FC) bacteria and 3 events for the E.coli bacteria. There are fifteen time-variable sources (inputs with different discharges and bacteria concentrations) along the northern shoreline of Sarnia Bay. A planning-level model was employed to provide the bacterial loading from these outfalls (Marsalek et al., 1992). The background bacteria concentration of the river for the dry weather conditions was 50 counts / 100 ml, and 200 counts /100 ml for the wet-weather conditions. An additional two days (forty-eight hours) after the cessation of storm was also included to examine the duration of after-effects of the storm. For the purpose of simplicity, only one case is presented in detail. Similar analysis can be applied for all storm events.

The case selected here is 900804, a seven hour storm during 15:00 - 21:00 of August 4, 1990. The flow rates and coliform bacterial concentrations from each outfall are shown in Fig. 8.4 (a) and (b), respectively. The flowrates from these outfalls were very small compared with the flowrate of the river. The bacterial concentrations at SS110, CSO111, CSO113 and CSO114 were as high as 10^6 counts /100 ml during the storm, and relatively lower (10^4 counts / 100 ml) for the rest of outfall.

Fig. 8.5 and Fig. 8.6 present the simulated bacteria spatial distributions at the end of the storm, and at 2, 12, 24 hours after the cessation of the storm. At the end of the storm, and within two hours, the fecal coliform densities along the Sarnia water-front are as high as 10^6 counts /100

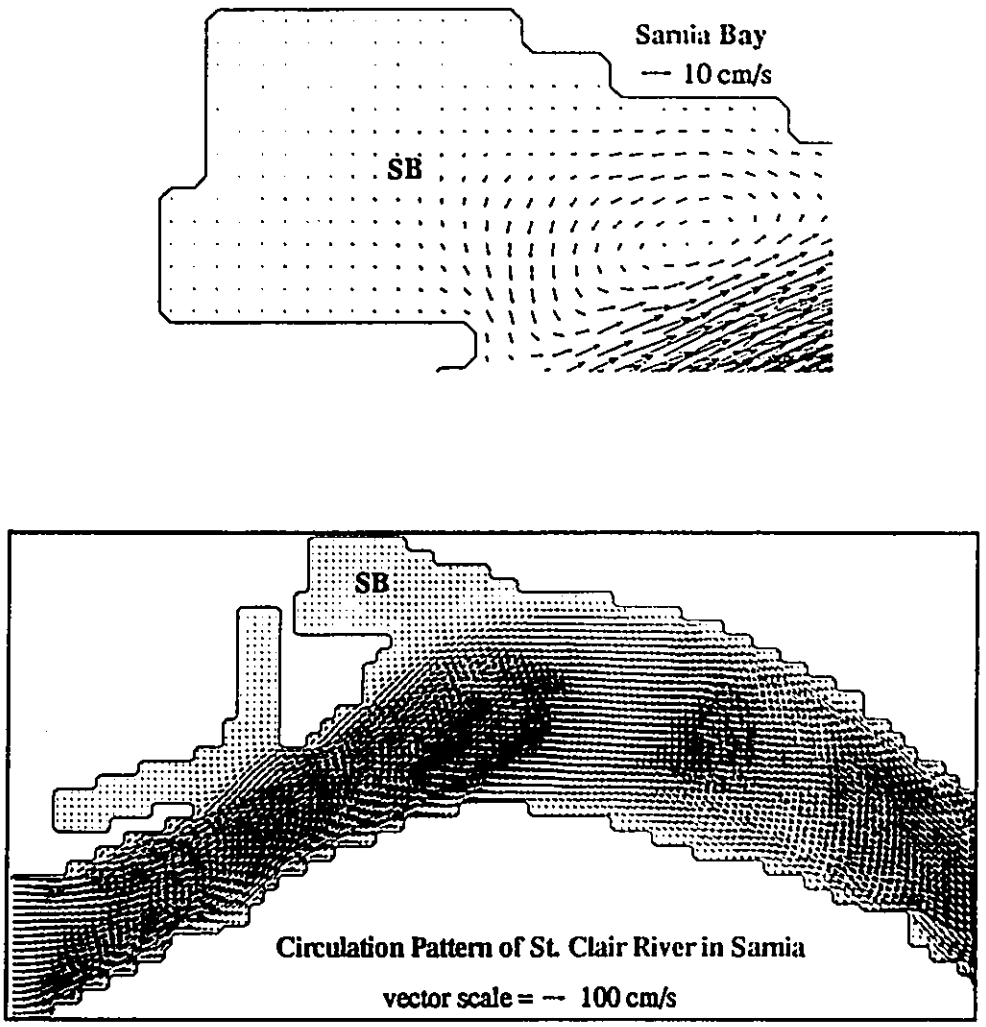

Fig. 8.3 A typical hydraulically-induced circulation pattern of the St. Clair River in Sarnia, simulated by the hydrodynamic model (with the bottom friction coefficient $C_b = 0.0025$).

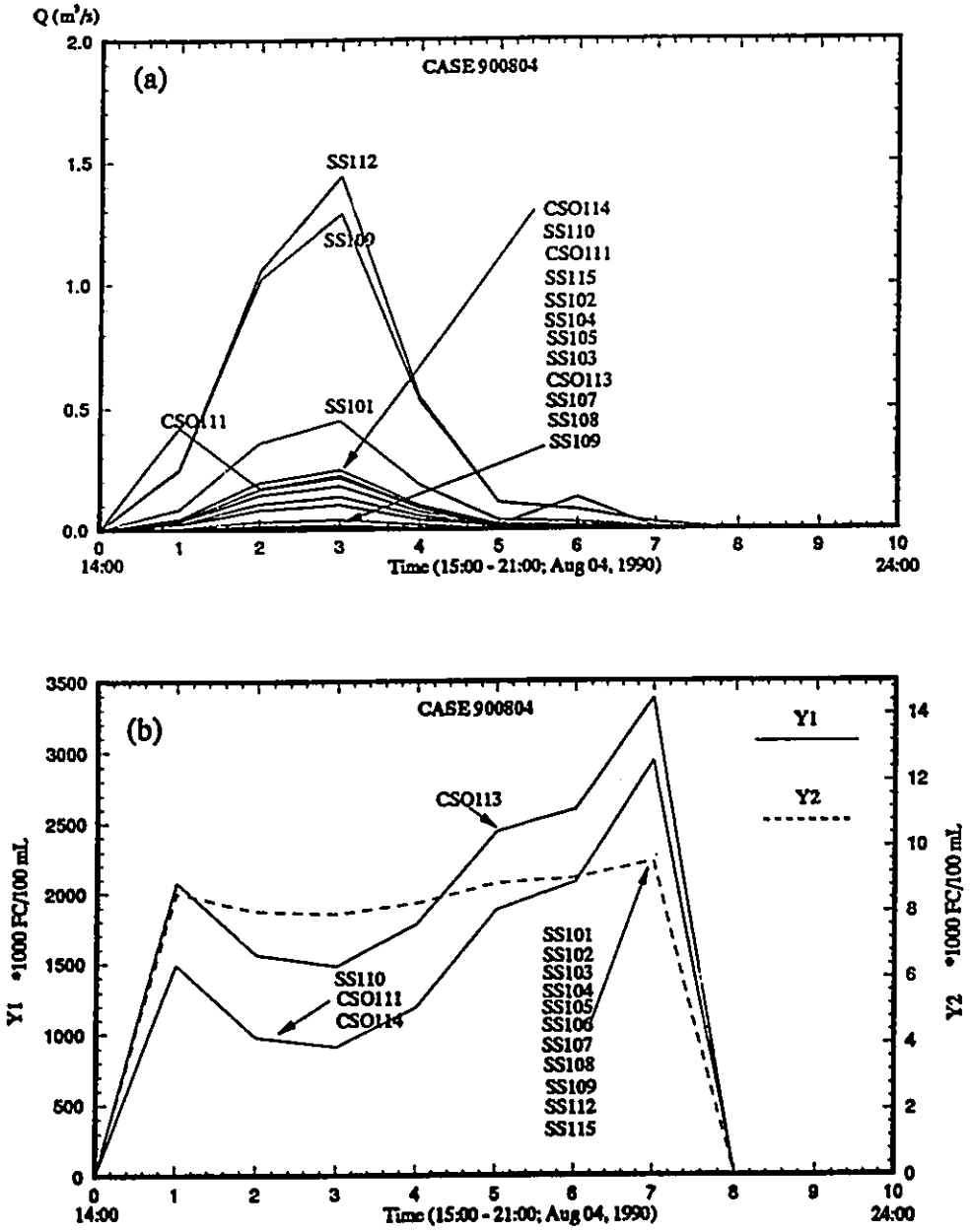

Fig. 8.4 Hourly data of (a) flowrate, (b) fecal coliform (FC) bacteria concentration from 15 storm sewers and combined sewer overflows for the case 900804 (15:00 - 21:00, August 4, 1990).

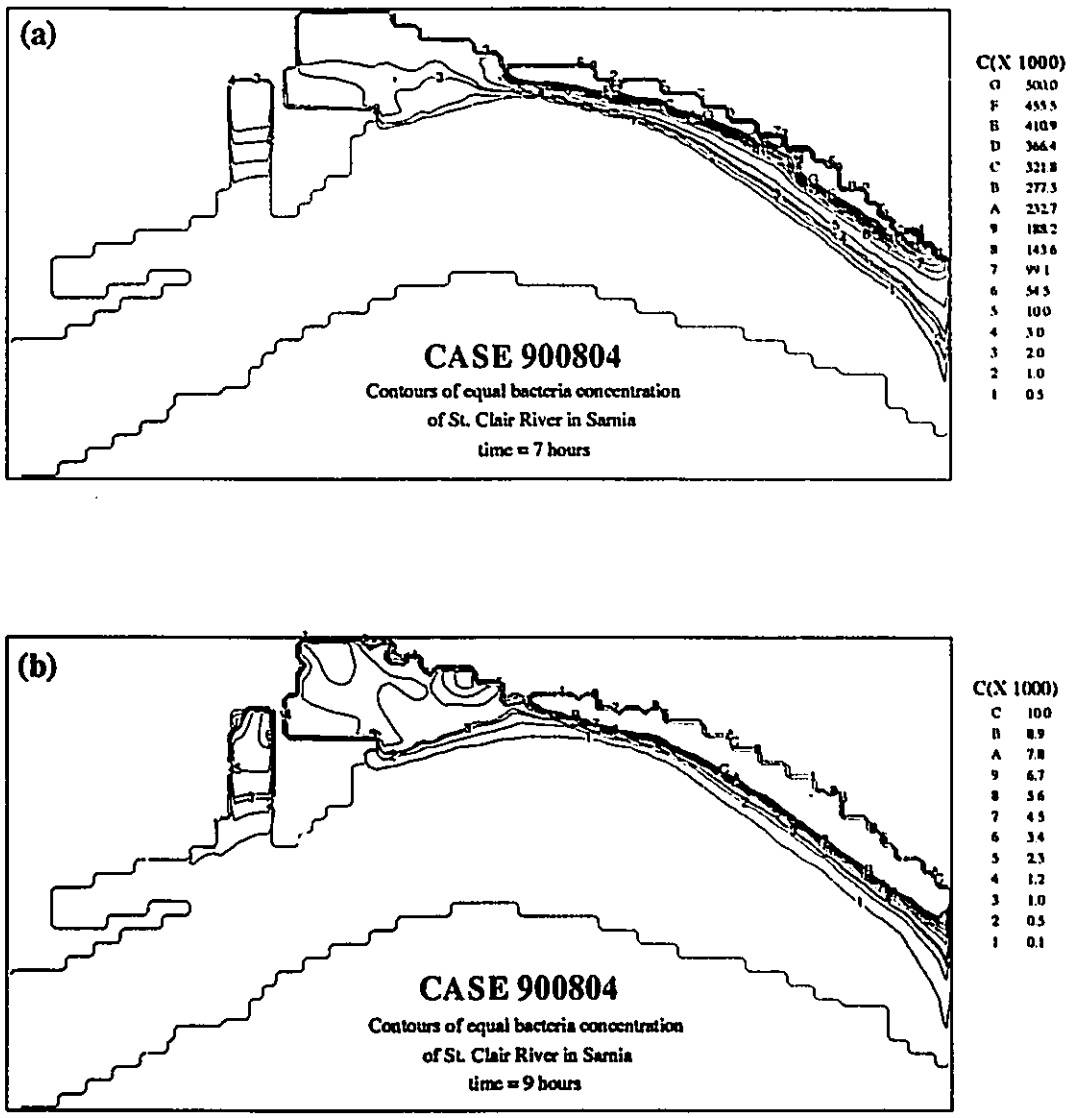

Fig. 8.5 Simulated fecal coliform bacteria spatial distribution for the case 900804 (15:00 - 21:00, August 4, 1990): (a) at end of a seven hour storm, (b) two hours after the storm.

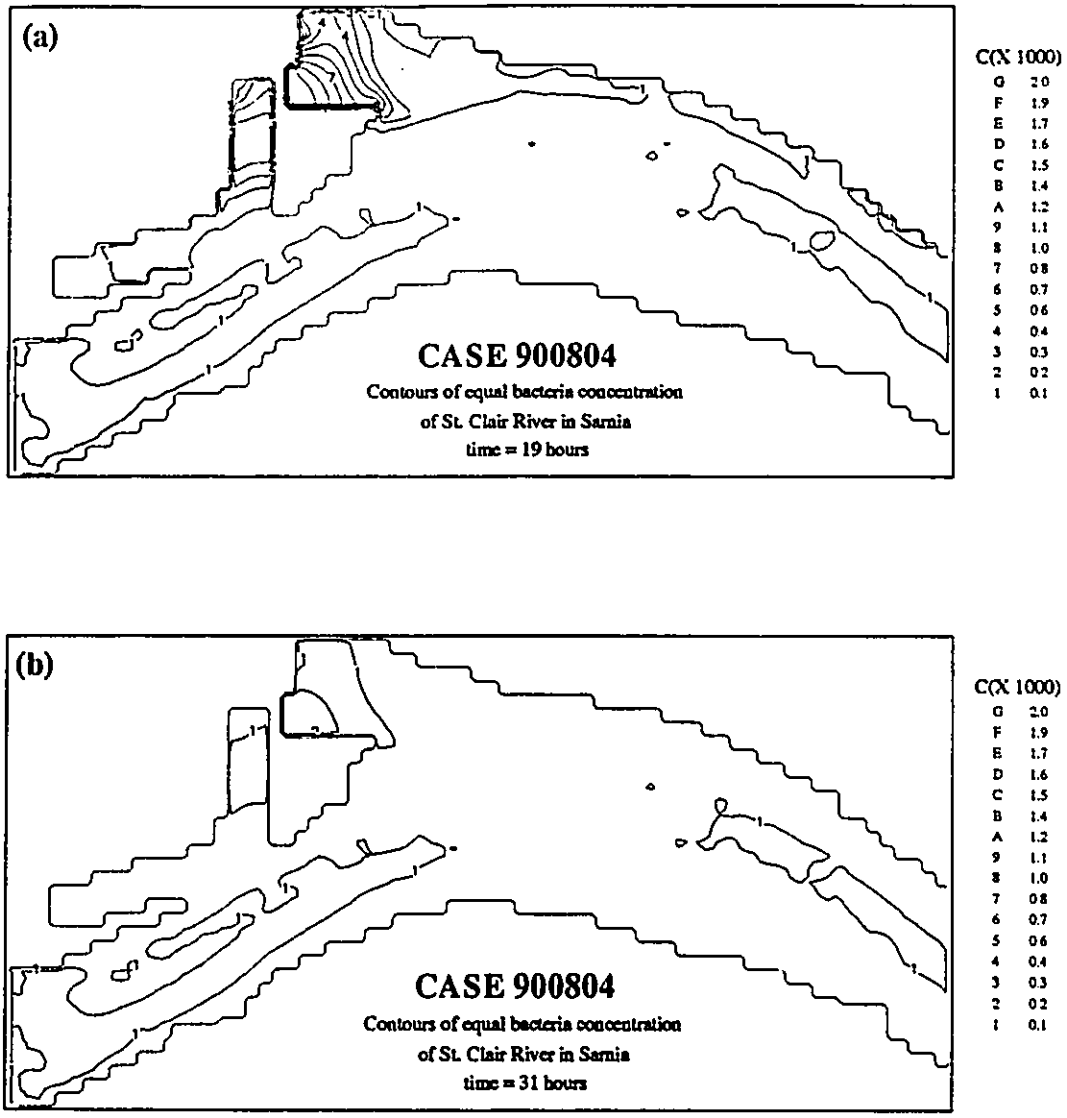

Fig. 8.6 Simulated fecal coliform bacteria spatial distribution for the case 900804 (15:00 - 21:00, August 4, 1990): (a) 12 hours, (b) 24 hours after the end of the storm.

ml, with typical values ranging from 10^4 to 10^5 counts / 100 ml. In the bay, the peak density is about 10^3 counts /100 ml. After 12 hours, the densities in the river drop to around 100 counts /100 ml, while above 100 counts/100 ml are attained throughout the Sarnia Bay, even at 24 hours, the densities in the southwestern corner of the bay are still higher than 100 counts /100 ml.

The field observations of bacterial densities showed great differences between dry and wet weather conditions (Marsalek et al., 1992). The ability to distinguish between the dry and wet weather data in field surveys is impaired by the fact that the wet-weather impacts may extend into dry periods long after the cessation of rain. Such after-effects can be caused by two factors: slow flushing of the receiving waters (or some zones of receiving waters), or by malfunctions of sewage systems allowing sanitary discharges even during dry weather. Only the first issue can be effectively addressed here, because the second one would require detailed surveys of all sewer outfalls in both dry and wet weather.

The duration of wet-weather after-effects in the receiving water can be estimated from the time series of bacteria concentrations at locations in different areas. In the 900804, the logarithm of the fecal coliform bacteria concentration, at locations *P2* to *P8*, and *P10*, *P11*, *P12*, as a function of time till twenty four hours after the beginning of the storm, is shown in Fig. 8.7. *P2*, *P3*, *P4* and *P10* are located in Sarnia Bay, and the rest of the points in the Sarnia river front (detailed location for each points is described in Table 8.2). The duration is considered as the time to reduce bacterial densities to the 100 counts/100 ml level (the water quality guideline for FC in swimmable waters). According to this definition, the durations of wet-weather after-effects for case 900804 are summarized in Table 8.1.

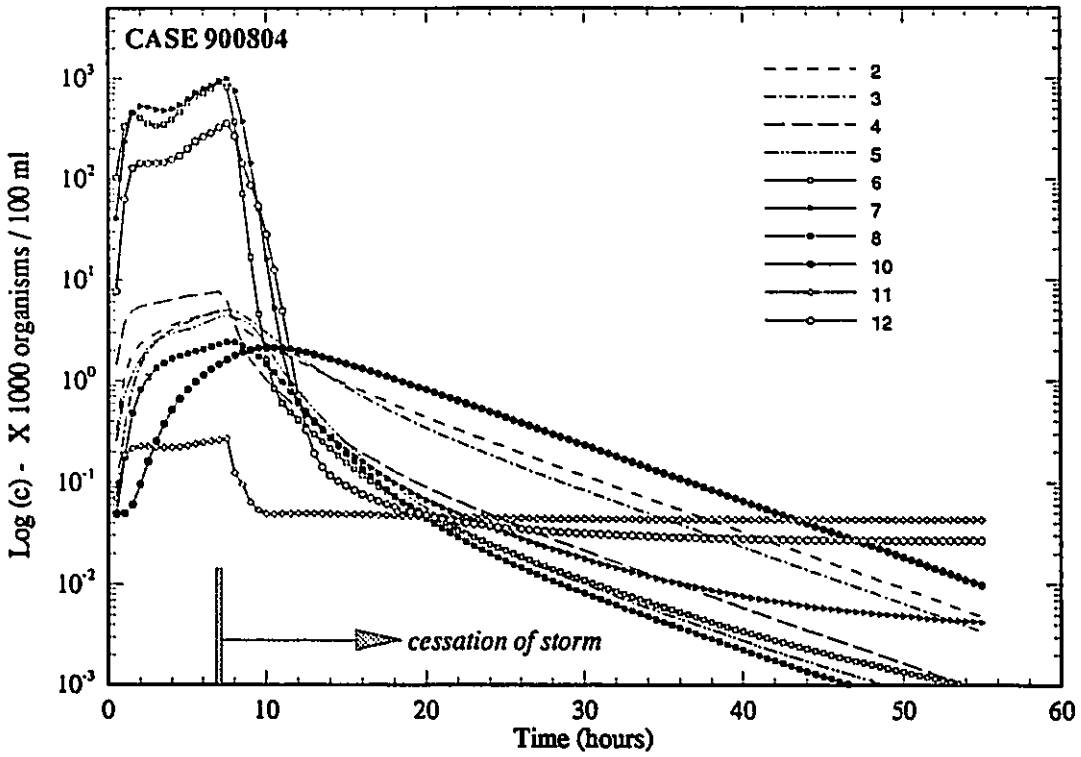

Fig. 8.7 The logarithm of the bacteria concentration at *P2* to *P8*, and *P10*, *P11*, *P12* (see Fig. 8.1(b)) as function of time from the beginning of the storm till forty-eight hours after the cessation of the storm in the case 900804.

Table 8.1 Modelled durations of bacterial densities persisting above the 100 organisms/100 ml limit after cessation of rainfall; Case 900804.

Point No.	Location	Duration (hours)
2	GH, 250 m east of entrance, 50 m south of north pier	26.0
3	Sarnia Bay, 150 m south and 50 m east of NW corner	21.7
4	Sarnia Bay, 50 m south and 100 m east of NW corner	13.0
5	Sarnia Bay, 150 m south and 25 m east of NW corner	10.9
6	Sarnia Bay, 250 m south and 25 m east of NW corner	9.9
7	Sarnia Bay, sampling St. G, 25 m offshore	11.0
8	Sarnia Bay Inlet, opposite Derby Lane, 175 m offshore	10.0
10	River, 50 m south of Wellington St. CSO, 50 m offshore	29.2
11	River, 150 m south of Wellington St. CSO, 200 m offshore	1.6
12	River, 1 km downstream of site 11, 175 m offshore	8.0

The results in Table 8.1 give a good indication of flushing times for various parts of the receiving water system. In the main river channel, the decline of bacterial densities after the rain cessation is very fast and points to strong advection transport. Any after-effects of wet-weather bacterial pollution inputs would have disappeared within 10 hours after the cessation of polluted discharges. Field observations indicating longer after-effects can be explained only by the continuation of pollution discharges in dry weather, and because of operational problems in the sewerage system. The durations of after-effects in the basins with limited flow circulation, namely the Sarnia Bay, are in the order of 10 to 30 hours. This slow flushing effectively extends the duration of wet weather impacts by these long periods. At the same time, the conditions in these basins, characterized by nutrient supply and favourable temperatures, may encourage the growth of Pseudomonas aeruginosa.

In the above section, when assessing the frequency and duration of noncompliance

with swimming water quality guidelines in wet weather, the dry-weather loading was ignored. The difficulties with assessing the dry-weather conditions follows from the lack of knowledge of dry-weather fecal bacterial discharges into the river. A test case was executed to examine the impact of dry-weather condition. Only one input source SS107 with bacteria concentration of 10^6 counts / 100 ml was introduced. Fig. 8.8 shows the simulated bacterial spatial distribution and the logarithm of the bacteria concentration at *P2* to *P8*, and *P10*, *P11*, and *P12* (see Fig. 8.1(b)) as a function of time in dry-weather conditions. It is revealed that a steady release of bacteria from sewer SS107 can cause a bacteria level as high as 3 X 10^4 counts / 100 ml at *P8*, and 1 X 10^4 counts / 100 ml at *P7* which is located 1000 m downstream.

8.4 SENSITIVITY ANALYSIS

The sensitivity of simulated results to wind conditions and bottom friction coefficients, which could affect circulation patterns and in turn affect the bacteria transport, were tested in the following numerical experiment. Fig. 8.9 presents the simulated circulation patterns, with bottom friction coefficients of 0.0025 and 0.01, and with 10 m/s east and west winds (using a bottom friction coefficient of 0.0025), respectively. Figs. 8.10 (a) and (b) are the logarithm of bacterial concentrations as a function of time at *P2* (in Sarnia Bay) and *P11* (in the river). These results indicate that the effects of wind conditions and bottom friction coefficients on the current and bacterial transport in the river are insignificant, while the effects on the Sarnia Bay are visible. In fact, the study area involves two type of water bodies, that is, the main river stream and two relatively small closed shallow basins. The river flow is so strong that the wind condition has little effect on its flow pattern. As a result, the overall patterns in Sarnia Bay under 10 m/s west (Fig. 8.9(c)) and east wind conditions (Fig. 8.9(d)) are very much similar to that without wind

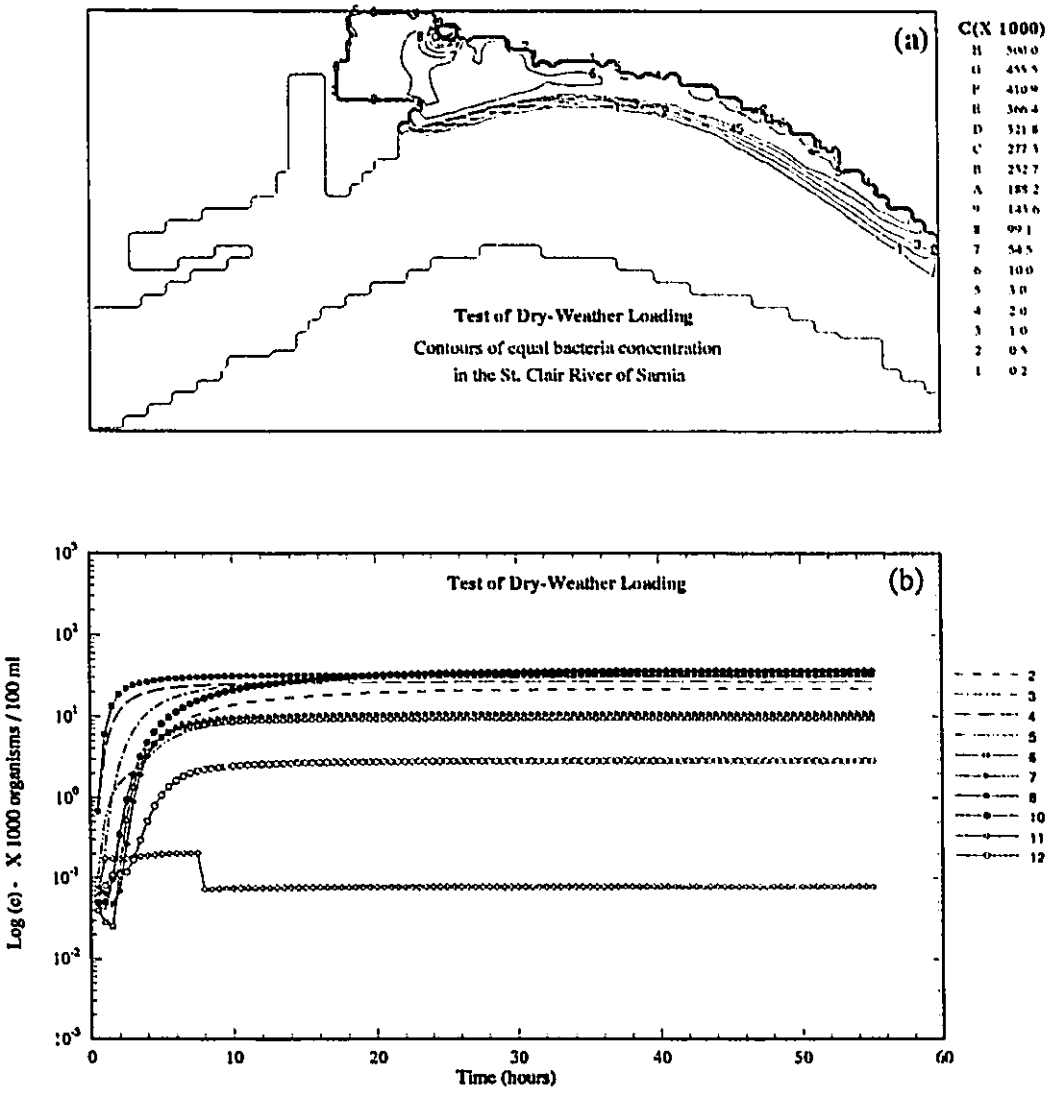

Fig. 8.8 Effect of dry-weather loading (a 10^6 counts / 100 ml FC is continuously emitted from SS107): (a) simulated bacteria spatial distribution, (b) the logarithm of the bacteria concentration for *P2* to *P8*, and *P10*, *P11*, *P12* (see Fig. 8.1(b)) as function of time in dry-weather condition.

(Fig. 8.9(a)), with a slightly enhanced current under an east wind which forces water out of the bay. As a result, the duration of wet-weather after-effect is slightly shorter in the east wind condition. The bottom friction coefficient has a significant effect on the circulation pattern in Sarnia Bay, as seen by comparing Fig. 8.9(b) with Fig. 8.9(a). The higher the bottom friction coefficient is used, the stronger the resistance presented. As a result, the counter-clockwise eddy in the bay-river area is destroyed when a large bottom friction of 0.01 is used. Consequently, the bacteria in Sarnia Bay is flushed away more quickly, see Fig. 8.10(a). As discussed earlier, the bottom friction coefficient of 0.0025 is a reasonable one. However, additional field data, which will be made in available future studies, are required to verify the selection of the coefficient.

There is no doubt that the die-off coefficient and horizontal dispersion coefficient will directly affect the fate and transport of bacteria in the receiving water. Fig. 8.11 shows the sensitivity of die-off coefficients on the durations at *P2* (in the Sarnia Bay) and at *P11* (in the river). Fig. 8.12 presents the sensitivity of dispersion coefficients on the durations at *P2* and at *P11*. In this test, three values of die-off coefficients, i.e, 0.1, 0.5 and 1.0 /day for the whole study area, and bacterial dispersion coefficients of 0.5, 0.8 and 1.0 m^2/s for the Sarnia Bay and Government Harbour are used (0.5 /day and 0.8 m^2/s are the suitable value from the literature for die-off and dispersion coefficient, respectively). The results indicate that effects of both die-off and dispersion coefficients on the bacteria fate and transport are insignificant in the river area. For the relative-closed Sarnia Bay, the effect of the die-off coefficient on the duration of after-effect is evident, though the effect during the rainfall period (within 7 hours) is negligible. The effect of bacterial dispersion coefficients is significant in the whole area.

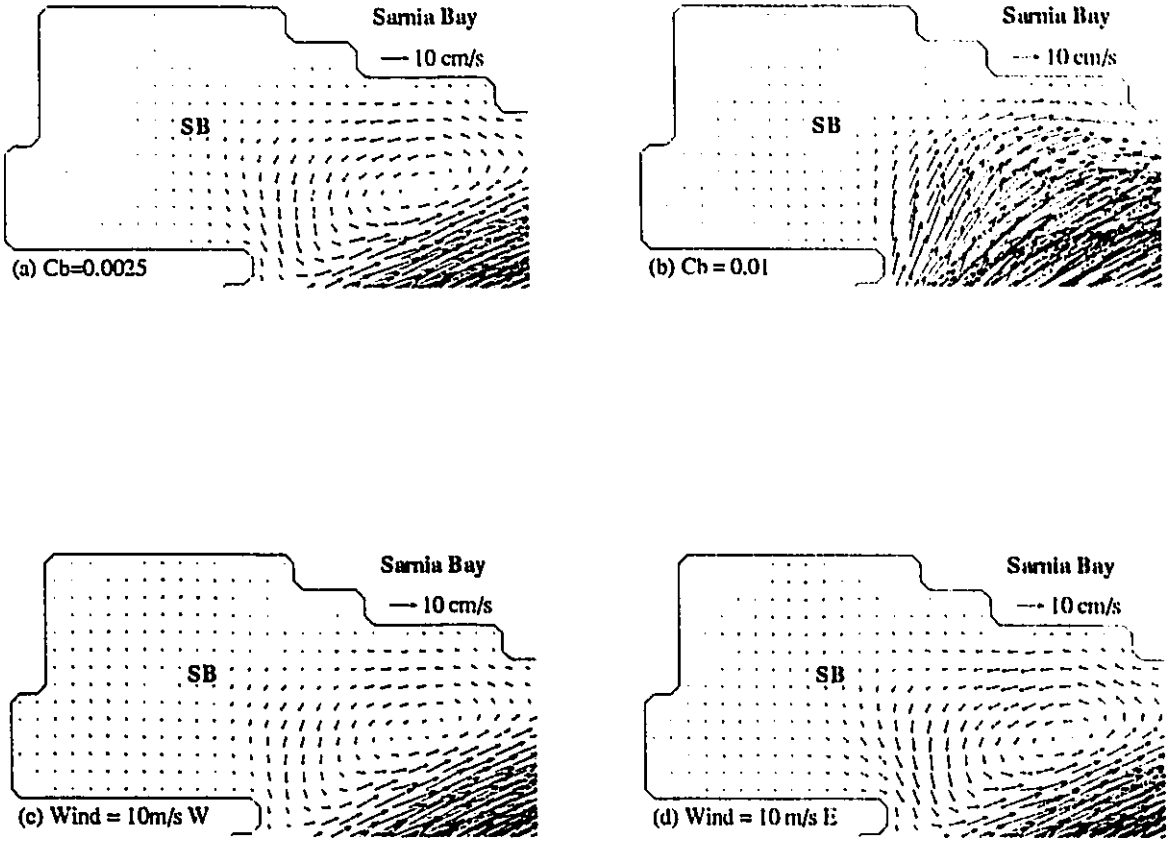

Fig. 8.9 Simulated circulation patterns in Sarnia Bay of the St. Clair River by the hydrodynamic model with: (a) bottom friction coefficient of C_b = 0.0025, (b) C_b = 0.01, and (c) 10 m/s west wind, and (d)10 m/s east wind.

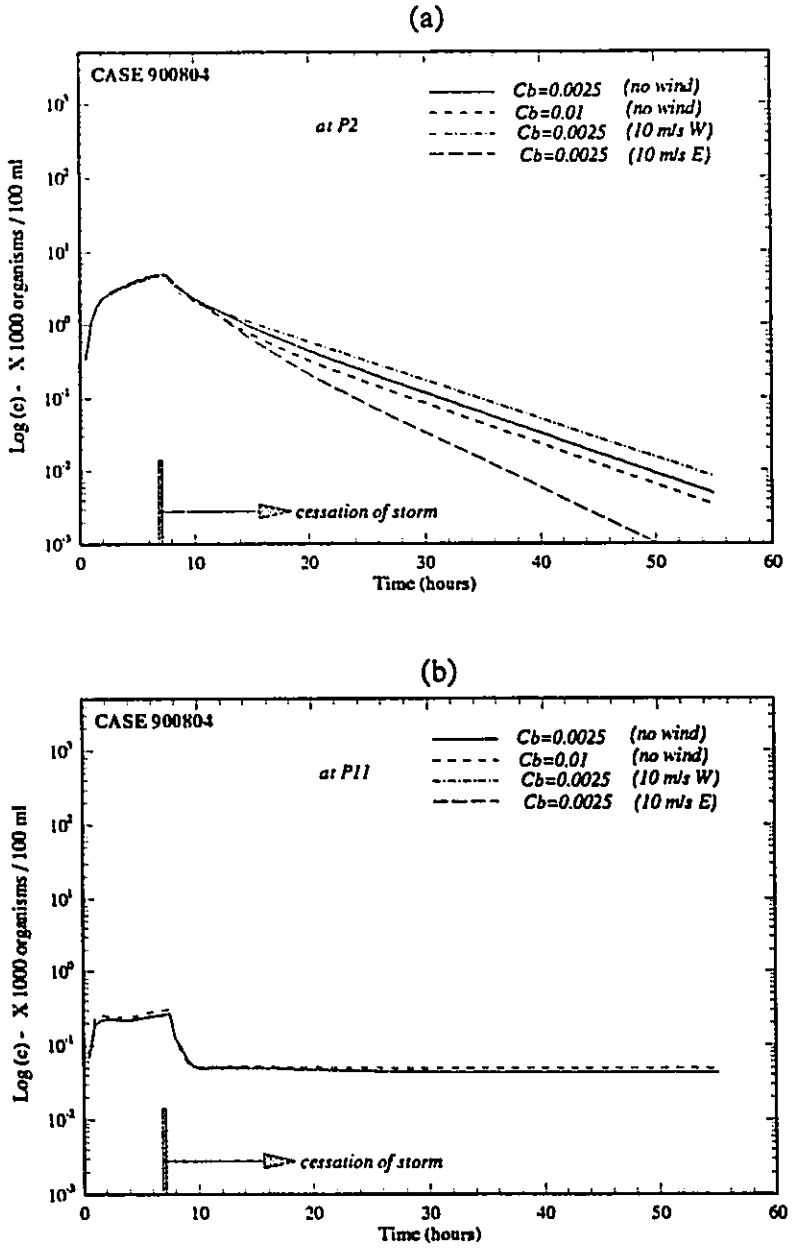

Fig. 8.10 Sensitivities of bottom friction coefficient C_b (0.0025 and 0.01) and wind condition (10 m/s west and 10 m/s east wind) on the transport of bacteria in the Sarnia Bay of the St. Clair River: (a) at P_2 which is located in the Bay, (b) at P_{11} which is located in the river stream.

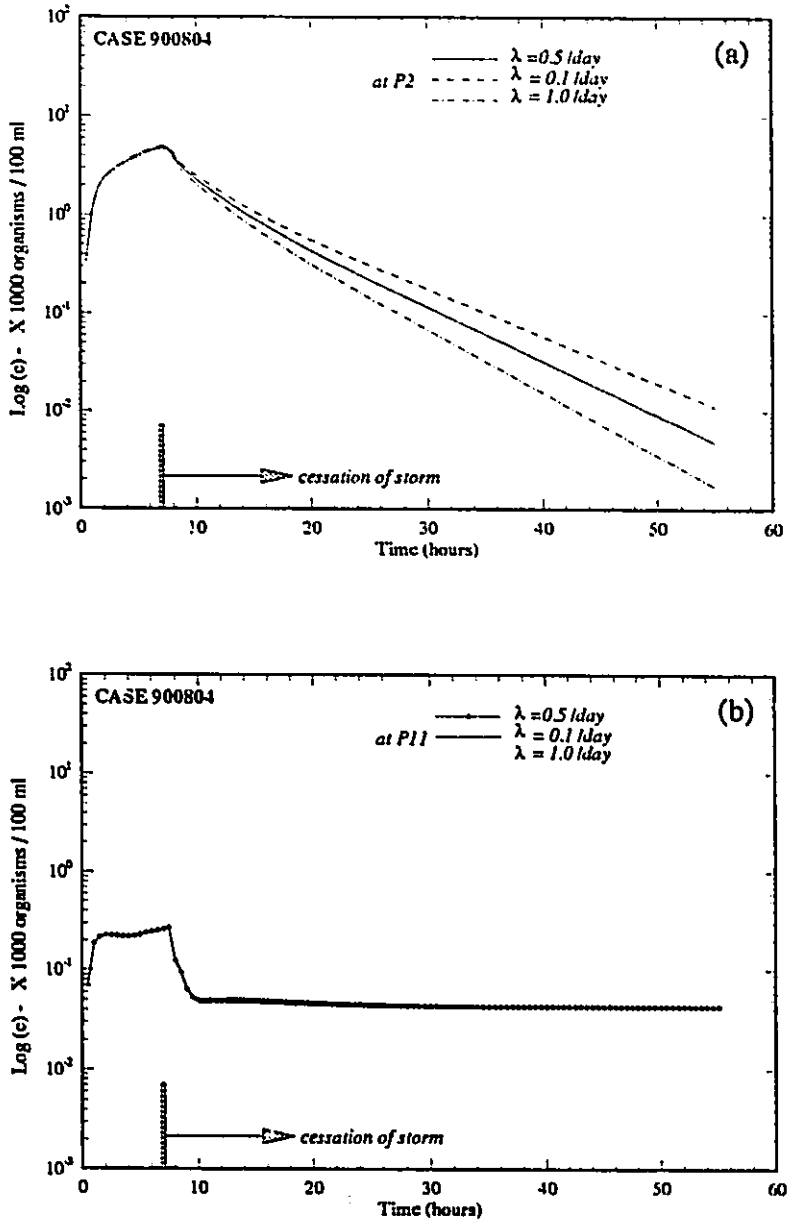

Fig. 8.11 Sensitivities of the die-off coefficient (three values, i.e., 0.1 / day, 0.5 /day and 1.0 /day are used) on the fate and transport of bacteria in the Sarnia Bay of the St. Clair River: (a) at P_2 which is located in the Bay, (b) at P_{11} which is located in the river stream.

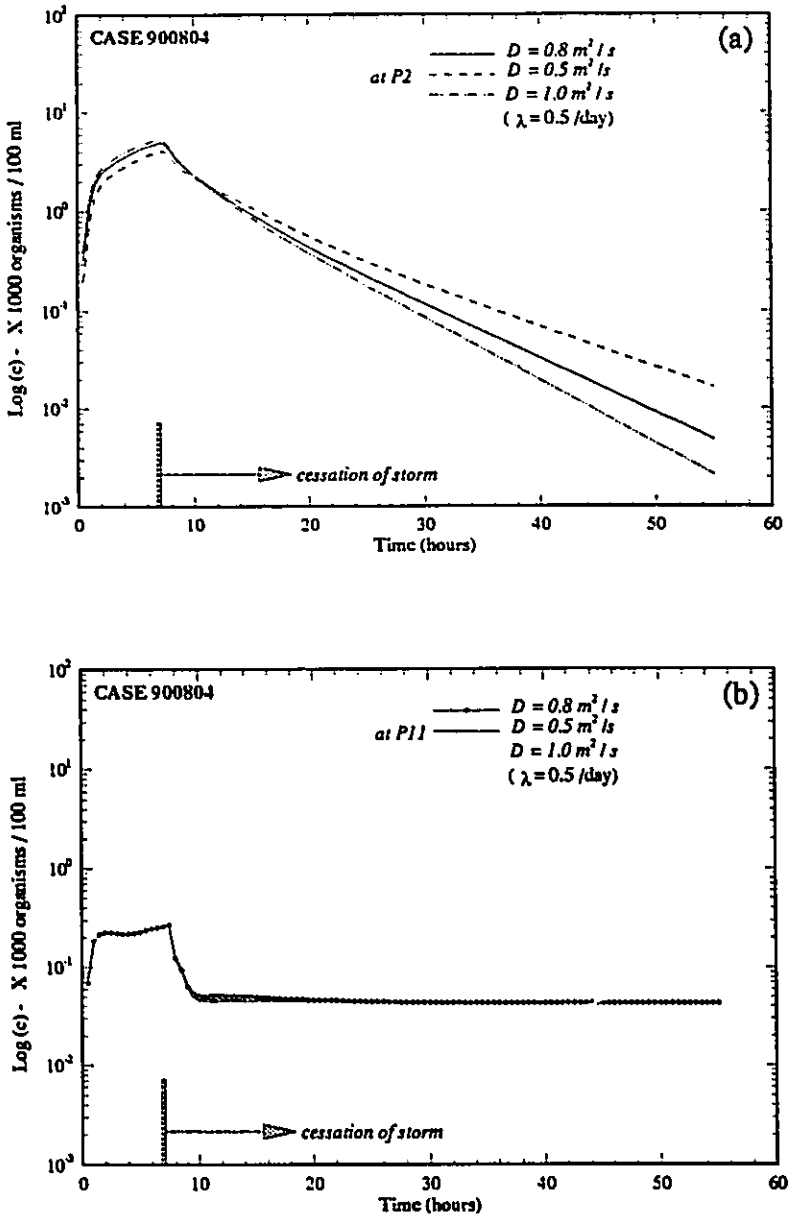

Fig. 8.12 Sensitivities of the horizontal dispersion coefficient (three values, i.e., 0.5 m^2/s, 0.8 m^2/s and 1.0 m^2/s are used) on the fate and transport of bacteria in the Sarnia Bay of the St. Clair River: (a) at P_2 which is located in the Bay, (b) at P_{11} which is located in the river stream.

8.5 REMEDIAL MEASURES

The remediation of water contamination problems in the Areas of Concern is addressed in the local Remedial Action Plans. These plans deal with all the issues of water use impairment using an integrated approach with multiple purpose objectives. The same integrated approach is taken in the Water Pollution Control Plans required by the Ministry of the Environment to address both wet and dry weather pollutions. A call for preparing such a plan for the City of Sarnia has been issued recently. Consequently, this study should be viewed as a planning-level analysis suggesting some selected remedial measures to be included in the future pollution control, in order to deal effectively with bacteriological contamination and impairment of water use in the study area.

The overall objective of remedial measures is to minimize the duration of wet-weather after-effects in Sarnia Bay under the 100 counts / 100 ml water quality guideline for fecal coliform in swimmable waters. In order to reduce the duration of bacteria in Sarnia Bay, cutting and relocating outfalls and enhancing exchange flow between the river and the bay are the essential approaches. Ten remedial measures were previously tested for alleviating the Sarnia Bay pollution problem (Tsanis and Wu, 1991). Five of them are examined here with some refinement, as presented in Table 8.2 and Fig. 8.13. The storm event 900804 is used as the reference case in this feasibility study.

The simulated circulation patterns in Sarnia Bay by the hydrodynamic model in these remediations are presented in Fig. 8.14. The pattern for case 900804 is also included for the comparison purpose (Fig. 8.14(a)). The logarithm of bacteria concentrations for various remediations at *P2* and *P3*, *P4* and *P10* in the Sarnia Bay are shown in Figs. 8.15 and 8.16, respectively.

Table 8.2 Hypothetical measures for Sarnia Bay in the St. Clair River

CASE	Remedial Measures (RM)
	standard case (900804)
RM1	1 m^3/s flushing flow at the northwest corner of Sarnia Bay
RM2	disconnect SS104, relocate SS105 to SS107 out of Sarnia Bay
RM3	build a straight barrier or dike
RM4	RM2 + RM3

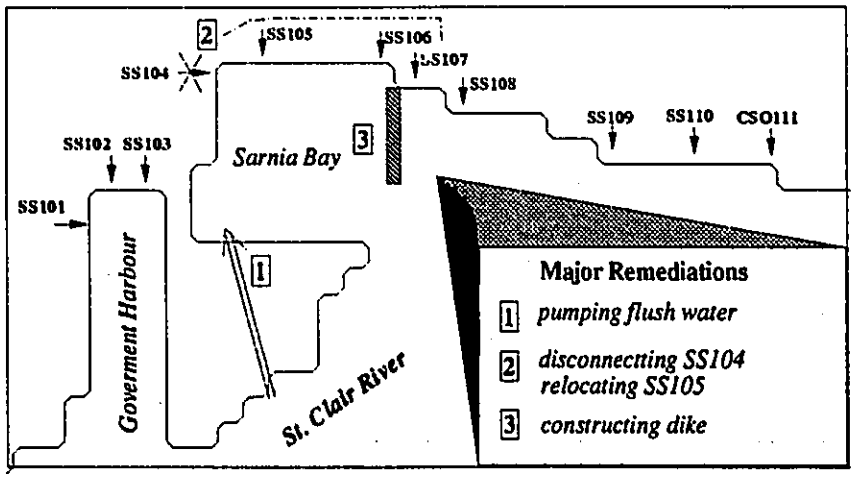

Fig. 8.13 Major remedial measures proposed for the St. Clair River in Sarnia, including getting flushing flow, disconnecting and relocating sources, constructing a dike.

In the first case (*RM1*), we increase the flushing of the bay by pumping in river water ($1\ m^3/s$) in the northwest corner of the bay. The flushing-induced current is very weak compared with the hydraulically-induced current by the river flow, see Fig. 8.14(b). As a result, the effect of pumping river water on the time series of bacterial concentration was negligible, see Figs. 8.15 and 8.16. In conclusion, this remediation is not feasible.

In the second case (*RM2*), the storm sewer SS104 is disconnected and SS105 is moved out of the bay to SS107. The impact on the bacteria transport is evident at *P2*, *P3*, and *P10* of Sarnia Bay, where the peaks are decreased about half and the durations of the after-effect are reduced about 5 hours.

In the third case (*RM3*), a straight dike is built at the mouth of the Bay diverting sewer discharges from the Bay and preventing counter-clockwise circulation. At the same time, this barrier retains the pollutants discharging into the Bay for longer period of time. These effects are working against each other. The first effect reduces the peak slightly, while the second effect increases the duration of the after-effect, when compared with the reference case, as shown in Fig. 8.14.

Then, combining *RM2* (disconnecting SS104 and relocating SS105) and *RM3* (with a dike), a test (*RM4*) is undertaken to reduce the peak due to usage of the dike. Fig. 8.17 shows the simulated concentrations at the locations of interest. Significant effects in peaks can be observed. The dike keeps the polluted water in the east shore away from the bay, so that, the cleaner water from upstream can enter the bay. The peaks are lower than 100 counts / 100 ml during and after the rain for the points in the bay, see Figs. 8.15 and 8.16. As a result, the remediation *RM4* is the most appropriate measure to alleviate the bacterial pollution problem in Sarnia Bay.

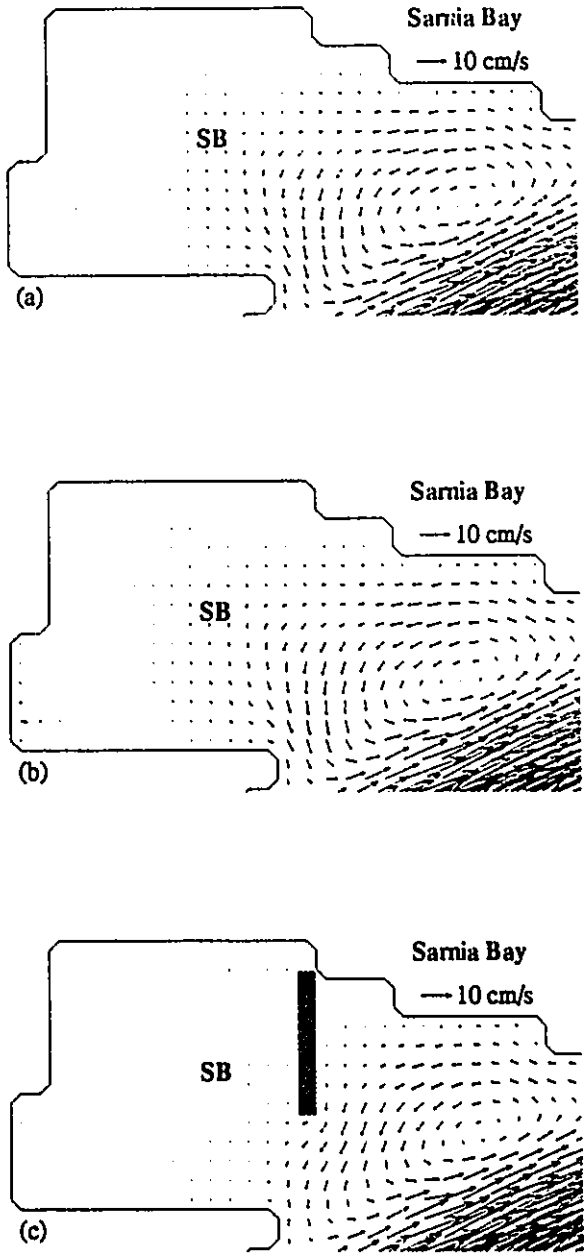

Fig. 8.14 Simulated circulation pattern in Sarnia Bay by the hydrodynamic model in the various remediations: (a) standard case - 900804, (b) 1 cms flushing flow introduced at the northwest corner of Sarnia Bay, and (c) with a straight dike.

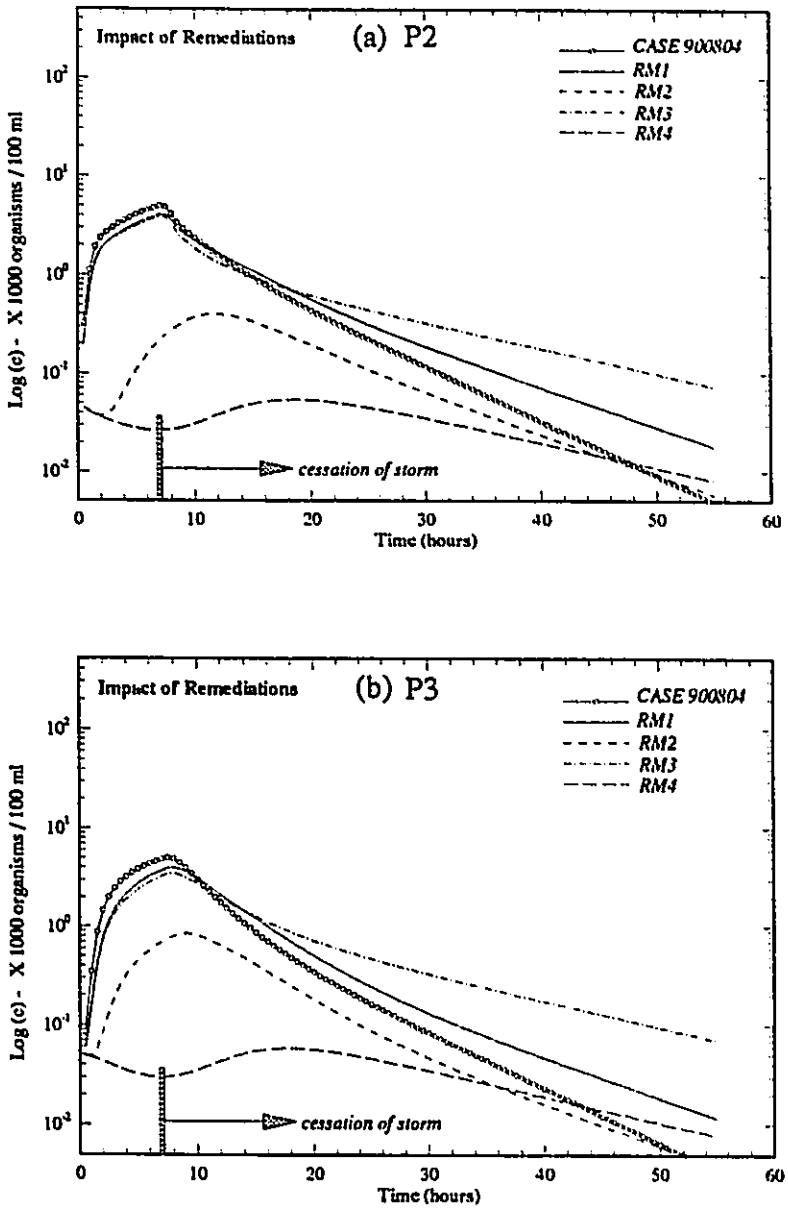

Fig. 8.15 Impact of various remedial measures (*RM1*, *RM2*, *RM3* and *RM4*) on the bacteria transport in Sarnia Bay: (a) at *P2*, (b) at *P3*.

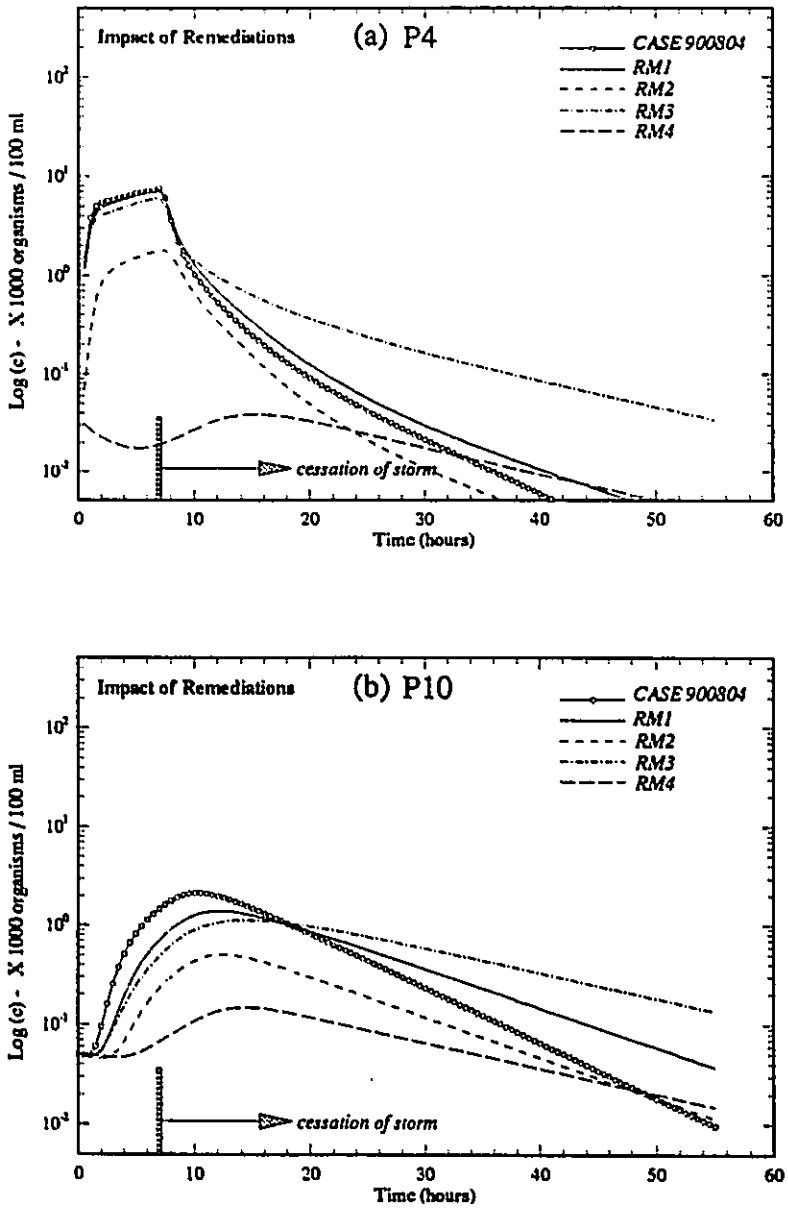

Fig. 8.16 Impact of various remedial measures (*RM1*, *RM2*, *RM3* and *RM4*) on the bacteria transport in Sarnia Bay: (a) at *P4*, (b) at *P10*.

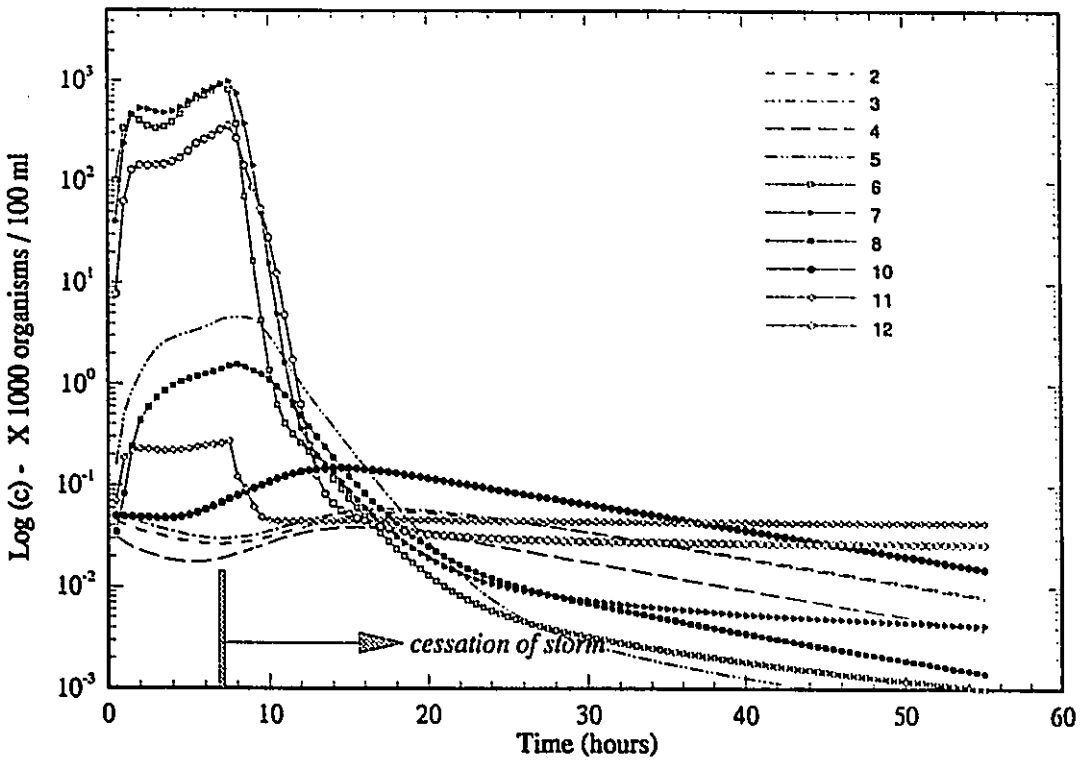

Fig. 8.17 The logarithm of the bacteria concentration for *P2* to *P7*, and *P10*, *P11*, *P12* (see Fig. 8.1(b)) as function of time from the beginning of the storm till forty-eight hours after the cessation of the storm, in the integrated remedial measure *RM4*.

8.6 SUMMARY

The simulation of storm events and the feasibility study of proposed remediations clearly indicates that the hydrodynamic and coupled pollutant fate and transport model is a successful tool for the study of bacterial pollution in the St.Clair River in Sarnia. The findings and conclusions include:

(1) The circulation in the St. Clair River in Sarnia is successfully simulated by the two-dimensional hydrodynamic model. The simulations indicated a very fast advective flow in the main river channel and a weak current and counter-clockwise eddy in both Sarnia Bay and Government Harbour.

(2) The temporal and spatial distributions of bacteria in the study area is modelled by the pollutant fate and transport model. Simulations of storm event including the recovering period, indicate that the duration of the after-effect of wet-weather is about 0.5 to 2 hours for the river due to its fast flow and 10 to 40 hours for Sarnia Bay. A sensitivity study is also conducted to examine the effect of the bottom friction coefficient, the wind condition, and the die-off and dispersion coefficients.

(3) The remediation *RM4* calling for the closure of the sewer SS104 and relocating SS105, and the building a dike at the mouth of Sarnia Bay is the most appropriate measure to alleviate the bacterial pollution problems in Sarnia Bay. This will assist in future remedial actions.

Some limitation and shortage of this study should also be mentioned. Firstly, there is a lack of field measurement on the currents which allows the model calibration and verification, so that the coefficients such as the die-off coefficient of bacteria and horizontal dispersion coefficient

and Manning's coefficient used in the model of the St. Clair river in Sarnia can be determined. Secondly, the measurements during some storm events and dry-weather loading are desirable for the calibration and verification of bacterial fate and transport modelling, though they are costly. And finally, it should be emphasised that the remedial measure is based on a preliminary study. Before proceeding with any conceptual measure, more detailed design/planning studies would be required.

Overall, the modelling bacterial pollution problem in the St. Clair River is successful and the model and approach used in this study will also be useful in all other environmental concern areas in the Great Lakes where remedial action plans are required.

PART IV - HAMILTON HARBOUR STUDY

On 6 July 1669, M. de LaSalle set out with 24 men and 7 canoes from Montreal, west along the St. Lawrencc River. LaSalle hoped that this river might be the road to China and Japan. Two months later, they passed through Lake Ontario, and arrived at the head of the lake (Burlington Bay or Hamilton Harbour), probably the first European exploration to reach this area (Charlton, 1884). With thc establishment and development of the cities of Hamilton and Burlington around this small harbour during the subsequent 320 years, the originally natural and clean water of the Harbour declined as a consequence of eutrophication, urban and industrial discharges, and other land-use practices. The harbour was identified as one of the environmental concern areas in North America by the Water Quality Board of the International Joint Commission in 1972. An intensive multidisciplinary remedial action plan (RAP) is being undertaking to restore the harbour as a vibrant centrepiece in the local community. As PART IV of this thesis, Chapter 9, 10 and 11 will concentrate on the study of Hamilton Harbour. The statistical features of currents and water levels during the 1990 &1991 field study periods will be revealed, and those field data will be used to verify the hydrodynamic model. As one of the projects for RAP in Hamilton Harbour, a nested-grid hydrodynamic/pollutant transport model is developed and applied in three near-shore areas, i.e., Western Basin, LaSalle Park and Northeastern Shorelines, to simulate the detailed current structure and transport of pollutants, and to examine the feasibility of various remedial measures.

CHAPTER 9

FIELD STUDIES

There are three approaches to model verifications, i.e., point-by-point comparison, spectral comparison, and spatial comparison (the details will be discussed in the next chapter). As a result, it is helpful to first understand the dynamic and spectral features of the physical processes such as the current and water level set-up from the field data, by using the climatological and spectral analysis methods. The field data analysis will help us to obtain the appropriate data sets for the model verifications, and to select the suitable numerical model and verification approach.

During the periods of 1990 & 1991, an extensive field study program for Hamilton Harbour was undertaken by the scientists at the National Water Research Institute (NWRI) at CCIW. In this chapter, this field study program is described, and the dynamic features of current and water level variation are revealed from the data analysis using climatological and spectral methods.

9.1 HAMILTON HARBOUR - AN ENVIRONMENTAL HOT SPOT

Hamilton Harbour is located at the west tip of Lake Ontario (Fig. 9.1). A sandbar

separates the Harbour from Lake Ontario and exchange with the lake is accommodated through the Burlington Ship Canal (820 m X 88 m X 9.5 m). The Harbour is triangular in shape with an east-west axis of 8 km and a north-south axis of 5 km. The surface area of Hamilton Harbour is 2150 hectares. With a mean depth of 13 m and a maximum depth of 26 m, the Harbour has a theoretical hydraulic residence time (i.e volume/inflow) of about 90 days.

Hamilton Harbour is polluted by the industries on the highly developed south shore, which use 27 m^3/s of water and return a similar amount of effluent to the Harbour. Municipal utilities use the Harbour as a recipient for 4.3 m^3/s of treated sewage (Barica, 1989). In addition, the Harbour receives flows from tributaries and untreated storm water runoff estimated at 3.5 m^3/s. Consequently, provincial water quality criteria are exceeded for ammonia and phosphorous in the Harbour water (Barica, 1989). The nutrient loadings result in the eutrophication, and, the severe hypolimnetic dissolved oxygen depletion. Contamination by toxic organic compounds (BHC, HCB's, PCB's and PAH's) is also high (Poulton, 1987). For these reasons, Hamilton Harbour is designated by the International Joint Commission (IJC) as an *Area of Concern*.

9.2 Physical Studies During the 1990 & 1991 Field Seasons

The Remedial Action Plan (RAP) has been set up since 1987, to improve the water quality in the Harbour. To achieve the objectives in the RAP, many physical, chemical, geological and biochemical field study programs have been executed over the past two decades, as summarized in a number of reports on the RAP for the Harbour by the Ministry of the Environment of Ontario (MOE, 1974; 1992) However, until 1990, there were no comprehensive field measurements on the current and water level changes in the Harbour. During the periods of 1990 & 1991, a field program was carried out by scientists at CCIW (Boyce and Chiocchio,

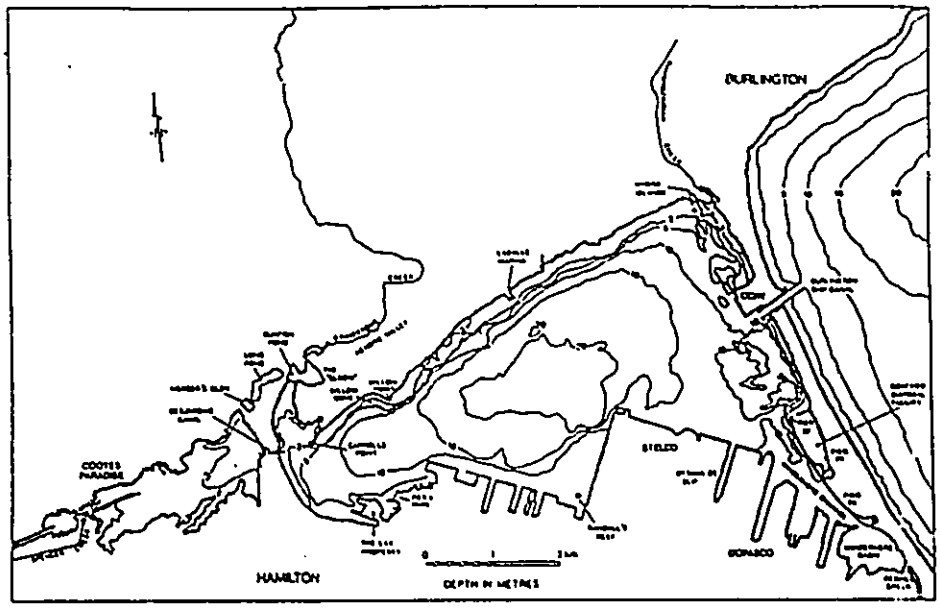

Fig. 9.1 Hamilton Harbour map

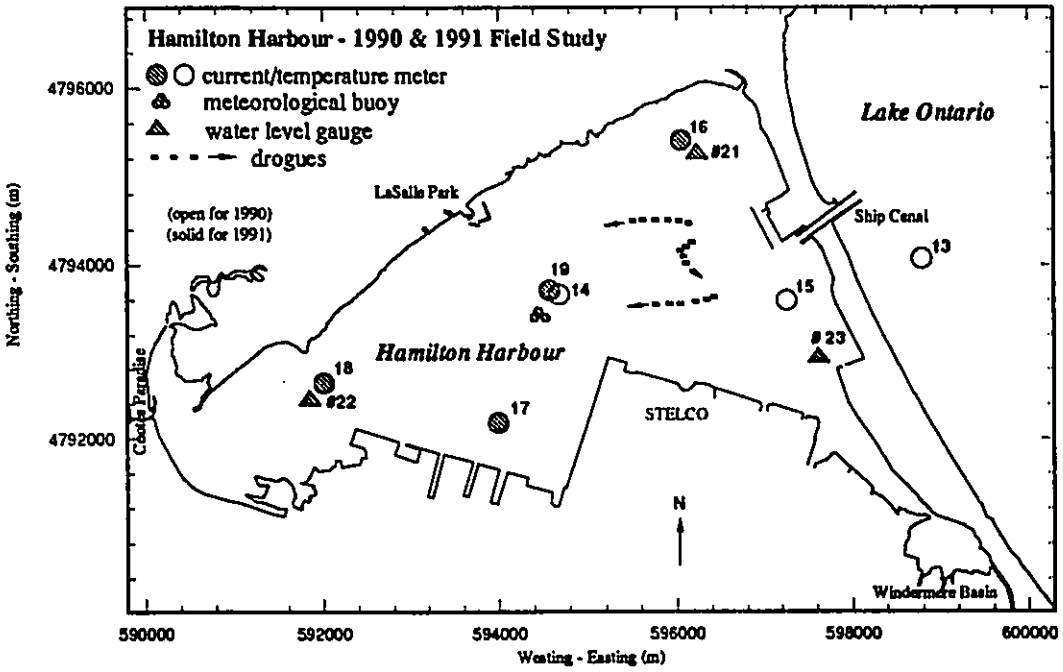

Fig. 9.2 Locations of meteorological and limnological observation stations in Hamilton Harbour during the 1990 and 1991 field study seasons.

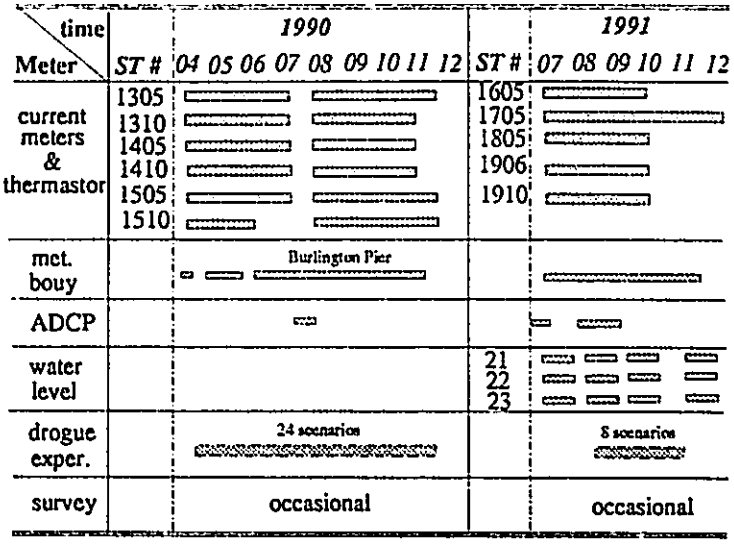

Fig. 9.3 Bar chart for the summary of the observed field data during the 1990 and 1991 field study seasons in Hamilton Harbour.

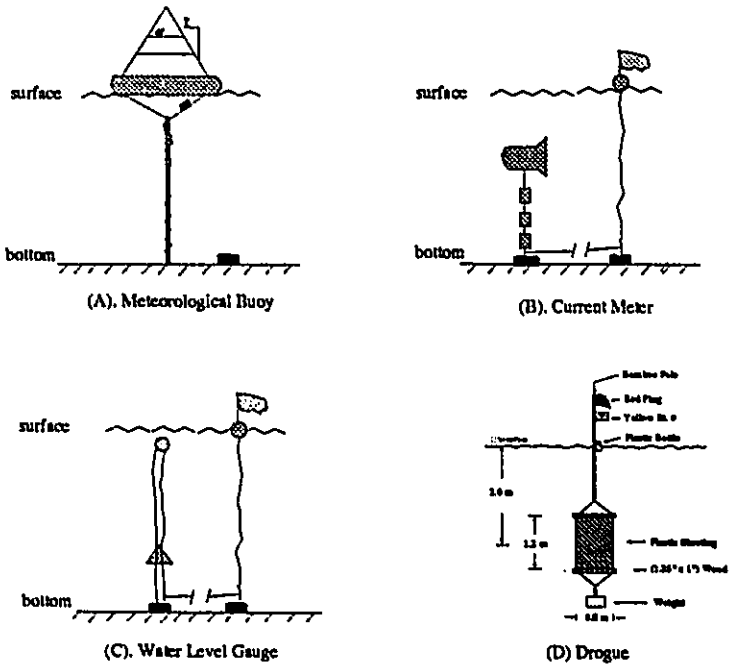

Fig. 9.4 Diagram of the instruments used in the 1990 & 1991 field study seasons in Hamilton Harbour. (a) meteorological buoy, (b) water level gauge, (c) current meter, and (d) drogue.

1991). The program was designed to provide a comprehensive data set of water currents, water levels, temperatures, wind direction and speed, and other meteorological elements, so that the features of hydrodynamics in the Harbour could be systematically examined and sufficient data could be available for the numerical model verifications.

The locations of the instrument installation in the 1990 & 1991 field studies are presented in Fig. 9.2. Fig. 9.3 shows a bar chart summary of the data return, and Fig. 9.4 shows the instruments used in the observation. The measurements were made during the open water period, i.e., from May to December. Eight Branker current meters were moored in 1990 at depths of 5 m and 10 m in three locations C13, C14, C15 (the open circles symbols as shown in Fig. 9.2). C13 was located in Lake Ontario near the ship canal. During the 1991 open water period, six Neil Brown acoustic current meters were installed at four sites C16, C17, C18 and C19 (solid circles in Fig. 9.2). Their nominal endurance was 150 days (July 3 to November 30, 1991). Three *Applied Micro-System* water level gauges (see Fig. 9.4) were installed on bottom stands at three locations: the Northeast Corner (#21), the East Shoreline (#23) and the West Basin (#22), as shown in Fig. 9.2. The gauges were set to record an integrated samples every 2 minutes. The integrating period is 90 seconds. The hourly level data were obtained from the 2 minutes data. The hourly water level data since 1970 were also available at the Burlington Pier (near the Ship Canal).

Wind speed and direction, air temperature, relative humidity, water temperature, and solar radiation were recorded by the meteorological buoy, as shown in Figs. 9.2 and 9.4, at the central Harbour. Wind data from the Burlington Pier (near the canal) and Royal Botanical Gardens (RBG) are used for the examination of spatial variety of wind field over the Harbour.

To supplement the mooring current meter measurements and provide direct measurements of horizontal mixing in Hamilton Harbour, drogue tracking experiments were undertaken within the harbour on 23 different occasions during the open water season of 1990 (April to November), and on 20 occasions in 1991 by the scientists in NWRI of CCIW (Boyce and Chiocchio, 1991). Each experiment lasted about 5 hours. The drogue shown in Fig. 9.4(d) was used in the survey. It consists of a plastic sheet approximately 1 square meter suspended from a bamboo pole. The positions of the drogues were determined by using a Motorola Mini Ranger in the four land stations located in the southern and eastern part of the harbour. As many as 12 drogues were launched and tracked. Most of them were at 2 meters below the water surface, though others were either at 5 meter or 6.5 meter depth. Drogue measurements were made in the southeast corner of the Harbour during 1990, and in northeastern shorelines and western basin during 1991.

9.3 CLIMATOLOGICAL FEATURES OF WATER LEVEL AND CURRENT

9.3.1 Water Level

Water elevation changes were measured for the first time in Hamilton Harbour (Boyce and Chiocchio, 1991). Fig. 9.5 shows a typical time series of water level changes at three stations together with wind. It is observed that the water level varies more than expected (it changes over 5 cm at several hours), and the water level changes do not follow the wind. Such a big change could happen only in the large lakes such as Lake Ontario (Donelan et al., 1974) and Lake Tai (Wu and Pu, 1989). The change in the Harbour would be expected to be 0.1 to 1.0 cm over several hours, if it did not connected with Lake Ontario. This local wind-induced setup has

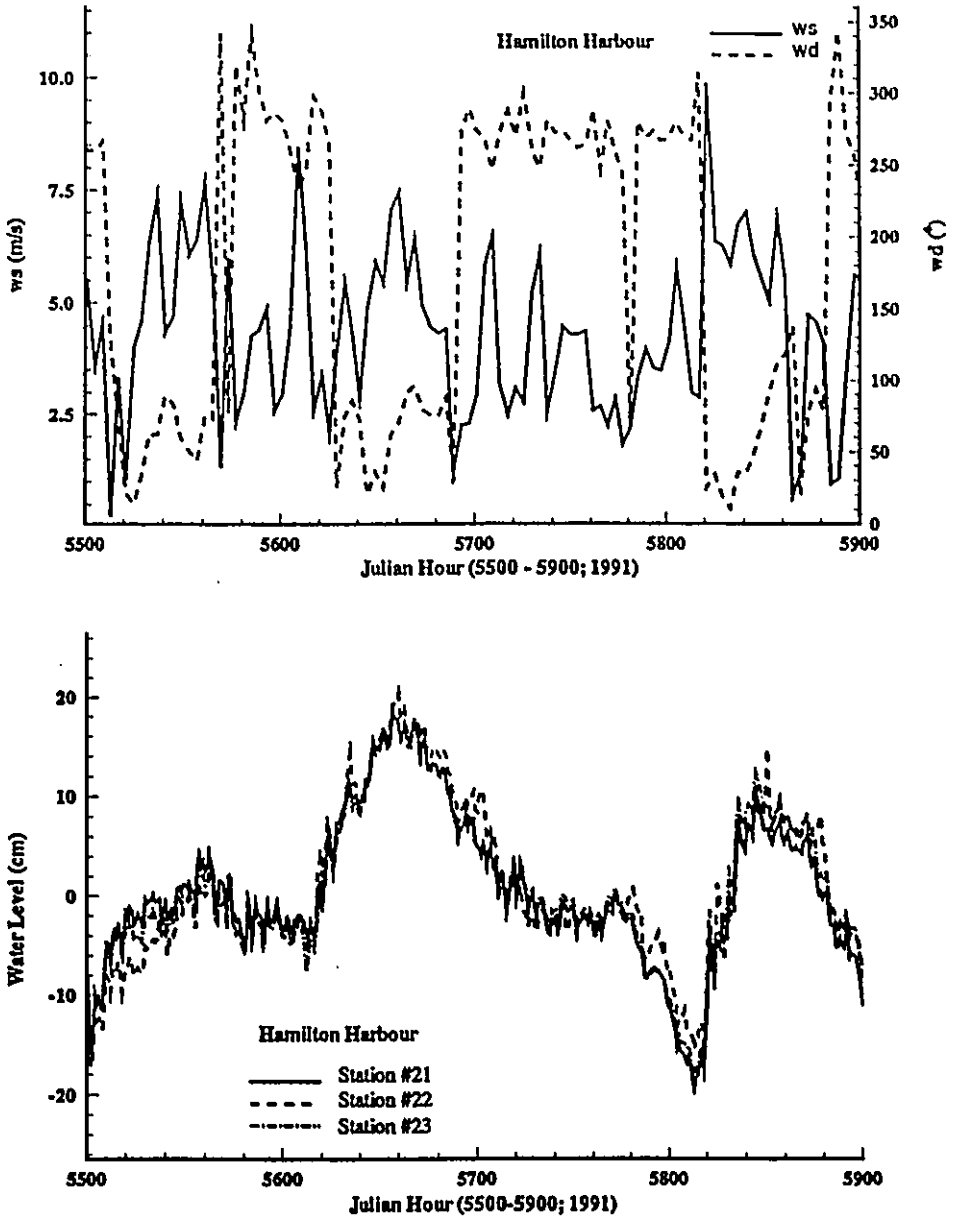

Fig. 9.5 Typical time series of wind (at buoy) and water elevations at stations #21, #22, #23 in Hamilton Harbour during Aug. 18 - Sep. 2, 1991.
(Source of data: NWRI)

little contribution to the water level changes compared to the pumping effect from Lake Ontario. The Harbour's water goes up and down with the water in Lake Ontario.

9.3.2 Current

The minimum, maximum and mean wind and current speeds at all stations are listed in Table 9.1. Frequency distributions of wind and current speeds, and directions at buoy and current meters during 1990a (Julian hour = 1943-4335, March 22 - July 29), 1990b (Julian hour = 5253-7849, Aug. 6 - Nov. 23) and 1991 (Julian hour = 4434-6854, July 3 - Oct. 13) are presented in Figs. 9.6, 9.7 and 9.8, respectively.

Over the observation periods, a maximum wind speed of 13.01 m/s was recorded during 1990 and 11.58 m/s during 1991. The mean wind speed was about 3.9 m/s. Maximum current was over 30 cm/s, recorded at CM13 (5 m), located in the west end of Lake Ontario. These maximum currents, at locations in Hamilton Harbour, were much less, from 11.5 cm/s to 18.7 cm/s. It is observed that the maximum speed at lower depth (10 m) was not always smaller than one at the upper depth (5 m), indicating the existence of effects other than winds, such as thermal stratification. Mean current speeds were very close at all stations ranging from 2.3 cm/s to 4.28 cm/s, while slightly bigger at the mid-harbour station (CM14) and the station in Lake Ontario (CM13). The mean speed at 10 m depth was lower than the one at 5 m depth at all stations except at CM15, where the stratification was very strong (confirmed from temperature observations) and exchange flows between the Harbour and Lake Ontario through the Burlington Ship Canal might have had some effect, because its location was near the Canal. At 80% of the time at all stations, the current speeds remained in 0 to 4 cm/s, and the time when speeds exceeded 10 cm/s was lower than 2 %.

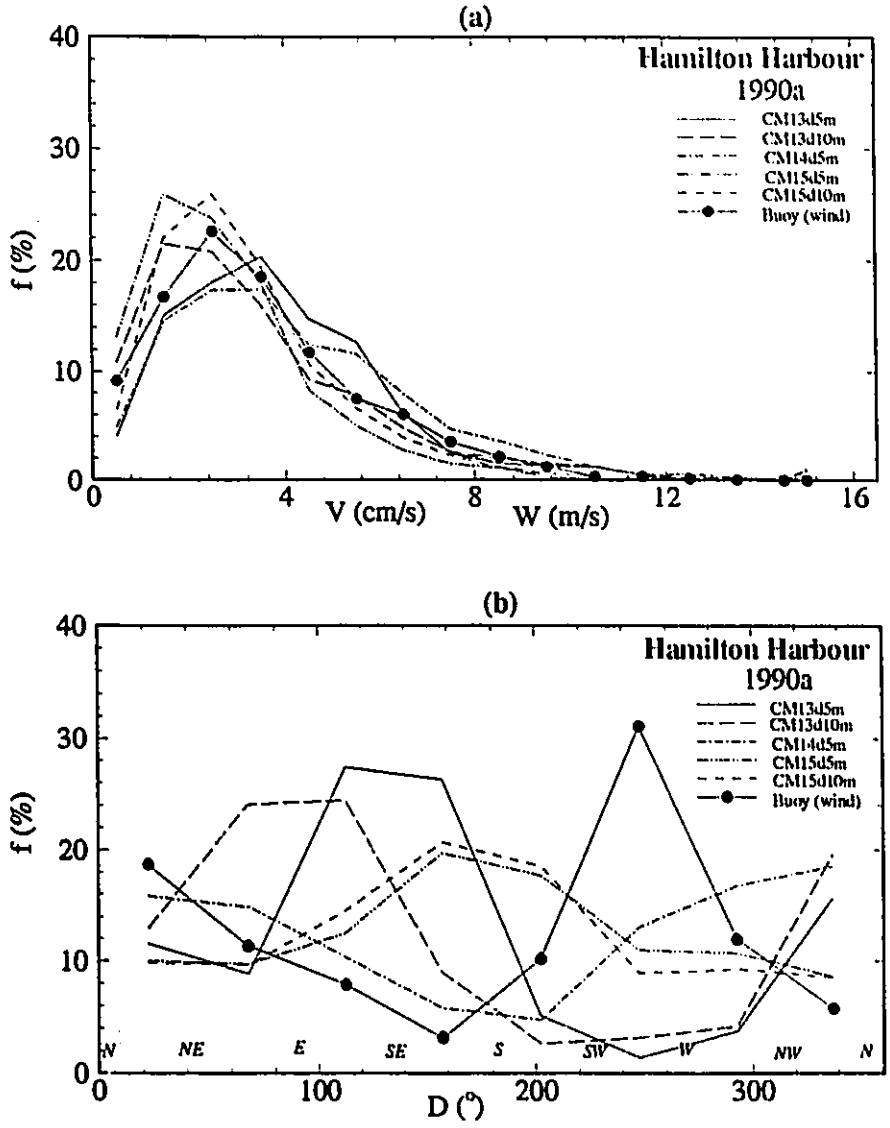

Fig. 9.6 Frequency distributions of wind and current speeds and directions at buoy and mooring current meters during period 1990a (Julian hour = 1943-4335, March 22 - July 29, 1990), Hamilton Harbour.
(Source of data: NWRI)

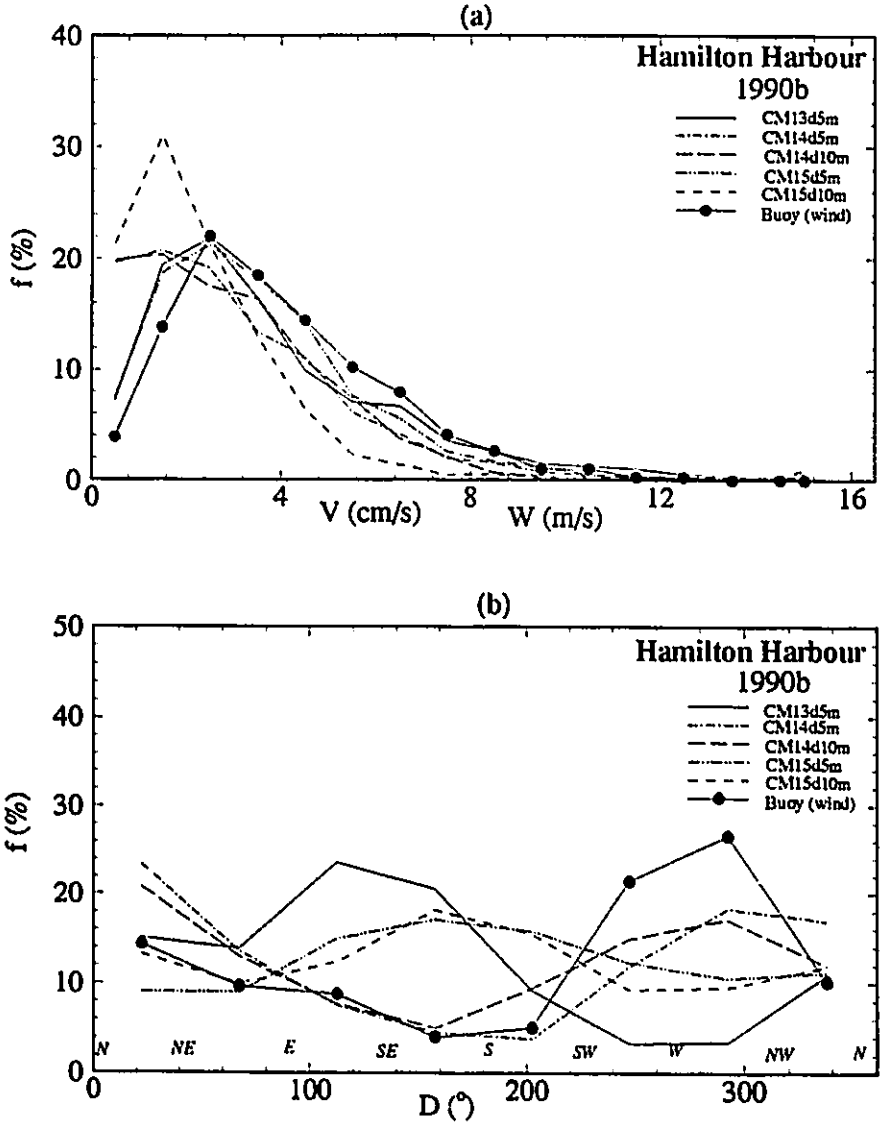

Fig. 9.7 Frequency distributions of wind and current speeds and directions at buoy and mooring current meters during period 1990b (Julian hour = 5253-7849, Aug. 6 - Nov.23, 1990), Hamilton Harbour.
(Source of data: NWRI)

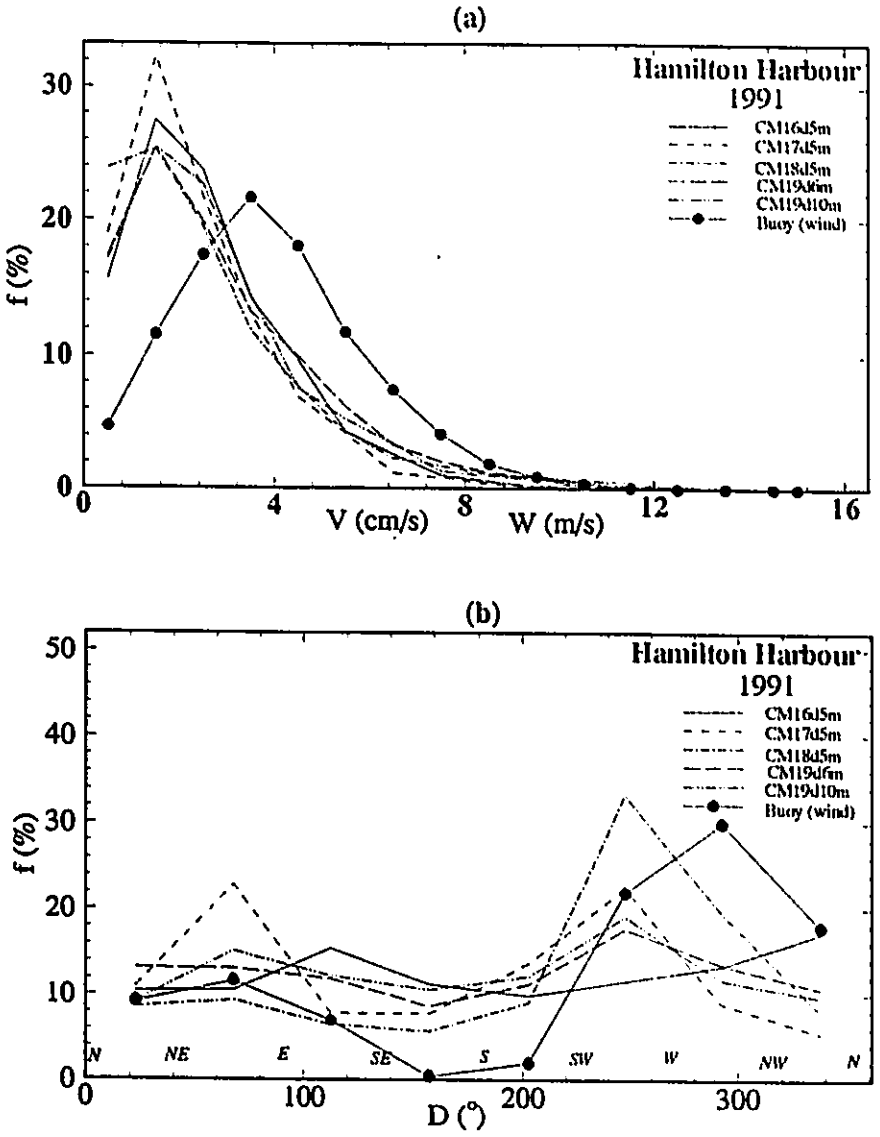

Fig. 9.8 Frequency distributions of wind and current speeds and directions at buoy and mooring current meters during period 1991 (Julian hour = 4434-6854, July 3 - Oct. 13, 1991), Hamilton Harbour.
(Source of data: NWRI)

Table 9.1 Minimum, maximum, mean values of wind and current speed during the 1990 and 1991 open water seasons in Hamilton Harbour

Period	Station	Min	Max	Mean	Notes
1990a	Buoy(wind)	0.00	13.01	3.48	m/s
	CM13d5m	0.00	31.14	4.08	cm/s
	CM13d10m	0.00	26.05	3.52	cm/s
	CM14d5m	0.14	18.72	4.28	cm/s
	CM14d10m	0.00	41.92	9.06	unreliable
	CM15d5m	0.00	14.40	2.78	cm/s
	CM15d10m	0.00	15.89	3.22	cm/s
1990b	Buoy(wind)	0.00	12.24	3.90	m/s
	CM13d5m	0.10	18.57	4.08	cm/s
	CM13d10m	0.00	0.00	0.00	unreliable
	CM14d5m	0.00	20.57	3.15	cm/s
	CM14d10m	0.00	17.75	2.83	cm/s
	CM15d5m	0.10	16.18	3.55	cm/s
	CM15d10m	0.10	13.86	2.26	cm/s
1991	Buoy(wind)	0.00	11.58	3.93	m/s
	CM16d5m	0.08	13.50	2.62	cm/s
	CM17d5m	0.04	12.11	2.32	cm/s
	CM18d5m	0.02	18.00	2.61	cm/s
	CM19d6m	0.04	13.95	2.83	cm/s
	CM19d10m	0.02	13.90	2.76	cm/s

Although the physical mechanism for the variation of wind direction (the wind comes from) and current direction (flow towards to) was very complex, there was a relationship between wind direction and current direction, which was affected by the topography and directions of shore lines.

During the 1990a & 1990b, over 50% of the time at the meteorological buoy, the winds came from SW-NW quadrants (west winds) while over 70% during the 1991 observation period, which is the longitude-axis direction for Hamilton Harbour. Over 70% of the time at 5 m of CM13, current directions remained in the SE quadrant, and the NW-W quadrant, which indicates movement along the shore. A slight shear was presented between the current at 5 m and 10 m at CM13, due to the fact that the major direction was in NE-E-SE quadrants at 10 m depth. Due to the effect of the eastern shorelines, the currents at CM15 did not follow the dominant wind direction (SW-W); it turned to the shoreline direction, i.e., SE-E direction. At central Harbour station CM14, the persistent current direction was in the NW-N and N-NE quadrants, due to the effect of local topographical circulation patterns in the right and left areas to the station.

From the selected experiments in which the wind velocities were 1 to 6 m/s, drogue experiments showed that current speeds of 2.0 cm/s to 15 cm/s were obtained at 2 m depth below the water surface, and 0.5 cm/s to 9.7 cm/s at 5 m depth.

It is observed from the time series of wind and currents that the current peaks followed the peaks of wind with little time lag. Although the water level in the Harbour is governed by the water level change of Lake Ontario, the exchange flow with the Lake has little effect on the current within the Harbour and may affect only the area near the Canal.

As discussed in Chapter 1, it is known from a number of field observations and

theoretical studies that the thermal stratification has significant effect on the current vertical structure in lakes, estuaries, reservoirs and harbours. Measurements with high temporal and vertical spatial resolutions are required for a better understanding of the process of vertical mixing. A vertical Automatic Profiling System (VAPS) has been employed recently in the Great Lakes, such as in Hamilton Harbour (Chiocchio, Boyce, and Royer, 1980). Although at this time the measurements in Hamilton Harbour at VAPS observation station (near CM19 in Fig. 9.2) during the summer of 1981 are not available for the model verification in this study, the plots in the report by Chiocchio et al. (1980) provide a visual understanding on the effect of the temperature profile on the velocity profile in Hamilton Harbour.

Fig. 9.9 gives an example of the vertical profiles of temperature, and of the two horizontal velocity components in Hamilton Harbour on September 17, 1981. The temperature profiles are characterized by a sharp thermocline at a depth of about 11-13 m, and a gradual decrease of its distance to the water surface. The current profile in the Harbour was very complex. The current was not simply characterized by a drift current in the upper layer and a return current in the lower layer. There were several zero velocity points, and there were fluctuations due to the internal waves induced by the thermal stratification. A strong current belt was evident around the thermocline layer, especially in the North-South component. This belt can be explained by the vertical mixing theory. These results confirmed the vertical mixing model using the Richardson number, as tested in chapter 6 where a strong current belt was obtained around the thermocline regime.

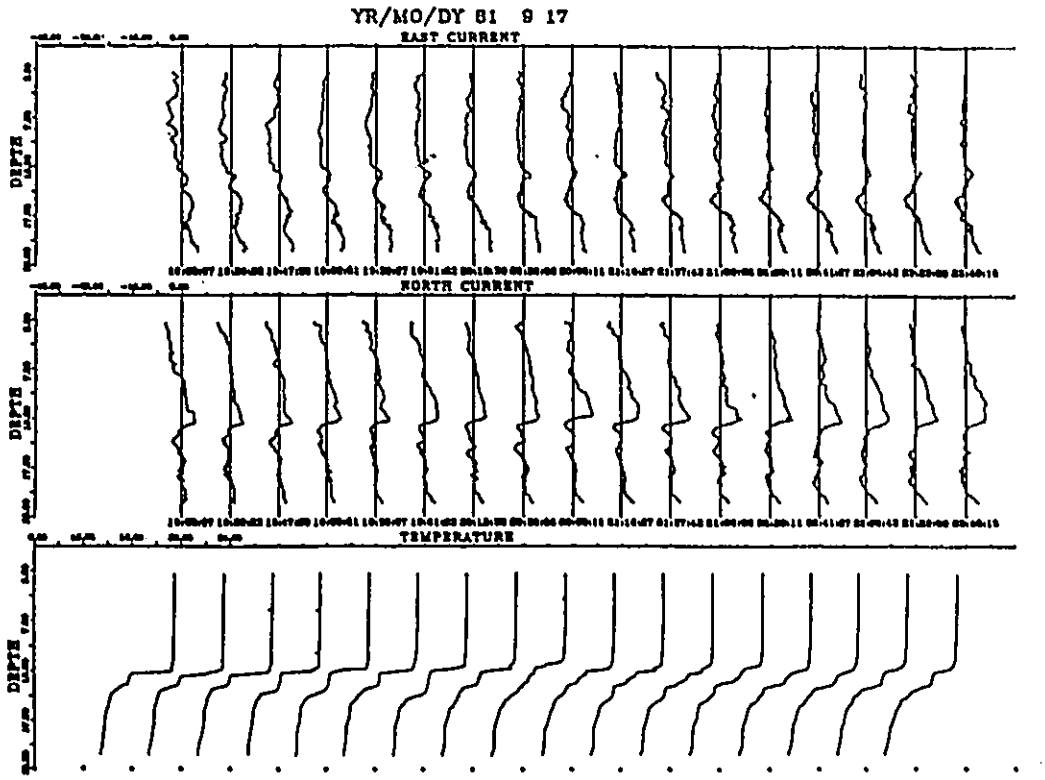

Fig. 9.9 Vertical velocity profiles of E-W and N-S current components and temperature from 18:05:07 to 23:45:15 of 17 September 1981 at central station of Hamilton Harbour. The dots indicate the 8^0 position to the left of each temperature profile. (Chiocchio et al., 1980)

9.4 SPECTRAL FEATURES OF WATER LEVEL AND CURRENT

Spectral analysis is a powerful tool for identifying certain flow characteristics. It illustrates how the kinetic energy associated with different scales of motions, frequencies and eddy sizes cascade in a turbulence field, and also demonstrates the periods of water oscillation from the water level data. It has been widely employed to analyze the mooring current data in the Great Lakes, such as in Lake Erie (Elzawahry, 1985), Lake Ontario (Tsanis et al., 1990), and in other lakes and oceans (Penicka, 1987). To obtain the spectra of field data in the Hamilton Harbour during 1990 and 1991, a spectral analysis program in the MATLAB package was employed. Specifically, if provided with the column data set of any variables such as the time series of water elevations or current velocity components, the power spectra, cross spectra, coherence, and phases between two variables can be obtained and displayed in the graphics windows. For the detailed calculation and usage of this package, see Appendix II. The significance level of the spectra in MATLAB spectral package is set as 95%. The determinations of confidence limits on spectra and significance levels of the coherence statistic can be found in Julian (1974), Bishop and Donelan (1988).

9.4.1. Seiche - Spectral Analysis of Water Level Data

According to Defant (1953), the seiche of a closed basin is defined as the free oscillations in which the wave lengths have same order of the basin size. Therefore, the period of seiche T_s can be approximately evaluated by the basin length L and mean water depth over the basin as follows

$$T_s = \frac{2L}{n\sqrt{gh}} \tag{9.1}$$

where, n is the nodal number of seiche, g is the gravity acceleration, and n = 1 refers to the fundamental seiche. Defant (1953) developed a finite section method to include the geometric variations of the basin. However, this method was not accurate due to the neglect of the bottom friction and Coriolis effect. When the observed water level data is available, the spectral method became the most accurate method. By using this method, the periods and averaged amplitudes above the background of seiche can be exactly determined.

Theoretical periods in Lake Ontario and Hamilton Harbour are presented in Table 9.2. Using Eq. (9.1), the fundamental period of seiche of Lake Ontario and Hamilton Harbour is 5.27 hours and 23.6 minutes, respectively. The inertial period due to the earth rotational effect is 17.23 hours (for averaged latitude 44 degree). Astronomical (diurnal) tide with the period of 12.42 hours is observed in Lake Ontario. The *pumping mode* or *Helmholz mode* represents the balance between the kinetic energy of water through the narrow connecting canal, and the potential energy from the rise in mean water level within the Harbour. The frequency of such a mode can be determined by (Freeman et al., 1974):

$$\Omega_0 = \sqrt{gA} \sum_{i=1}^{n} \frac{S_i}{L_i} \tag{9.2}$$

where A is the surface area of the Harbour, S_i is the cross-section area of the canal and L_i is the length of the canal. For the Hamilton- Burlington Ship Canal system, the period of the Helmholz mode is 2.2 hours from the above equation.

It is observed from the spectra of water elevations at the Burlington Ship Canal for 1990, 1991, 1987 - 1991 and the summer season of 1991, as shown in Fig. 9.10, that the most significant peaks are at 12.2 and 5.27 hours, which are the astronomical tide and the fundamental seiche of Lake Ontario. Energy in the lower frequences are high for the longer time series. The

Table 9.2 Theoretical periods of water movement in Hamilton Harbour and Lake Ontario

Type	Formula	Parameters	Period
Major Seiche of Hamilton Harbour	$\frac{2L}{\sqrt{gH}}$	$L = 8000\,m$ $g = 9.82\,m^2/s$ $H = 13\,m$	23.6 min
Major Seiche of Lake Ontario	$\frac{2L}{\sqrt{gH}}$	$L = 300000\,m$ $g = 9.82\,m^2/s$ $H = 100\,m$	5.27 hours
Inertial Wave	$\frac{2\pi}{2\Omega Sin\,\phi}$	$\Omega = 7.29 * 10^{-5}\ /s$ $\phi = 44^0$	17.23 hours
Astronomical Tide			12.42 hours
Diurnal Tide			23.93 hours
Helmholz Resonance of Hamilton Harbour	$\sqrt{gA}\,(\sum_{i=1}^{N}\frac{S_i}{L_i})$	$A = 2.15\,X\,10^7\,m^2/s$ $S = 8360\,m^2/s$ $L = 820\,m$	2.5 hours

peak, with a period of 2.7 hours, reflects the second mode of seiche (n=2) in Lake Ontario. The inertial oscillation did not appear in the Lake Ontario spectra, because the station was close to the shore.

Fig. 9.11 shows the spectra of 2 minute and hourly water elevation data of stations #21, #22, #23 in Hamilton Harbour during the summer of 1991. It is observed that there are predominant peaks with a period of 22 minutes (amplitude of 1.0 mm) and 10 minutes which are the fundamental and second mode seiche of the harbour. The spectra of hourly data show significant peaks are located at 12.0, 5.22, 2.2 and 1.1 hours, which are the astronomical tide and seiche of Lake Ontario, reflecting the effect of Lake Ontario through the Burlington Canal.

This finding can be further confirmed from the cross-spectral analysis. Figs. 9.12 and 9.13 show the coherences and phases of cross-spectra among the hourly water level data at three stations in the harbour; and between the Burlington Canal and these three stations, respectively. Coherences are high at periods of greater than 24 hours. They are in phase at this band, indicating that the harbour water was up and down with the water in Lake Ontario at periods over one day. Lower coherences were found between stations at short period (high frequency) bands (wind dominates these bands), except at 5.5 hours, 2.2 hours which are the periods of seiche in Lake Ontario.

9.4.2 Spectral Analysis of Wind, Temperature and Current Data

Fig. 9.14 shows the x- and y-component spectra of wind stress during the 1991 observation period. The spectra has its peak energy in the meteorological forcing band (60 - 200 hours). The spectra of water temperature at a mooring current meter (CM14d5m) is presented in Fig. 9.15. A diurnal (24 hours) period and semi-diurnal (12 hours) period were revealed in the

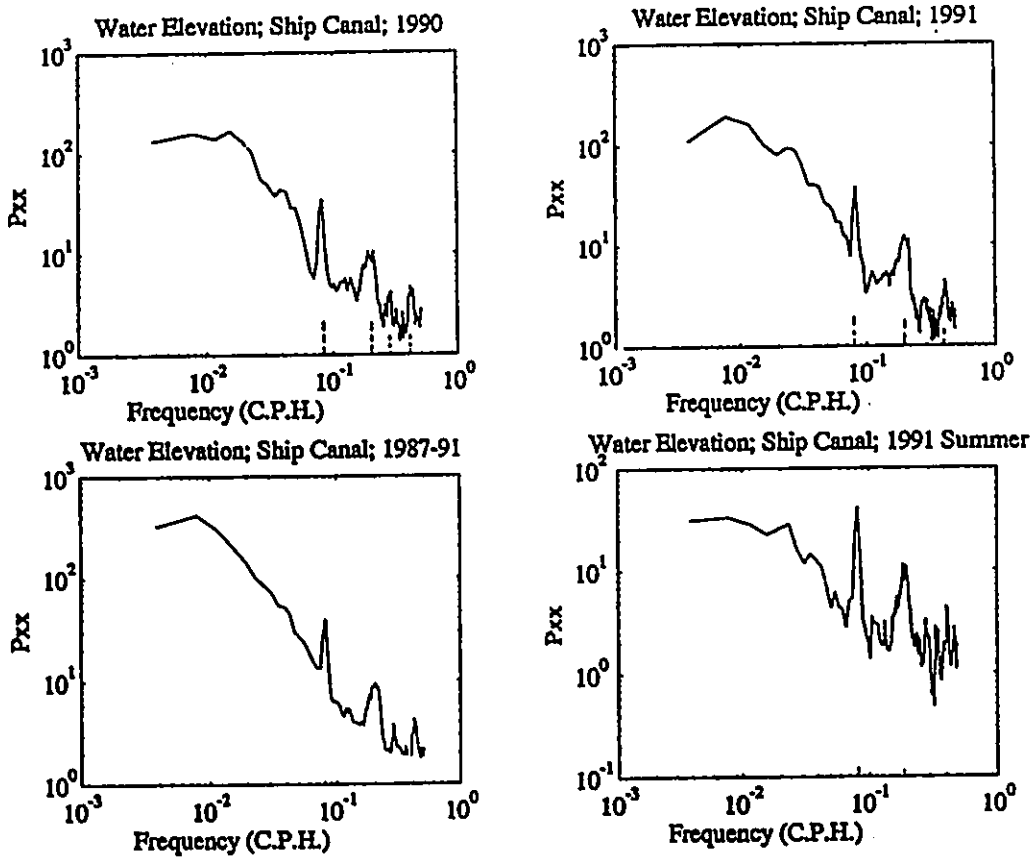

Fig. 9.10 Spectra of water elevations at Burlington Ship Canal for 1990, 1991, 1987-1991, and summer of 1991.
(Source of data: MEDS)

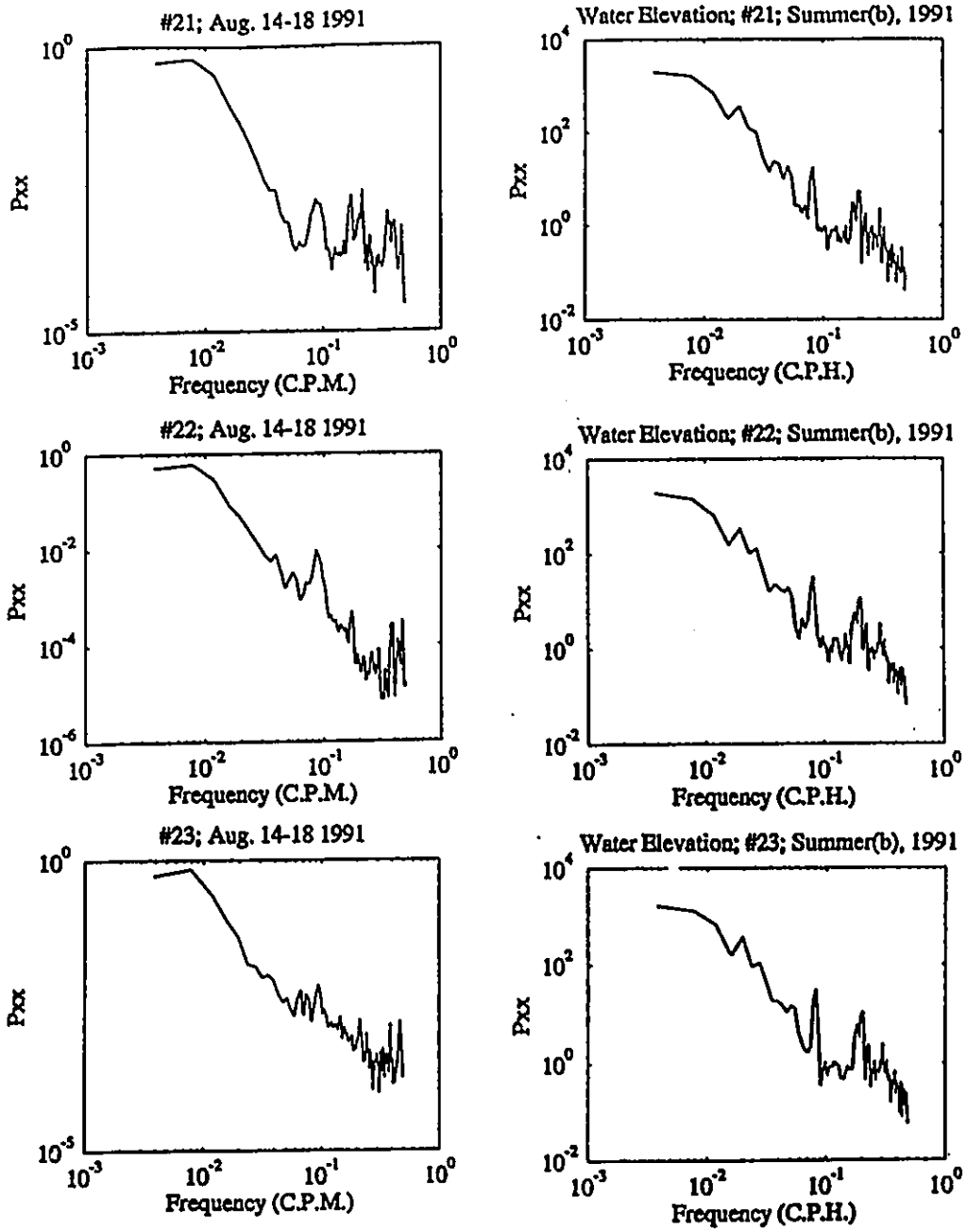

Fig. 9.11 Spectra of 2 minute and hourly water elevation data at three stations #21, #22, #23 in Hamilton Harbour (The period for hourly data is from Aug. 12 to Oct. 8, 1991; the period for 2 minute data is from 14 to 18, August, 1991).
(Source of data: NWRI)

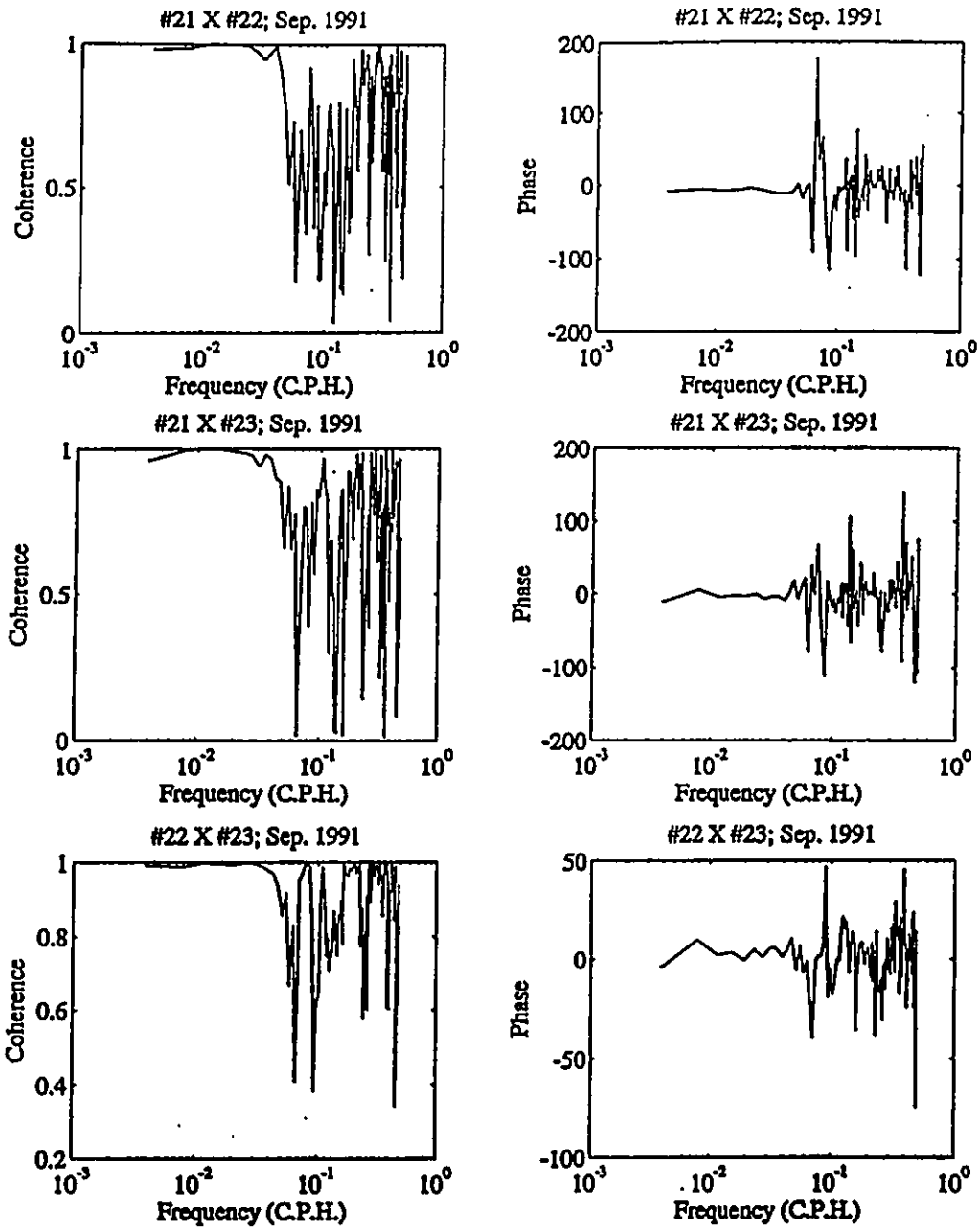

Fig. 9.12 Coherences and phases for the hourly water level data among the three stations #21, #22, and #23 in Hamilton Harbour during September of 1991.
(Source of data: NWRI)

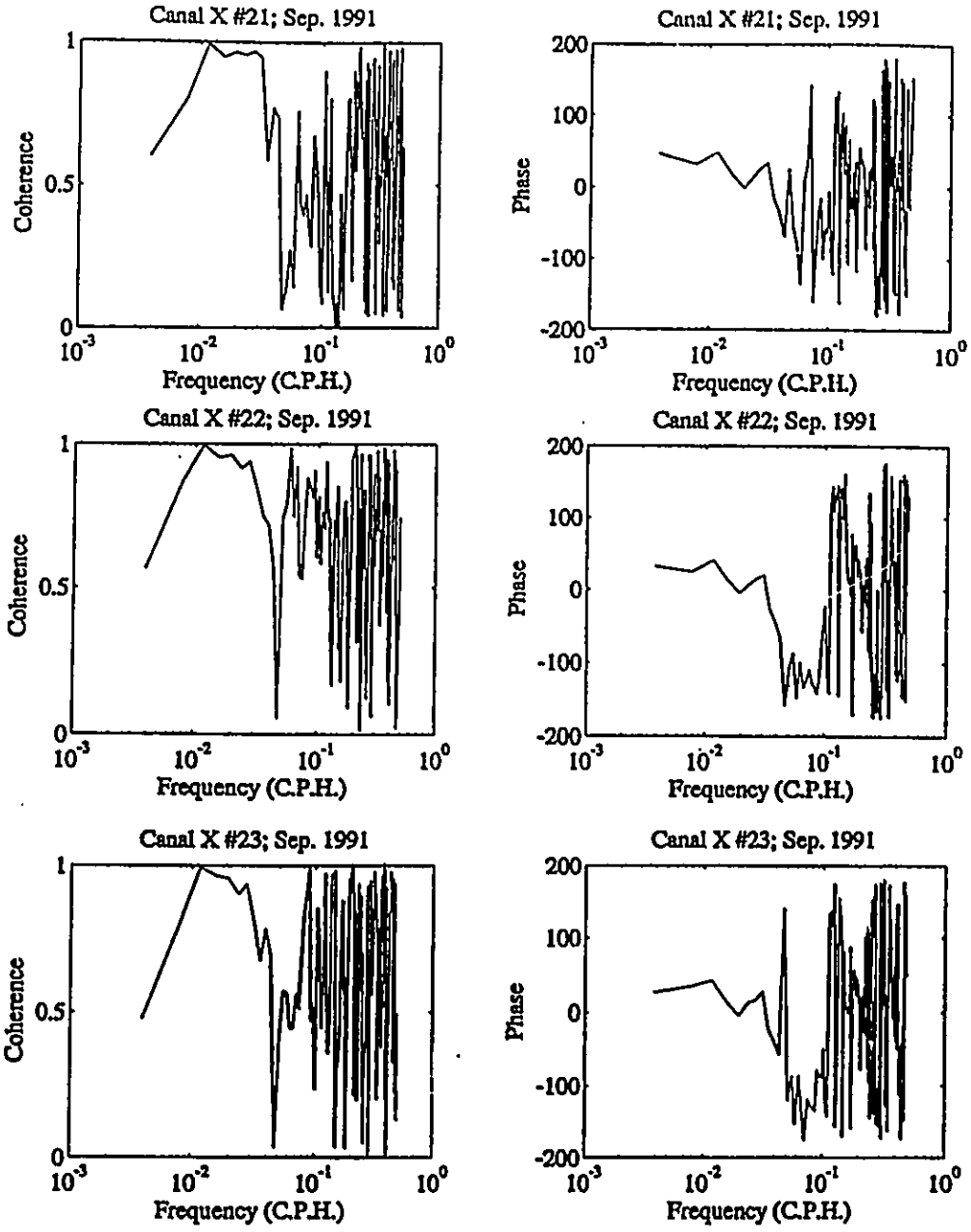

Fig. 9.13 Coherences and phases for the hourly water level data between Burlington Ship Canal and the three stations #21, #22, and #23 in Hamilton Harbour during September of 1991.
(Source of data: NWRI & MEDS)

spectra.

The horizontal current spectra (total, x- and y-components) at two depths (5 m and 10 m), and the cross-spectra between these two depths have been obtained for all current meter data. As an example, only the results from CM19 are presented. Fig. 9.16 presents the distribution of the energy of the horizontal motion over the frequency. The maximum energy is in the meteorological band (60 to 200 hours). This is the band over which wind forcing is particularly strong. Through the turbulent cascade process, the large scale motions associated with higher frequencies will transfer energy to smaller scale motions associated with high frequencies. The energy will decrease with increasing frequency, due to the energy loss to friction at all scales. The inertial peak (17.5 hour) is evident in the spectra of currents. As shown in Fig. 9.17, the coherences between the current at 6 m and the current at 10 m reveal that the currents are in the same phase around the inertial peak, and the coherences are very low in most of the frequency domain due to the complexity of current structure.

9.5 Summary

Climatological and spectral features of current, water level, and temperature in Hamilton Harbour during the 1990 and 1991 field study seasons have been revealed in this chapter. In summary, the following results have been obtained: (1) The currents in Hamilton Harbour were mainly wind-induced, with the mean speeds of 2.3 cm/s to 4.28 cm/s, and the maximum speeds of 11 to 18 cm/s at the mooring current meters. Due to the complicated shorelines and small size of the basin, dominant current directions were not found, and the variations were significant. (2) The complete spectra of water elevation of Hamilton Harbour was obtained for the first time. The significant peaks of 12.0, 5.22, 2.2 and 1.1 hours which are the

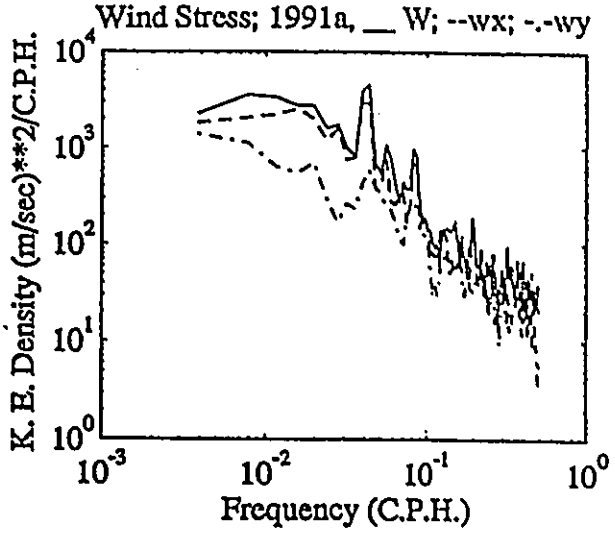

Fig. 9.14 Wind stress spectra in the meteorological buoy in Hamilton Harbour during the 1991 field study season.
(Source of data: NWRI)

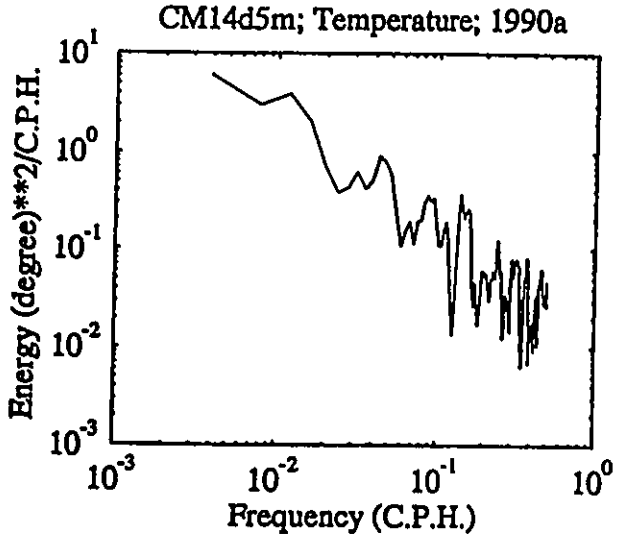

Fig. 9.15 Temperature spectra in current meter station CM14d5m in Hamilton Harbour during the 1991 field study season.
(Source of data: NWRI)

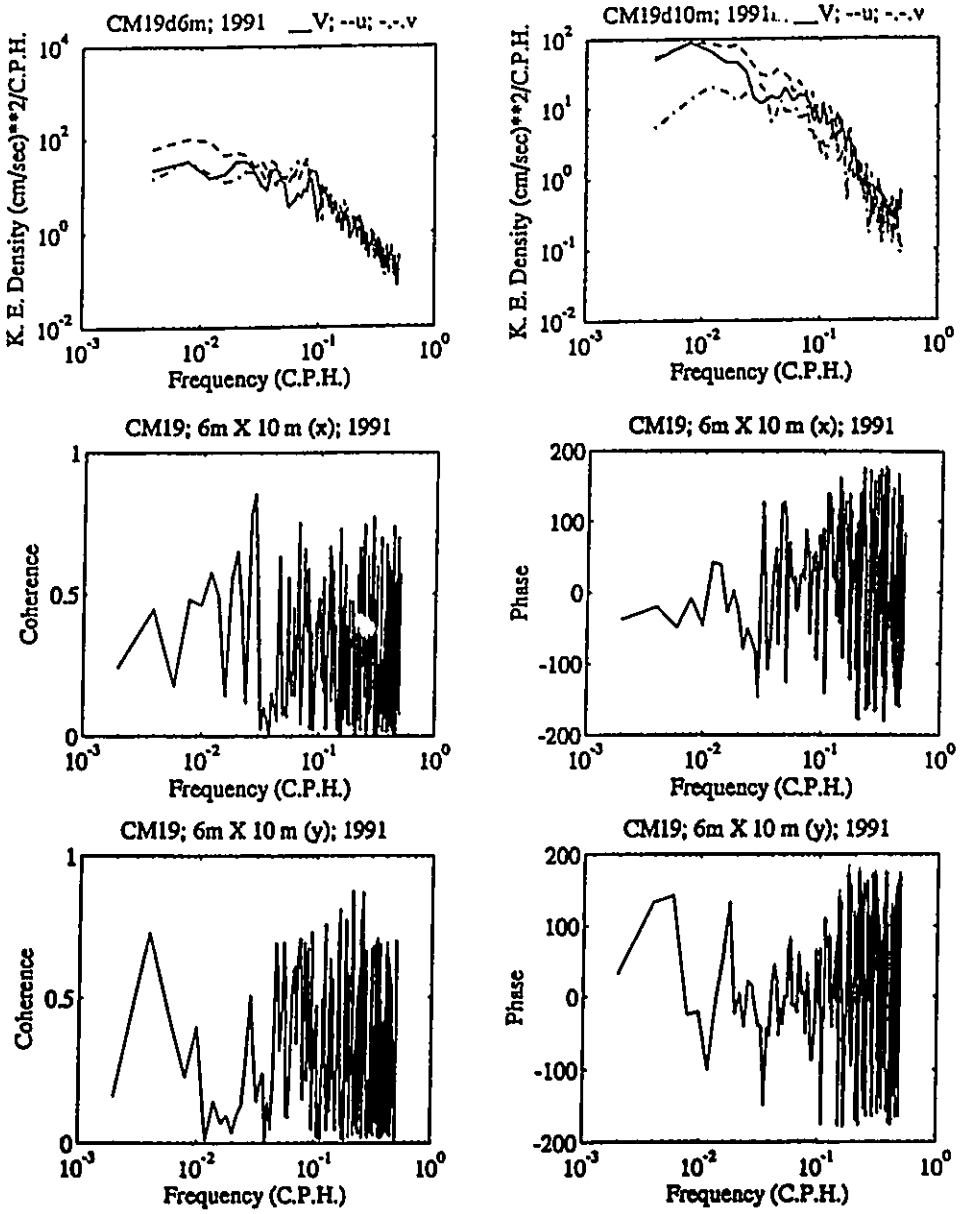

Fig. 9.16 Total, x and y component spectra and coherence and phase for the surface (6m) and middle layer (10m) currents measured at mooring current meter CM19 in Hamilton Harbour during the summer of 1991.
(Source of data: NWRI)

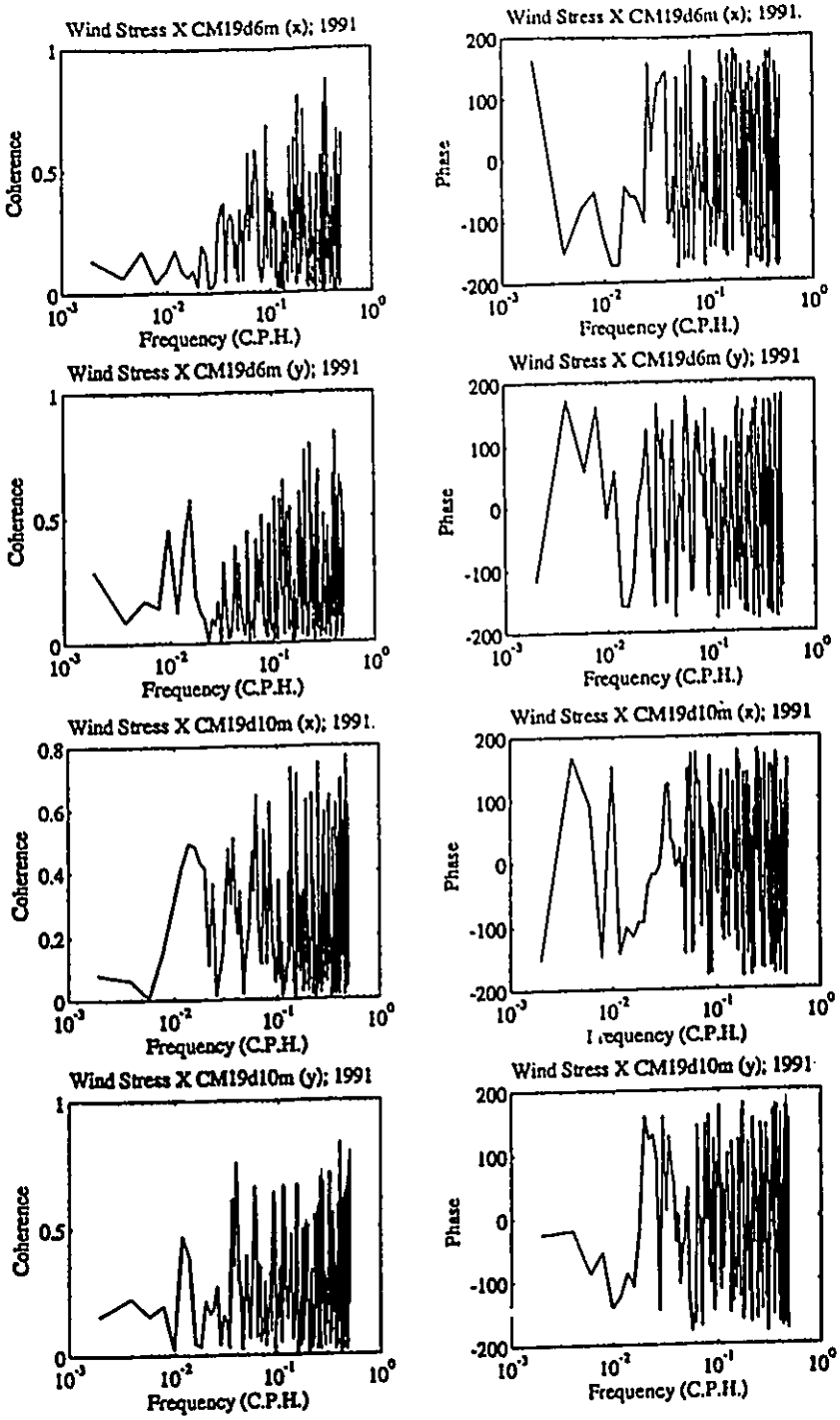

Fig. 9.17 Coherence and phase between wind stress and the surface (6m) and bottom (10m) currents measured in the mooring current meter CM19 in Hamilton Harbour during the summer of 1990.
(Source of data: NWRI)

astronomical tide and seiche of Lake Ontario were found in the water elevation spectra at all three stations in the harbour, reflecting the effect of Lake Ontario through the Burlington Canal. In other words, the water elevation change in Hamilton Harbour is controlled by the change of elevation in Lake Ontario. The uni-nodal seiche with a period of 22 minutes and an amplitude of 1.0 mm along with a period of 11 minutes were evident from the spectra of 2 min elevation data. Finally, the spectra of current meter data are analyzed.

CHAPTER 10

MODEL VERIFICATIONS WITH FIELD DATA

Model verification using field data is a very important aspect in model development and application. Model parameters can be determined from the verification. Although much data have been obtained in Hamilton Harbour, there is no model to utilize these data for verification purposes. In recent years, many projects in the Harbour could make use of hydrodynamic and pollutant transport model, so that the currents and mass transport can be simulated and applied for engineering problems. Before applying the model to the Harbour, the verification with field data is necessary. In the Hamilton Harbour restoration program, an understanding of current movements in the Harbour is essential. As discussed in Chapter 2, there were two previous studies conducted on modelling the current movements in the Harbour (MOE, 1974; James & Eid, 1978). The coarse grid used in their models was unable to describe in detail the shoreline and the Harbour's bathymetry, and, the verifications were insufficient. Therefore, a high resolution model must be employed, and adequate model verifications are required. The high resolution model with a 100 m grid is designed for Hamilton Harbour in this study, as shown in Fig. 10.1. The system is rotated counter-clockwise 23.8 degrees from the north, to better represent the eastern and northeastern shorelines. This grid system is sufficient to represent the shorelines and to verify the model.

In this chapter, three methods will be used for the model verifications using current

meter, drogue trajectory, and water level data. The first method is to compare model results with field data in the time domain (point-by-point comparison). A circulation model is judged to be successful if it yields simulations of flow at the points where observations were collected that closely resemble the time series of the observation. However, a quantitative verification of the model with mooring current data is particularly difficult since a meaningful comparison of observed and computed vector quantities must involve both direction and magnitude. The performance of comparison depends on the location of station and mooring depth, because the current meter is sometimes located in a region of flow reversal, while in other cases the meter is located in a region of unidirectional current. The second method is to compare simulated trajectories with the field measurements (spatial comparison). This method is easily visualized and statistically evaluated. The last method focus on the spectral and long-term features of current and level, i.e., compare the spectra based on the simulation results with the spectra from the field data (spectral comparison). There are very few efforts using the last method in the Great Lakes so far due to the lack of field data and extensive simulations.

10.1 VERIFICATION WITH CURRENT METER DATA

Current data from mooring current meters were collected during the 1990 & 1991 field seasons in Hamilton Harbour. In this section, three scenarios - HH910717, HH911002 and HH910830 in the 1991 field season are simulated. The simulated currents are compared with the measured data at five mooring meters - #16d5m, #17d5m, #18d5m, #19d6m and #19d10m (see Fig. 9.4). The comparison will be made by the point-by-point method, and three statistical criteria will be used to evaluate the comparisons.

The first scenario HH910717, see Fig. 10.2, is a three-day west wind event, from 16:00 July 16 to 14:00 July 19, 1991. The wind directions were between 210 to 310 degrees, and the maximum wind speed was 9.3 m/s on July 17. A comprehensive water quality measurement was undertaken at 25 stations, among them 3 stations outside of the Ship Canal in Lake Ontario, as shown in Fig. 10.3(a). The temperature profiles were obtained in these stations, from which an initial temperature field for the 3D stratified model can be interpolated. Figs. 10.3(b), (c), (d) and (e) show four typical temperature profiles at station #905, #907, #909 and #914 on July 17, 1991. Each profile is used to present the area identified by the range of numbers shown in the box in each plot. The temperatures were quite uniform within 5 m depth and below 20 m, a large gradient existed between 5 m to 15 m, where the temperature difference was about 12^0 (1.2^0 / m). These are the typical temperature profiles in the Harbour during the summer seasons. The horizontal temperature distributions, at two layers, in σ coordinates for the 3D stratified model, are presented in Fig. 10.4. As discussed in Chapters 6 and 9, such a thermal structure would have a great effect on the current structure, and it seems that a stratified three-dimensional model is essential for a good simulation.

The three-dimensional model VHI3D was first applied. The λ value in the vertical eddy viscosity distribution was tested and chosen as 0.05. Figs. 10.5 and 10.6 present the simulated current velocity components (U = west-east component and V = south-north component), along with the measured data at #16d5m, #17d5m, #19d6m and #19d10m, respectively. The simulations are in agreement with the field data at most stations. However, many large peaks are found in the measured data which are not found in the model simulations. Such peaks are not induced by the wind variation, such as the large peak around Julian hour 4770 in #17d5m. The best simulation is achieved for #16d5m. The stratified multi-layered three-dimensional

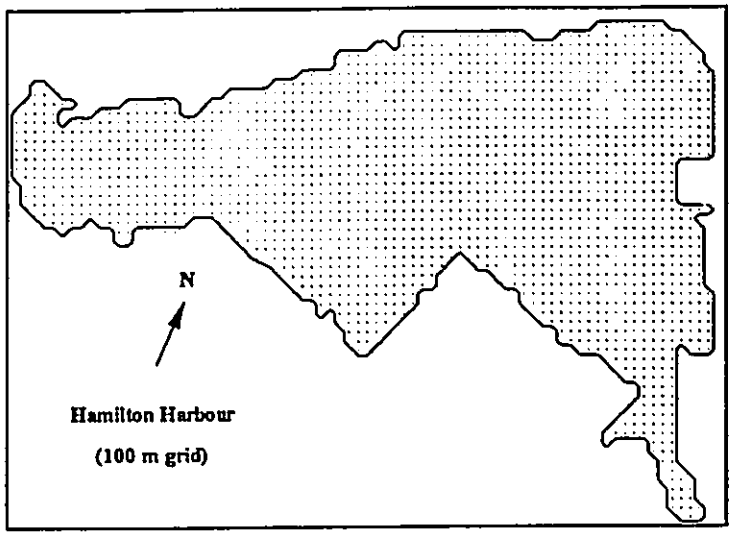

Fig 10.1 A high resolution (100 m grid) finite difference model for Hamilton Harbour. The grid is rotated 23.8 degree anticlockwise from the North to better represent the shorelines.

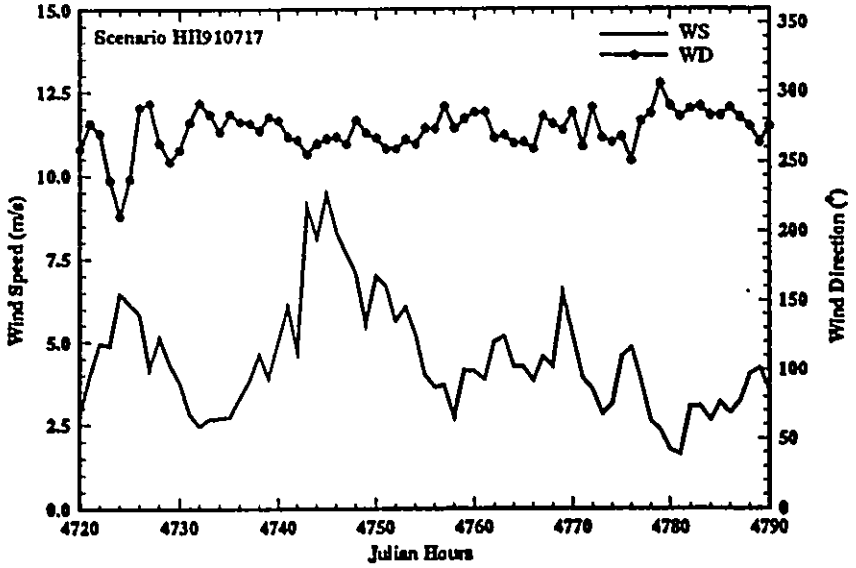

Fig. 10.2 Wind speed and direction of scenario HH910717 (16:00 16 - 16:00 19 July, 1991) in Hamilton Harbour.
(Source of data: NWRI)

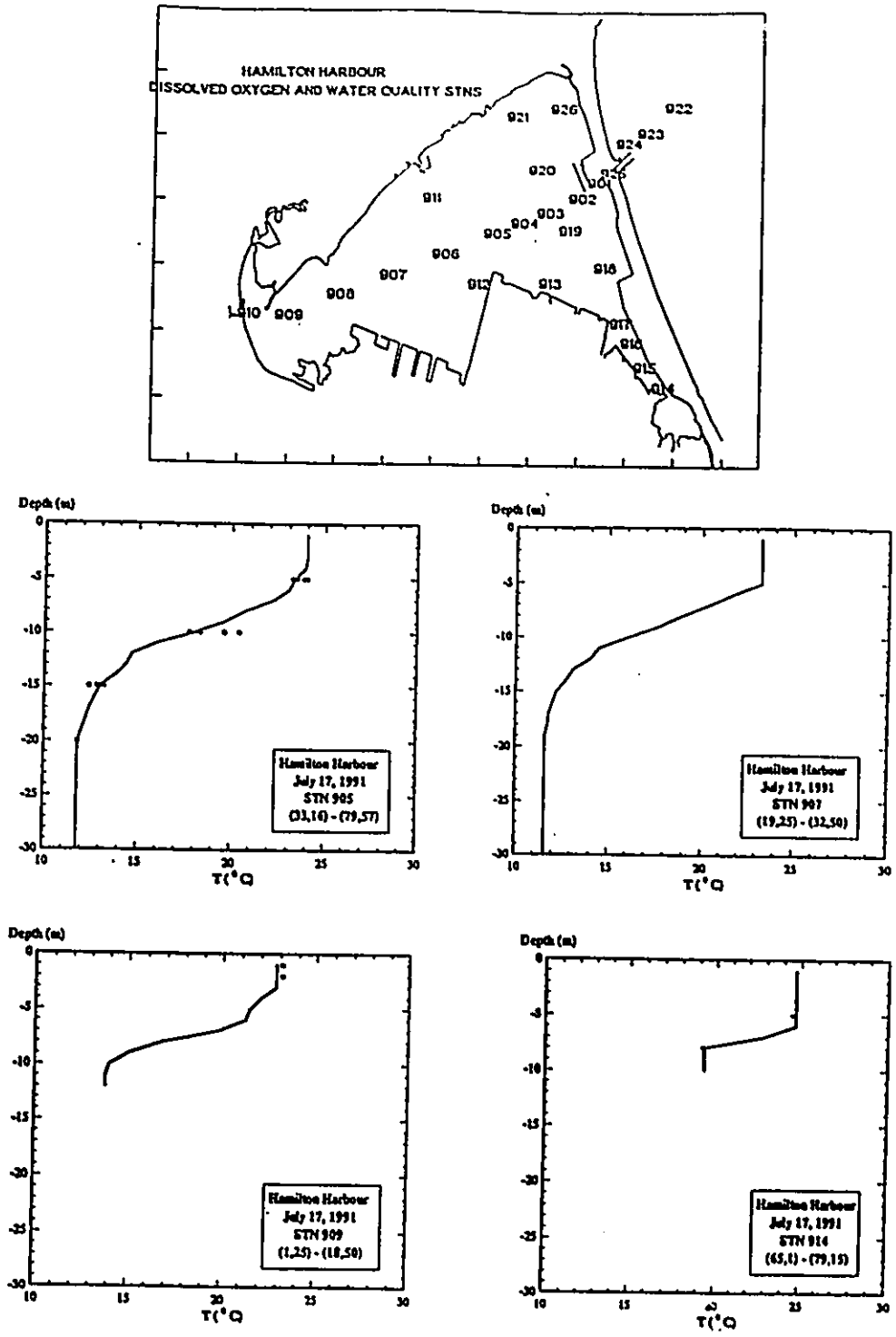

Fig. 10.3 Top: Temperature measurement stations during HH910717 in Hamilton Harbour. Four typical temperature vertical profiles at station #905, 907, 909 and 914. Each profile is used to represent the area identified by the range shown in the box in each plot. The dotted symbols are data from the neighbouring stations in each area.
(Source of data: NWRI)

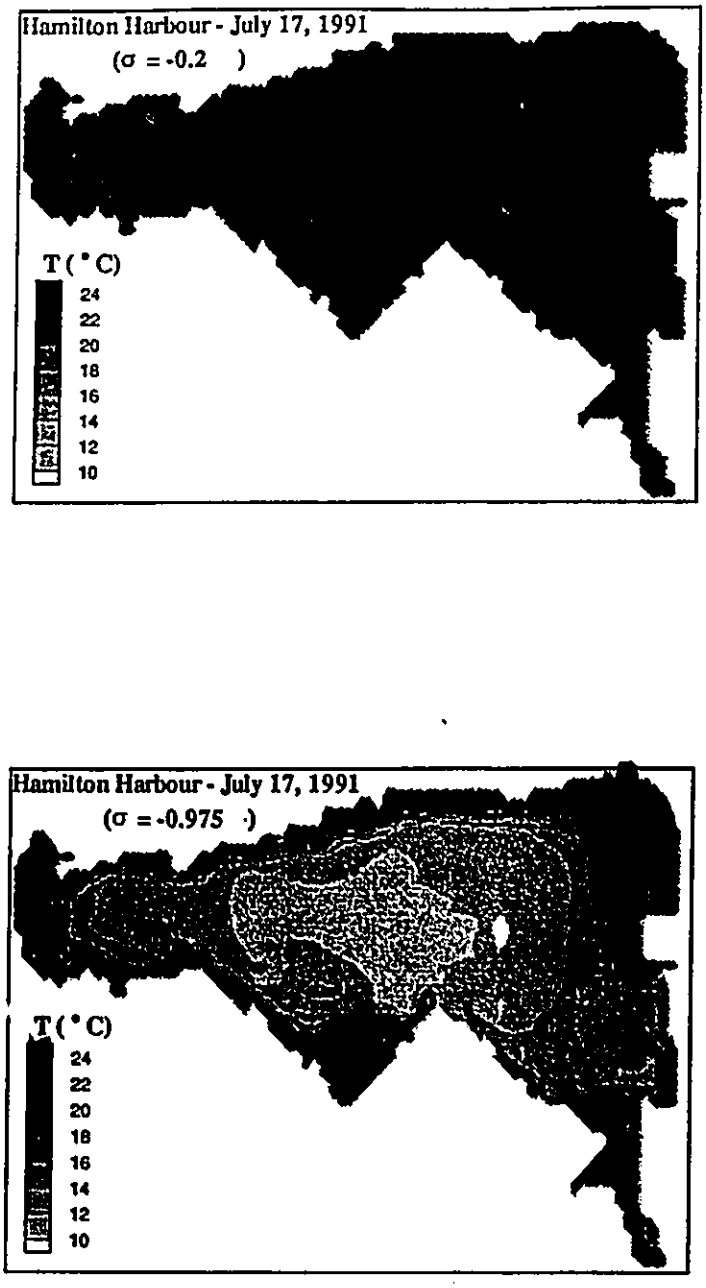

Fig. 10.4 Horizontal temperature distribution at upper layer $\sigma = -0.2$ and lower layer $\sigma = -0.975$, which are derived from the measured temperature data during HH910717, Hamilton Harbour.
(Source of data: NWRI)

circulation model was then applied. The simulations are presented in Figs. 10.7 and 10.8, together with the measurements. Compared with Figs. 10.5 and 10.6, the simulations did not improve significantly.

The magnitude of the vertical eddy viscosity has a significant effect on the simulated velocity profile. The mooring depth during the field season was 5 m or 6 m below the water surface. This depth is usually below the surface drift flow layer, where the current mainly follows the wind, and is located in a transient regime where the current is very weak. Fig. 10.9 shows the effect of the magnitude of the vertical eddy viscosity and mooring depth on the simulations at the mooring meter #16d5m.

The scenario HH911002 was a one-day (Oct. 2, 1991) process with a moderate west wind (below 5 m/s), see Fig. 10.10(a). The temperature data from the mooring meters revealed that the harbour can be considered as isothermal during this period. Therefore, the VHI3D model is suitable for this scenario. Figs. 10.11 and 10.12 present the computed and measured current components at #16d5m, #17d5m, #18d5m and #19d6m, respectively. At #16d5m, the current was opposite to the wind direction, indicating that the mooring current meter (at 5 m depth) was in the return flow regime (notice that the water depth at this location is 8.0 m). A 10 cm/s strong current towards the south was observed around 6620 (Julian hour), which aligns with the eastern shoreline. Such a current feature is well simulated by the numerical model. The currents at #17d5m (water depth of 7.0 m) were very weak, only about 1 to 3 cm/s. This is due to the fact that the mooring current meter was close to the bottom. For #18d5m (water depth of 13.5 m), the simulated currents were close to the measured currents, except for the period greater than 6625, where a high current of more than 10 cm/s was observed in the field measurement. The strong current did not follow a strong wind, which may be induced by the large change of the thermal

stratification. At #19d6m (water depth of 23.0 m), both velocity components U and V are well simulated by the model.

The scenario HH910830 was a strong north-east wind process, as shown in Fig. 10.10(b). The wind speeds were about 3 to 7.5 m/s. The VHI3D model was applied. Figs. 10.13 and 10.14 present the computed and measured current components at #17d5m, #18d5m, #19d6m and #19d10m, respectively. The simulations were not satisfactory. The large variations observed from the field data were not well simulated by the numerical model.

The following statistical criterion (Schwab et al., 1989) can be used to evaluate the above comparisons: (1) α_1 representing the ratio of the energy in the time-variable part of the current to the total energy in the current for observed current

$$\alpha_1 = \frac{\sum\left[(u_0-\overline{u_0})^2+(v_0-\overline{v_0})^2\right]}{\sum(u_0^2+v_0^2)} \tag{10.1}$$

where (u_0, v_0) are the eastward and northward components of the observed currents; (2) α_2 comparing the differences between observed and computed values for the total flows

$$\alpha_2 = \frac{\sum\left[(u_0-u_c)^2+(v_0-v_c)^2\right]}{\sum(u_0^2+v_0^2)} \tag{10.2}$$

and (3) α_3, the ratio of the root mean square value of the computed currents to the root mean square value of the observed currents, i.e.

$$\alpha_3 = \frac{\sqrt{\sum(u_c\,u_c+v_c\,v_c)}}{\sqrt{\sum(u_0\,u_0+v_0\,v_0)}} \tag{10.3}$$

The statistical comparisons between computed and measured currents are listed in Table 10.1. It can be seen that almost all the energy is in the time-variable current because α_1 are over 0.95 at

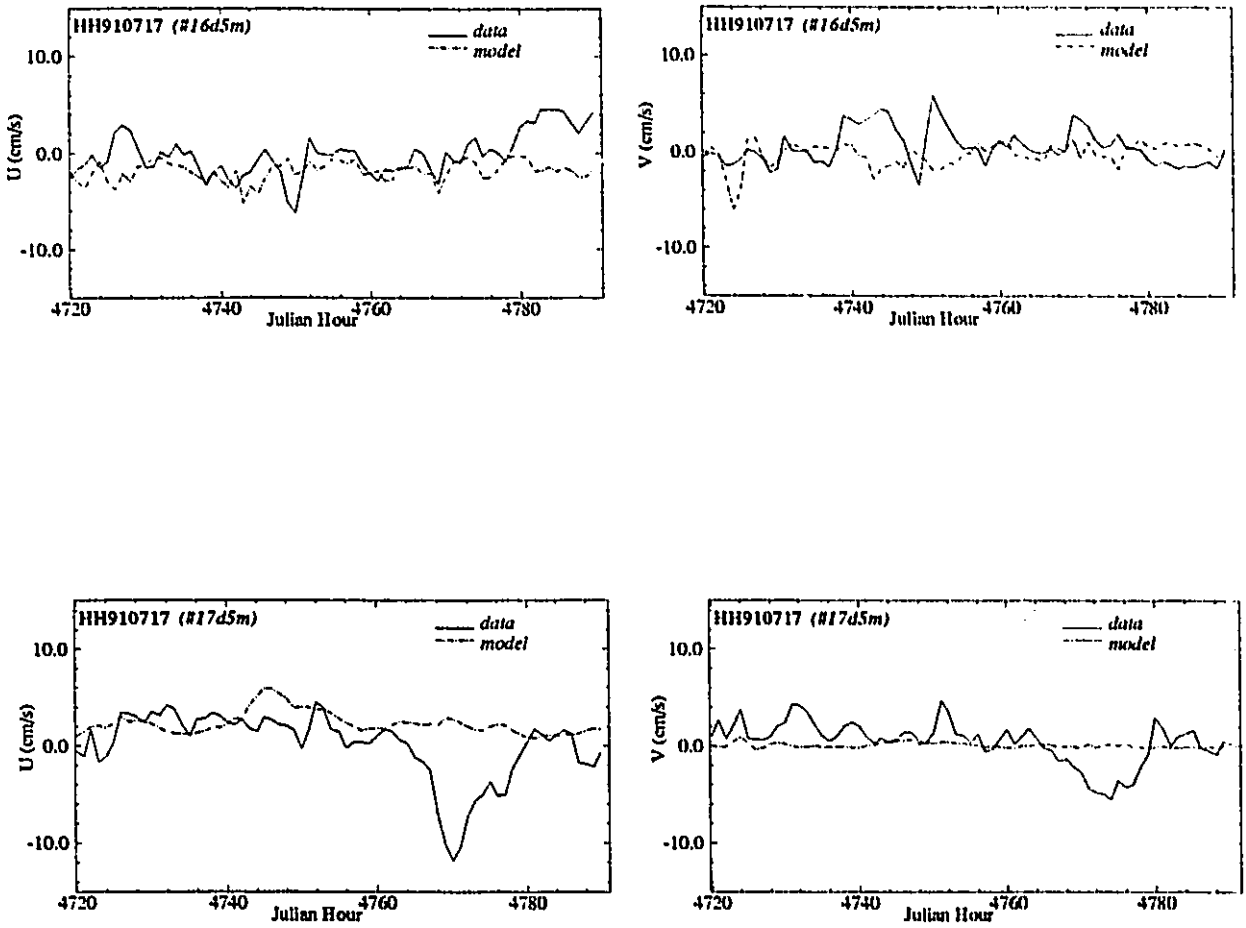

Fig. 10.5 Measured (solid line) and simulated (dashed-dot for the VHI3D model) current components (U, in the west-east direction; V, in the south-north direction) at the mooring stations #16d5m and #17d5m, scenario HH910717, Hamilton Harbour. (Source of data: NWRI)

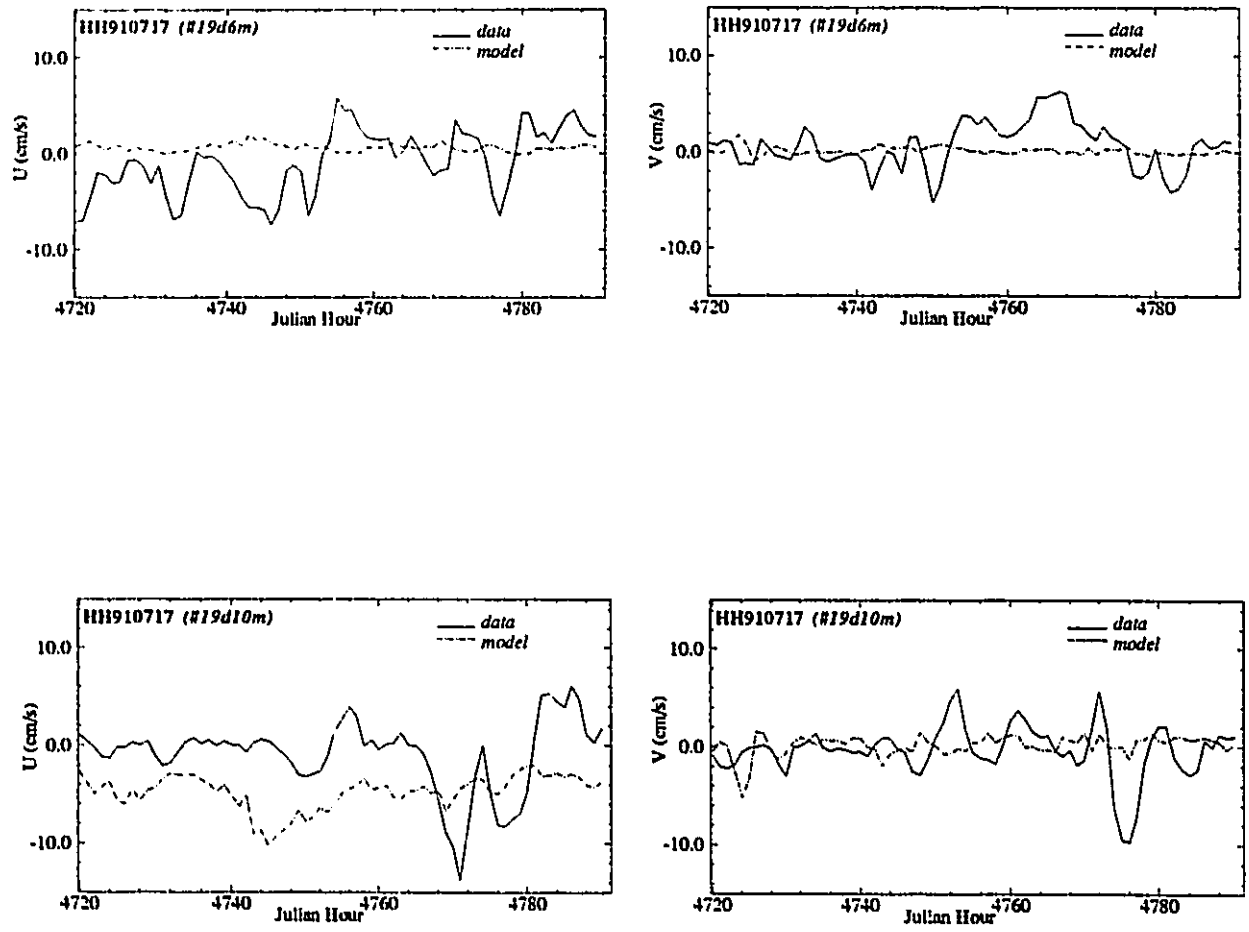

Fig. 10.6 Measured (solid line) and simulated (dashed-dot for the VHI3D model) current components (U, in the west-east direction; V, in the south-north direction) at the mooring stations #19d6m and #19d10m, scenario HH910717, Hamilton Harbour. (Source of data: NWRI)

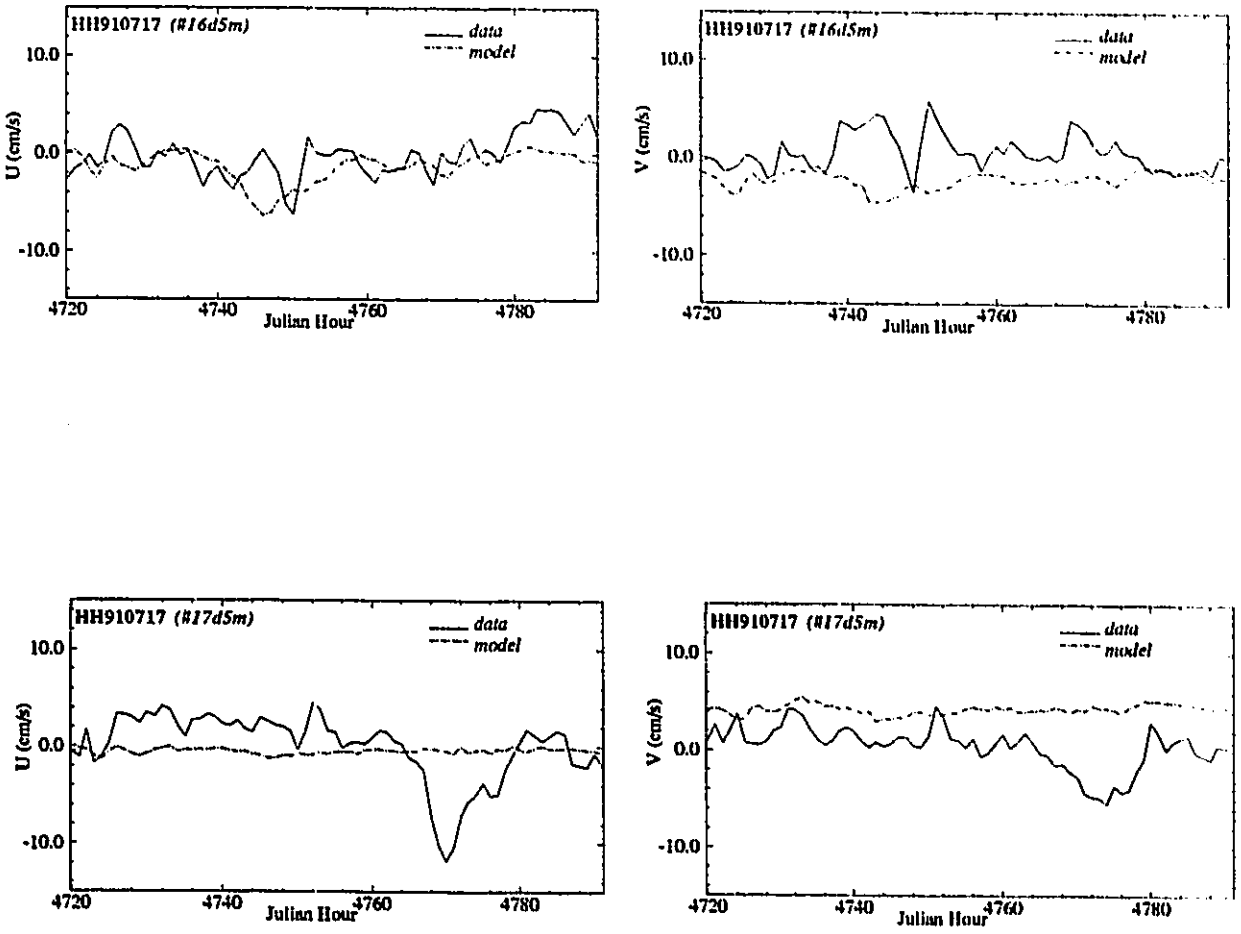

Fig. 10.7 Measured (solid line) and simulated (dashed-dot for 3D model) current components (U, in the west-east direction; V, in the south-north direction) at the mooring stations #16d5m and #17d5m, scenario HH910717, Hamilton Harbour.
(Source of data: NWRI)

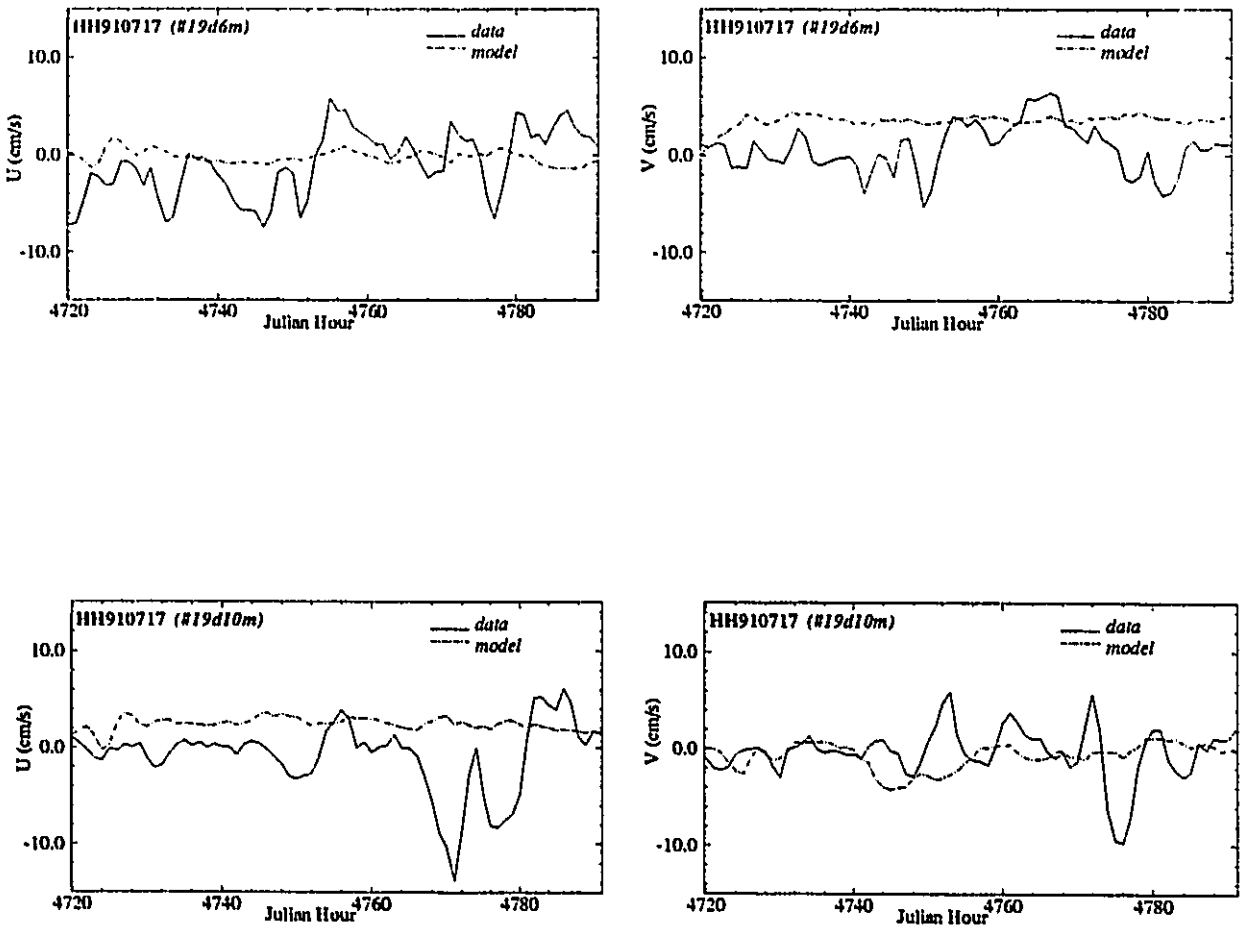

Fig. 10.8 Measured (solid line) and simulated (dashed-dot for 3D model) current components (U, in the west-east direction; V, in the south-north direction) at the mooring stations #19d6m and #19d10m scenario HH910717, Hamilton Harbour.
(Source of data: NWRI)

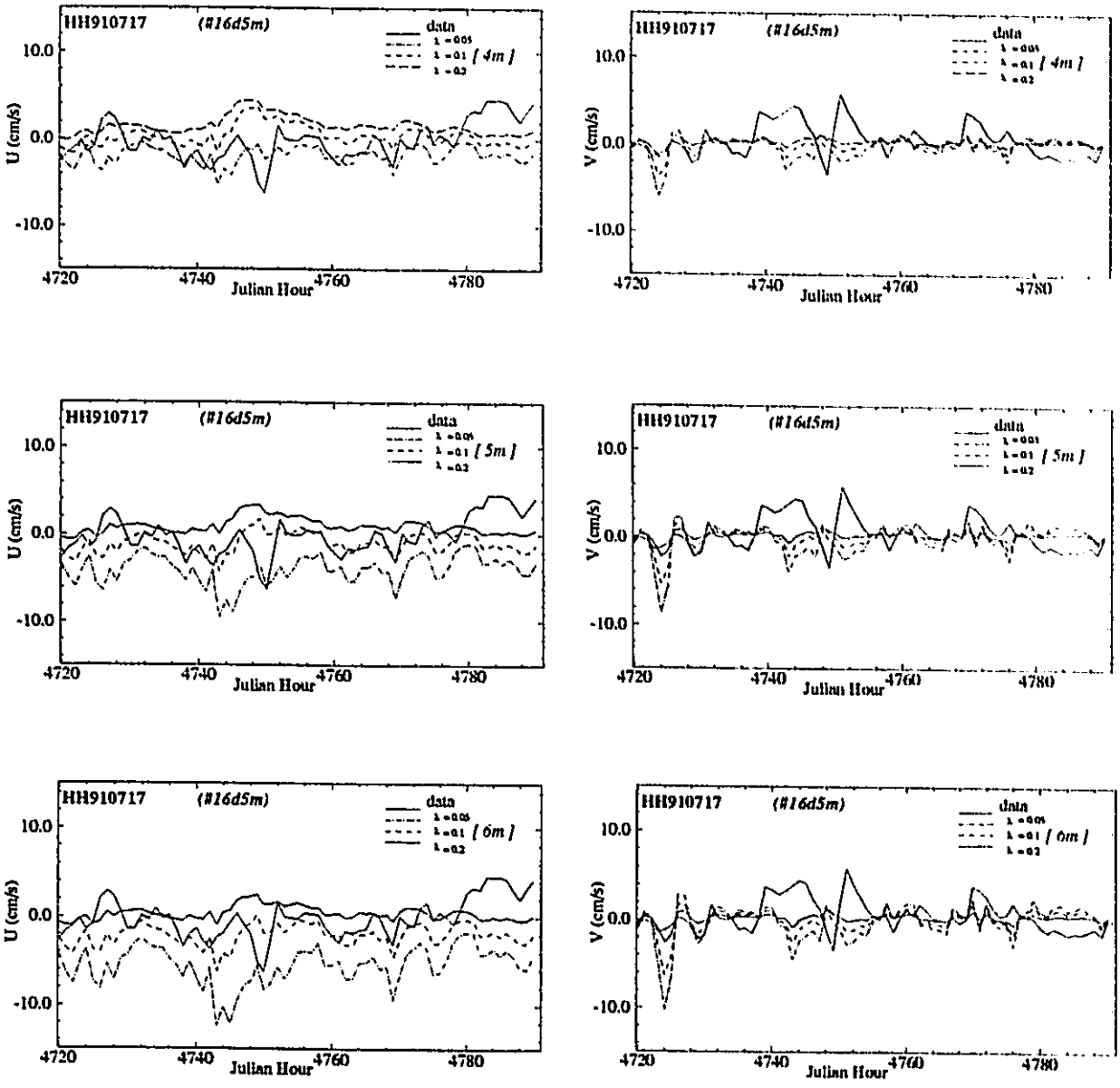

Fig. 10.9 Sensitivity of coefficient in vertical viscosity distribution and mooring depth of current meter - measured (solid line) and simulated (at 4m, 5m and 6m below surface from VHI3D model) current components at the mooring station #16d5m, scenario HH910717, Hamilton Harbour.
(Source of data: NWRI)

all stations. The typical value of α_2 is about 1.2, and α_3 0.3 to 1.2. Overall, the model verification with the mooring current meter data is not satisfactory. A large variation in the field data which did not follow the wind is not well simulated in the numerical model. Good simulations are only made in some mooring locations. The wind field over Hamilton Harbour is taken as a uniform field in the model. This may be not justified and contribute to the variation in the current meter data. Another reason might be the insufficiency of temperature data and the assumed profile for the vertical viscosity coefficient in the numerical model. Each model has its own parameters, though most parameters such as the wind drag coefficient, and the horizontal diffusivity coefficient were taken as constants. The simulations are mainly affected by the vertical viscosity coefficient. However, this coefficient has taken different forms in the different models. For example, a constant was used in the Q3D model, a parabolic distribution was used in the VHI3D model and a normal parabolic one in the 3D model for an isothermal lake, and a modified parabolic one for stratified lakes. Therefore, the coefficients can not be compared in certain cases, especially when one tries identify the differences at one depth of a single current mooring station.

Table 10.1 Comparison of observed and calculated currents in Hamilton Harbour

	Ratio	#16d5m	#17d5m	#18d5m	#19d6m	#19d10m
Data	α_1	0.95	0.99	0.97	0.95	0.97
VHI3D	α_2	1.21	1.29	0.94	1.13	1.89
	α_3	1.02	0.64	0.29	0.42	1.20
Data	α_1	0.96	0.99	0.97	0.93	0.96
3D	α_2	2.22	1.21	1.44	2.81	1.65
	α_3	1.07	0.54	0.84	1.53	0.64

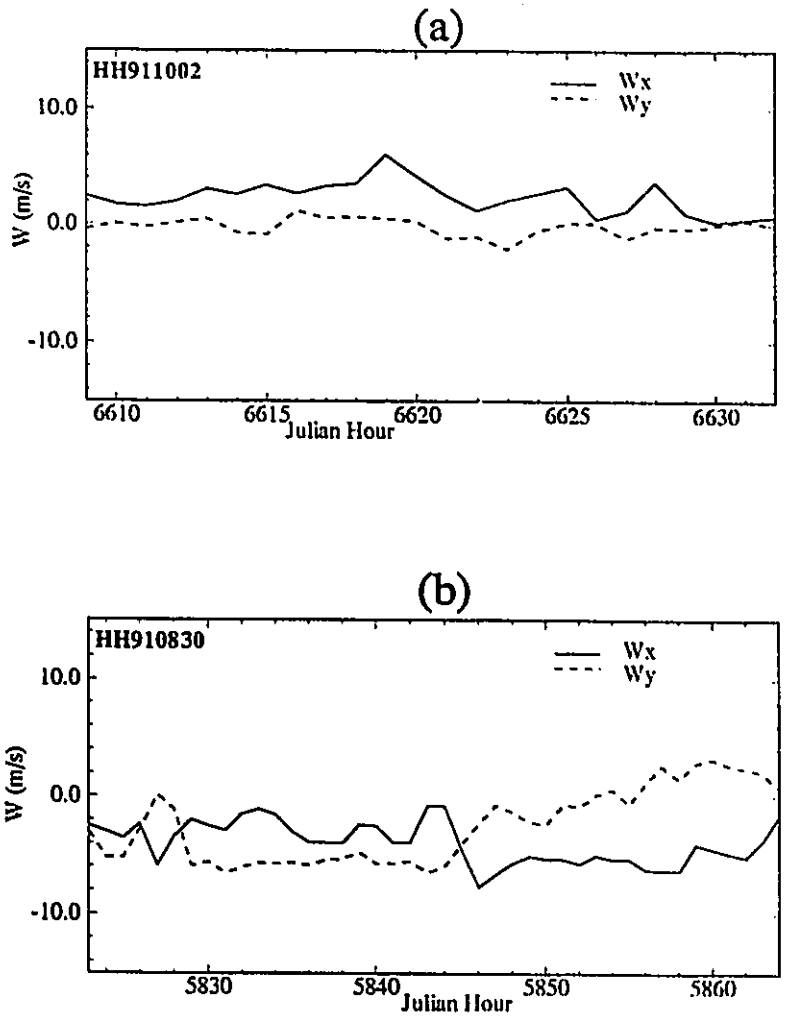

Fig. 10.10 Time series of wind velocity components in scenario (a) HH911002 (11:00, Oct. 2 - 11:00, Oct. 3, 1991), (b) HH910830 (15:00 Aug. 30 - 08:00 Aug. 31, 1991), in Hamilton Harbour.
(Source of data: NWRI)

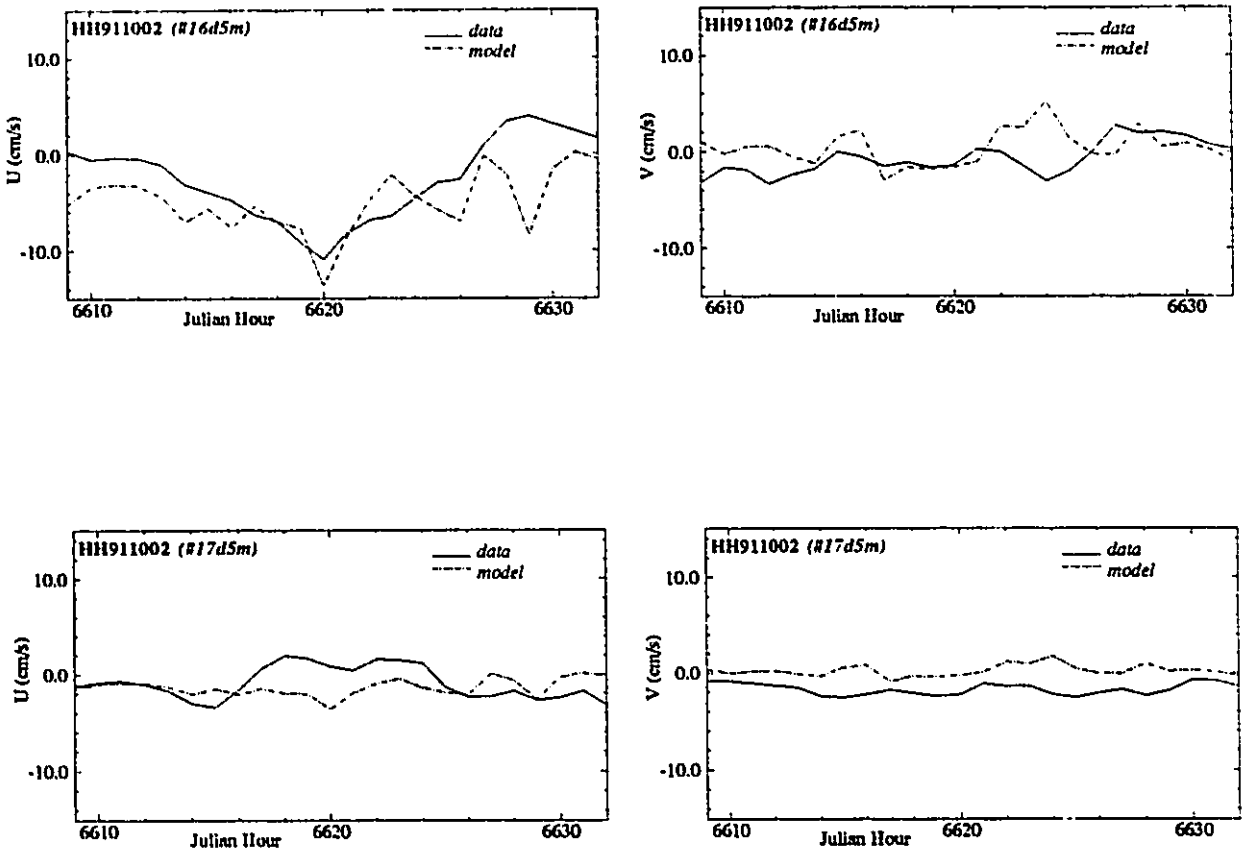

Fig. 10.11 Measured (solid line) and simulated (dashed-dot for the VHI3D model) current components (U, in the west-east direction; V, in the south-north direction) at the mooring stations #16d5m and #17d5m, scenario HH911002, Hamilton Harbour. (Source of data: NWRI)

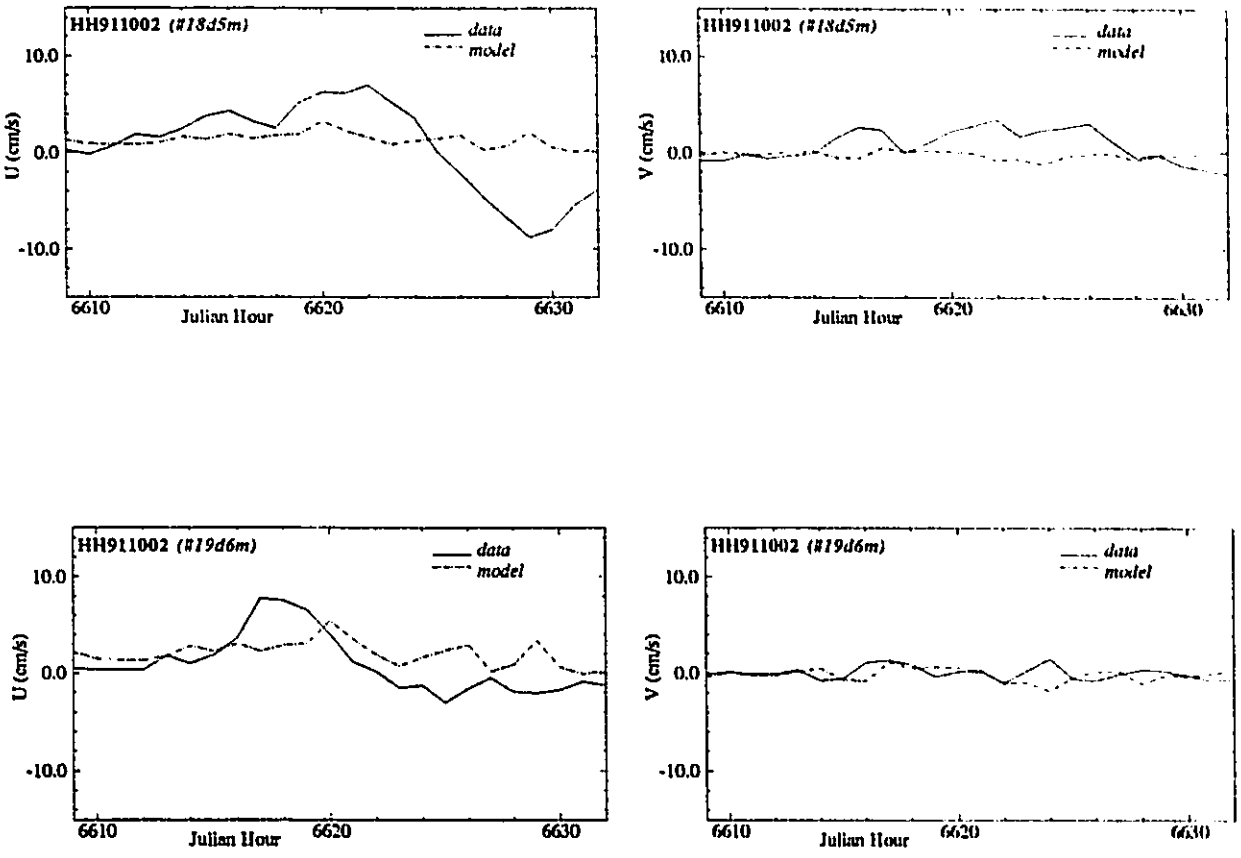

Fig. 10.12 Measured (solid line) and simulated (dashed-dot for the VHI3D model) current components (U, in the west-east direction; V, in the south-north direction) at the mooring stations #18d5m and #19d6m, scenario HH911002, Hamilton Harbour. (Source of data: NWRI)

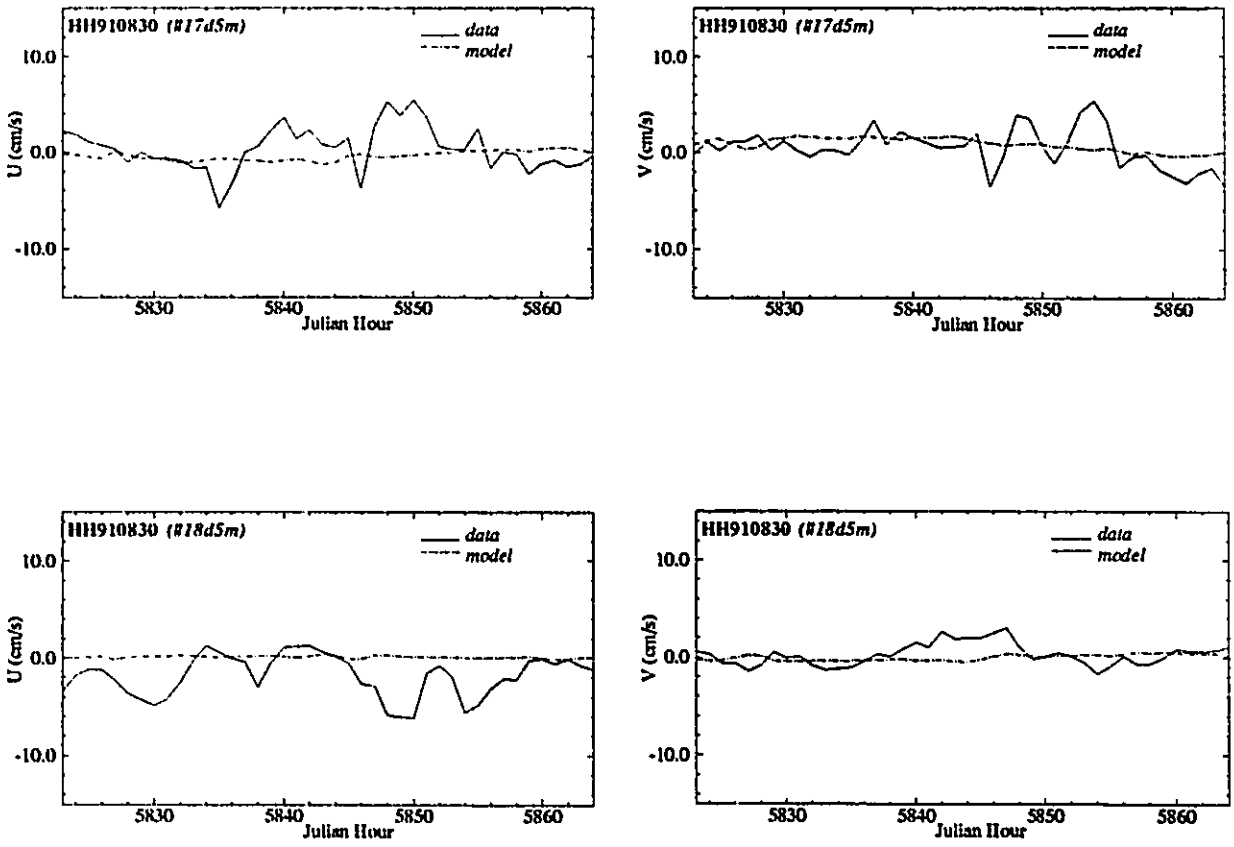

Fig. 10.13 Measured (solid line) and simulated (dashed-dot for the VHI3D model) current components (U, in the west-east direction; V, in the south-north direction) at the mooring stations #17d5m and #18d5m, scenario HH910830, Hamilton Harbour. (Source of data: NWRI)

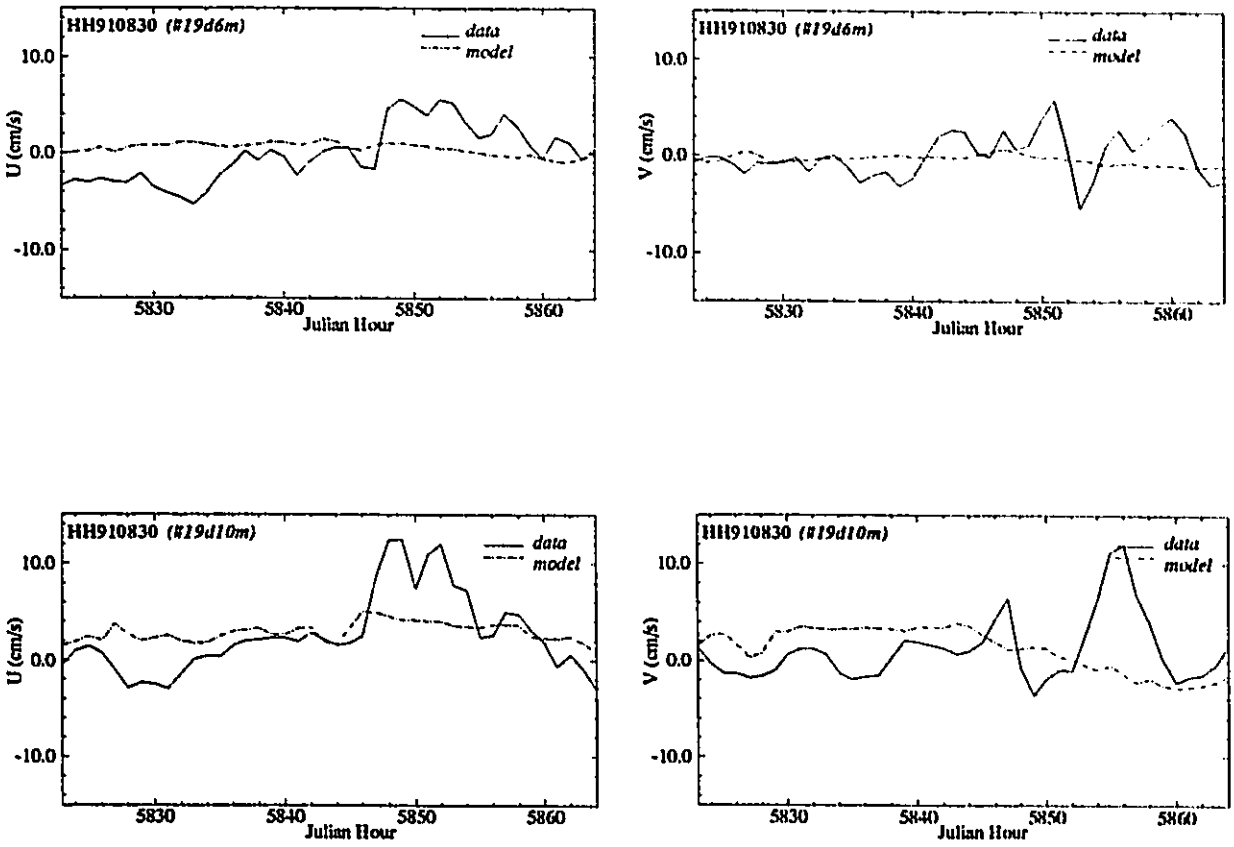

Fig. 10.14 Measured (solid line) and simulated (dashed-dot for the VHI3D model) current components (U, in the west-east direction; V, in the south-north direction) at the mooring stations #19d6m and #19d10 m, scenario HH910830, Hamilton Harbour. (Source of data: NWRI)

10.2 VERIFICATION WITH DROGUE MEASUREMENT DATA

In order to understand current patterns in lakes, many drogue experiments have been undertaken in the Great Lakes, such as in Lake Erie (Schwab et al., 1989), and Lake Ontario (Tsanis et al., 1990). The drogue experimental data provides an excellent opportunity to verify the three-dimensional circulation model, because the comparison is easily visualized and statistically analyzed. The three-dimensional circulation model is essential to simulate the drogue movement at various depths at different locations.

Table 10.2 Scenarios of drogue measurements during the 1990 field study in Hamilton Harbour

NO.	Scenario (*)	Period	Duration (*Hours*)	Wind (**) *WS (m/s)*	*WD*	Drogues
1	TR900620	12:00 - 14:30	2.5	2.2	E	9
2	TR900628	10:30 - 14:00	3.5	3.2	E	9
3	TR900720	11:00 - 14:00	3.0	3.4	W	8
4	TR900815	10:30 - 13:30	3.0	2.8	W	6
5	TR900920	11:30 - 15:00	3.5	2.9	NW	10
6	TR900927	10:30 - 14:30	4.0	1.2	NW	12
7	TR901031	10:30 - 14:30	4.0	1.3	E	12
8	TR901102	10:30 - 12:30	2.0	2.4	SW	9

Note: (*) = the scenario TR900620 refers to the measurement on June 20, 1990
(**) = wind speed and direction listed in this table present the averaged condition during the period of drogue measurement

10.2.1. Comparison of Model Results with Drogue Measurements

The locations for each drogue in the Harbour's grid of the northing and easting in meters, are first converted into the model grid system (rotated 23.8 degree clockwise from North).

For convenience of comparison, the data are interpolated so as to have the same start and end times, and the same time interval (half hour in this study) for all the drogues in each experiment.

The 100 meter grid of Hamilton Harbour is used in the coupled circulation and trajectory prediction model. Hourly wind speed and direction are input to the model. The trajectory model is a second-order model as described in Chapter 6. Because the drogues were deployed at either 2 m or 5 m below the water surface (relatively to the depth of 10 m - 20 m), the drogue movements mainly represented the currents in the upper layer. Each experiment lasted for less than 5 hours, as a result, the change of thermal structure could be ignored, and the VHI3D model is feasible in those cases. The current fields at 2 m and 5 m below the water surface, which were the depths for the drogues, are directly calculated when the VHI3D model is applied. The trajectories for each drogue will be predicted in each time step (a time step of 4 seconds was used in the numerical model), while only recorded at half hour intervals.

The drift velocity v_d is assumed to be the sum of the current velocity v_c (simulated) and an unknown windage, i.e.,

$$v_d = v_c + a\,W \tag{10.4}$$

where W is the wind velocity and a is the windage factor. A least squares procedure is used to determine the optimal value of the windage factor for each drogue.

For statistical comparison purposes, the following ratios were designed (Schwab et al., 1989): γ_1 - the ratio of the variance of the difference between the observed drogue velocities and the computed currents to the variance of the observed drogue velocities; γ_2 - the ratio of the variance of the difference between the observed drogue velocities and the wind velocities multiplied by windage factor to the variance of the observed drogue velocities; γ_3 - the ratio of the variance of the difference between the observed drogue velocities and the combined

computed velocity (current plus windage) to the variance of the observed drogue velocities, i.e.,

$$\gamma_1 = \frac{\sum\left[(u_d - u_c)^2 + (v_d - v_c)^2\right]}{\sum(u_d{}^2 + v_d{}^2)} \tag{10.5}$$

$$\gamma_2 = \frac{\sum\left[(u_d - aW_x)^2 + (v_d - aW_y)^2\right]}{\sum(u_d{}^2 + v_d{}^2)} \tag{10.6}$$

$$\gamma_3 = \frac{\sum\left[(u_d - u_c - aW_x)^2 + (v_d - v_c - aW_y)^2\right]}{\sum(u_d{}^2 + v_d{}^2)} \tag{10.7}$$

Eight scenarios are selected from the experiments during the 1990 field season. The duration, mean wind velocity and direction, and number of drogues in each experiment are listed in the Table 10.2. Figs. 10.15-18 show the observed drogue trajectories (solid line, solid circle) and the predicted trajectories (dashed line, open circle). The start point is that close to the number for each drogue. The statistical comparisons are shown in Tables 10.3 and 10.4, in which the averaged velocities derived from trajectories for both field and model data, windage a, ratio γ_1, γ_2, γ_3 are listed for each drogue in each scenario. No attempt is made to analyze the simulation for all the scenarios. Only two of them are presented in detail.

In the scenario TR900620 (on June 20, 1990), nine drogues were released in the southeastern basin in Hamilton Harbour, see Fig. 10.15. Among them, seven drogues were at 2 m below the surface, and two drogues at 6.5 m. Winds were about 1.2 to 1.9 m/s from 213 to 216 degrees from the north (it was a very weak wind condition). In general, all drogues followed the wind direction and a slight deflection for the drogues at 6.5 m depth. The velocity ranged from 2 to 4 cm/s (see Table 10.3). The computed trajectories are quite close to the observed trajectories

for drogues #1, #4, #5 and the ratio of variance of difference (γ_1) is less than 0.5. For drogue #6, due to the extremely small current in the measurement, the comparison is insensitive. Except for #2 and #6, the ratios of the variance of the difference between the observed drogue velocities and the computed currents to the variance of the observed drogue velocities γ_1 are below 1.38 (below 0.7 for six drogues).

In scenario TR901102 (on Nov. 2, 1990), a 2.4 m/s south-western wind prevailed. Six drogues were released at 2 m and four at 5.0 m. The observed and computed drogue trajectories are presented in Fig. 10.18. Excellent simulations are obtained, and γ_1 values for all drogues are below 0.95.

10.2.2 Numerical Experiments on the Drogue Trajectory Predictions

The particle trajectories are not uniquely defined by the local velocity field, and may be affected by the turbulence and diffusion, as in the case of pollutant dispersion, due to the sub-grid scale processes. The simulated trajectories in the above section can be considered as the central line of a diffusive path or cloud. There are two methods to add the dispersion effect into the model. In the first method, random displacements evaluated by random numbers and horizontal diffusion coefficients are added to the movement computed from the flow field, see Chapter 4. The second method is based on the advection-diffusion model. The conventional advection-diffusion equation can be applied for the movement of the cloud of particles,

$$\frac{\partial P}{\partial t} = -U_p \frac{\partial P}{\partial x} - V_p \frac{\partial P}{\partial y} + K_x \frac{\partial^2 P}{\partial x^2} + K_y \frac{\partial^2 P}{\partial y^2} \tag{10.8}$$

where, P is the "concentration" of particles; U_p and V_p are the velocity components; K_x and K_y are the diffusion coefficients in x and y directions, respectively. Supposing that a 100 unit particle is continuously released at one location, the contours, will present the mostly likely range for the

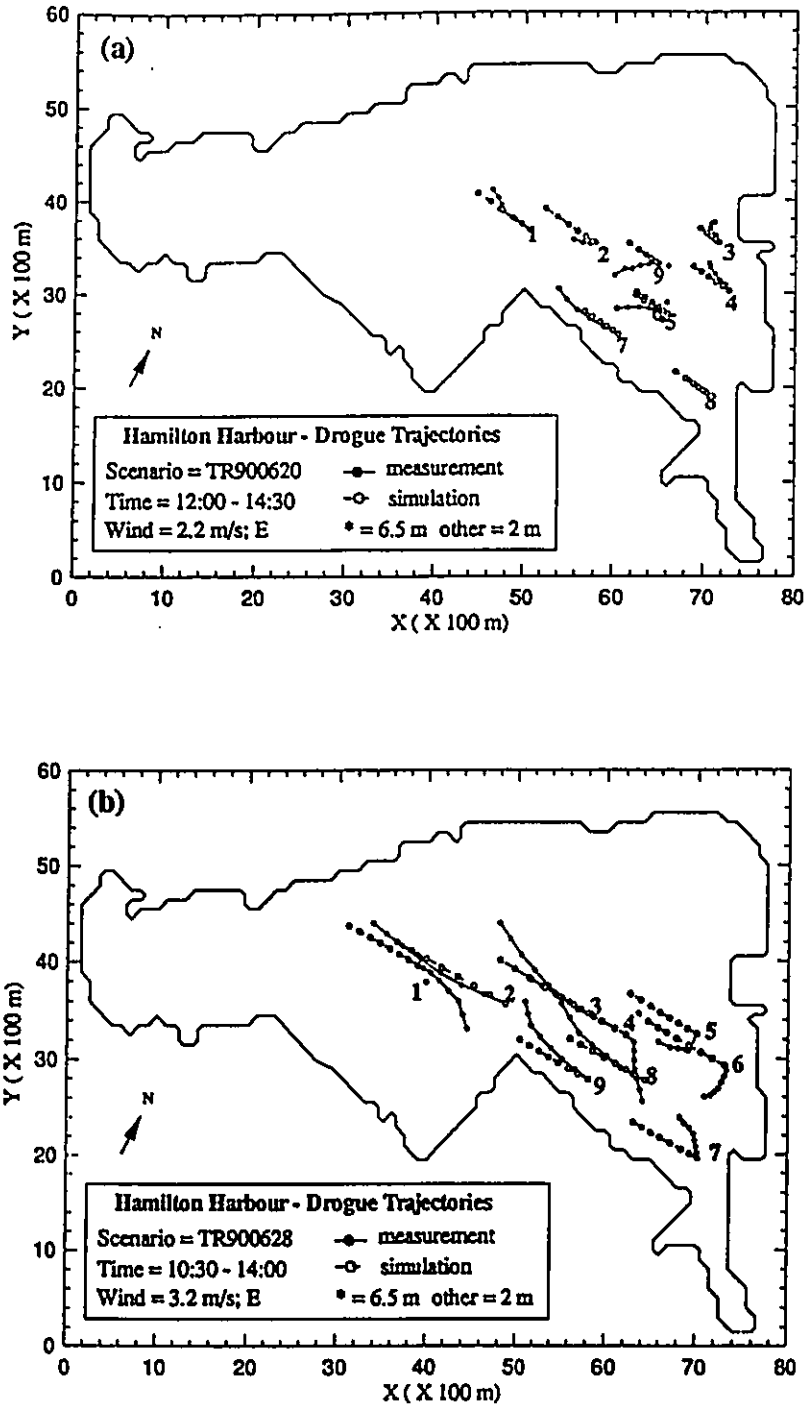

Fig. 10.15 The Measured (solid line with solid circle) and the simulated (dashed line with open circle) drogue trajectories for: (a) HH900620, (b) HH900628, in Hamilton Harbour. (Source of data: Boyce & Chiocchio, 1991)

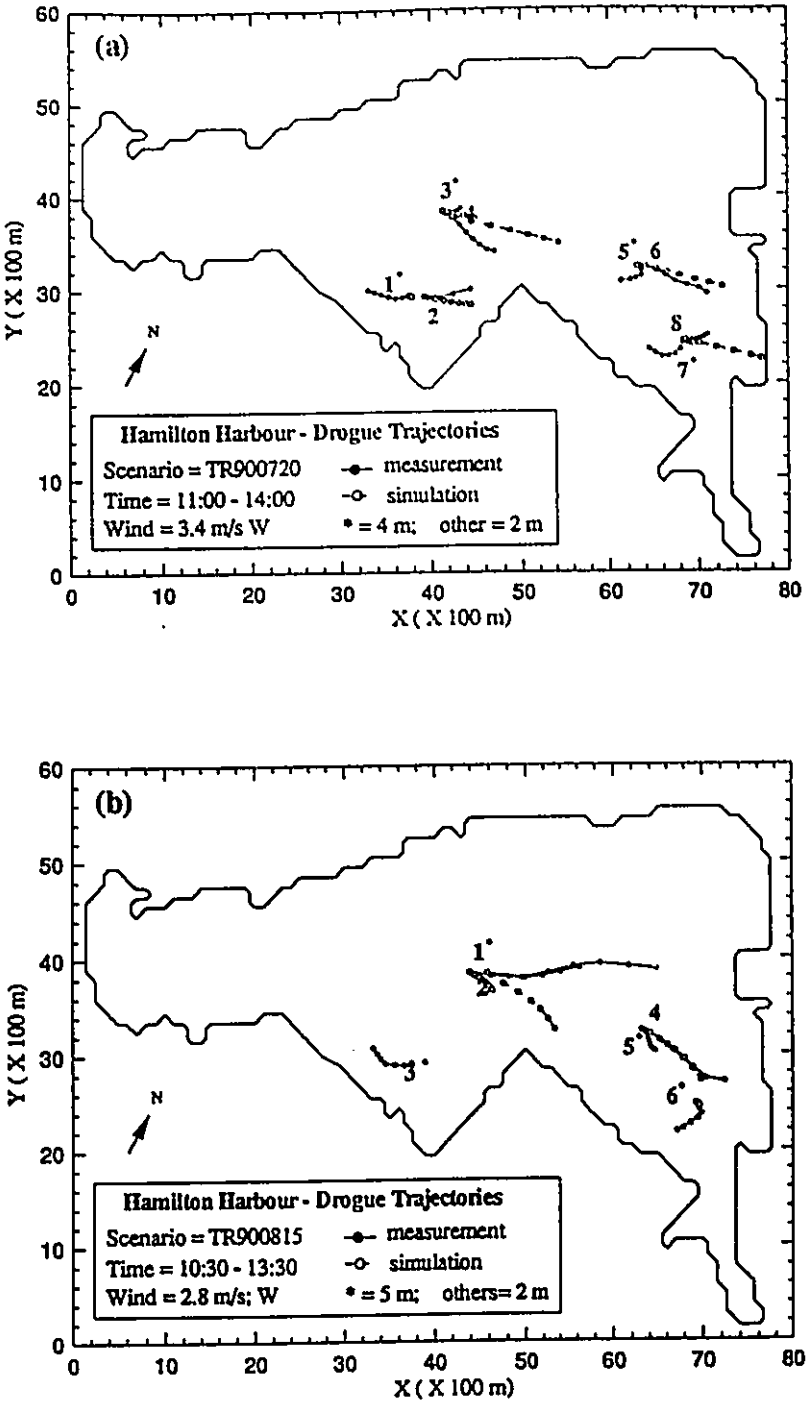

Fig. 10.16 The Measured (solid line with solid circle) and the simulated (dashed line with open circle) drogue trajectories for: (a) HH900720, (b) HH900815, in Hamilton Harbour. (Source of data: Boyce & Chiocchio, 1991)

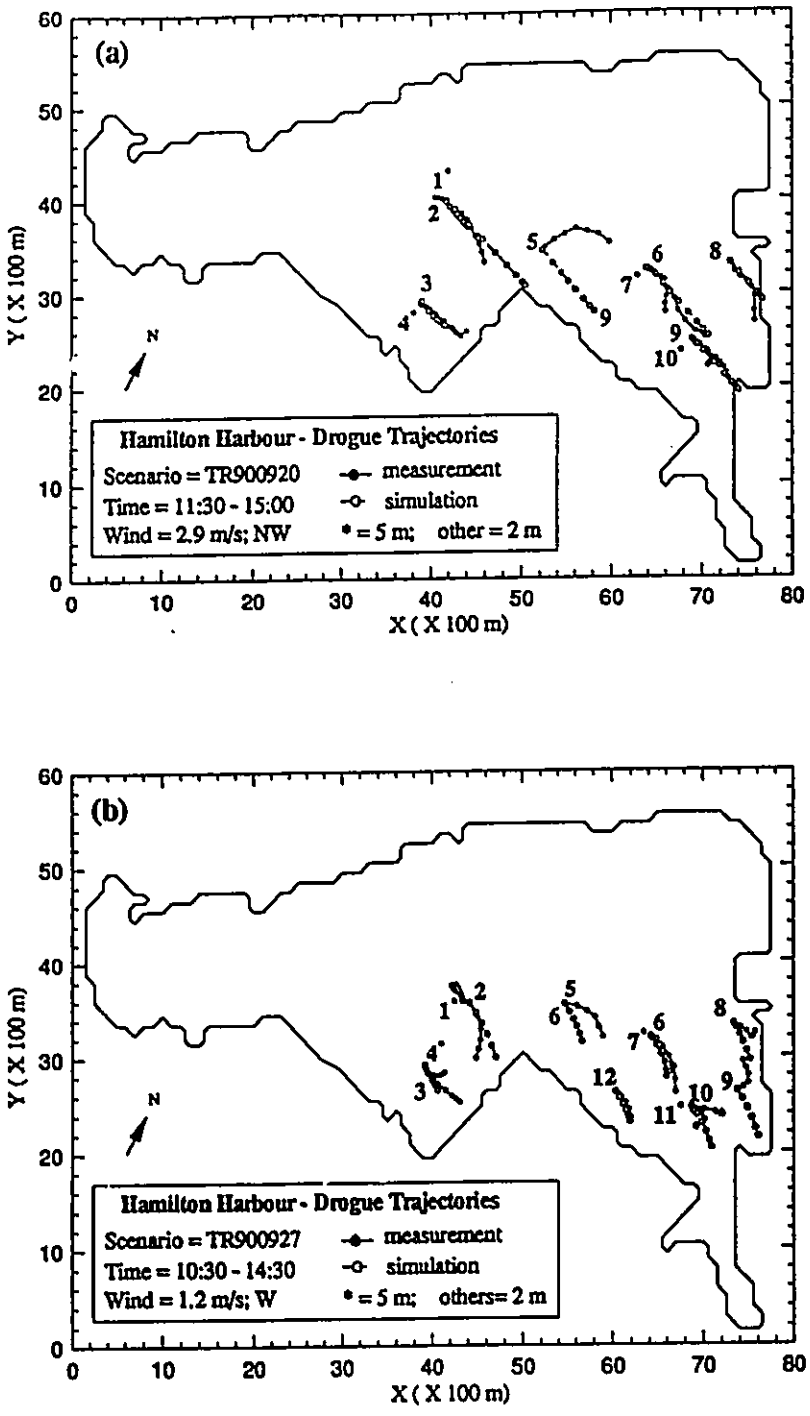

Fig. 10.17 The Measured (solid line with solid circle) and the simulated (dashed line with open circle) drogue trajectories for: (a) HH900920, (b) HH900927, in Hamilton Harbour. (Source of data: Boyce & Chiocchio, 1991)

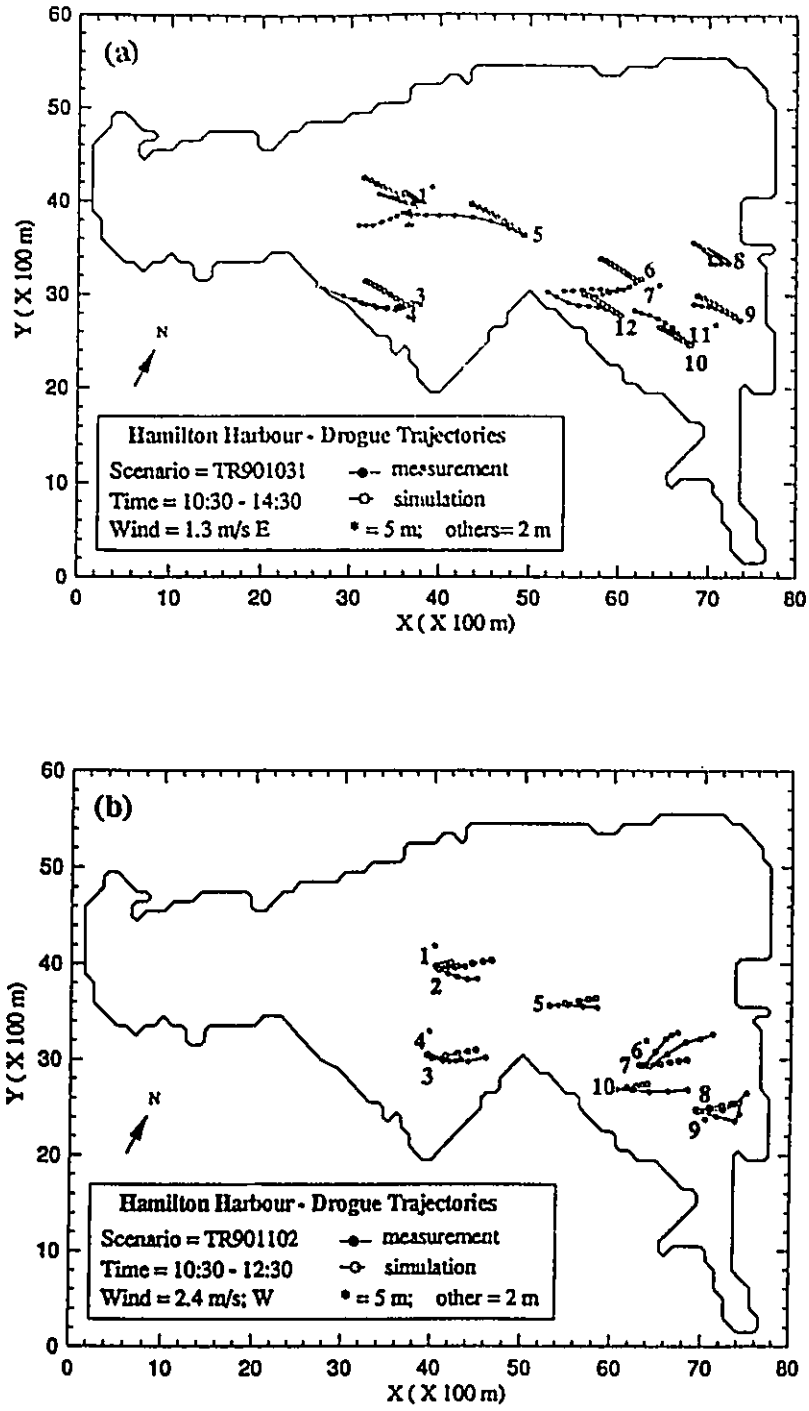

Fig. 10.18 The Measured (solid line with solid circle) and the simulated (dashed line with open circle) drogue trajectories for: (a) HH901031, (b) HH901102, in Hamilton Harbour. (Source of data: Boyce & Chiocchio, 1991)

Table 10.3 Comparison of drogue measurements and model simulations (Group 1)

Scenario	#	D (m)	u_d (cm/s)	v_d (cm/s)	u_c (cm/s)	v_c (cm/s)	α	γ_1	γ_2	γ_3
TR900620	1	2.0	-3.94	4.03	-5.41	3.69	-0.0106	0.4792	1.3062	0.4155
	2	2.0	-1.92	0.25	-4.84	3.33	-0.0207	2.1014	3.2256	1.1467
	3	2.0	-0.42	1.94	-1.81	1.41	-0.0087	1.3755	1.3733	1.1467
	4	2.0	-1.93	2.74	-3.49	2.42	-0.0080	0.3303	1.5513	0.1826
	5	2.0	-5.31	0.56	-3.25	2.24	-0.0002	0.3092	1.0079	0.3099
	6	6.5	-0.33	-0.16	-3.25	2.24	-0.0227	14.8716	10.8369	4.6807
	7	2.0	-6.03	4.53	-3.35	2.28	0.0173	0.2541	0.5902	0.1395
	8	2.0	-1.68	1.22	-3.06	2.07	-0.0100	0.6110	2.4599	0.1516
	9	6.5	-4.53	-1.11	-3.07	2.07	-0.0093	0.7468	1.3579	0.7161
TR900628	1	6.5	3.83	-4.52	-5.39	2.84	-0.0399	3.5757	1.0655	1.7029
	2	2.0	-10.39	5.82	-8.50	4.43	0.0075	0.0579	0.8224	0.0389
	3	2.0	-7.38	6.66	-7.34	3.98	0.0060	0.1100	0.8392	0.1035
	4	6.5	1.28	-4.75	-7.34	3.98	-0.0428	5.8159	2.2116	2.7097
	5	2.0	-2.87	-0.56	-5.12	2.88	-0.0122	1.3191	1.8446	1.0366
	6	2.0	-1.49	-2.26	-5.75	3.14	-0.0232	5.5217	3.8904	3.0700
	7	2.0	-1.32	2.93	-4.91	2.58	-0.0080	1.2718	1.8341	0.8495
	8	2.0	-6.32	5.50	-5.61	3.00	0.0077	0.1367	0.7645	0.1117
	9	2.0	-4.97	5.55	-5.39	2.84	0.0052	0.2090	0.8244	0.2046
TR900720	1	5.0	-3.58	0.50	0.32	-0.13	-0.0065	1.1840	0.6837	0.8187
	2	2.0	4.09	0.61	4.16	-0.70	-0.0037	0.6303	1.1711	0.6229
	3	5.0	1.60	0.21	2.84	-0.61	-0.0032	0.8939	1.5607	0.6812
	4	2.0	3.55	-2.92	9.42	-2.25	-0.0072	1.6281	1.5304	1.2401
	5	5.0	-1.80	-1.17	-0.36	0.09	0.0020	0.8781	1.0785	0.9311
	6	2.0	5.43	-2.24	6.73	-1.67	-0.0001	0.0938	1.0064	0.0929
	7	5.0	-3.14	-0.60	0.89	-0.22	-0.0044	1.3891	0.8537	1.1669
	8	2.0	1.89	0.42	6.67	-1.62	-0.0110	7.3246	3.8478	5.0169
TR900815	1	5.0	9.69	0.35	1.86	-1.48	0.0134	0.7039	0.8056	0.5938
	2	2.0	15.01	0.33	5.98	-4.64	0.0103	0.4852	0.8777	0.4528
	3	5.0	-3.27	1.36	0.07	0.05	-0.0095	1.0162	0.7125	0.7265
	4	2.0	6.52	-3.98	4.54	-3.86	0.0037	0.1593	0.9013	0.1469
	5	5.0	0.83	-1.56	-0.31	0.12	0.0054	1.2853	0.7508	0.9093
	6	5.0	-1.70	-2.26	0.29	-0.23	0.0012	0.9859	0.9930	0.9873
TR900920	1	5.0	-0.86	0.34	1.68	-1.87	-0.0111	6.7133	2.6417	3.4104
	2	2.0	2.17	-3.94	5.29	-5.74	-0.0117	1.1069	2.0453	0.8052
	3	2.0	3.48	-2.03	1.84	-1.60	0.0018	0.3576	0.9199	0.3511
	4	5.0	2.54	-1.97	0.04	0.25	0.0111	1.0699	0.5357	0.5258
	5	2.0	5.18	0.57	4.07	-4.52	-0.0102	1.2501	1.3967	1.1013
	6	2.0	3.77	-4.61	4.03	-4.55	-0.0013	0.1034	1.0624	0.1014
	7	5.0	0.98	-2.93	-0.47	0.24	0.0107	1.2100	0.6897	0.7638
	8	2.0	1.85	-4.32	2.45	-2.75	0.0002	0.6309	0.9888	0.6307
	9	2.0	2.70	-2.89	3.50	-3.82	-0.0035	0.3836	1.2977	0.3501
	10	5.0	1.17	-1.97	0.39	-0.42	0.0059	0.6748	0.6400	0.4554

Table 10.4 Comparison of drogue measurements and model simulations (Group 2)

Scenario	#	D (m)	u_d (cm/s)	v_d (cm/s)	u_c (cm/s)	v_c (cm/s)	α	γ_1	γ_2	γ_3
TR900927	1	5.0	-0.45	-0.02	0.72	-1.52	0.0102	2.5806	1.0010	2.2026
	2	2.0	0.66	-5.39	2.65	-5.34	0.0141	0.2258	1.0750	0.1803
	3	2.0	2.91	-2.19	0.64	-1.04	-0.0108	0.4987	0.8992	0.4347
	4	5.0	1.72	0.12	-0.36	0.84	-0.0093	1.6564	0.8738	1.4583
	5	2.0	3.87	-3.26	1.81	-3.72	-0.0047	0.2717	0.9665	0.2661
	6	2.0	2.02	-5.11	1.47	-3.17	-0.0001	0.1795	0.9994	0.1795
	7	5.0	1.36	-3.70	-0.21	0.25	-0.0092	1.1565	0.9702	1.1157
	8	2.0	2.16	-0.96	1.66	-3.55	0.0074	1.4303	1.1418	1.3853
	9	2.0	0.58	2.81	2.16	-4.41	0.0264	4.7111	1.0466	4.2659
	10	2.0	2.92	-0.59	1.93	-3.86	0.0104	1.0452	1.0723	0.9902
	11	5.0	0.46	-1.93	0.24	-0.49	0.0087	0.7923	0.9621	0.7281
	12	2.0	1.54	-2.46	1.44	-2.87	-0.0012	0.2233	0.9807	0.2220
TR901031	1	5.0	-2.75	0.52	-0.99	0.57	-0.0067	0.4299	0.7988	0.3453
	2	2.0	-3.84	-1.16	-3.47	1.99	0.0146	0.6792	1.3765	0.6336
	3	2.0	-6.03	1.22	-2.72	1.58	-0.0137	0.4486	0.8341	0.3905
	4	5.0	-3.96	0.31	-0.09	0.06	-0.0165	0.9707	0.7985	0.7804
	5	2.0	-8.10	1.34	-3.55	2.04	-0.0173	0.3519	0.8147	0.2856
	6	2.0	-5.02	-0.71	-2.49	1.44	0.0011	0.4711	1.0187	0.4752
	7	5.0	-3.56	-1.06	0.06	-0.01	-0.0091	1.0275	0.8864	0.9097
	8	2.0	-2.34	1.35	-1.43	0.88	-0.0059	0.3694	0.8409	0.3309
	9	2.0	-3.13	1.08	-2.85	1.64	0.0018	0.0790	1.0617	0.0794
	10	2.0	-3.66	2.18	-1.88	1.11	-0.0123	0.2993	0.7412	0.2173
	11	5.0	-0.99	0.55	0.00	0.01	-0.0046	0.9957	0.9080	0.9035
	12	2.0	-5.07	1.54	-2.51	1.43	-0.0110	0.2708	0.8106	0.2117
TR901102	1	5.0	3.59	-0.05	1.86	0.41	-0.0007	0.3884	1.0328	0.3955
	2	2.0	4.70	-1.12	6.46	1.05	-0.0033	0.5594	1.1520	0.4681
	3	2.0	6.63	0.06	5.46	0.91	-0.0033	0.1819	1.0967	0.1755
	4	5.0	4.19	-0.48	0.20	0.04	0.0022	0.9210	0.9300	0.8570
	5	2.0	5.82	-0.19	5.67	0.87	-0.0016	0.2933	1.0599	0.2852
	6	5.0	3.96	3.77	-0.61	-0.03	0.0010	1.1575	0.9736	1.1270
	7	2.0	7.56	3.67	4.53	0.71	0.0002	0.2840	0.9947	0.2818
	8	2.0	6.19	1.87	5.26	0.77	-0.0017	0.1697	1.0589	0.1775
	9	5.0	5.15	1.08	0.22	0.03	0.0074	0.9474	0.8435	0.7997
	10	2.0	8.82	-0.02	3.95	0.62	0.0033	0.3567	0.9226	0.3262
TR910831	1	2.0	12.38	-0.71	18.47	-2.73	0.0097	0.6744	1.6341	0.4676
	2	2.0	13.82	0.27	17.38	-2.58	0.0076	0.3303	1.4383	0.2482
	3	2.0	8.92	-0.44	17.78	-2.62	0.0120	1.5995	2.4355	0.8762
	4	2.0	12.77	-2.22	19.77	-2.89	0.0100	0.6957	1.6181	0.4633
	5	5.0	2.93	-1.95	4.39	-0.77	0.0014	0.7176	1.1882	0.6391
	6	5.0	-0.16	-2.75	3.46	-0.40	0.0017	1.5797	1.0966	1.3400
	7	2.0	9.73	-2.66	19.03	-2.81	0.0112	1.2839	2.0598	0.7127

movement of particles released at this location.

Fig. 10.19(a) shows the locations after 2 hours (open circle) of 1000 drogues released at the same point, i.e., the first point in scenario TR900620 using random-walk approach. The concentration at each mesh could be calculated by adding the number of drogues located in this mesh. The contours from a continuously release of a 100 unit "particle" after 2 hours from advection-diffusion modelling are shown in Fig. 10.19(b). It is observed that both methods provide similar results. It is important to determine a standard value of γ_i for the model verification. Table 10.5 shows the mean, minimum and maximum values of γ_i under the dispersion coefficients of 0.1, 1.0 and 5.0 m^2/s, which are the typical values in lakes. The value of γ_i is increased with the increase of the dispersion coefficient. The mean γ_i could be 1.651 when the coefficient is 5.0 m^2/s. Then we can say if the coefficient for any comparison is below 1.651, the simulation is acceptable. In this sense, most of the simulations listed in Tables 3 and 4 are acceptable.

Table 10.5 Theoretical value of γ_i from random-walk modelling

A_h (m^2/s)	Mean	Min	Max
0.1	0.099	0.002	0.579
1.0	0.555	0.016	5.429
5.0	1.651	0.073	17.29

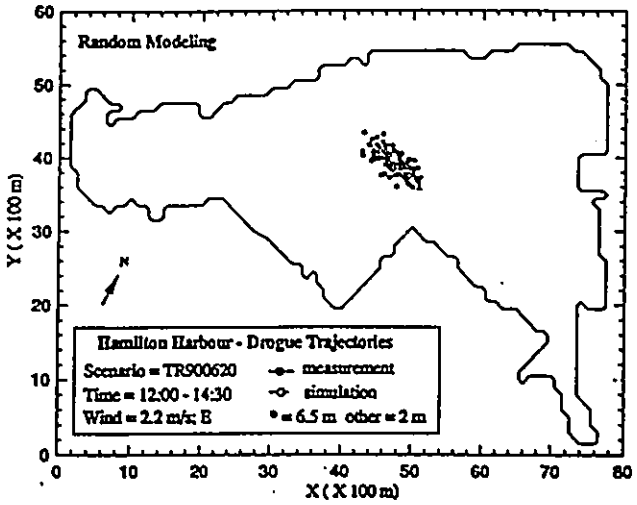

(a)

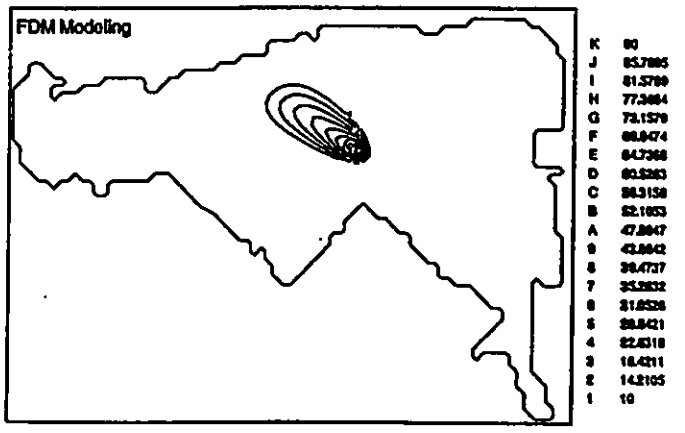

(b)

Fig. 10.19 Experiments on the trajectory predictions: (a) movement of 1000 particles at 2 hours after released at the first drogue location in Scenario HH900620 in Hamilton Harbour, using the trajectory prediction model coupled with a Monte-Carlo random-walk approach. (b) contours of equal concentration of pollutant (equivalent to a cloud of particles) at 2 hours after emitted from the first drogue location in Scenario HH900620, using finite difference advection-diffusion model.

10.3 VERIFICATION WITH WATER LEVEL DATA

The water level change in a lake may be induced by the wind (wind-induced set-up), in/outflows, precipitation, and evaporation. In the short term, assuming no major precipitation or rainfall event, the wind-induced change should be dominant, for most lakes except for some small lakes, with high volumes of in/outflows. The magnitude of wind-induced water level change depends on the wind speed and fetch or size of the lake. For example, in Lake Ontario (140 km x 40 km), there is a 6 cm difference of water level between the two ends of the basin for a 10 m/s westerly wind over several hours. The water level changes follow the wind change both from field data and model simulation (Simons, 1980). However, for Hamilton Harbour, it was found in Chapter 9 that the water level change does not follow the wind change, and the magnitude of change is much higher than expected (for such small size basin). The only possible reason is the influence of Lake Ontario.

To confirm the above observation and for model verification purposes, the scenario HH910314 (Aug. 14-16, 1991) was simulated. This was a three-day west wind storm, with the wind speed over 2-9 m/s, as shown in Fig. 10.20(a). The water level history at the Burlington Ship Canal during this period is presented in Fig. 10.20(b). The water level change was about 1-8 cm over three days. About a 8 cm decrease in water level was presented in a couple of hours during the second day, when the wind increased about 7 m/s.

At first, the water level change at Burlington Ship Canal was not coupled in the simulation. Fig. 10.21 shows the pure wind-induced water level changes at three locations (station #21, #22, #23, see Fig. 9.2). As expected, the water level changes about 0.1-0.5 cm, mainly following the wind change. Then, the water level change in the canal was coupled as a boundary condition in the simulation. Fig. 10.22 presents the simulations (dashed-line), and the

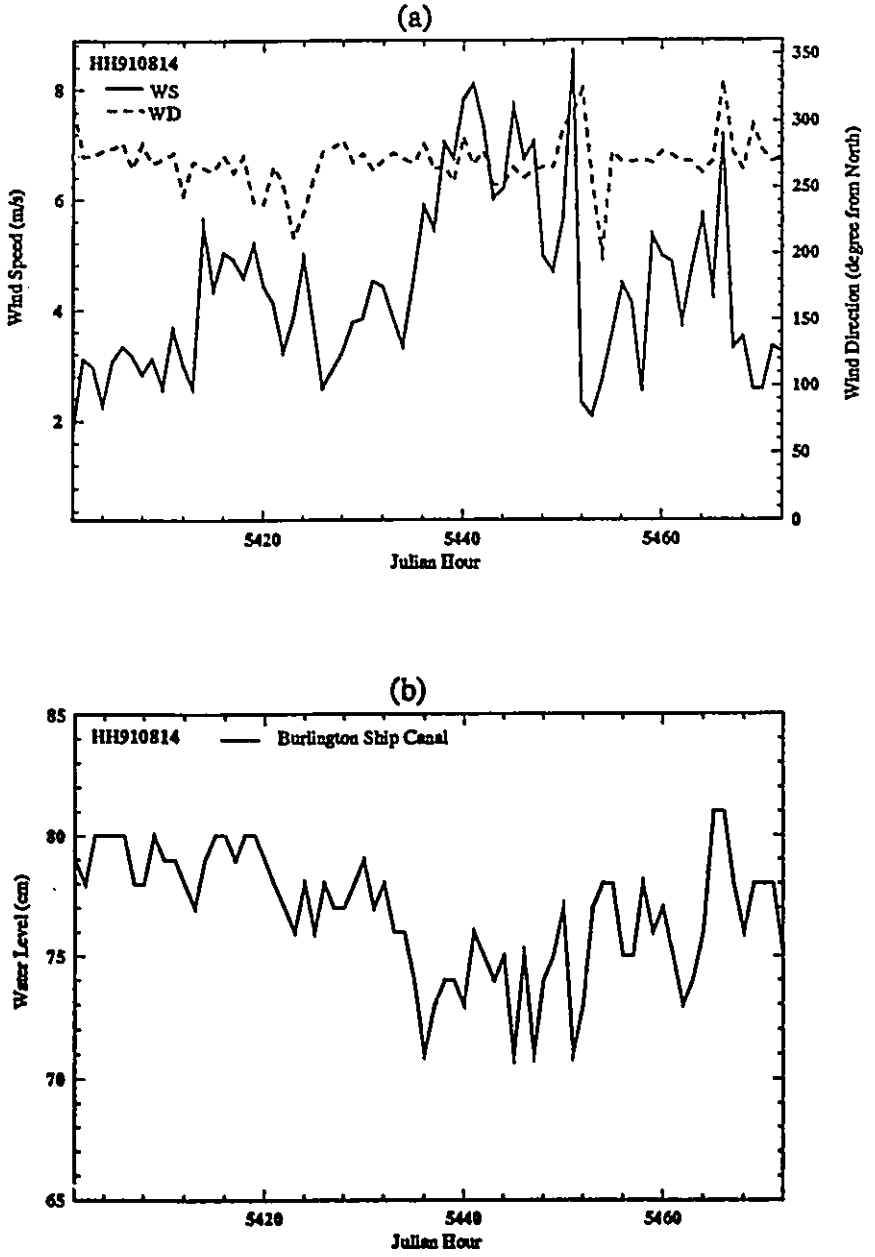

Fig. 10.20 Time series of (a) wind speed and direction, (b) water level at Burlington Ship Canal during 14-16, Augest, 1991, Hamilton Harbour.
(Source of data: NWRI & MEDS)

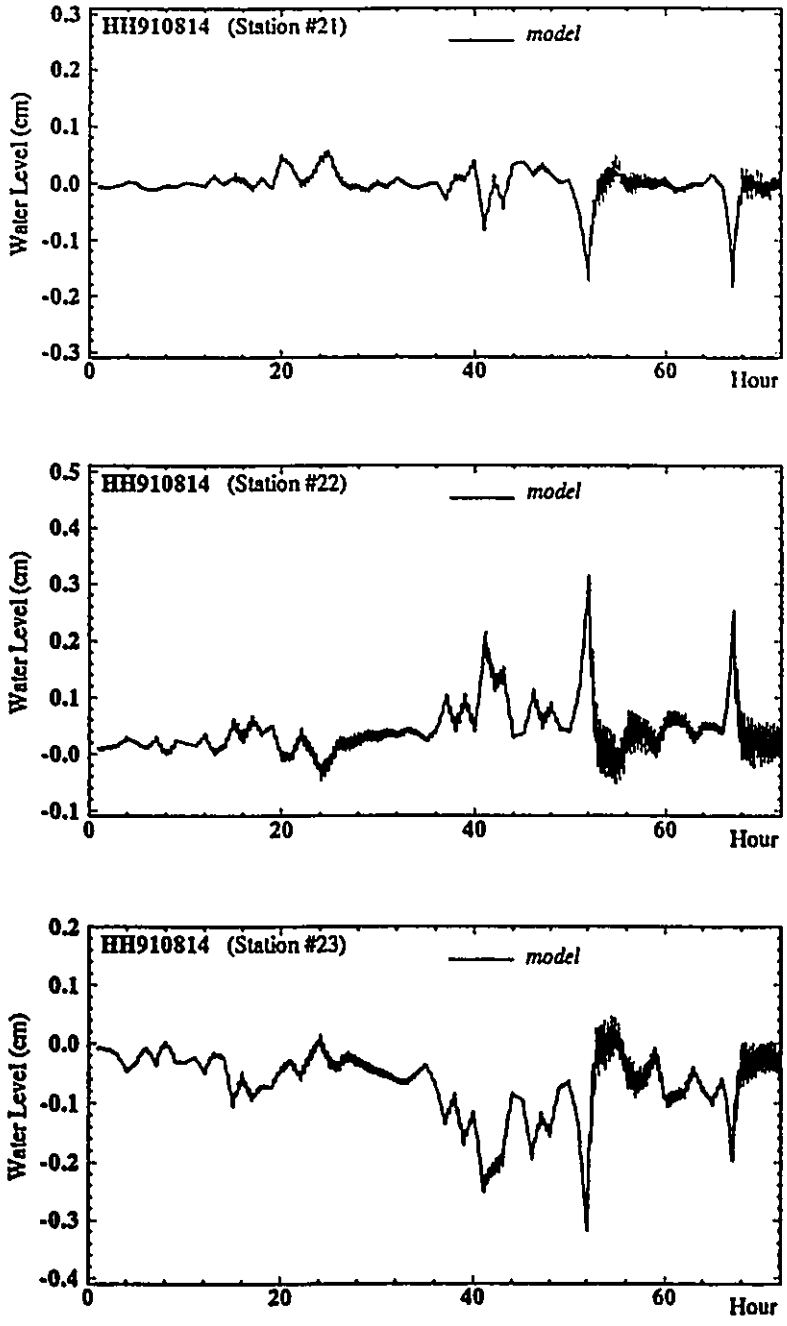

Fig. 10.21 Simulated water level at three station #21, #22, #23 in Hamilton Harbour during 14-16, Augest, 1991. The influence of Lake Ontario through Burlington Ship Canal was excluded in the model.

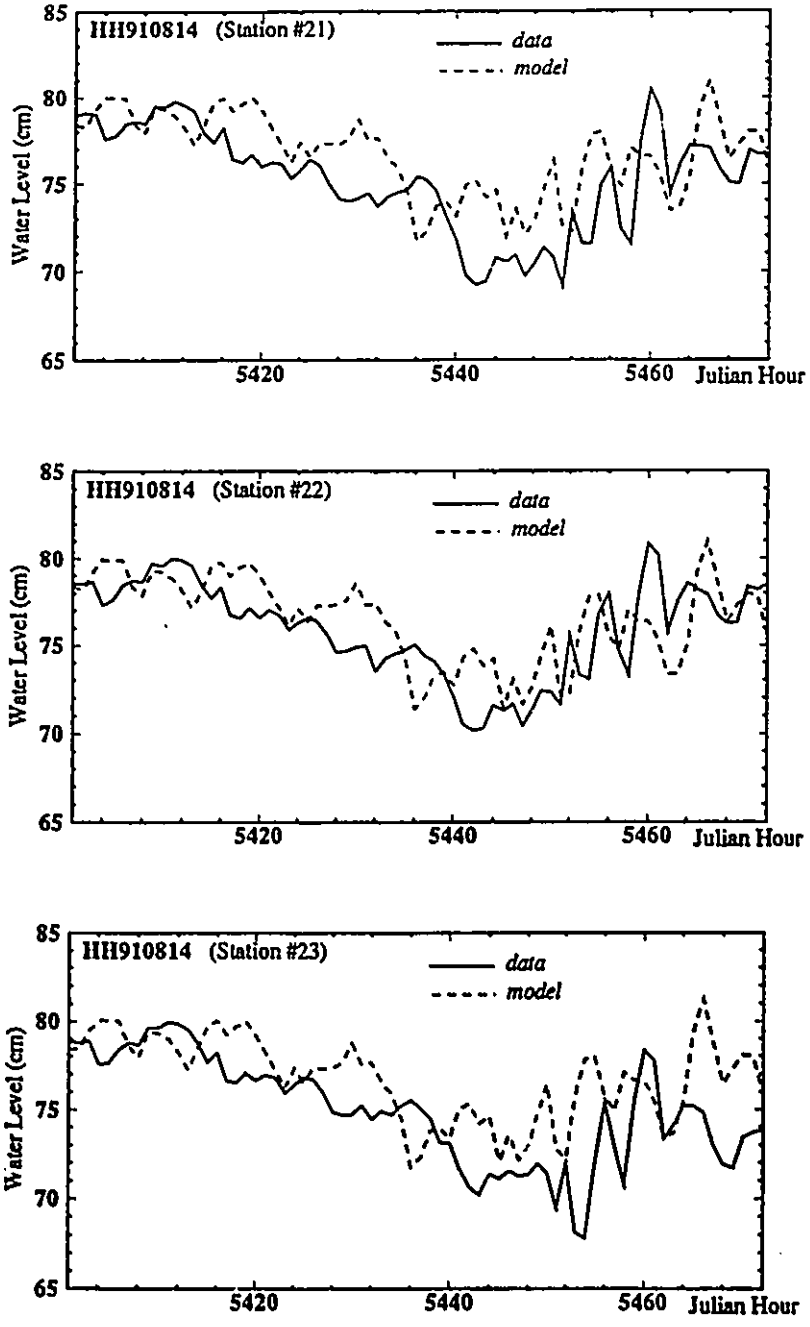

Fig. 10.22 Simulated (dash line) and observed (solid line) water level at three station #21, #22, #23 in Hamilton Harbour during 14-16, Augest, 1991. The influence of Lake Ontario through Burlington Ship Canal was included in the model.
(Source of data: NWRI)

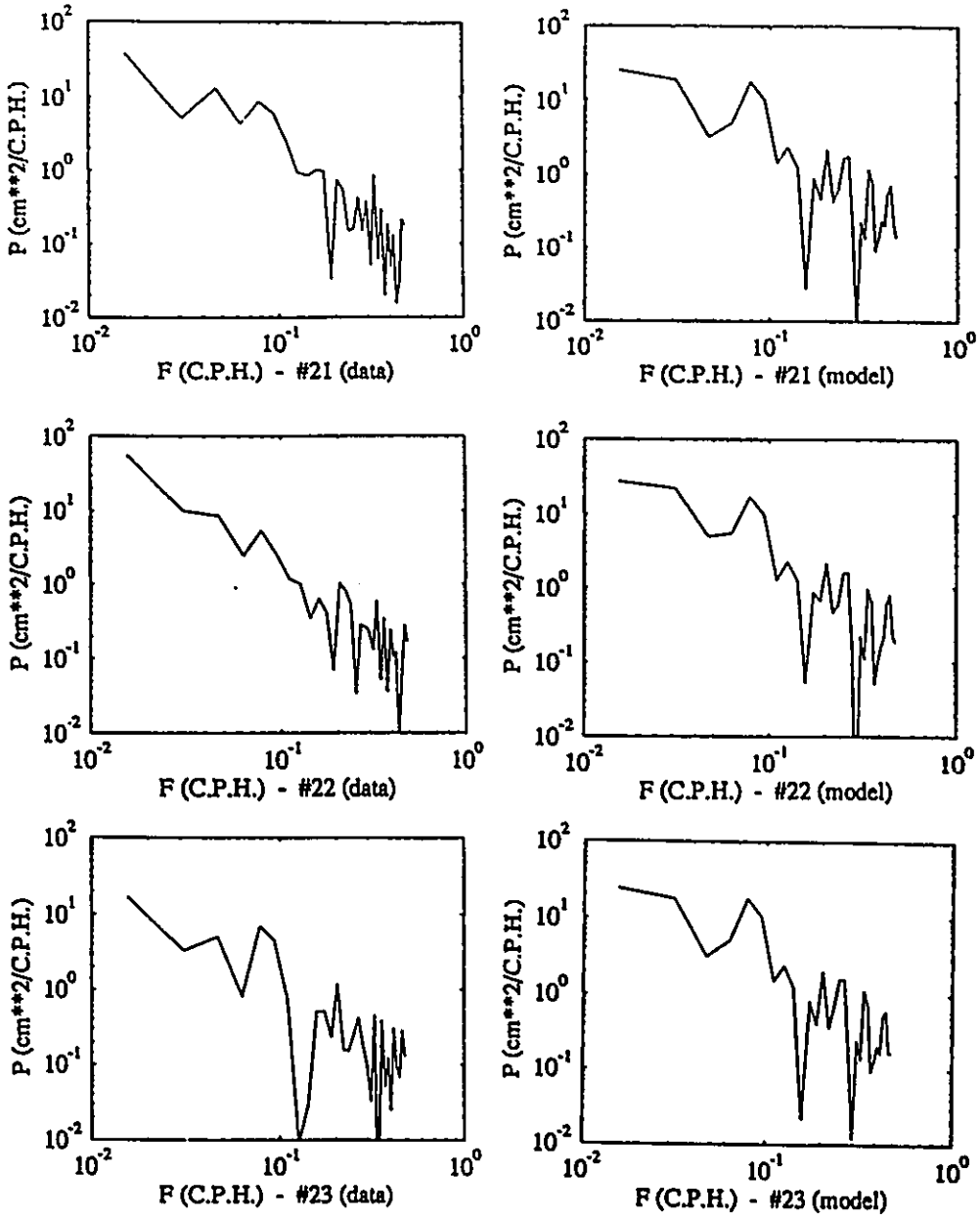

Fig. 10.23 Spectra of hourly water level data from measurement and model simulation at three station #21, #22, #23 in Hamilton Harbour during 14-16 Augest, 1991.
(Source of data: NWRI)

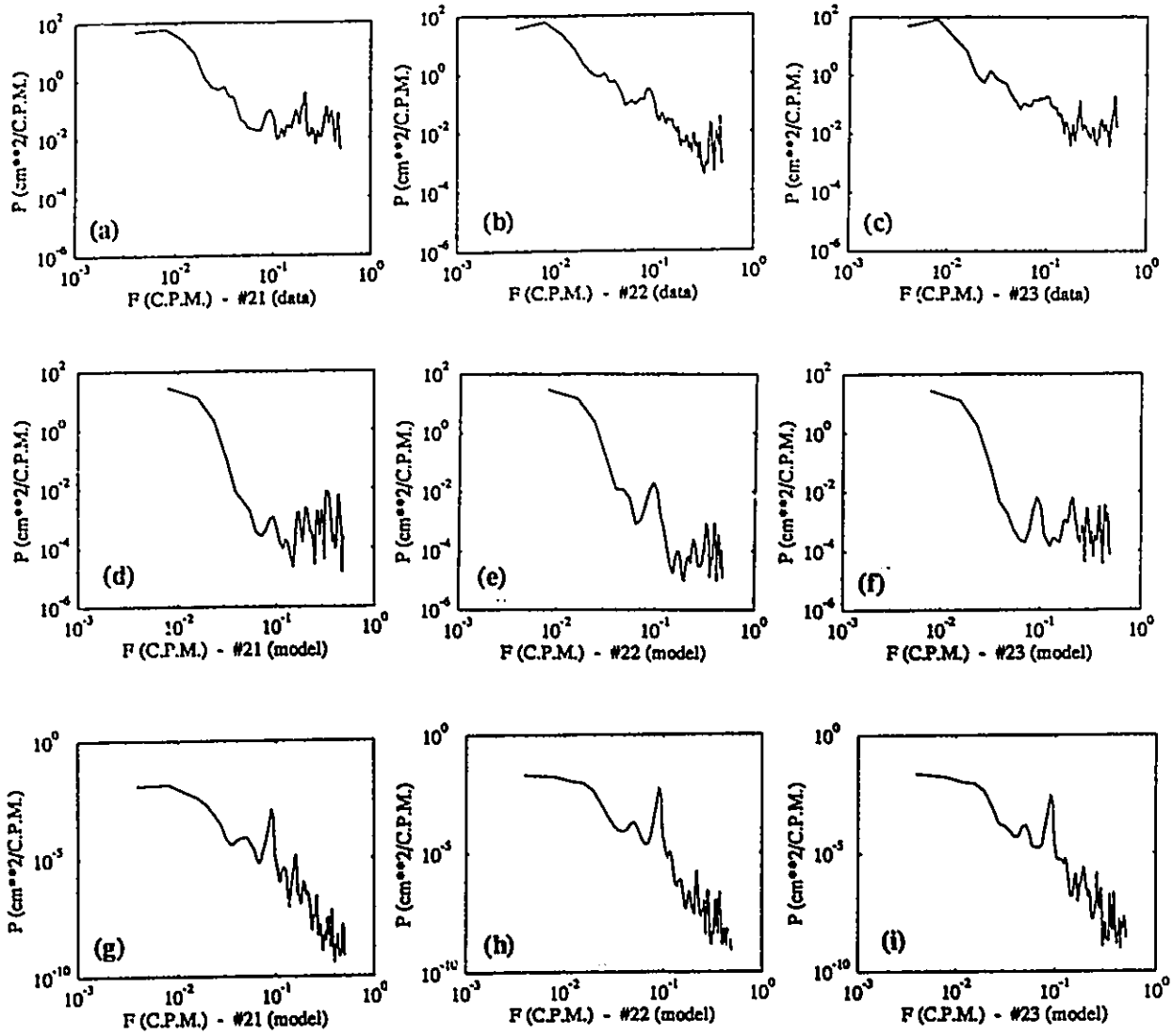

Fig. 10.24 Spectra of two-minute water level data from measurements - (a), (b) and (c); model simulations coupling water level change of Lake Ontario - (d), (e) and (f); and model simulations without coupling water level change of Lake Ontario - (g), (h) and (i), at station #21, #22, #23 in Hamilton Harbour during 14-16 Augest, 1991.
(Source of data: NWRI)

field measurements (solid line) at three stations. The simulations are in good agreement with the measurements. The water level changes are as high as 10 cm. In conclusion, the influence of Lake Ontario must be included in predicting the water level change in Hamilton Harbour. Another comparison approach other than the point-by-point comparison is based on the spectral analysis. Fig. 10.23 is the spectra from the hourly field data and simulation result. A peak with period of 5.5 hours is observed in both spectra which is the seiche of Lake Ontario. As we already noticed, the seiche of Hamilton Harbour is about 22 minutes. Therefore, spectral analysis should be based on the two minute data. Fig. 10.24 shows the spectra of the two-minute water level data from the measurements, model simulations coupling the water level change of Lake Ontario, and model simulations without coupling water level change of Lake Ontario at stations #21, #22, #23, respectively. The unimodal seiches with a period of 22 minutes, along with the bimodal seiche with a period of 11 minutes, are revealed both from data and simulations.

10.4 SUMMARY

A model verification with field data during the 1990 & 1991 field seasons in Hamilton Harbour was undertaken using three approaches, i.e, point-by-point, particle trajectories and spectra analysis. The effort made in this chapter enhances our understanding of model predictions of actual processes in the natural lake. In contrast to the comparison with current data, the comparison with drogue trajectory data is much more successful, and a quantitative criterion of comparison has been established. Finally, from the verification with water level data, it is concluded that the model is capable of modelling the seiche of the harbour, and, the water level change from Lake Ontario must be included in the prediction of the water level in Hamilton Harbour.

CHAPTER 11

CIRCULATION / POLLUTANT TRANSPORT IN HAMILTON HARBOUR

The final significant application of engineering deals with the modelling of current movement and pollutant transport in Hamilton Harbour. The features of horizontal mixing and flushing in the Harbour are examined, using the pollutant transport model. A nested-grid modelling technique will be developed and applied in three nearshore areas with the 25 m fine grid model (100 m coarse grid for the whole Harbour). The effect of various configurations of artificial islands is examined and final recommendations on the engineering design of islands will be provided to the City of Hamilton.

11.1 HYDRODYNAMICS OF HAMILTON HARBOUR

The collection of current and drogue data was insufficient to give an overall description of the Harbour flow field that would be useful for water quality modelling. Therefore, numerical models must be employed for such a purpose. Confidence in the model performance has been obtained through verifications using the field data in Hamilton Harbour. The developed 2DH, VHI3D and 3D models can be employed to provide flow fields under various conditions.

11.1.1 Circulation Patterns

First, the hydraulic flow was calculated by the 2DH circulation model to examine the

impact of exchange flow between Hamilton Harbour and Lake Ontario through the Burlington Canal and other inflows. The inflow from Cootes Paradise was taken as 3.8 m^3/s, 2.2 m^3/s from CSO's, 2.4 m^3/s and 3.6 m^3/s from the Burlington and Hamilton STP's, respectively. The outflow through Burlington Canal was taken as 12.0 m^3/s. Fig. 11.1 shows the simulated hydraulic flow pattern. It is observed that the flow is very weak, only about 0.1 to 1.0 cm/s. This is due to the large size of the Harbour and small amount of in/outflows.

In the simulation of wind-induced circulation, the total kinetic energy under various wind speeds, as shown in Fig. 11.2, reaches a steady state condition in a very short period, because the lake is shallow, and due to the bottom friction, damping is very large. For example, it only takes 2 hours to reach 80 % of the steady state value for a 10 m/s (west) wind. A test result on a variable wind process indicates that the Harbour's water responds very quickly to the wind changes.

To obtain the wind-induced circulation pattern, an idealized 10 m/s wind with directions from eight compass points (at 45 degree interval) was applied for Hamilton Harbour. The simulated results from the VHI3D model are presented in Figs. 11.3, 11.4, 11.5, and 11.6. The depth-averaged currents follow the wind close to the shore (aligned in a way that is parallel to the shore) and are against the wind in the middle deeper part of the Harbour. Three to four smaller eddies are the major features of the depth-averaged current patterns. The first large eddy occupies the northeastern Harbour and has clockwise rotation for north, northwest and west winds, and a counterclockwise rotation for south, southeast and east winds. For the cases of northwest and southwest winds, the large eddy splits into two counter-clockwise eddies. The second large eddy occupies the south central Harbour and has a clockwise rotation for southeast, east, northeast and north winds, and a counterclockwise rotation for northwest, west, southwest

and south winds. The size of these eddies changes with the wind direction. For example the western end of the Harbour is dominated by a counterclockwise eddy for northwest and north winds. It has a clockwise eddy for south and southeast winds, and two counter-rotating eddies for west, southwest, east and northeast winds. A test was performed using different wind speeds (7 m/s, 15 m/s and 20 m/s). The circulation features are very similar among all wind speeds, with the only difference being the current speed (the depth-averaged currents are higher in the shallower parts of the Harbour when compared to the currents in the deeper parts for increasing winds).

A typical multi-layer circulation pattern from the 3D model with 10 σ levels is shown in Fig. 11.7 for the case of a 5 m/s east wind. Surface currents are about 10 to 15 cm/s, in the same direction as the wind. At the middle and bottom layers, the currents in the central part of the lake are 180° out of phase to the wind. In the shallow north-east shore, the current is along the shoreline and for the most part follows the wind direction. The hydraulically-induced flow is very small when compared to the wind-induced flow, due to the small in/outflow compared with the strong wind. The vertical current structure may be viewed from a vector plot at a cross-section from Cootes Paradise to the Burlington Canal, as shown in Fig. 11.8. Return currents are obvious at lower layers.

11.1.2 Pollutant Transport

The Regional Municipality of Hamilton-Wentworth identified twenty-two major CSO outfalls in the Harbour area. Pollutants from these outfalls enter the Harbour water body and transport by the mean and turbulent flow fields. A numerical experiment, between the fourth and eighth of November of 1990, was undertaken in which 100 ppm of pollutant were emitted from

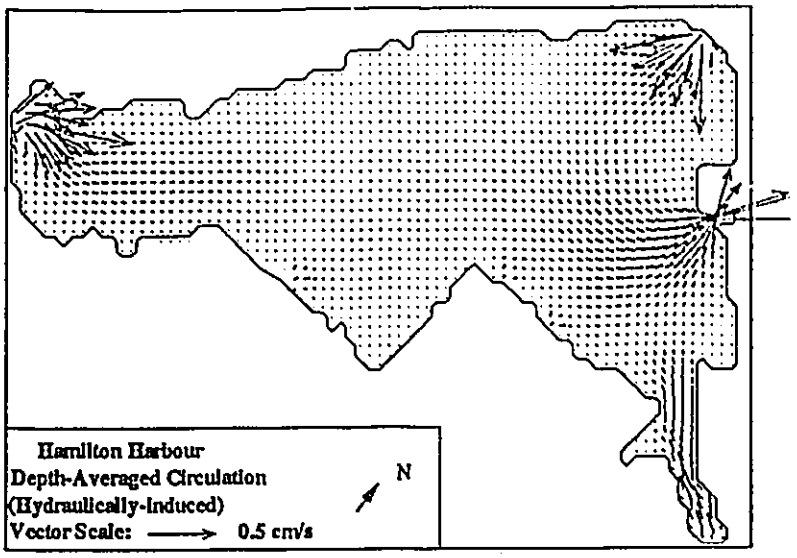

Fig. 11.1 Hydraulically-induced circulation pattern in Hamilton Harbour simulated by the 2DH circulation model. The in/outflow rates are taken to be averaged value.

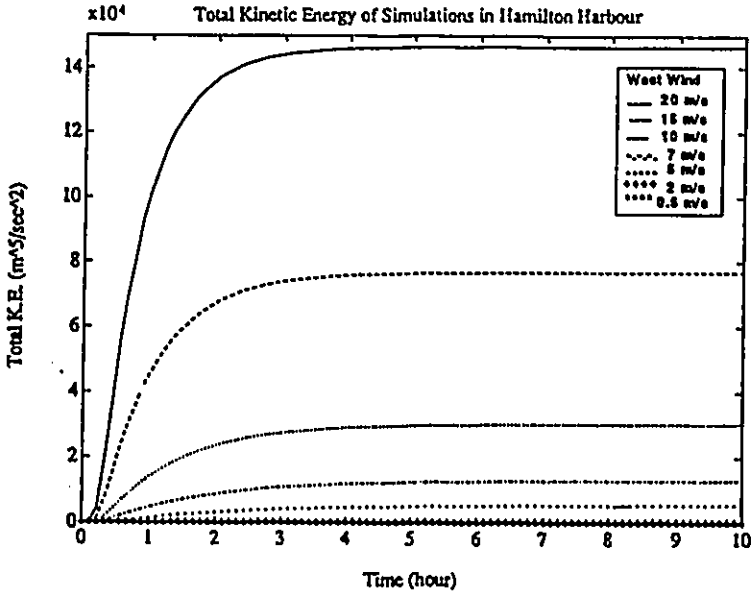

Fig. 11.2 Kinematic energy process of simulations under the west wind with various wind speeds.

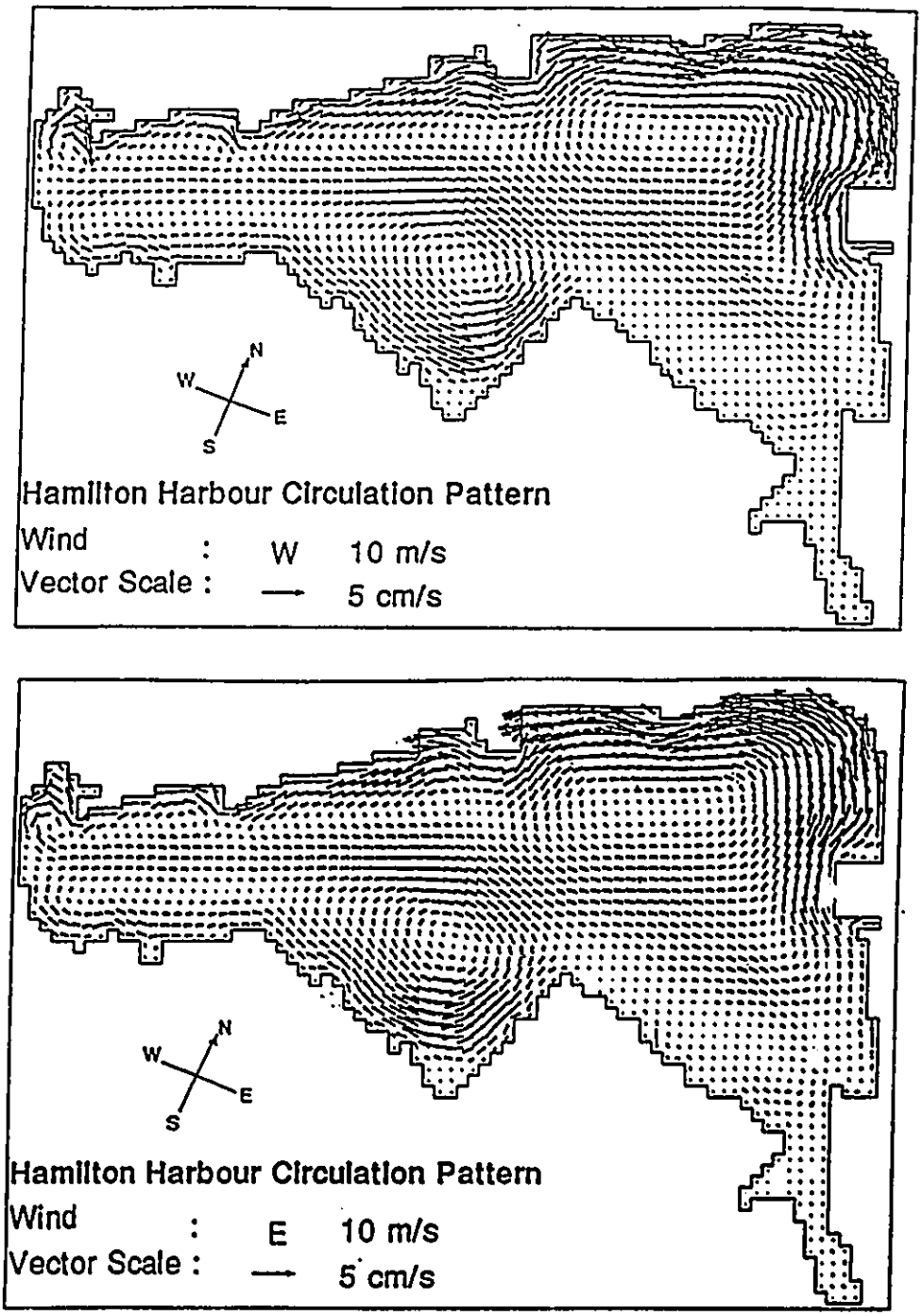

Fig. 11.3 The simulated depth-averaged circulation patterns under a 10 m/s west wind and a 10 m/s east wind in Hamilton Harbour.

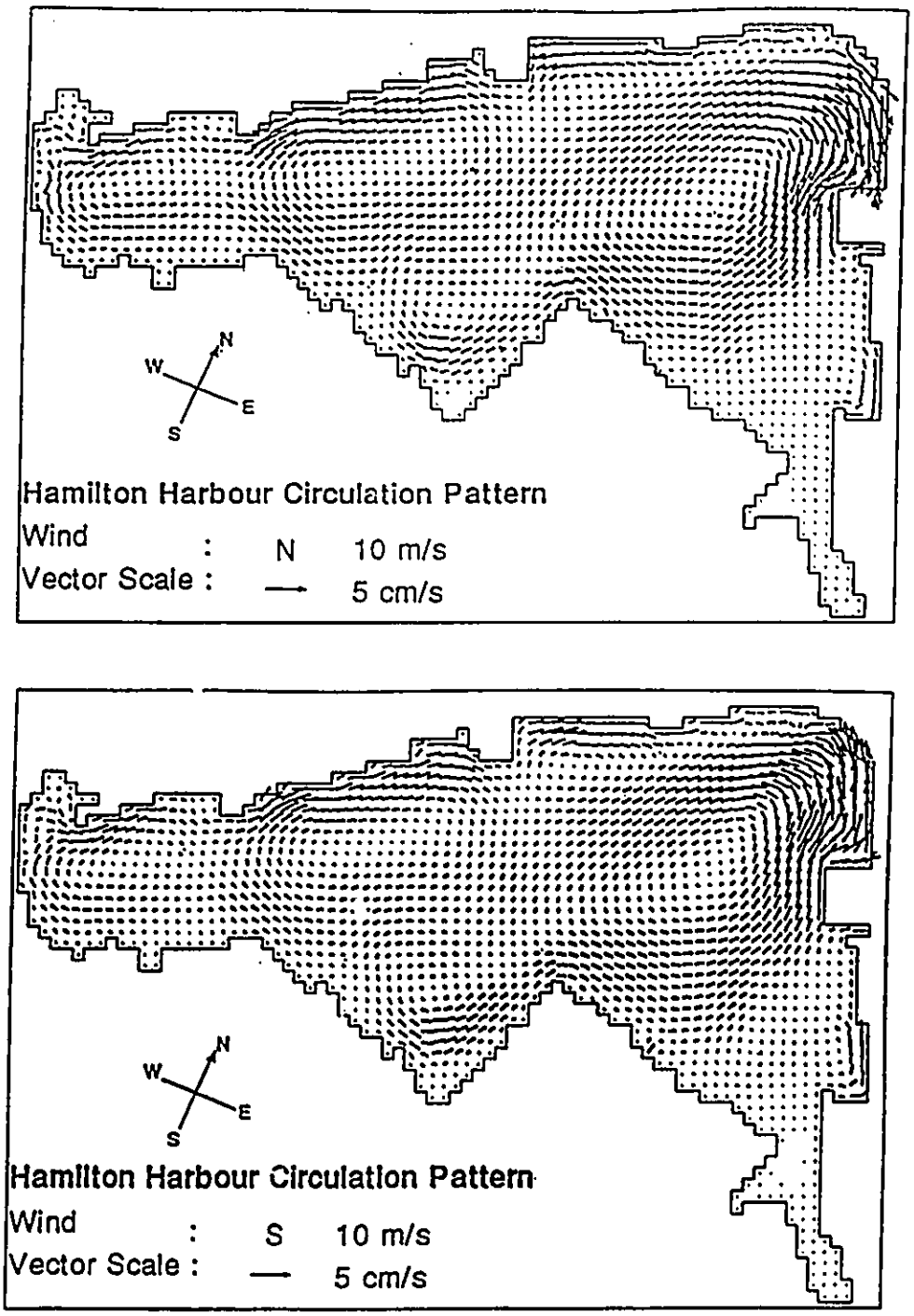

Fig. 11.4 The simulated depth-averaged circulation patterns under a 10 m/s north wind and a 10 m/s south wind in Hamilton Harbour.

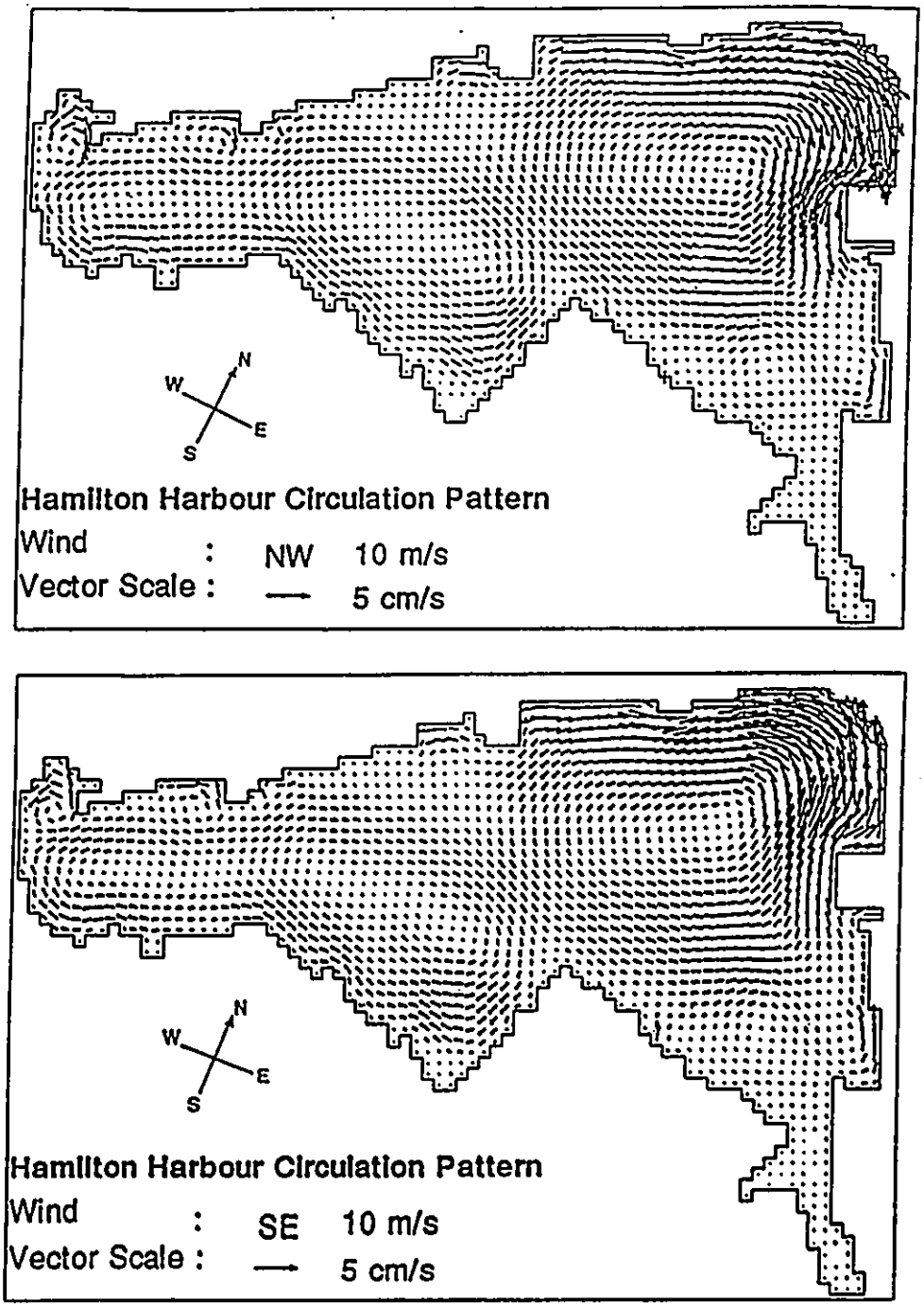

Fig. 11.5 The simulated depth-averaged circulation patterns under a 10 m/s northwest wind and a 10 m/s southeast wind in Hamilton Harbour.

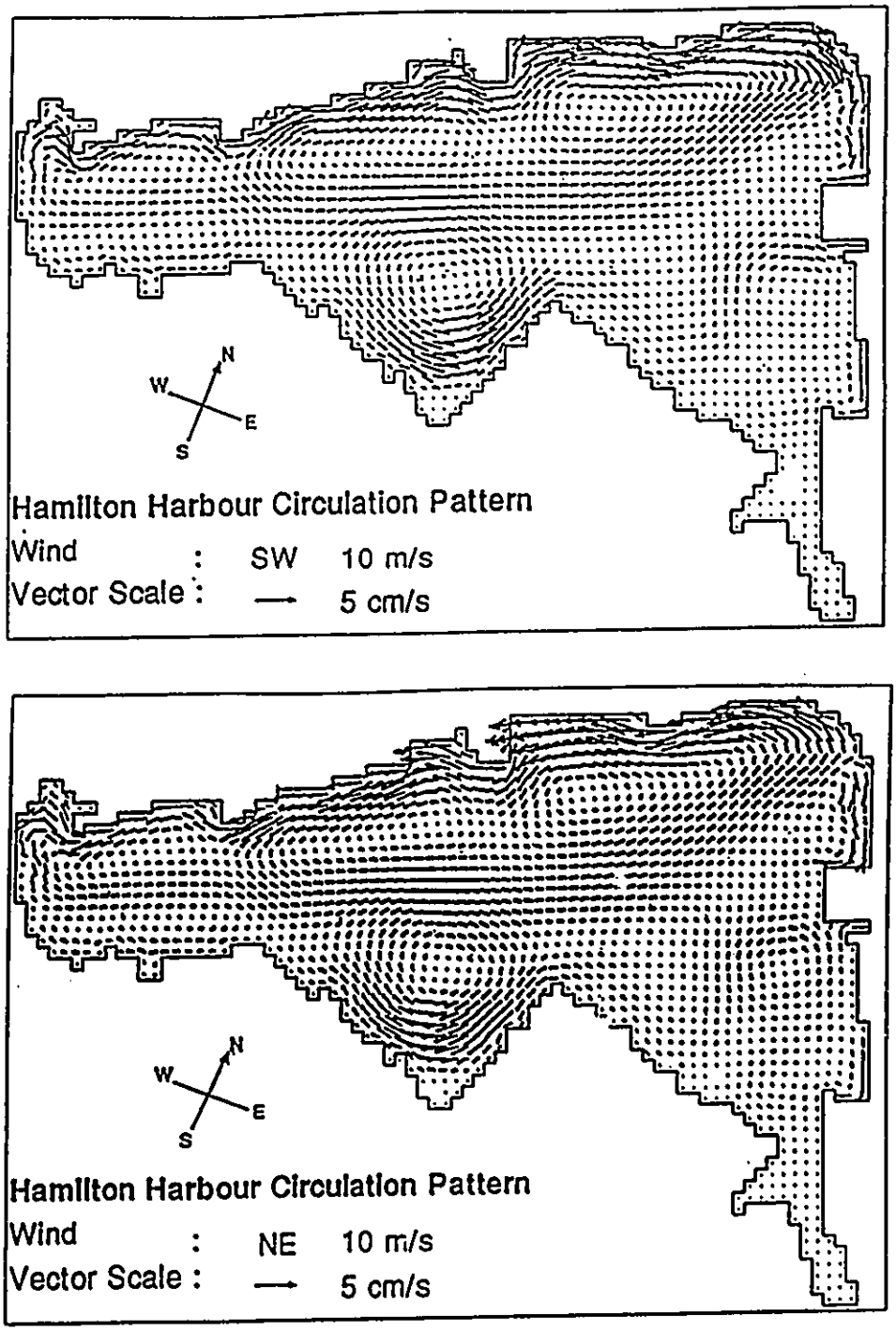

Fig. 11.6 The simulated depth-averaged circulation patterns under a 10 m/s southwest wind and a 10 m/s northeast wind in Hamilton Harbour.

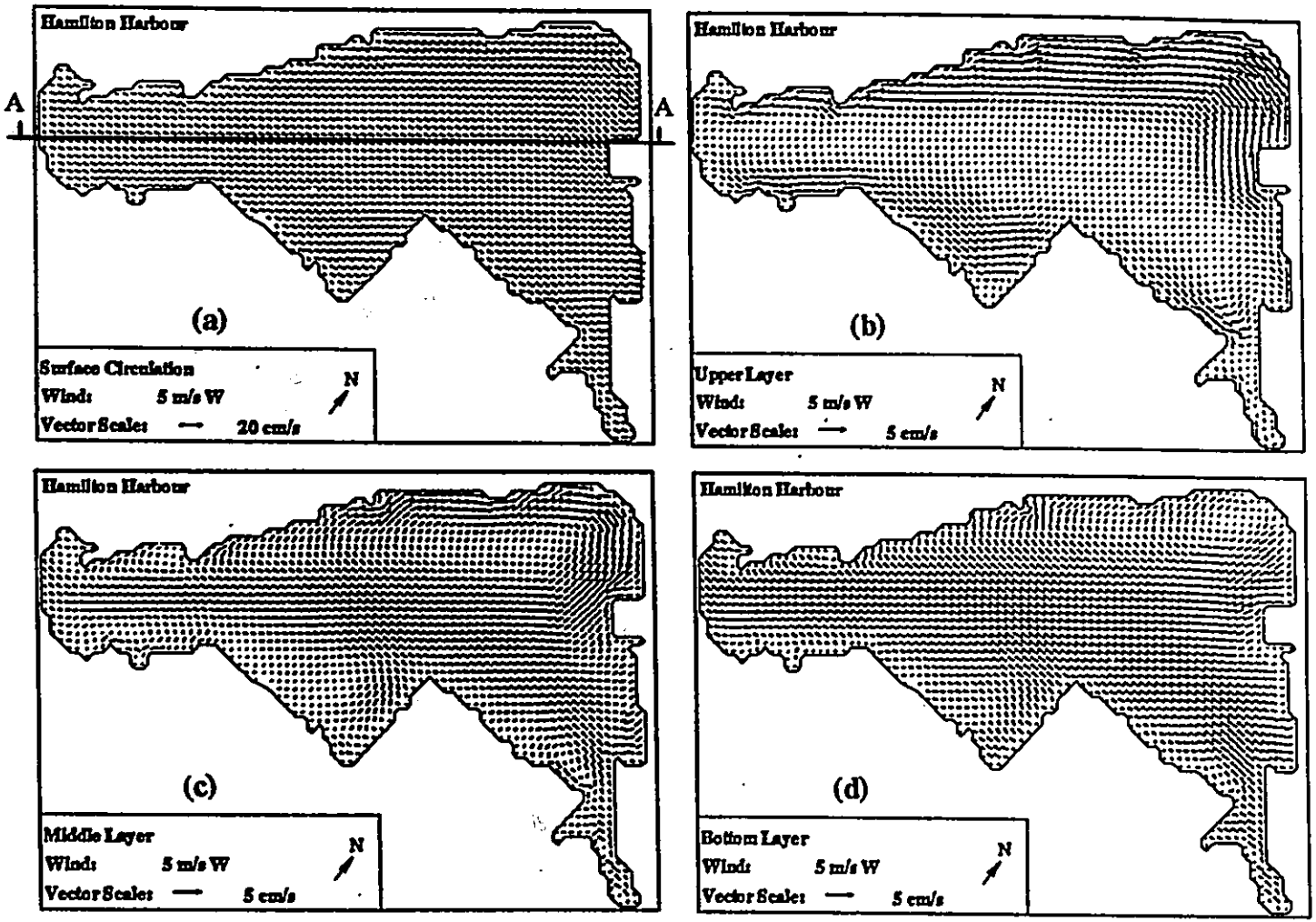

Fig. 11.7 Multi-layered circulation patterns: (a) surface layer ($\sigma = 0$), (b) upper layer ($\sigma = -0.15$), (c) middle layer ($\sigma = -0.45$), (d) bottom layer ($\sigma = -0.9$) in Hamilton Harbour under a 5 m/s west wind.

fifteen sources. The winds were about 1-13 m/s having the directions W-NE-W, as shown in Fig. 11.9. Figs. 11.10 and 11.11 show the equal concentration contours at 24, 48, 72, and 96 hours from the beginning of the experiment, respectively. The pollutants enter the Harbour and are advected, via the prevailing current, and are diffused at the same time. Once again, the changes in current speed and direction, due to the wind change, are reflected in the path of the pollutants. The pollutants take a long time to enter the central area of the large-scale eddy, but stay there for a longer time once they enter this regime. The pollutants reach the central basin in about one day, under the west wind condition. They are forced west during the second day under an east wind. Finally, during the third and fourth days they move towards the east shore.

11.1.3 Mixing Time

In the study of the interlocking of physical and bio-geochemical processes, an important time scale is the horizontal mixing time of the basin. It can be defined as the time taken, on the average, for an amount of a conservative contaminant, introduced at a point within the basin, to be mixed uniformly throughout the basin. A test can then be designed for Hamilton Harbour to determine this horizontal mixing time with the aid of the circulation and pollutant transport models. A 100 ppm pollutant was introduced at four typical locations: A (western basin), B (south shore), C (southeastern corner) and D (northeastern corner), as identified in Fig. 11.12(a).

A 10 m/s wind from four directions (N, S, E, W) was applied uniformly to the Harbour and produced different flow patterns. The maximum concentration (C_{max}) was recorded and the simulation was stopped when C_{max} reached 1 ppm. At this time, the initial blob of pollutant was considered to be fully mixed under the ambient current. As an example, Fig. 11.12 shows the

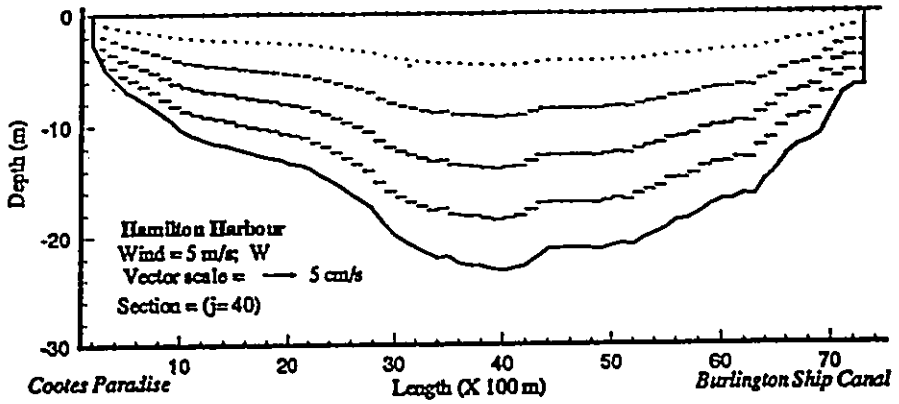

Fig. 11.8 Circulation pattern in a vertical section from the Cootes Paradise to the Ship Canal (section A-A in Fig. 11.7(a)), under a 5 m/s west wind in Hamilton Harbour.

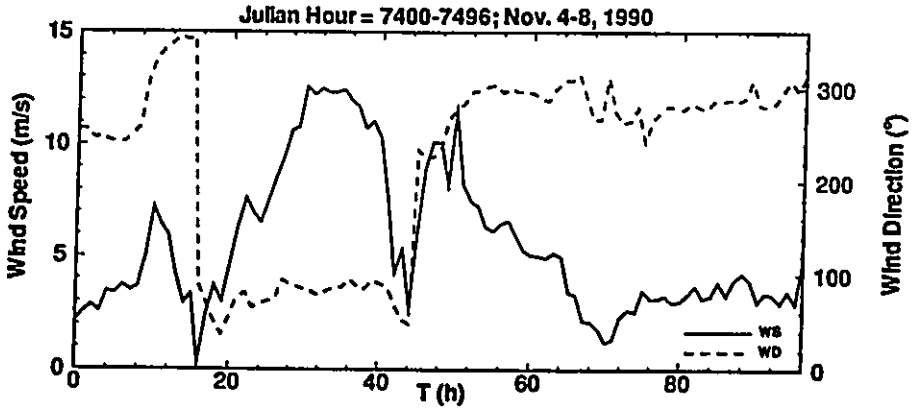

Fig. 11.9 The wind process at the buoy in Hamilton Harbour during Nov. 4-8, 1990. (Source of data: NWRI)

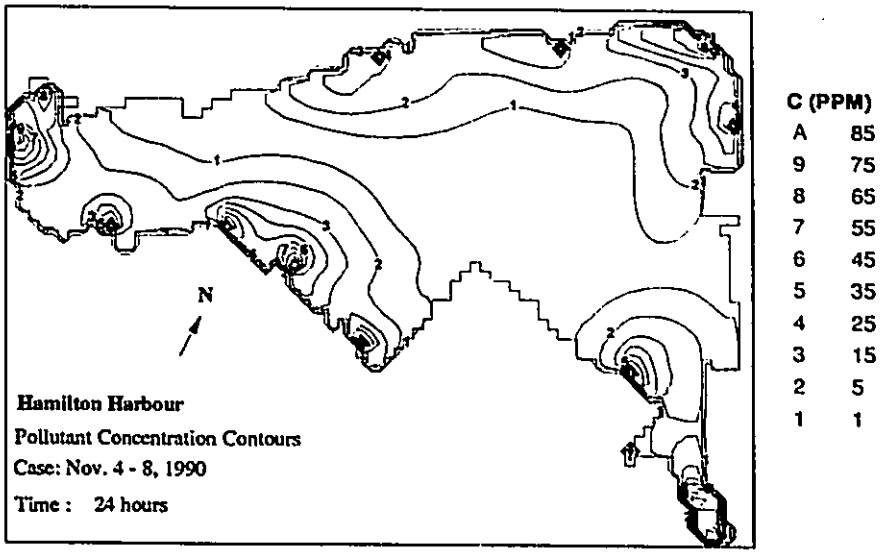

(a)

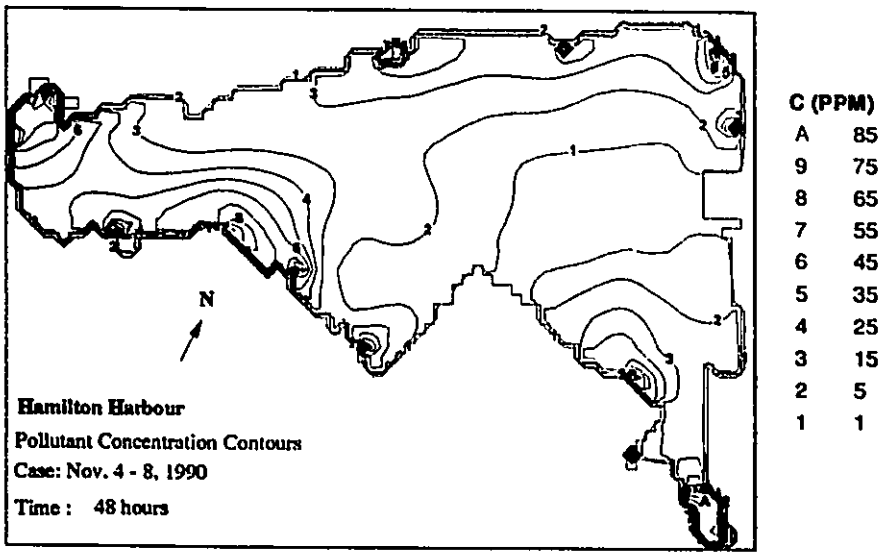

(b)

Fig. 11.10 The simulated concentration contours at (a) 24 hours, and (b) 48 hours after 15 pollutant sources were introduced into Hamilton Harbour (Case = Nov. 4-8, 1990).

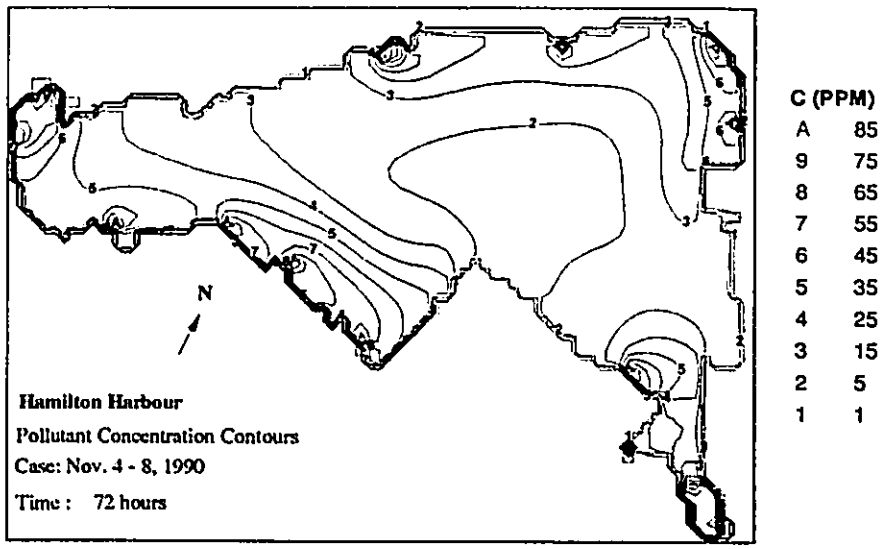

(a)

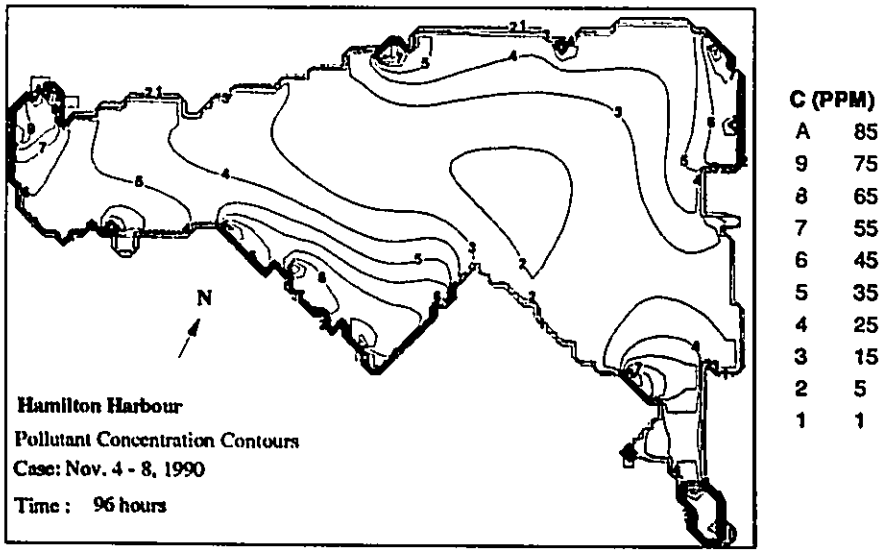

(b)

Fig. 11.11 The simulated concentration contours at (a) 72 hours, and (b) 96 hours after 15 pollutant sources were introduced into Hamilton Harbour (Case = Nov. 4-8, 1990).

equal concentration contours of a pollutant at a fully mixed state at four locations under the west wind. It clearly presents the extent and outline of the pollutant released at different locations. For locations B and D, the currents were highly advective (see Fig. 11.3). Consequently, the pollutants were moved away from the initial location at the same time of diffusion. In contrast, the pollutants mainly stayed around A and C after being released due to the existing weak current and well-mixed eddy around these locations. Figs. 11.13(a), (b), (c), (d) show the curves of C_{max} as a function of time, and, (e) the mixing time at A, B, C, D under the four wind conditions. In general, the horizontal mixing times in Hamilton Harbour are about one to two days, and over three days in some wind directions and locations (west wind at C and south wind at A).

It should be pointed out that the mixing time may become longer for lower wind speeds. It also depends on the horizontal dispersion coefficient (a typical value of 0.5 m^2/s (McCorquodale et al., 1986) was used in the simulation). Sensitivity tests of wind speed and the dispersion coefficient can be easily undertaken.

11.2 A NESTED-GRID MODELLING TECHNIQUE FOR NEAR-SHORE AREAS

11.2.1 Modelling Approach for Nearshore Areas in Lakes

Nearshore areas are the largest environmental concerns because they directly receive the effluent from outfalls and rivers. Obtaining the detailed current pattern is essential to the water quality modelling and design of any remedial measures. It is necessary to employ a high resolution or fine grid model for better representing the complicated shoreline, including small in/outflow and sewage sources. It is impossible to employ such a fine grid model for the whole

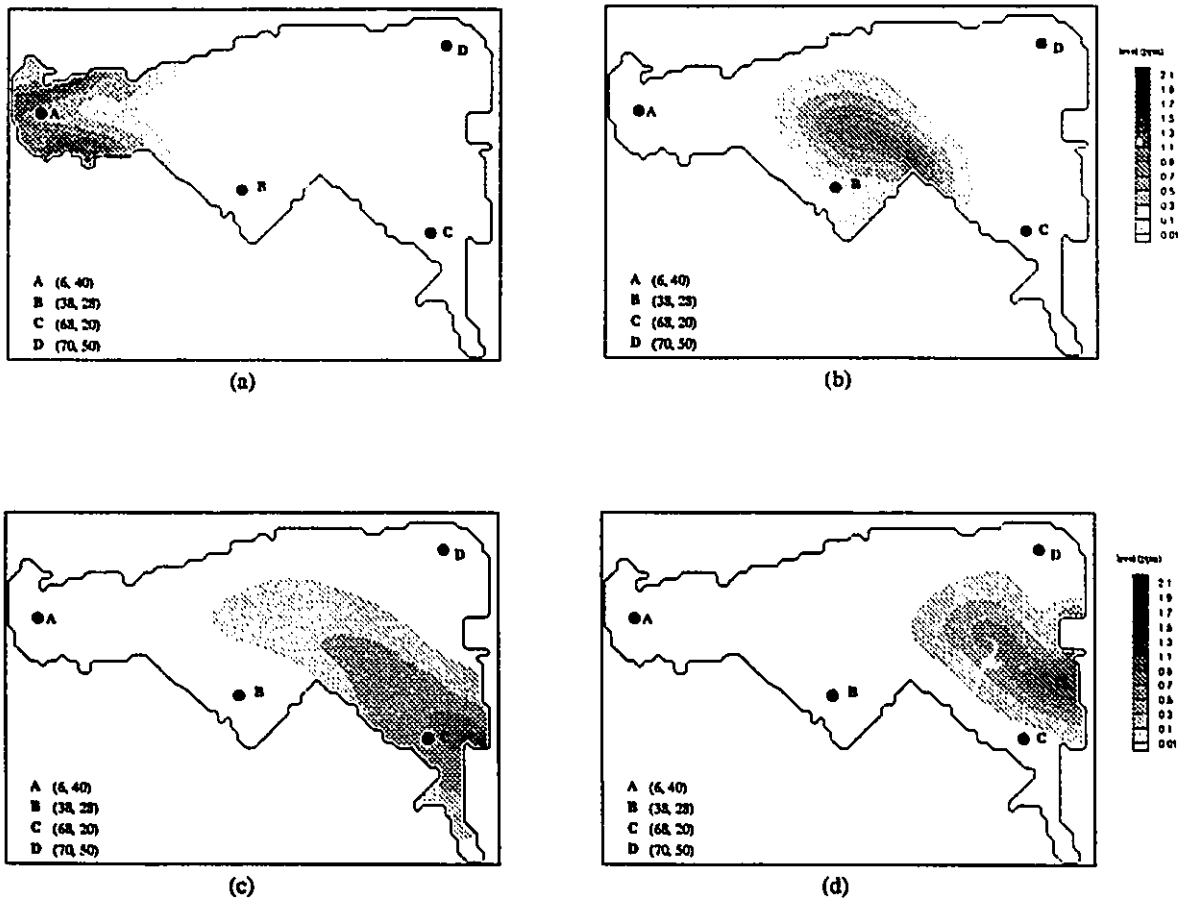

Fig. 11.12 Numerical experiment on the horizontal mixing time scale in Hamilton Harbour: equal-concentration contours when a block of 100 ppm pollutant released from various locations are fully mixed under a 10 m/s west wind, (a) at location A (west basin), (b) at location B (south shore), (c) at location C (southeastern shore) and (d) at location D (northeastern corner).

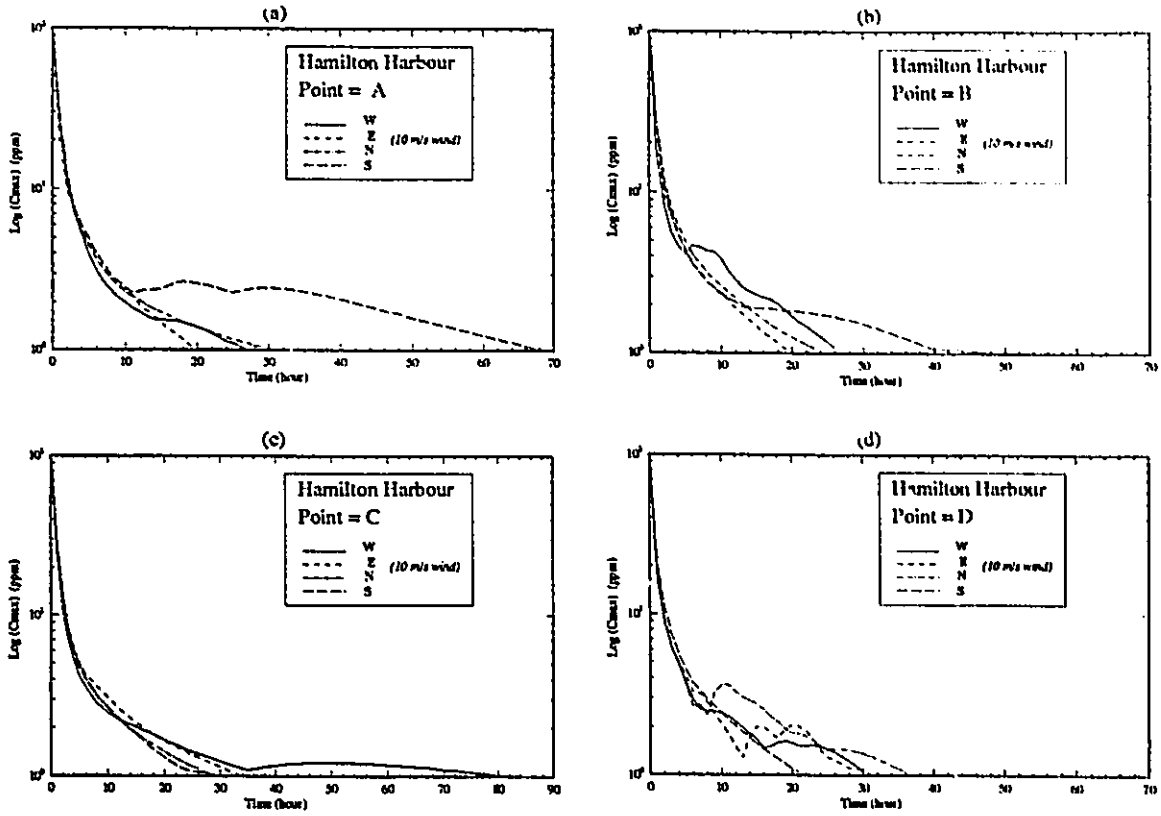

(e)

point \ wind / time (h)	W (10 m/s)	E (10 m/s)	N (10 m/s)	S (10 m/s)
A	27.01	24.09	30.55	68.64
B	27.00	20.19	24.75	48.11
C	82.97	34.07	29.26	29.93
D	30.61	31.28	36.92	21.60

Fig. 11.13 Numerical experiment on the horizontal mixing time scale in Hamilton Harbour: time series of maximum concentration under a 10 m/s wind with four typical four wind directions (W, E, N, S) at (a) location A, (b) location B (c) at location C, (d) at location D; (e) horizontal mixing time at A, B, C, and D under the four wind conditions. (the time, taken for a block of 100 ppm pollutant block of 100 ppm pollutant to be fully mixed to level of 1 ppm).

basin, an efficient and reliable method must be developed.

In recent years, a two-dimensional circulation model (RAND) was developed to simulate water movements in the nearshore areas of Lake Ontario, i.e., the Toronto Waterfront, using *in-situ* measured current as the open boundary conditions (MOE, 1989). However, there were a few major problems: (a) the field observations are expensive; (b) a coarse current meter array fails to provide the detailed structure on the open boundaries because the boundaries are complicated and currents varies with wind conditions, and no interpolation can follow such changes; and (c) measurement cannot provide water elevations at each mesh along the open boundaries. That may cause the violation of continuity and artificial eddies near open boundaries. Finally, this technique cannot *predict* circulation and transport which is an important aspect of the model's application, because the model is driven by the measured current or water level at the open boundary. As a result, a better approach is required.

Numerically, two approaches can be employed. The first approach is to formulate free radiation boundary conditions which allow disturbances to 'radiate' out of the modelling domain with a minimum amount of boundary reflection. Descriptions of such boundary conditions can be found in Miller & Thorpe (1981), and Krestenitis (1987). The most frequently used method is the Sommerfeld condition, with its modified form. Krestenitis (1987) presented five different open boundary conditions, constructed from the free radiation, Neuman and Sommerfeld conditions, for the open-sea boundary of a coastal area. The behaviour of those open boundary conditions were examined by the application of the model to the Thermaikos Gulf, in Greece. The results, in terms of free surface contours and current circulation pattern, are not always realistic, especially for the water elevation. Besides, it is difficult to verify those open boundary conditions, in terms of the circulation pattern and water elevation field.

The second approach is the grid nesting method whereby a much larger domain such as the whole lake or harbour is first modeled using a coarse grid model, along with the evolving fields, which are used to determine the boundary conditions for the sub-boundary. This technique is widely used in meteorological science. Murthy, Simons and Lam (1986) applied this method to the transport modelling of the Niagara River plume in Lake Ontario. However, there are no detailed descriptions of numerical schemes, and some results were speculative.

For ocean coastal modelling, it is necessary to first use the approach for the open boundary condition for large areas. Tide elevation is driven by the observation data (Blumberg, 1987). The second approach might be used for bays or nearshore areas in the oceans (Crean, Murty and Stronach, 1988). However, it is more feasible to employ the nested-grid modelling approach for the nearshore areas in lakes, because unlike in oceans, the whole lake can first be modelled using the coarse grid model. The primary objective of this section is to achieve the satisfactory operation of a limited area model with the employment of the nested-grid modelling technique.

11.2.2 A Nested-Grid Modelling Technique

A nested grid system consists of small, fine grid domains embedded in larger, coarse grid domains. The depths in the fine grid model could be re-schematized from hydrographic charts for a better representation of topography, as well as for other engineering designs. In order to remain unaffected by local changes in depths, the open boundaries with the coarse grid model should be located far away from the region of interest. Also, it is better to keep the same depth along the open boundaries in the fine grid model to ensure the conservation of transport.

Open boundary conditions can be obtained for the fine grid model from the coarse grid model. The water elevations and velocities at open boundaries in the coarse grid model are stored at certain time intervals, such as 15 minutes or one hour. The time step used in the fine grid model is usually smaller that the one used in the coarse grid model. Therefore, a temporal interpolation scheme is needed to provide the corresponded values in the open boundary for the fine grid model at each time step.

Spatial interpolation is necessary to prescribe the velocities and elevations along the open boundaries from the coarse grid model. Simple interpolation can be used here. The errors introduced are small, because the interpolation is within one grid. Only the elevation and one velocity component need such an interpolation (u component at southern and northern boundaries and v component at western and eastern boundaries); while another component can be directly prescribed from the coarse grid model. A typical interpolation for a western open boundary for a fine grid model with the grid size of one quarter of the coarse grid size is shown in Fig. 11.14(a), along with the variable arrangement. The spatial interpolation schemes are

$$u_1 = u_2 = u_3 = u_4 = U_{ij} \tag{11.1}$$

$$v_1 = V_{ij} \tag{11.2}$$

$$v_2 = v_3 = v_4 = SI(V_{ij}, V_{ij+1}) \tag{11.3}$$

$$\zeta_1 = \zeta_2 = \zeta_3 = \zeta_4 = SI(\zeta_{i-1j}, \zeta_{ij}) \tag{11.4}$$

where, $SI(V1, V2)$ refers to a linear interpolation between two variables $V1$ and $V2$. A more accurate scheme for Eqs. (11.3) and (11.4) may include values from additional neighbouring grids.

There are two methods to prescribe the open boundary conditions: (a) prescribes only the velocity components, and (b) prescribes both the velocities and the elevations. Eventually,

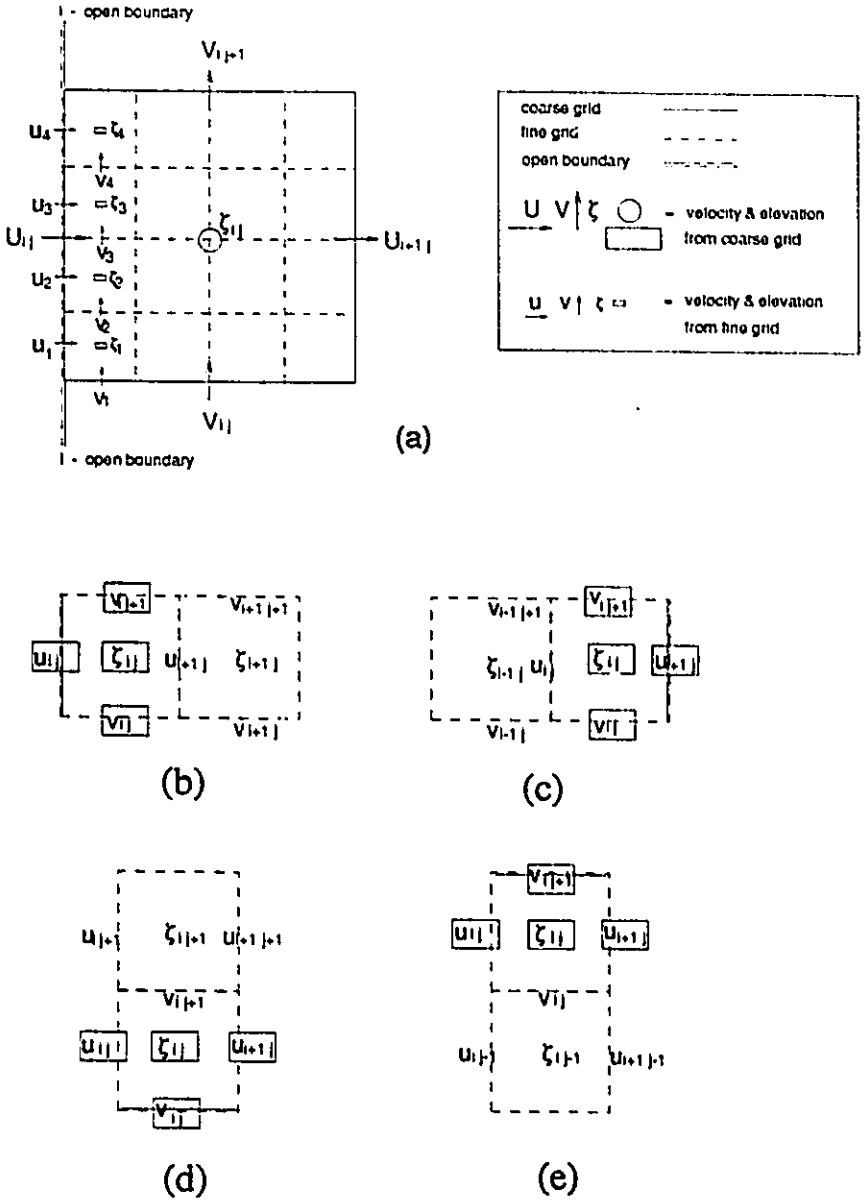

Fig. 11.14 Open boundary conditions in the nested-grid modelling: (a) the detailed variable arrangement and spatial interpolation diagram at a west open boundary mesh in both the overall and fine grid system. The implementation of open boundary conditions for (b) west, (c) east, (d) south and (e) north open boundary in the fine grid system.

method (b) will be used in this study, because both velocity and elevation along an open boundary can be derived from the coarse grid model. The arrangement of velocity components for the different open boundaries, i.e., north, south, east and west, are different, as shown in Figs. 11.14(b), (c), (d), (e), respectively. This arrangement results in additional complexity in the calculation program, yet the mass continuity is satisfied.

11.3 MODELLING THREE NEARSHORE AREAS IN HAMILTON HARBOUR

11.3.1 Remedial Action Plan

There are over 40 recommendations under the Remedial Action Plan (MOE report, 1992) for the Hamilton Harbour. Six of them are shown in Fig. 11.15. Except for Pier 27 and the Windermere Basin, the three areas, i.e., North Shore & Waterfront Park and Pier 4, together form the Western Basin (Area I), LaSalle Park Waterfront (Area II) and Northeastern Shoreline (Area III), will be the target areas in this study. New artificial islands are proposed for these nearshore areas, which will help protect the shoreline, promote fish and waterfowl habitat, and act as public access for fishing and wildlife appreciation.

Before any of these projects can proceed, the federal environmental review process will screen the implications of the projects with respect to impact on both the natural and the social environment. It is therefore necessary to know (a) the existing state of current movement within the Harbour under various wind and environmental conditions; (b) the effect of islands on currents; and (c) the effect of islands on pollutant transport. It is both difficult and expensive to construct any conventional physical models for the above task. Therefore, there is a requirement to develop a numerical modelling system for the simulation of hydrodynamics and water quality

as an evaluative tool for the assessment of various options. The developed nested-grid modelling technique is used for such a purpose, where a coarse grid is designed for the whole Harbour, and a fine grid for nearshore areas.

11.3.2 A Nested-Grid Model

A nested-grid system for Hamilton Harbour and three nearshore areas, i.e. Western Basin, LaSalle Park Waterfront and Northeastern Shoreline is presented in Fig. 11.16 and Table 11.1, where a coarse grid of 100 m X 100 m is used for the whole Harbour, and a fine grid of 25 m X 25 m for the three areas. As mentioned, the coarse grid model for the Harbour is rotated 23.4 degrees clockwise from the North, for better representation of the eastern and northern shorelines. Likewise, the fine grid model for the three nearshore areas are also rotated in same manner. The shorelines and topography in the fine grid models are modified to include detailed variations which are unable to be represented in the coarse grid model for the whole Harbour. It is expected that such modifications will have little effect on the simulation.

Table 11.1 Parameters of the nested-grid model for three nearshore areas in Hamilton Harbour

Name	Area	Grid	Size	imax	jmax	Open B.
Hamilton Harbour		coarse	100 m	79	57	
Western Basin	Area I	fine	25 m	75	79	1
LaSalle Park Waterfront	Area II	fine	25 m	63	43	3
Northeastern Shoreline	Area III	fine	25 m	35	67	2

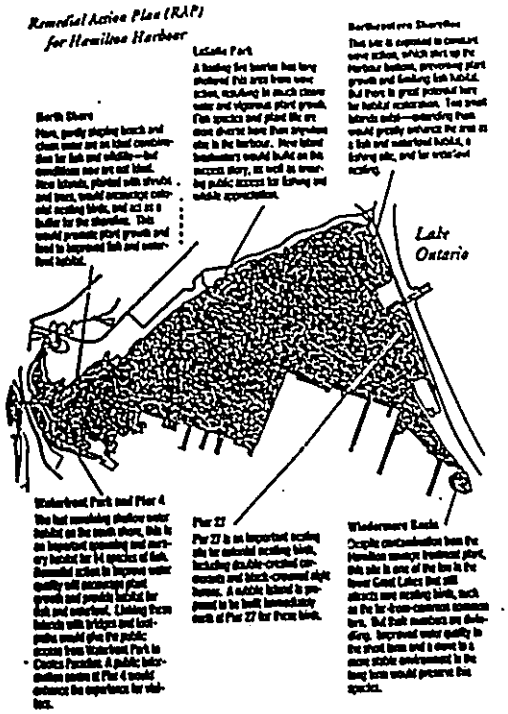

Fig. 11.15 Locations of major remedial action plan in Hamilton Harbour (MOE, 1992).

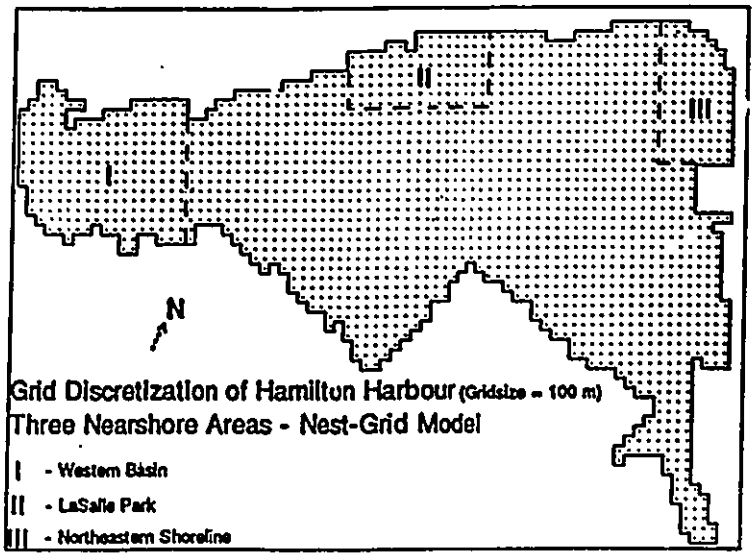

Fig. 11.16 A nested-grid modelling system for Hamilton Harbour and three nearshore areas, i.e., Western Basin (I), LaSalle Park Waterfront (II) and Northeastern Shoreline (III). The grid size is 100 m for the coarse-grid model and 25 m for the fine-grid model.

11.3.3 Circulation Patterns

Obviously, to justify the nested-grid modelling technique, the overall standard is whether both the circulation and water elevation from the fine grid model is the same as the those from the coarse grid model for the modelling area.

The simulated circulation patterns by the VHI3D model from the coarse and fine grid models under a 10 m/s west wind for the three nearshore areas are presented in Figs. 11.17, 11.18 and 11.19, respectively. Because the shorelines are mostly straight, strong flow belts parallel to the shorelines have always existed close to the shorelines: west to east for the western and southern winds, and east to west for the eastern and northern winds. In the case of both west and east winds, the belts are stronger because these wind are parallel to the shorelines. Weak eddies exist in the open water areas. Compared to the results from the coarse grid model, the fine grid model keeps conformity while, it reveals a more detailed resolution of the velocity field. As in the case of north and west winds, the weak gyre in the central area becomes more detailed in the fine grid model. In the case of a south wind, two gyres are evident in the fine grid model which are not clear in the coarse grid model. Detailed currents are also provided close to the shorelines, where the grids in the coarse grid model are too coarse to reflect detailed features.

For the purpose of comparison, a total kinetic energy (KE) in the simulation at each time step is computed from the sum

$$KE^n = \sum_{i=1}^{i=imax} \sum_{j=1}^{j=jmax} \left((U_{ij}^{\,n} + U_{i+1j}^{\,n})^2 + (V_{ij}^{\,n} + V_{ij+1}^{\,n})^2 \right)(h_{ij} + \zeta_{ij})\Delta x \Delta y / 8 \qquad (11.5)$$

It is also can be used as a steady criterion in the simulation, i.e., the steady state is reached when the ratio $|KE^{n+1} - KE^n|/KE^{n+1}$ becomes less than a test convergence value (10^{-5}). The kinetic energy for a 10 m/s west wind in both the coarse and fine grid models for the LaSalle Park

Waterfront is illustrated in Fig. 11.20. The curves are very close, indicating that the fine grid model was successful. The small amount of difference is due to a slight change in bathymetry. The whole lake seiche (oscillation) may have some effect on this local area, in the coarse grid model.

Because that the realistic water elevation field in a nearshore area largely depends on the relative location in the whole lake. The model, using direct open boundary conditions such as free radiation or the Sommerfeld open boundary conditions, are hard to reflect the effect of the relative location. As a result, it is not surprising that the water elevation field is very difficult to be simulated (mass continuity is not satisfied), when using the direct open boundary conditions as tested by Krestenitis (1987). However, using the nested-grid modelling technique developed in this study, the water elevation field is dramatically well simulated. The flooding contours clearly display the distribution of water elevations for various wind conditions. Fig. 11.21 presents the contours of wind-induced elevation in LaSalle Park Waterfront under a 10 m/s west wind. The elevations from the fine grid model agree well with the ones from the coarse grid model. Contours for other conditions again are in good agreement.

11.3.4 Remedial Measures

The consulting team working on this project has proposed a series of preliminary locations of artificial islands for each area. The VHI3D hydrodynamic model and the two-dimensional pollutant transport model are used to examine the effects of islands on the current and pollutant transport. In the western basin, preliminary proposed islands were tested. For many reasons, no islands will be built in this area. As a result, the feasibility studies will focus on the LaSalle Park Waterfront and Northeastern Shoreline.

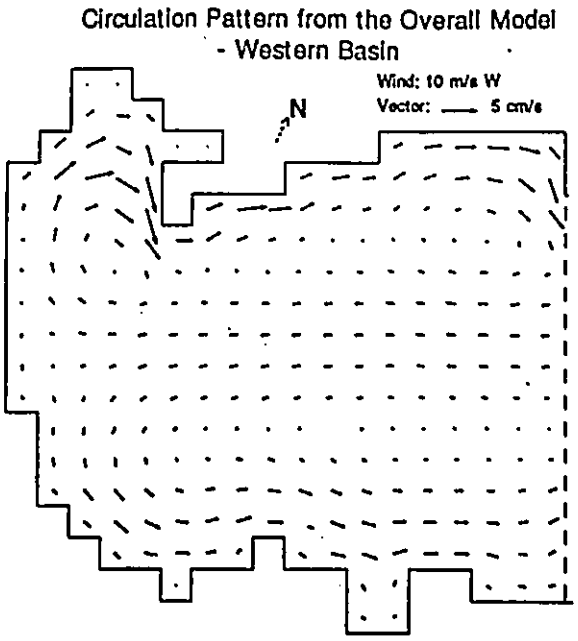

(a)

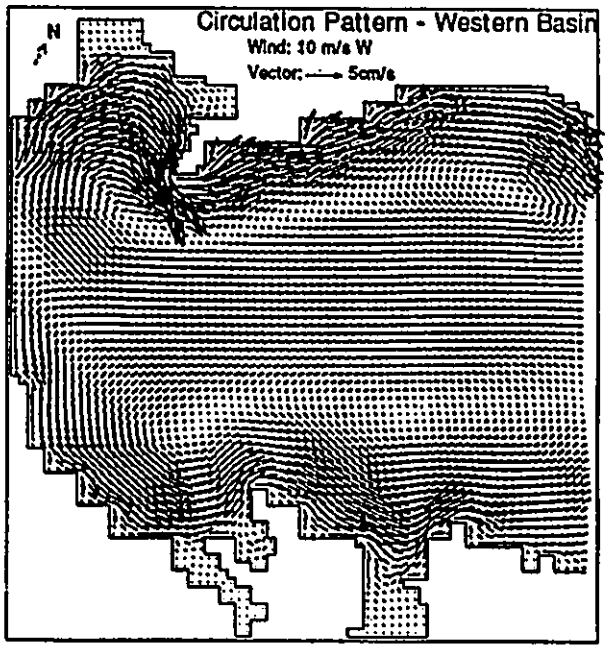

(b)

Fig. 11.17 The simulated depth-averaged circulation pattern in Western Basin, for a 10 m west wind from (a) the overall (coarse-grid) model, and (b) the fine grid model.

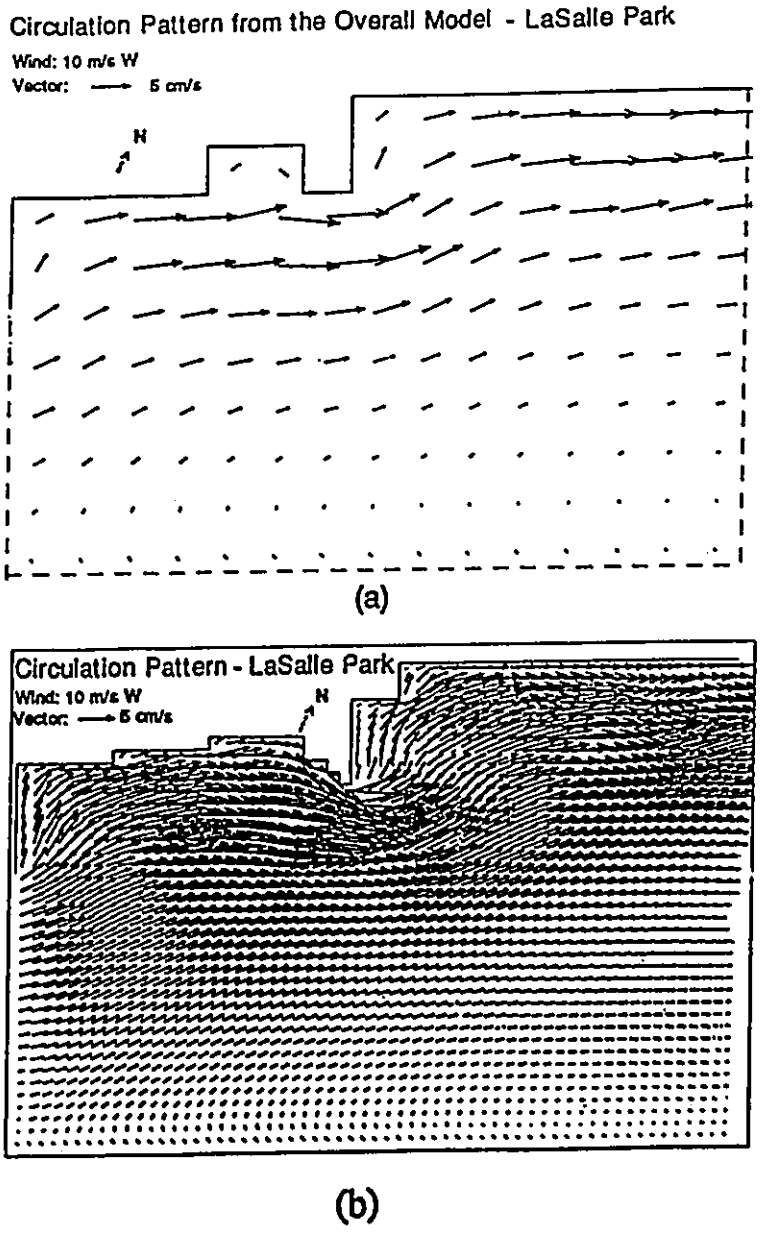

Fig. 11.18 The simulated depth-averaged circulation pattern in LaSalle Park Waterfront, for a 10 m west wind from (a) the overall (coarse-grid) model, and (b) the fine grid model.

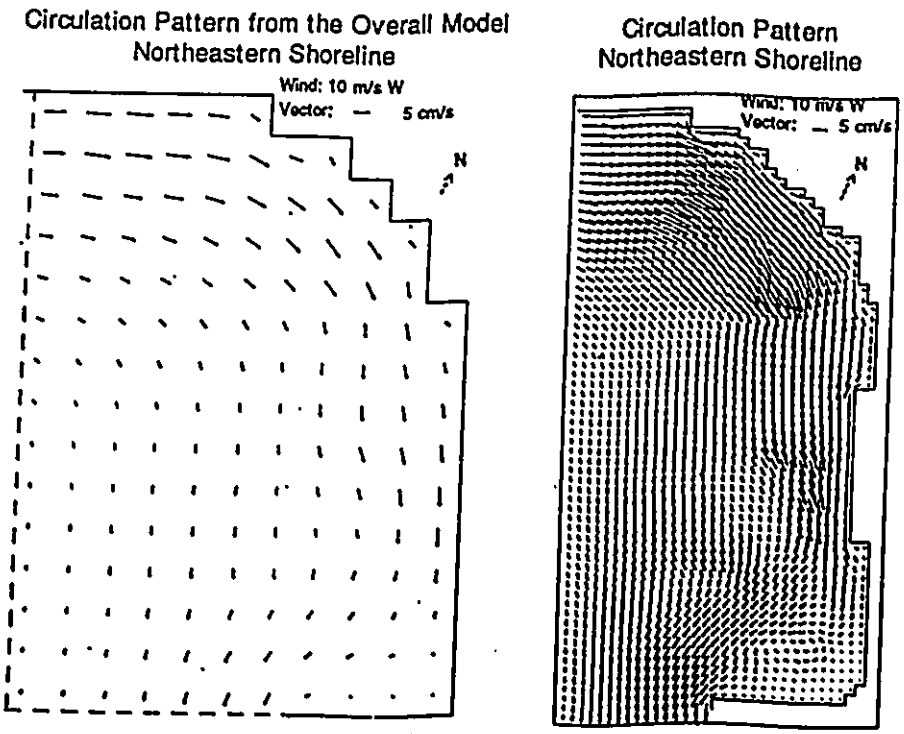

Fig. 11.19 The simulated depth-averaged circulation pattern in Northeastern Shoreline, for a 10 m west wind from (a) the overall (coarse-grid) model, and (b) the fine grid model.

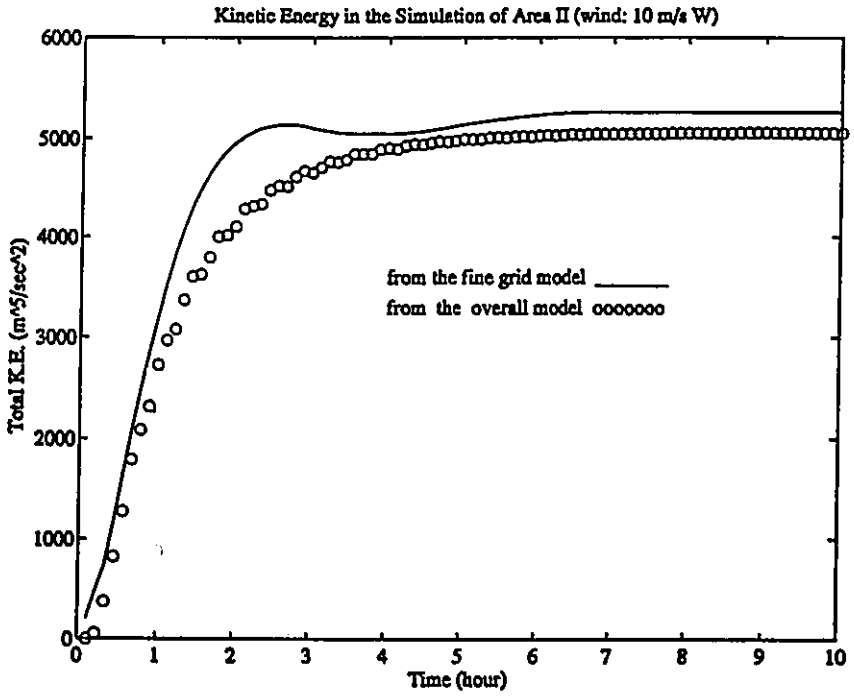

Fig. 11.20 The kinematic energy process in the simulations from both the overall and fine-grid model of LaSalle Park Waterfront for a 10 m east wind.

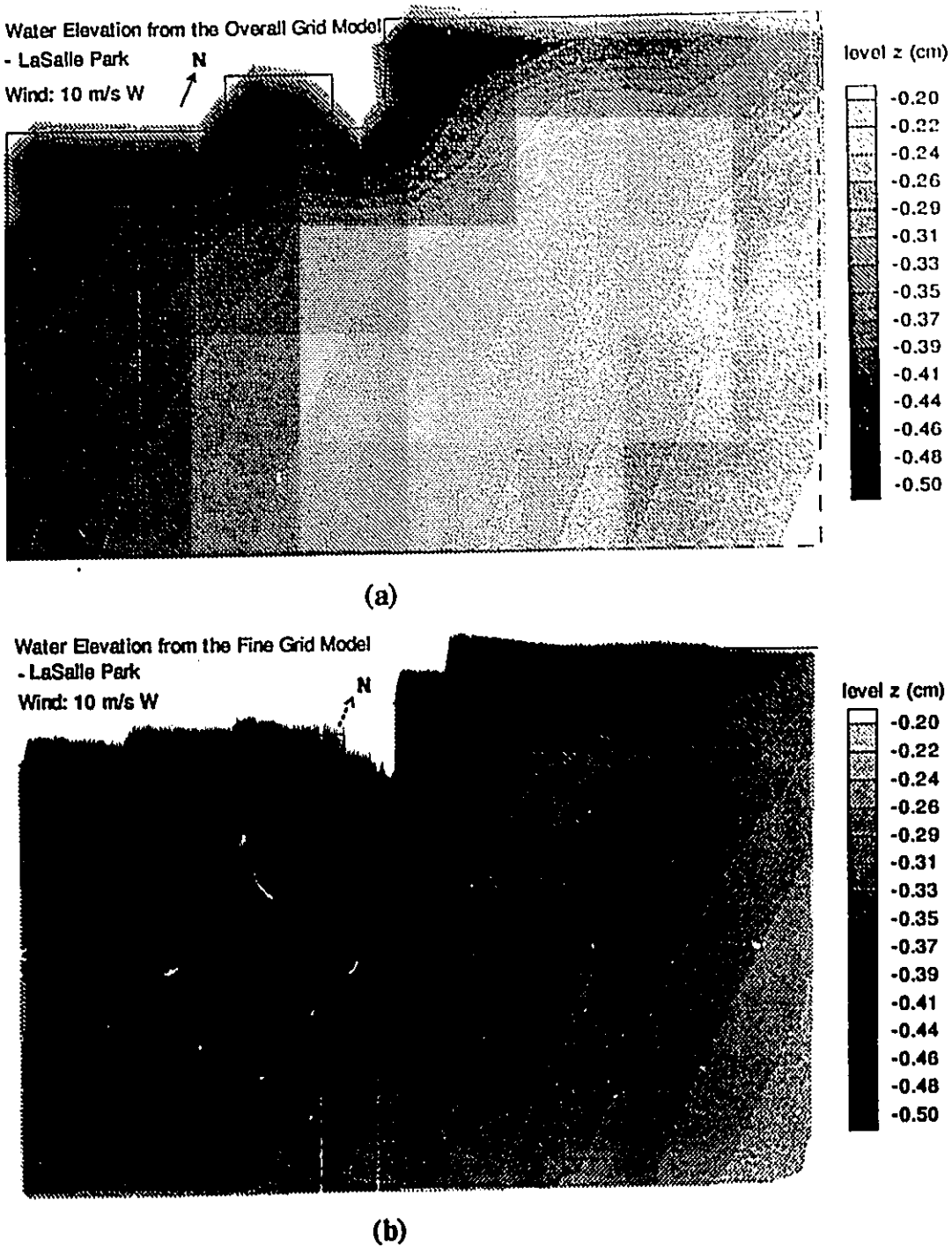

Fig. 11.21 The water elevation fields in LaSalle Park Waterfront for a 10 m west wind from (a) the overall (coarse-grid) model, and (b) the fine-grid model.

Table 11.2 Features of concentration time histories (10 m/s W; LaSalle Park Waterfront)

Point	C_{imax} (ppm)	C_{max} (ppm)	T_i (h)	T (h)	A_i/A
C 1	27.53	21.73	6.50	4.67	1.31
C 2	2.47	22.69	13.17	5.33	0.19
C 3	2.81	9.73	12.50	5.17	0.47
C 4	1.81	7.18	15.33	13.17	0.35
C 5	1.69	5.83	15.17	12.50	0.41
C 6	1.24	3.37	21.00	15.83	0.59
C 7	0.75	2.58	16.17	13.17	0.41
C 8	26.68	26.31	16.67	13.67	0.95
C 9	50.09	52.72	8.83	5.17	0.99
C10	0.00	0.00	0.00	0.00	0.00

C_{max} = *maximum concentration (without islands)*

C_{imax} = *maximum concentration (with islands)*

T = *duration of pollutants with concentration above zero (without islands)*

T_i = *duration of pollutants with concentration above zero (with islands)*

A = *area under the concentration curve (without islands)*

A_i = *area under the concentration curve (with islands)*

In the LaSalle Park Waterfront, two proposed configurations of artificial islands were tested by the model. The proposed final design is presented in Fig. 11.22(b). The major island will be built on the south side of LaSalle Park, away from the shore, but attached via bridges. Two small islands will be built in the north east corner of the park, together with several underwater islands (using half depth in the model). The effect of islands on the current pattern is obvious, as indicated in Fig. 11.22 for a 10 m/s west wind. Pollutants from two sources were introduced. Fig. 11.23 shows the equal concentration of pollutants at various times with and without islands. Fig. 11.24 shows the time series of concentration at ten locations (C1 to C10) of concern. The pollutant from the eastern source has no effect on this area under west wind. The

main island blocks the pollutant from the western source, and as a result, the concentrations at all locations except C1, C8 and C9 were lower, compared with the case without islands. Table 11.2 presents the assessments in the LaSalle Park Waterfront under the west wind. The reduction of peak concentration and concentration exposure were clearly presented.

Table 11.3 Features of concentration time histories (10 m/s N; Northeastern Shoreline)

Point	C_{imax} (ppm)	C_{max} (ppm)	T_i (h)	T (h)	A_i/A
C1	16.35	16.28	23.83	23.17	1.00
C2	1.92	1.94	21.50	20.83	1.01
C3	10.99	10.86	23.50	23.33	1.02
C4	6.15	7.43	22.50	20.83	0.96
C5	8.71	8.86	22.83	23.00	1.00
C6	8.10	8.20	22.00	22.33	0.98
C7	6.80	7.74	22.00	22.17	1.06
C8	9.47	9.41	23.33	21.67	1.07
C9	7.64	7.87	21.50	21.67	0.97
C10	6.55	7.45	21.50	21.50	1.05

C_{max} = *maximum concentration (without islands)*

C_{imax} = *maximum concentration (with islands)*

T = *duration of pollutants with concentration above zero (without islands)*

T_i = *duration of pollutants with concentration above zero (with islands)*

A = *area under the concentration curve (without islands)*

A_i = *area under the concentration curve (with islands)*

In the Northeastern Shoreline, three alternatives of island configurations including 8 small islands along eastern shorelines have been preliminarily proposed, and numerically studied. The proposed final design is shown in Fig. 11.25(a). It can be seen from the last section that the clockwise circulation parallel to the shoreline exists in the case of north and west winds, while counter-clockwise patterns for south and east winds. There are two major pollutant

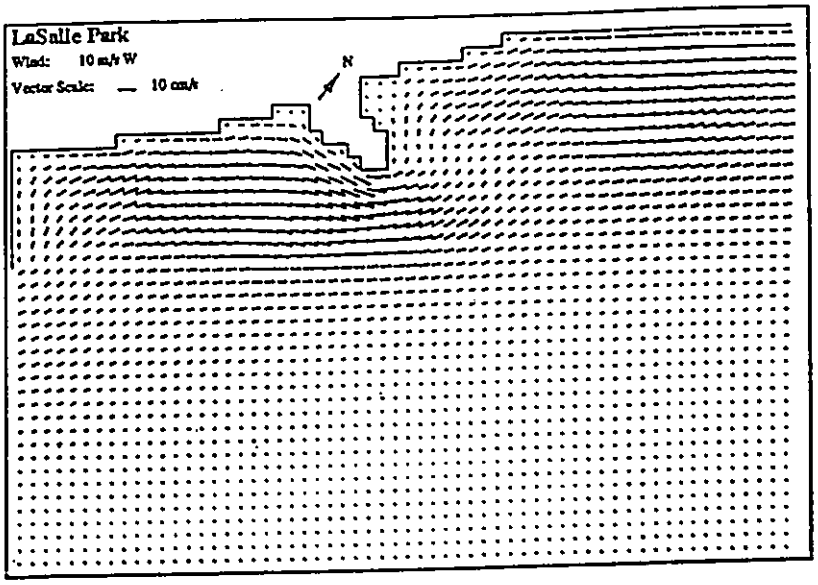

(a)

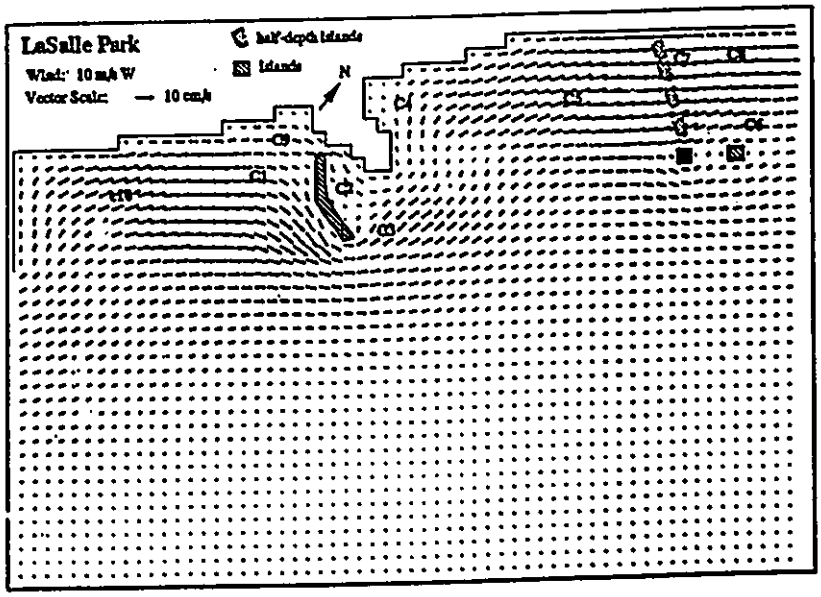

(b)

Fig. 11.22 Remedial measures in LaSalle Park Waterfront: (a) the circulation pattern without islands, and (b) the circulation pattern with islands (final design) from the fine grid model of the basin. (A 10 m/s west wind was applied).

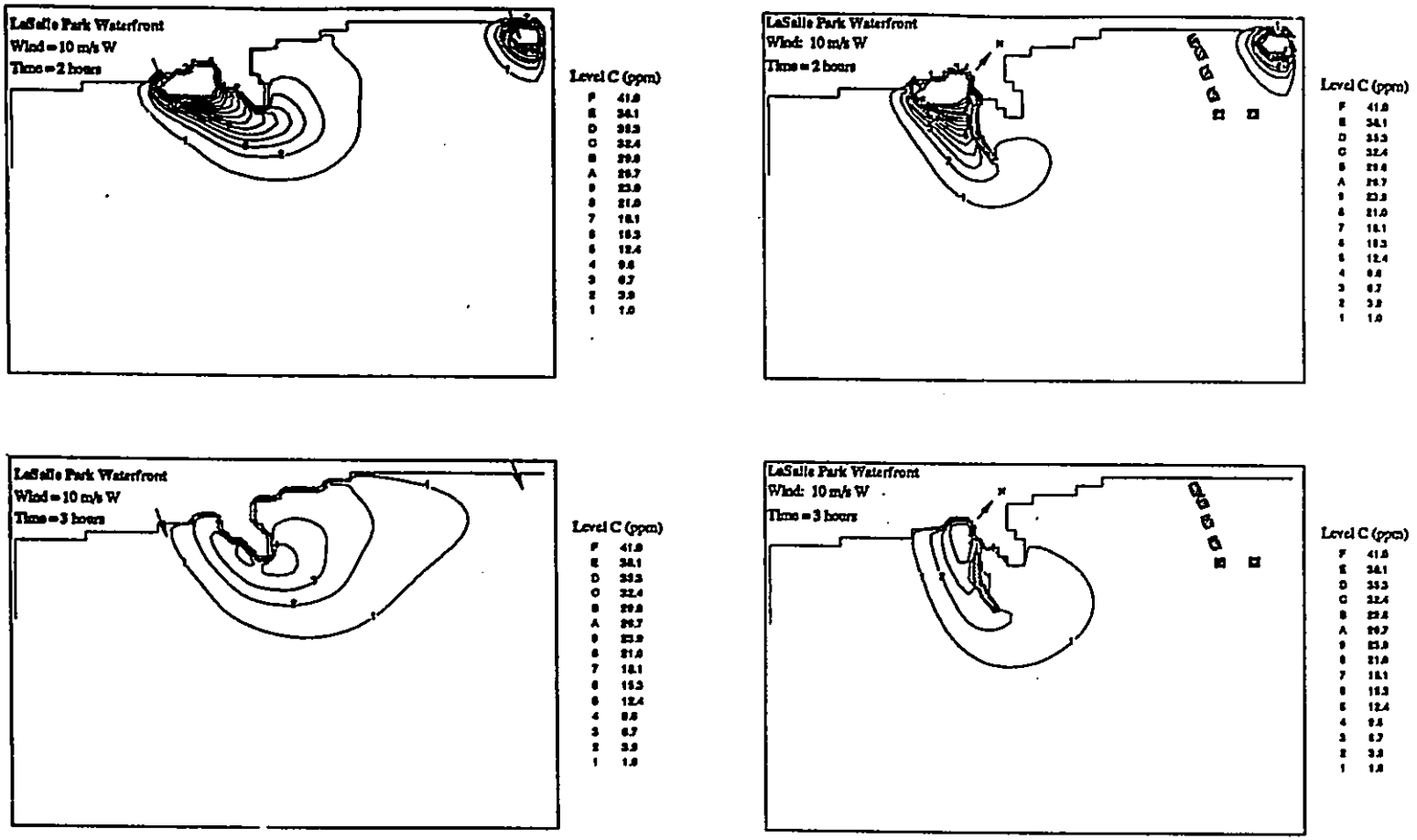

Fig. 11.23 The contours of pollutant concentration in LaSalle Park Waterfront from the fine grid model without and with islands under a 10 m/s west wind, 2, 3 hours after the cessation of 2 hour emission of pollutant from two sources.

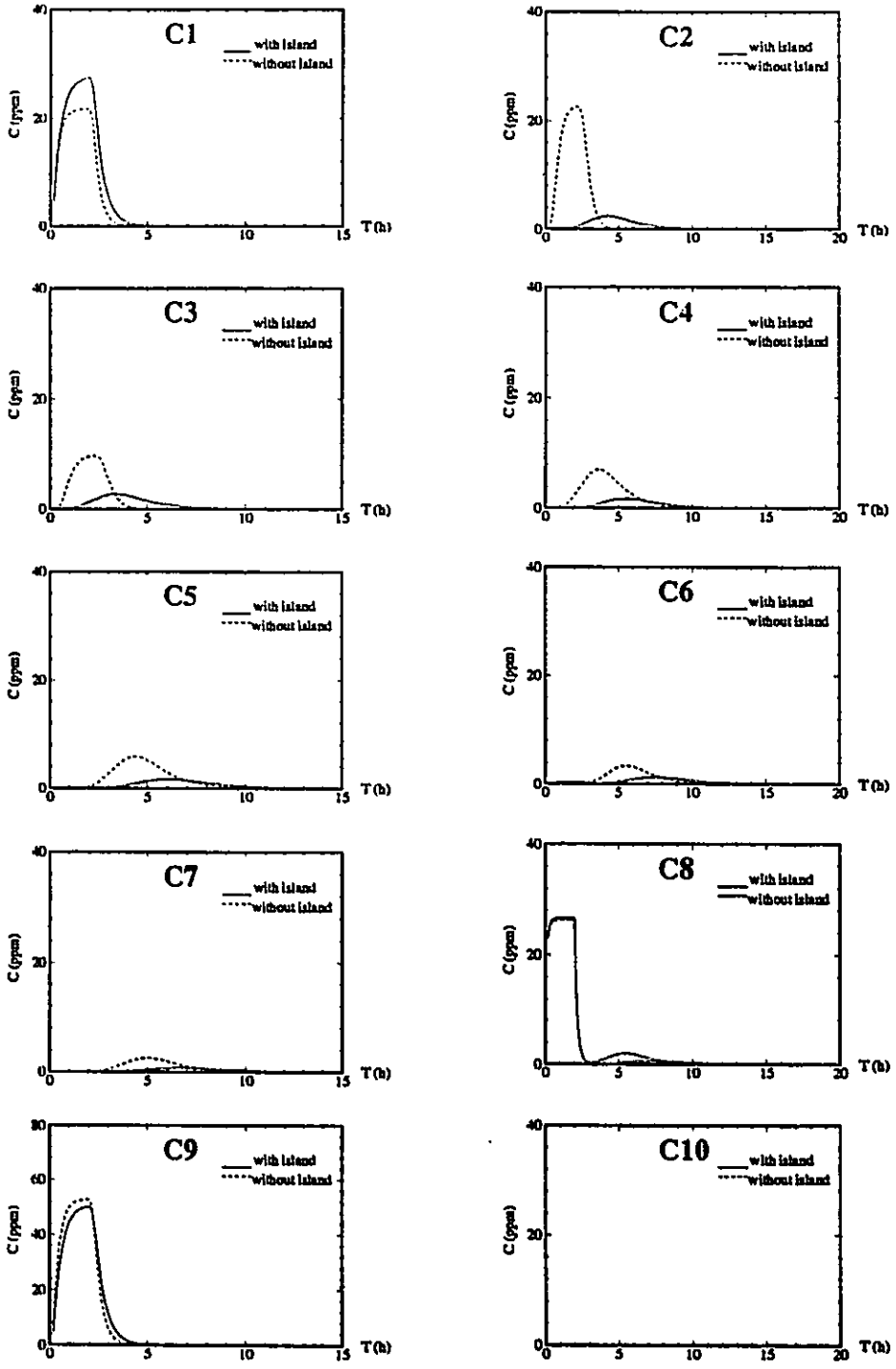

Fig. 11.24 Time series of pollutant concentration at ten locations of concern in LaSalle Park Waterfront without and with islands, under a 10 m/s west wind.

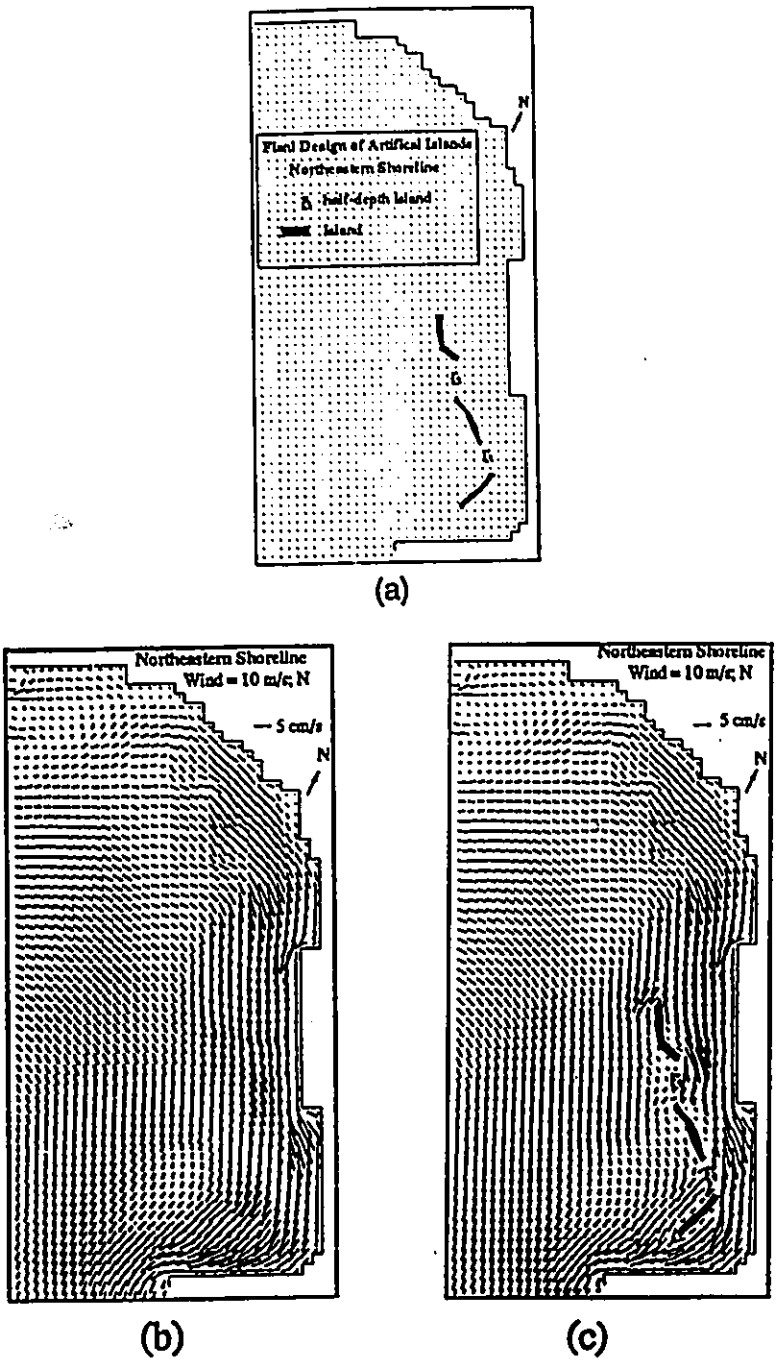

Fig. 11.25 Remedial measures in Northeastern Shoreline: (a) configuration of artificial islands in the final design, (b) the circulation pattern without islands, and (c) the circulation pattern with islands from the fine grid model. (A 10 m/s west wind was applied).

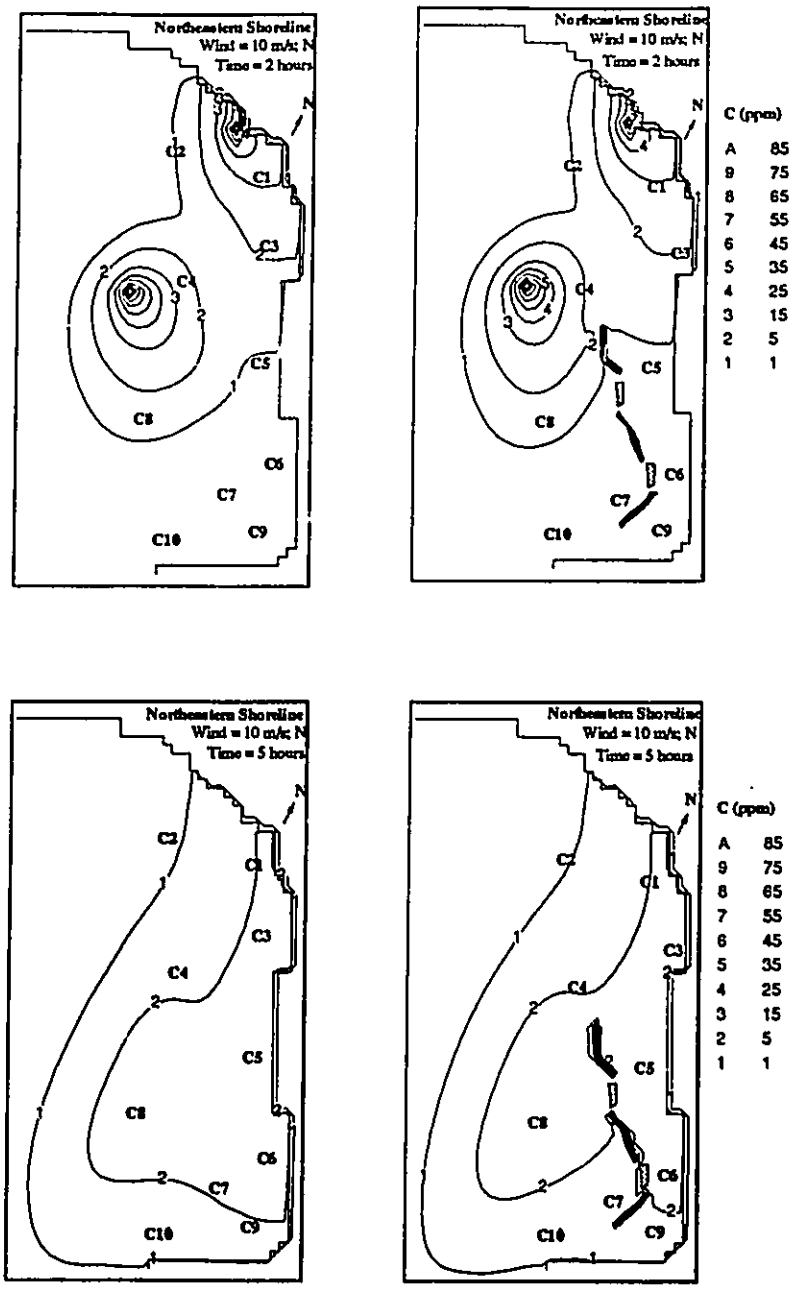

Fig. 11.26 The contours of pollutant concentration in Northeastern Shoreline from the fine grid model without and with islands under a 10 m/s west wind, 2, 5 hours after the cessation of 2 hour emission of pollutant from two sources.

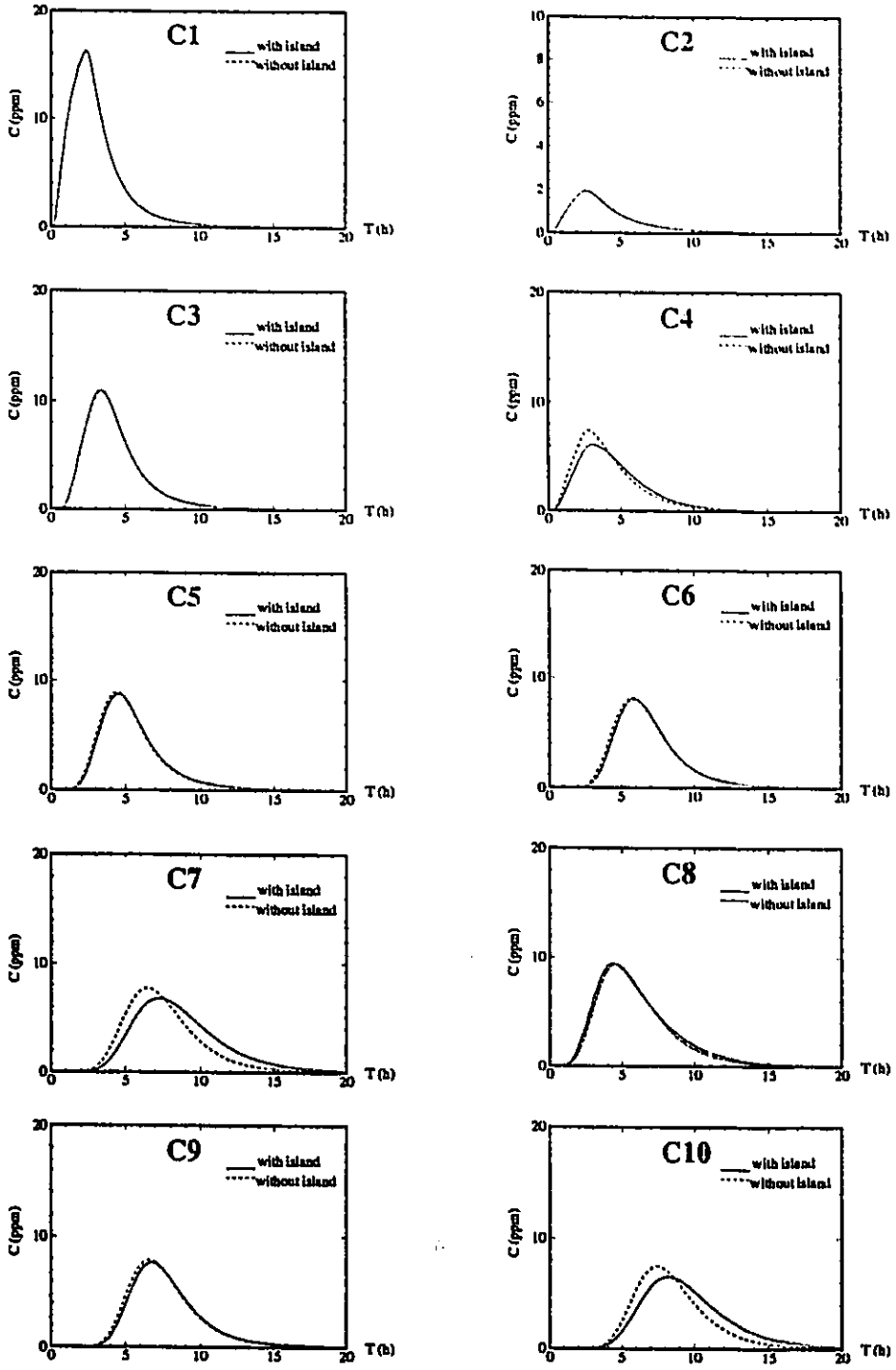

Fig. 11.27 Time series of pollutant concentration at ten locations of concern in Northeastern Shoreline without with islands, under a 10 m/s north wind.

sources, i.e., one from the Indian Creek, and another from the outfall of the Burlington's STP in the middle of the basin, see Fig. 11.26. The most significant impacts of the islands are expected under the northwest wind. As an example, the north wind case is presented. Fig. 11.26 shows the equal concentration of pollutants at 2 and 5 hours after the pollutant released from the two sources, with and without islands. The concentration curves at ten locations of concern are presented in Fig. 11.27, and, the assessment is listed in Table 11.3. It is observed that the impact of islands is insignificant.

11.4 SUMMARY

The general feature of depth-averaged circulation patterns under various wind conditions has been revealed from the simulation results by the two- and three-dimensional hydrodynamic models. The depth-averaged currents follow the wind close to the shore (aligned in a way to be parallel to the shore), and are against the wind in the middle basin, and deeper part of the Harbour. The major features of the depth-averaged current patterns are: (a) two large eddies with opposite rotation covering almost half of the Harbour's area, and (b) three to four smaller eddies. The model reaches the steady state in less than 2 hours, which indicates that under any wind change, the circulation will be established in a short time. The hydraulically-induced current, due to the inflow/outflow, is much weaker than the wind-induced current due to the large size of the harbour and small inflow/outflow.

A case simulation clearly demonstrates that the pollutant transport model, coupled with the circulation model, is capable of simulating the temporal and spatial distributions of pollutants emitted from multiple sources. With the aid of this modelling system, the horizontal mixing time in Hamilton Harbour is revealed for the first time. In general, the time scale under a 10 m/s wind)

is about one to two days, depending on the location.

A nested-grid modelling technique has been developed in which a coarse grid model is first applied for the whole Harbour, and the velocity and water elevation along the open boundaries are provided for the fine grid model for the nearshore area. The model simulations in three nearshore areas in Hamilton Harbour clearly indicatepwd that the model can predict, in detail, the current structure, while mass conservation is satisfied. The impact of artificial islands was examined by studying changes in current patterns, pollutant peaks, exposure, and flushing time in different locations of concern.

CHAPTER 12

CONCLUSIONS

12.1 ACHIEVEMENTS OF THE PRESENT STUDY

The achievements of this dissertation will be presented in four parts: (a) model developments, (b) model performance evaluations, (c) analysis of field data, and (d) model applications.

12.1.1 Model Developments

Development of various hydrodynamic and pollutant transport models was the essential subject of this dissertation. Specifically:

* A comprehensive review of existing circulation theory and numerical models was achieved.
* A multi-layered three-dimensional circulation model (3D) was developed for both homogeneous and stratified lakes.
* A computationally efficient three-dimensional wind-induced model (VHI3D) was developed using a vertical-horizontal integrating (VHI) approach.
* A nested-grid modelling technique was developed for the simulation of detailed current structure and pollutant transport in the nearshore areas of the Great Lakes.
* Various schemes were proposed to the pollutant transport model, and a second-order

trajectory model coupling with a Monte-Carlo random-walk approach was presented to predict the movement of drogue or drifter in lakes.

* Finally, an integrated lake modelling system (LMS) including all of the above models was developed. The system operates in an interactive environment and is equipped with powerful graphics.

12.1.2 Model Performance Evaluations

Model performance evaluation was an important aspect in model development and application. Creditability and confidence have been established from various model calibrations and verifications with analytical solutions, experimental results and field data. Specifically:

* The depth-averaged circulation model (2DH) was calibrated in the physical model of the Windermere Basin using the measured hydraulically-induced flow pattern.

* The 2D advection-diffusion model was successful in modelling the transport of dye in the physical model of the Windermere Basin. Numerical experiments were executed to demonstrate how the various zones such as advective flow, mixed and dead zones affect the dye transport and distribution.

* Comparison with newly developed analytical solutions and the experimental results obtained by Baines et al. (1965) and Tsuruya et al. (1985) indicate that the multi-layer three-dimensional circulation model (3D) was successful in simulating the wind-induced current. It was found from numerical experiments that the distribution of vertical eddy viscosity plays a very important role in the simulation of the wind-induced current, and, a high resolution of vertical layer discretization must be adopted to precisely predict the surface drift and near

bottom boundary current.

* Comparison among the Q3D, 3D and VHI3D models in a simplified lake basin indicated that the VHI3D model can successfully simulate the three-dimensional wind-induced current with similar and even better accuracy than the 3D model, while significantly less computational time is needed.

* The numerical experiment using the multi-layered 3D circulation model in a stratified basin provided us with some insight of current structure in the presence of temperature stratification.

* Three methods were applied to the model verification with current meter data , drogue trajectories, and water level data during the 1990 & 1991 open water seasons in Hamilton Harbour. The simulation results were found to be in good agreement with the field data. The water level in Hamilton Harbour was governed by the water level in Lake Ontario through the Burlington Canal, while except for the canal region, the currents were mainly determined by the wind and thermal stratification. The statistical criterion for model comparison with drogue trajectory data were established for the first time by employing the trajectory model with a random simulation.

12.1.3 Analysis of Field Data

It is the first time that the statistical features of the current and water level in Hamilton Harbour have been revealed. Specifically:

* The currents in Hamilton Harbour were mainly wind-induced, with the mean speeds of 2.3 cm/s to 4.28 cm/s, and the maximum speeds of 11 to 18 cm/s at mooring current meters. Due

to the complicated shorelines and small size of the basin, dominant current directions were not found.

* The significant peaks of 12.0, 5.22, 2.2 and 1.1 hours which are the astronomical tide and seiche of Lake Ontario were found in the water elevation spectra at all three stations in the Hamilton Harbour, reflecting the effect of Lake Ontario through the Burlington Canal.

* The fundamental seiche of Hamilton Harbour has a period of 22 minutes and an amplitude of 1.0 mm.

* A complete auto- and cross-spectra of the wind, temperature and current have been obtained for Hamilton Harbour.

12.1.4 Model Applications

The developed lake modelling system LMS was applied to the Great Lakes and their tributaries, including Sarnia Bay and Hamilton Harbour. Specifically:

* The Q3D and VHI3D circulation models are used to efficiently predict the three-dimensional circulation patterns in the Great Lakes including Lake St. Clair. The results were used as a database for the Atmospheric Environment Service (AES) of Environment Canada in order to predict spill movement in the event of a marine oil-spill emergency.

* The integrated two-dimensional hydrodynamic/pollutant transport model was applied in the St. Clair River in Sarnia to study the bacterial pollution, as well as the feasibility of various remedial measures. This study provides a general approach to other environmental concern areas in the Great Lakes where remedial action plans are required.

* The general feature of depth-averaged circulation patterns under various wind conditions has been revealed from the simulation results by the two- and three- dimensional hydrodynamic models. A pollutant transport model coupled with the circulation model was employed to predict the temporal and spatial distributions of pollutants emitted from multiple sources. With the aid of this modelling system, the horizontal mixing time in Hamilton Harbour was revealed for the first time.

* A nested-grid model was applied to the entire Hamilton Harbour in a 100 m grid, and three nearshore areas in a 25 m grid for the simulation of wind-induced circulation patterns and pollutant transport. The effect of various configurations of artificial islands was examined and final recommendations on the engineering design of islands were made for appropriate authorities.

12.2 RECOMMENDATIONS FOR FURTHER STUDY

12.2.1 Model Aspect

Although many efforts were made in the model development, some considerations remain for further study.

It should be pointed out that the horizontal eddy viscosity was often taken as a constant. It only affects the magnitude of current, and has less effect on the current pattern. The proper value may be determined through calibration and verification processes, such as the work in the model of the Windermere Basin. The vertical eddy viscosity significantly affects the prediction of the vertical current structure. Although a parabolic distribution was proven to be appropriate in simulating countercurrent flow, and while a sophisticated turbulence model may

be used in the lake circulation models, much more computational effort is required. Verification of turbulence models still needs to be studied. Furthermore, the formulation of the effect of thermal stratification on the vertical eddy viscosity requires further study.

Wave-induced current was excluded in the developed circulation model, through it may be significant in the nearshore areas in lakes, where the water is shallow and the wave is refracted and broken. It may be included in the circulation model through wave-induced shear stress terms, which are evaluated by wave period or height direction and fetch.

12.2.2 Model Verification & Field Study

Complete model evaluation has been undertaken this dissertation. It was found that the numerical circulation model was excellent in simulating the countercurrent flow in the closed channel, and hydraulically-induced flow in the physical model. However, it was not effective in modelling current in natural lakes. The reasons behind this finding involve many aspects. In the closed channel and physical model of lakes, the force (wind or in/outflow) was uniquely applied, and the domain was simple. In contrast, many factors such as unsteady and uneven winds, topography, shorelines and thermal stratification were involved in the natural lakes. The representation of the natural basin may be distorted in the numerical model, and, the model input may be spatially and temporally insufficient. For example, a significant difference of wind speed and direction over Hamilton Harbour (only 8 km x 7 km) was detected by the scientists at CCIW. It was due to the differences found around the Harbour (city and plants along the north and south shores, open land and water along west and east shores). As a result, a constant wind over the whole Harbour in the model may not suitable. On the other hand, the error due to the instruments may be involved in the field current data, which should be carefully analyzed. From the results in

the verification with field data, it was realized that a well-designed field observation program is still required, in which up to six meteorological buoys and high resolution moored current and temperature meter arrays should be deployed, to obtain the temporal and spatial features of the wind and currents in the field.

12.2.3. Model Application Aspect

The developed 3D circulation transport model may be coupled with another water quality model such as WASP4 (Ambrose et al., 1987), and sediment transport model such as SED3D (Sheng et al., 1991), so that, the lake modelling system (LMS) can be capable of modelling pollutants in both aqueous and sediment environments in the Great Lakes.

REFERENCES

[1] Abbott, M.B., Lindberg, S. and Havno, K. (1991). "The fourth generation of numerical modelling in hydraulics". *J. Hydr. Res.*, Vol. 29, No. 5, pp. 581-600.

[2] AL-Rabeh, A.H., Gunay, N. (1992). "On the application of a hydrodynamic model for a limited area". *Coastal Eng.*, 17, pp. 173-194.

[3] Ambrose, R. B., Wool, T. A., Martin, J. L., Connolly, J. P., and Schanz, R. W. (1987). "WASP4, a hydrodynamic and water quality model - model theory, user's manual, and programmer's guide (reversion for WASP4.3X)." Environmental Research Laboratory, U. S. Environmental Protection Agency, Athens, Georgia.

[4] Andreasson, P. (1991). "A numerical investigation of energy conversions in geophysical boundary layers". *Ph.D. Dissertation*. Lulea University of Technology.

[5] Backhau, J.O. (1983). "A semi-implicit primitive equation model for shelf seas, outline and practical aspects of the scheme". *Cont. Shelf Res.*, Special issue on JONSMOD'82.

[6] Barica, J. (1989). "Unique limnological phenomena affecting water quality of Hamilton Harbour, Lake Ontario". *J. Great Lakes Res.*, 15(3), pp. 519-530.

[7] Baines, W.D., Knapp, D. J. (1965). "Wind driven water currents". *J. Hydr. Div.*, ASCE, 91(2), pp. 205-221.

[8] Baptista, M. (1987). "Solution of advection-dominated transport by Eulerian-Lagrangian methods using the backwards method of characteristics". *Ph.D. Dissertation*. MIT.

[9] Bedford, K., Yen, C.C., Kempf, J., Schwab, D., Marshall, R and Kuan, C. (1990). "A 3D-stereo graphics interface for operational Great Lake forecasts". *Estuarine and Coastal Modelling*, pp. 249-257.

[10] Bennett, J.R., Clites, A.H. (1987). "Accuracy of trajectory calculation in a finite difference circulation model". *J. Comp. Phys.*, 68, pp. 272-282.

[11] Bishop, C.T. and Donelan, M.A. (1988). "Waves and wave forecasting". *Civil Engineering Practice 3 - Geotechnical/Ocean Engineering*, Chap. 20, pp. 653-695.

[12] Blaisdell, M.A. (1990). "Numerical model study of circulation in the Windermere Basin". *Master Thesis*. McMaster University.

[13] Blaisdell, M.A., Tsanis, I.K. and Kerstenitis, Y. (1991). "Modelling the steady-stage circulation in a distorted physical model of the Windermere Basin". *J. Civil Eng.*, Vol. 18, No. 5, pp. 756-764.

[14] Blumberg, A.F. (1986), "Turbulent mixing processes in lakes, reservoirs and impoundments". *Physics Based Modelling of Lakes, Reservoirs and Impoundments*,

edited. Gray, W.G. ASCE, New York, NY, pp. 79-104

[15] Blumberg, A.F., Mellor, G.L. (1987). "A description of a three-dimensional coastal ocean circulation model". *Three-Dimensional Coastal and Ocean Models*, edited by Heaps, N.S. Coastal and Estuarine sciences 4, AGU.

[16] Boyce, F.M. (1974). "Some aspects of great lakes physics of importance to biological and chemical processes". *J. Fisheries Research*, Vol. 31, No. 5, pp. 689-730.

[17] Boyce, F.M., Chiocchio, F. (1991). "Drogue measurements - Hamilton Harbour 1990". National Water Research Institute (NWRI), CCIW, *Technical Note* No. LRB-91-TN-08.

[18] Brissette, F.P. (1992). "Estimation of wave directional spectra and applications to the study of surface gravity water waves ". *Ph.D. Dissertation.* McMaster University.

[19] Brissette, F.P., Tsanis, I.K. and Wu, J. (1993). "Wave directional spectra and current interaction in Lake St. Clair". *J. Great Lakes Res.*, Vol. 19, No. 4.

[20] Casulli, V. (1990). "Semi-implicit FDM for the two-dimensional shallow water equations". *J. Comp. Phy.*, Vol. 86, pp. 56-74.

[21] Chamberlain, C.E., Mitchell, R. (1978). "A decay model for enteric bacteria in natural waters". *Water Pollution Microbiology*, edited by Mithell, R., Vol. 2, Wiley. pp. 325 -348.

[22] Charlton, B.E. (1884). "The discovery of Burlington Bay". *J. Proc. Hamilton Assoc.* 1884, pp. 41-56.

[23] Cheng, R. T., Powell, T. M., and Dillon, T. M. (1976). "Numerical models of wind-driven circulation in lakes." *Appl. Math. Modelling*, Vol. 1, pp. 141-159.

[24] Cheng, R. T., Smith, P. E. (1990). "A survey of three-dimensional numerical estuarine models". *Estuarine and Coastal Modelling*, edited by Spaulding, M.L. ASCE, pp. 1-15.

[25] Chiocchio, F., Boyce, F. and Royer, L. (1980). "Vertical automatic profiling system (VAPS), Hamilton 1981 data report". National Water Research Institute (NWRI), *Technical Note*, No. LRB-90-TN-1.

[26] Chow, V. T. (1959). "Open channel hydraulics". McGraw-Hill Publishing Co., New York.

[27] Crean, P. B., Murty, T. S., and Stronach, J. A. (1988). *Mathematical Modelling of Tides and Estuarine Circulation*, Springer - Verlag.

[28] Chrystal (1905). "On the hydrodynamical theory of seiches". *Trans. Roy. Soc.*, Edinburgh, 41, pp. 599-649.

[29] Csanady, G.T. (1982). "Circulation in the coastal ocean". D.Reidel Publishing Company, Dordrecht, Holland.

[30] Davies, A. M. (1980). "On formulating a three-dimensional hydrodynamic sea model with arbitrary variation of vertical eddy viscosity." *Comput. Methods Appl. Mech. Eng.*, 22, pp. 187-211.

[31] Davies, A. M. (1985). "Application of the Dufort-Frankel and Saul'ev methods with time-splitting to the formulation of a three dimensional hydrodynamic sea model". *Int. J. Numer. Methods Fluids.*, Vol. 5, pp. 405-425.

[32] Davies, A. M. (1987). "Spectral models in continental shelf sea oceanography". *Three-Dimensional Coastal Ocean Models*, edited by Heaps, N.S. pp. 71-106.

[33] Davies, A. M. (1991). "On the accuracy of finite difference and modal method for computing tidal and wind wave current profiles". *Int. J. Num. Met. in Fluids.*, Vol. 12, pp. 101-124.

[34] Defant, F. (1953). "Theorie der seiches des michigansees und ihre abwand lung durch wirkung der corioliskraft". *Arch. Met. Geoghys.*, Bioklimatol. Wien. A6, pp. 218-241.

[35] Ditmars, J.D., Adams, E.E. and Bedford, K.W. (1987). "Performance evaluation of surface water transport and dispersion models". *J. Hydr. Eng.*, Vol. 113, No. 8, pp. 961-979.

[36] Donelan, M., Elder, F.C. and Hamblin, P.F. (1974). "Determination of the aerodynamic drag coefficient from wind set-up (IFYGL)". *Proc. 17th Conference Great Lakes Research*, International Association for Great Lakes Research, pp. 778-788.

[37] Donelan, M.A. (1980). "Similarity theory applied to forecasting of wave heights, periods and directions". *Proc. Canadian. Coastal Conf.*, pp. 47-61.

[38] Eid, B.M.F. (1981). "Investigation into interfacial transports and exchange flows for lake models". *Ph.D. Dissertation.* McMaster University.

[39] Engel, P. (1988). "Hydraulic model study of the new Windermere Basin". Report to the Research and applications Branch, National Water Research Institute, Canada Centre for Inland Waters, Burlington, ON.

[40] Elzawahry, A.E. (1985). "Advection, diffusion and settling in the coastal zone of Lake Erie". *Ph.D. Dissertation.* McMaster University.

[41] Fischer, H.B., Hanamura, T. (1974), "The effect of roughness strips on transverse mixing in open channels". *Water Resources Res.*, Vol. 11, No. 2, pp. 362-364.

[42] Fischer, H.B., List, E.J., Koh, R.C.Y., Imberger, J. and Brooks, N.H. (1979). "Mixing in inland and coastal waters". Academic Press, New York, NY.

[43] Freeman, N.G., Hamblin, P.F. and Murty, T.S. (1974). "Helmholtz resonance in harbours of the Great Lakes". *Proc. 17th Conference Great Lakes Res.*, 1974. pp. 399-411.

[44] Goossens, L.T., Van Pagee, H.J.A. and Tessel, P.J (1982). "Vertical diffusion in air driven water flows". *J. Hydr. Div.*, ASCE, 108(2), pp. 995-1009.

[45] Graf, W.H., Mortimer, C.H. (1979). " Hydrodynamics of lakes". Elsevier.

[46] Halfon, E. H., Simons, T.J. and Schertzer, W.M. (1990). "Modelling the spatial distribution of seven halocarbons in Lake St. Clair in June 1984 using the TOXFATE model". *J. Great Lakes Res.*, Vol. 16, No. 1.

[47] Haney, R. L. (1991). "On the pressure gradient force over steep topography in sigma coordinate ocean model". *J. Phy. Oceano.*, Vol. 21, pp. 610-619.

[48] Heaps, N.S. (1972). "On the numerical solution of the three-dimensional equations for the tides and storm surge. *Mem. Soc. r. Sci. Liege, 6e series, tome I*, pp. 143-180.

[49] Heaps, N.S. (1984). "Vertical structure of current in homogeneous and stratified lakes". *Hydrodynamics of Lakes*, edited by Hutter, K., Springer-Verlag, pp. 153-202.

[50] Heaps, N.S. (1987). "Three-dimensional coastal and ocean models". *Coastal and Estuarine Sciences 4*, AGU.

[51] Hinz, S. C., Katopodes, N., Freedman, P., Sullivan, M and Freuberg, S. (1990). "Modelling total residual Chlorine in the upper potomac estuary". *Estuarine and Coastal Modelling*, edited by Spaulding, M.L. ASCE, pp. 229-238.

[52] Holly, F. (1984). "Dispersion simulation in two-dimensional tide flow." *J. Hydr. Eng.*, Vol. 110, No. 7, pp. 905-925.

[53] Huang, J.C.K. (1977). "A general circulation model for lakes". NOAA Technical Memorandum ERL GLERL-16.

[54] Huey, L.J., Williamson, J. W. (1974). "Plane turbulent couette flow with zero net-flow". *J. Appl. Mech.*, 41, pp. 885-890.

[55] Hutter, K. (1984). "Hydrodynamics of lakes". Springer-Verlag.

[56] Ibrahim, K. A., McCorquodale, J. A. (1985). " Finite element circulation model for Lake St. Clair". *J. Great Lakes Res.*, Vol. 11, No. 3, pp. 208-222.

[57] IFYGL (1981). "IFYGL - The international field year for the Great Lakes". edited by Aubert, E.J. and Richards, T.L. National Oceanic and Atmospheric Administration, Great Lakes, Environmental Research Laboratory.

[58] Irvine, D.E. (1987). "Extreme waves in the Agulhas - a case study in wave-current interaction". *J. Hopkins APL Technical Digest.*, 8(1), pp. 100-106.

[59] James, W., Eid, B. (1978). "A three-dimensional model of Hamilton Harbour incorporating spatial distribution of transient surface drag". *J. Civ. Eng Can.*, 5, pp. 479-488.

[60] Jin, X.Y. (1993). " Quasi-three-dimensional numerical modelling of flow and dispersion in shallow water". *Ph.D. Dissertation*, Delft University.

[61] Jin, X. Y., Kranenburg, C. (1993). "Quasi-3D numerical modelling of shallow-water circulation". *J. Hydr. Eng.*, Vol. 119, No. 4, pp. 458-473.

[62] Johnson, B. H., Kim, K. W., Sheng, Y. P. and Heath, R. E. (1990). "Development of three-dimensional hydrodynamic model of Chesapeake Bay". *Estuarine and Coastal Modelling*, edited by Spaulding, M.L. ASCE, pp. 162-172.

[63] Julian, P. R. (1975). "Comments on the determination of significance levels of the coherence statistic". *J. Atmos. Sci.*, Vol. 32, No. 4, pp. 836-837.

[64] Koutitas, C., O'Connor, B. (1980). "Modelling three-dimensional wind-induced flo vs". *J. Hydr. Div.*, ASCE, 106(11), pp. 1843-1865.

[65] Koutitas, C.G., Gousidou-Koutita, M. (1986). "A comparative study of three mathematical models for wind-generated circulation in coastal areas". *Coastal Eng.*, 10, pp. 127-138.

[66] Koutitas, C.G. (1988). "Mathematical models in coastal engineering", Pentech Press, London, U.K.

[67] Krestenitis, Y. N. (1987). "Numerical study of the wind-induced circulation and examination of open-sea boundary conditions - case study of Thermaikos Gulf." (unpublished document).

[68] Lam, D.C.L., Murthy, C.R., Simpson, R. B. (1984). "Effluent transport and diffusion models for the coastal zone". Springer-Verlag.

[69] Lam, D.C.L., Schertzer, W.M. and Fraser, A.S. (1983). "Simulation of Lake Erie water quality responses to loading and weather variations". Environment Canada, *Scientific Series*, No. 134.

[70] Lardner, R.W. and Cekirge, H.M. (1988). "A new algorithm for three-dimensional tidal and storm surge computations". *Applied Mathematical Modelling*, Vol. 12, pp. 471-481.

[71] Large, W. G. and Pond, S. (1981). "Open ocean momentum flux measurements in moderate to strong winds". *J. Phys. Oceanogr.*, Vol. 11, pp. 324-336.

[72] Leendertse, J.J. (1967). "Aspects of a computational model for long-period water-wave propagation". The RAND Corporation, Memorandum, RM-5294-PR.

[73] Leendertse, J. J., Alexander, R.C. and Liu, S.K. (1973). "A three-dimensional model for estuaries and coastal seas: Vol. I, Principles of computation". The RAND Corporation, R-1417-OWRR.

[74] Leendertse, J.J., Liu, S.K. (1975). "A three-dimensional model for estuaries and coastal seas: Vol. II, Aspects of computation". The RAND Corporation, R-1764-OWRT.

[75] Leendertse, J.J., Liu, S.K. (1977). "A three-dimensional model for estuaries and coastal seas: Vol. IV, Turbulent energy computation". The RAND Corporation, R-2187-OWRT.

[76] Leonard, B.P. (1979). "A stable and accurate convective modelling procedure based on quadratic upstream interpolation". *Comput. Methods Appl. Mech. Eng.*, 19, pp. 59-98.

[77] Leonard, B.P. (1988). "Simple high-accuracy resolution program for convective modelling of discontinuities". *Int. J. Num. Methods in Fluids.*, Vol. 8, pp. 1291-1318.

[78] Li, C. Y., Kiser., K. M., and Rumer, R. R. (1975). "Physical model study of circulation patterns in Lake Ontario". *Limnology and Oceanography*, V. 20 (3).

[79] Liu, S.K., Leendertse, J.J. (1987). "Modeling the Alaskan continental shelf waters". The RAND Corporation, R-3567-NOAA/RC.

[80] Marsalek, J., Dutka, B.J. and Tsanis, I.K. (1992). "Urban impacts on bacteriological pollution of the St. Clair River in Sarnia: sources and cleanup". National Water research Institute contribution 92-138, Burlington, Ontario.

[81] McCorquodale, J.A., Ibrahim, K. and Hamdy, Y. (1986). "Fate and transport modelling of perchloroethylene in the St. Clair River". *Water Poll. Res. J. Canada*, 21(3), pp. 398-410.

[82] Mellor, G.L. (1973). "Analytic prediction of the properties of stratified planetary surface layers". *J. Atmos. Sci.*, 30, pp. 1061-1069.

[83] Miller, A.C., Richardson, E.V. (1974), "Diffusion and dispersion in open channel flow", *J. Hydraulics Div.*, ASCE, Vol. 100, No. HY 1, pp. 159-171.

[84] Miller, M. J., Thorpe, A.J. (1981). "Radiation conditions for the lateral boundaries of limited-area numerical models". *J. R. Met. Soc.*, 107, pp. 615-628.

[85] Miller, M. J., Blumberg, A. (1985). "Modeling vertical and horizontal diffusivities with the sigma coordinate system". *Monthly Weather Review*, Vol. 113, pp. 1379-1383.

[86] MOE (1974). "Hamilton Harbour study". Water Resources Branch, Toronto.

[87] MOE (1982). "Windermere Basin study" *Technical Support Section, West Central Region*, December 1982, pp. 35.

[88] MOE (1989). "Toronto Waterfront RAP: rand model simulation". Great Lases Section, MOE, Toronto.

[89] MOE (1992). "Collingwood Harbour remedial action plan - stage 2 report". Water Resources Buanch, MOE, Toronto.

[90] MOE (1992). "Remedial action plan for Hamilton Harbour: environmental conditions and problem definitions (RAP stage 1)".

[91] MOE (1992). "Remedial action plan for Hamilton Harbour: goals, options and recommendations (RAP stage 2)".

[92] Murthy, C. R., Simons, T. J. and Lam, D. C. L. (1986). "Dynamic and transport modelling of the Niagara River plume in Lake Ontario". *Rapp. P.-v. Reun. Con. int. Explor. Mer, 186*, pp. 150-164.

[93] Nicollet, G. (1989), "River models". *Recent Advances in Hydraulic Physical Modelling*, edited by Martins, R., Kluwer Academic Publishers, Dordrecht, The Netherlands, pp. 39-64.

[94] Nydegger, P. (1979). "Water circulation in lakes, research in situ, using revolving lake models and comparisons with the latest umnosedimen to logical results". *Hydrodynamics of Lakes*, edited by Graf, W.H. and Mortimer, C.H. ELSEVIER, pp. 161-170.

[95] Pearce, B.R., Cooper, C.K. (1981). "Numerical circulation model for wind- induced flow". *J. Hydr. Div.*, ASCE. 107(3), pp. 285-302.

[96] Phillips, O. W. (1981). "The structure of short gravity waves on the ocean surface". *Spaceborne Synthetic Aperture Radar for Oceanography*, edited by Beal, R.C., DeLeonibus, P. S. and Katz, I., Johns Hopkis University Press, pp. 24-31.

[97] Penicka, F. (1987). "An analysis of current and temperature measurement made in the vicinity of the Pennsylvania Ridge, Lake Erie". Fisheries and Environment Canada Report.

[98] Poulton (1987). "Trace contaminant status of Hamilton Harbour". *J. Great Lakes Res.*, 13(2), pp. 193-201.

[99] Ramming, H. and Kowalik, Z. (1980). "Numerical modelling of marine hydrodynamics". Elsevier, Amsterdam, 368 pp.

[100] Rao, D.B., Murth, T.S. (1970), "Calculation of the steady state wind-driven circulations in Lake Ontario", *Arch. for Meteorology, Geophysics, and Bioclimatology*, Ser. A, Vol. 19, pp. 195-210.

[101] Reichardt, H. (1956). "Ueber die geschwindigkeitsvertteilung in einer gradlinigen turbulenten couettesteoemung". *Z. Angew. Math. Mech.* S26-S29.

[102] Reid, R.O. (1957). "Modification of the quadratic bottom-stress law of turbulent channel flow in the presence of surface wind-stress."*Tech. Mem.*, 93, Beach Erosion Board, US Department of the Army, Washington, D.C.

[103] Roache, P.J. (1972). "Computational fluid dynamics". Hermosa Publishers.

[104] Roberson, J. A. and Crowe, C. T. (1990). "Engineering Fluid Mechanics". Houghton Mifflin Company.

[105] Rodi, W. (1978). "Turbulence models and their application in hydraulic - A state of the art review". *Technical Report No. SFB 80/T/127*,. Univ. Karlsruhe, Germany.

[106] Rumer, R.R., Hoopes, J.A. (1970), "Modelling great lakes circulations". *Proceedings of Symposium on the Water Environment and Human Needs*, M.I.T., pp. 212-247.

[107] Ryan, P.J. (1971). "Prediction of the annual cycle of temperature change in a stratified lake or reservoir". *Mathematical Model and User's Manual*, MIT, Report, No. 137.

[108] Schlichting, H. (1968). *Boundary Layer Theory*. McGraw-Hill, New York, N.Y.

[109] Schwab, D.J. (1979). "Simulation and forecasting of Lake Erie storm surges". *Mon. Wea. Rev.*, 106, pp. 1476-1487.

[110] Schwab, D.J. (1981). "A two-dimensional lake circulation modelling system". NOAA Technical Memorandum ERL GLERL-38. Ann Arbor ,Michigan , USA.

[111] Schwab, D.J. (1983). "Numerical simulation of low frequency current fluctuations in Lake Michigan". *J. Phys. Oceanogr.*, 13, pp. 2213-2224.

[112] Schwab, D.J., Bennett, J.R. (1987). "Lagrangian comparison of objectively analyzed and dynamically modeled circulation patterns in Lake Erie". *J. Great Lakes Res.*, 13(4), pp. 515-529.

[113] Schwab, D. J., Clites A. H. and Murthy C.R. (1989). "The effect of wind on transport and circulation in Lake St. Clair". *J. Geophy. Res.*, Vol. 94, No. C4, pp. 4947-4958.

[114] Schwab, D. J. (1989). "Hydrodynamic modelling in the Great Lakes from 1950 to 1990 and prospects for the 1990s". in *Chemical Dynamics in Fresh Water Ecosystem*, Edited by A. Gobas and J.A. McCorquodale. LEWIS Publishers.

[115] Schwab, D. J. (1992). "Hydrodynamic modeling in the Great Lakes from 1950 to 1990 and prospects for the 1990s". *Chemical Dynamics in Fresh Water Ecosystems*, Edited by F. A.P.C. Gobas, and J. A. McCorquodale. LEWIS Publishers.

[116] Shen, H.H. (1991). "Numerical analysis of large-scaled flows and mass transports in lakes". *Ph.D. Dissertation*. Kyoto University.

[117] Sheng, Y. P. (1983). "Modelling of three-dimensional coastal current and sediment dispersion, Vol. 1, model development and application". *Technical Report CERC-83-2*, Coastal Engineer Research Centre, U.S. Army Engineer Waterways Experiment Station, Vicksburg, MS.

[118] Sheng, Y.P. (1990). "Evolution of a three-dimensional curvilinear-grid hydrodynamic model for estuary, lakes and coastal waters: CH3D". *Estuarine and Coastal Modelling* , Edited by Spaulding, M. L., American society of Civil Engineering.

[119] Sheng, Y. P., Choi, J. K. and Kuo, Y. (1990). "Three-dimensional numerical modelling of tidal circulation and sanitary transport in the James River estuary". *Estuarine and Coastal Modelling*, edited by Spaulding, M. L. ASCE, pp. 209-218.

[120] Sheng, Y. P., Eliason, D., Chen, X. J., and Choi, J. K. (1991). "A three-dimensional numerical model of hydrodynamics and sediment transport in lakes and estuaries: theory, model development, and documentation." *UFL/COEL Report.*

[121] Simons, T.J. (1971). "Development of numerical models of Lake Ontario", *Proc. 14th Conf. Great Lakes Res. 1971, Internat. Assoc. Great Lakes Res.*, pp. 654-669.

[122] Simons, T.J. (1972). "Development of numerical models of Lake Ontario: Part 2", *Proc. 15th Conf. Great Lakes Res. 1972, Internat. Assoc. Great Lakes Res.*, pp. 655-672.

[123] Simons, T.J. (1973), "Development of three-dimensional numerical models of the Great Lakes". Scientific Ser. No. 12, Environment Canada, Inland Waters Directorate, Canada Centre for Inland Waters, Burlington, ON.

[124] Simons, T.J. (1976). "Continuous dynamical computations of water transports in Lake Erie for 1970". *J. Fish, Res. Board Can.* 33, pp. 371-384.

[125] Simons, T.J. (1978). "Wind-driven circulations in the southwest Baltic". Tellus, 30, pp. 272-283.

[126] Simons, T.J. (1980). "Circulation models of lakes and inland seas". Canadian Bulletin of Fisheries and Aquatic Sciences. Bulletin 203 , Ottawa, Canada.

[127] Simons, T.J. (1985). "Reliability of circulation models". *J. Phys. Oceanogr.* 15, pp. 1191-1204.

[128] Simons, T.J., Lam, D.C.L. (1986), "Documentation of a two-dimensional X-Y model package for computing lake circulations and pollutant transport", in *Physics Based Modelling of Lakes, Reservoirs, and Impoundments*, Edited by Gray, W.G., ASCE, New York, NY, pp. 258-308.

[129] Simons, T.J., Schertzer, W. M. (1989). "Modelling wind-induced water set-up in Lake St. Clair". *J. Great Lakes*, Vol. 15, No. 3, pp. 452-464.

[130] Simons, T.J., Schertzer, W. M. (1989). "The circulation of Lake Ontario during the summer of 1982 and the winter of 1982/1983". Environment Canada, *Scientific Series*, No. 171.

[131] Smith, S. D. and Anderson, R. J. (1984). "Spectra of humidity, temperature, and wind over the sea at Sable Island, Nova Scotia". *J. Geophys. Res.* , Vol. 89, pp. 2020-2040.

[132] Spaulding, M.L. (1990). "Estuarine and coastal modelling". *ASCE*.

[133] Spaulding, M.L., Howlett, E., Jayko, K., Anderson, E. and Isaji,T. (1992). "A shell approach to modelling oil spill trajectory and fate and search and rescue operations". *Estuarine and Coastal Modelling*, Edited by Spaulding, M.L., Bedford, K., Blumberg, A., Cheng, R. and Swanson, C.

[134] Spillane, K.T., Hess, G.D. (1978). "Wind-induced drift in contained bodies of water". *J. Phys. Ocean.*, 8, pp. 930-935.

[135] Svensson, U. (1978). "Mathematical model of the seasonal thermocline". Report No. 1002, Department of Water Resources Engineering, Univ. of Lund, Sweden.

[136] Swanson, J.C. (1986). "A three-dimensional numerical model system of coastal Circulation and Water Quality". *Ph.D. Dissertation*. University of Rhode Island, USA.

[137] Thackston, E.L., Shields, F.D. and Schroeder, P.R. (1987), "Residence time distributions of shallow basins". *J. Enviro. Eng.*, Vol. 113, No. 6, pp. 1319-1332.

[138] Tsanis, I.K. (1986). "Characteristics of shear-induced countercurrent flow". *Ph.D. Dissertation*. University of Toronto.

[139] Tsanis, I.K. (1989). "Simulation of wind-induced water currents". *J. Hydr. Eng. (ASCE)*, Vol. 115, No. 8, pp. 1113-1134.

[140] Tsanis, I.K., Murthy, C.R. (1990). "Flow distribution in St. Lawrence River System at Wolfe Island, Kingston Basin, Lake Ontario". *J. Great Lakes Res.*, 16(3), pp. 352-365.

[141] Tsanis, I.K., Blaisdell, M., Krestenitis, Y., Chu, V.H., Engrl, P. (1990). "Physical and mathematical model comparisons for Windermere Basin". *Proceedings of International Assoc. of Hydraulic Res. Conference*, Cambridge, 1990, M.I.T. Press, Cambridge, MA.

[142] Tsanis, I.K., Masses, A., Murthy, C.R., and Miners, K. (1990). "Summer circulation in the Kingston Basin, Lake Ontario". *J. Great Lakes Res.*, 17(1), pp. 57-73.

[143] Tsanis, I.K., Wu, J. (1990). "Hydrodynamic simulation of Lake St.Clair". *Atmospheric Environment Service (AES) Report*, September 1990.

[144] Tsanis, I.K., Wu, J. (1991). "Study of water currents in the Canadian Great Lakes". *Atmospheric Environment Service (AES) Report*, March 1991.

[145] Tsanis, I.K., Wu, J. (1991). "Modelling bacteria in the St. Clair River in Sarnia". *National Water Research Institute (NWRI) Report*, Rivers Research Branch, Environment Canada.

[146] Tsanis, I.K., Wu, J. (1992). "Remedial measures for Sarnia Bay". *National Water Research Institute (NWRI) Report*, Rivers Research Branch, Environment Canada.

[147] Tsanis, I.K. , Wu, J. (1993). "Modelling current movements in Hamilton Harbour". *Department of Fisheries and Oceans(DEFO) Report*, Phase I & II.

[148] Tsanis, I.K., Wu, J. and Charlton, M. (1993). "Mixing, fate and transport of toxic chemicals in Hamilton Harbour". GLURF Study 91-009.

[149] Tsuruya, H., Nakamo, S. and Kato, H. (1985). "Experimental study on wind driven current in a wind-wave tank--effect of return flow on wind driven current". The Ocean Surface, pp. 425-430.

[150] U.S. Army of Engineers (1983). "St. Clair River aerial drogue survey - surface velocities and directions, Spring of 1982, Detroit district, September 1983.

[151] Vepsa, H., Alasaarela, H., and Sarkkula, J. (1992). "Model development for operational use to help spill combating and sea rescure". *Estuarine and Coastal Modelling*, edited by Spaulding M. L. et al., ASCE, 1992, New York.

[152] Wang, J. and O'Connor, J. (1975). "Mathematical modelling of nearshore circulation". R. M. Parsons Lab. for Water Resources and Hydrodynamic T.R. 200 MIT.

[153] Wang, J.D., Blumberg, A.F. and Butler, H.L. (1990). "Transport prediction in partially stratified tidal water". ASCE Tide Hydraulics Verification Task Committee. Vol. 116, No. 3, pp. 380-396 .

[154] Wu, J. (1969). "Wind stress and surface roughness at air-sea interface." *J. Geophys. Res.*, Vol. 34, No. 2, pp. 444-445.

[155] Wu, J. (1973). "Prediction of near-surface drift currents from wind velocity". *J. Hydr. Div.*, ASCE, 99, pp. 1291-1302.

[156] Wu, J. (1975). "Wind-induced drift currents". *J. Fluid Mech.*, 68(1), pp. 49-70.

[157] Wu, J. and Pu, P. (1989). "Numerical simulations of the hydrodynamics of Lake Taihu using a irregular-grid finite difference model". *Memoirs of Nanjing Institute of Geography and Limnology, Academia Sinica*, Science Press, China.

[158] Wu, J. (1992). "Variation of the heat transfer coefficient with environmental parameters". *J. Phy. Oceanogr.*, Vol. 22, pp. 293-300.

[159] Wu, J., Pu, P., Wang, Q.Q. and Huang, Q. (1987). "Features of current and horizontal diffusion fields at Dapu River mouth in Lake Tai". *International Symposium in Lake Tai and Lake Biwa*, pp. 21-25.

[160] Wu, J., Tsanis, I.K. (1991). "Quasi 3D hydrodynamic modelling for Lake St. Clair". *11th CSCE Annual Conference*, May 29-31, Vancouver, B.C., pp. 26-35.

[161] Wu, J., Tsanis, I.K. (1991). "A 2D Circulation model for the Great Lakes". *34th Congress of the International Association of Great Lakes Research*, June 2-6, Buffalo, N.Y.

[162] Yalin, M.S. (1972). "Mechanics of sediment transport". Pergammon Press, New York, NY.

[163] Yanenko, N.N. (1971). "Method of fractional steps: the solution of problems of mathematical physics in several variables". in Holt M. (ed.), Springer-Verlag, New York.

[164] Yen, C.C.J., Keith, W., Bedford, M., ASCE, and Schwab, D.J. (1992). "Nowcast protocol for the Great Lakes forecasting system". *Estuarine and Coastal Modelling*, Edited by Spaulding, M.L., Bedford, K., Blumberg, A., Cheng, R. and Swanson, C.

APPENDIX 1

SEVERAL DERIVATIONS AND FORMULATIONS

In this appendix, several derivations and formulations which were used in the model development are presented. They include integrations used in the VHI3D model, transformation of the vertical coordinates in the multi-layered three-dimensional circulation model, Monte-Carlo random simulation for the particle trajectory model, and numerical scheme of error function used for the exact solution of 1D advection-diffusion problem.

A1.1 INTEGRATIONS USED IN VHI3D MODEL

The following integrations were used in the formulation of VHI3D model in chapter 4. Before the derivation, the following variables are defined: h = water depth. z_s, z_b, = thickness of viscous sublayer at surface and bottom, respectively (they very small portion of the depth). $z_{sh} = z_s/h$, $z_{bh} = z_b/h$, = relative thickness of viscous sublayer at surface and bottom, respectively.

$$\int_0^h \ln\left(\frac{z}{z_s}+1\right) dz = h\,(1+z_{sh})\left[\ln\left(1+\frac{1}{z_{sh}}\right)-1\right] + z_{sh}\,h \qquad \text{(A1.1)}$$

$$I_1 = \frac{1}{h}\int_o^h \ln^2\left(1+\frac{z}{z_s}\right) dz = \frac{z_s}{h}\int_0^{\ln\left(1+\frac{h}{z_s}\right)} X^2 e^X\, dX \qquad \left[set\ \ X = \ln\left(1+\frac{z}{z_s}\right)\right]$$

$$= (1 + z_{sh}) \left[\ln^2 (1 + \frac{1}{z_{sh}}) - 2 \ln (1 + \frac{1}{z_{sh}}) + 2 \right] - 2z_{sh} \tag{A1.2}$$

$$I_2 = \frac{1}{h} \int_o^h \ln (1 + \frac{z}{z_s}) \ln (1 - \frac{z}{z_b + h}) \, dz$$

$$\approx \frac{1}{h} \int_o^h \ln (1 + \frac{z}{z_s}) \left[-(\frac{z}{h}) - (\frac{z}{h})^2 \right] dz \qquad \left[due \; z_b \ll h \right]$$

$$= \frac{1}{2} (\ln z_{sh} + \frac{1}{2}) - z_{sh} (\ln z_{sh} + 1) + \frac{3}{4} z_{sh}^2 \tag{A1.3}$$

$$I_3 = \frac{1}{h} \int_o^h \ln^2 (1 - \frac{z}{z_b + h}) \, dz$$

$$= -\frac{z_b + h}{h} \int_0^{\ln (1 + \frac{h}{z_b + h})} X^2 e^X \, dX \qquad \left[set \;\; X = \ln (1 - \frac{z}{z_b + h}) \right]$$

$$= -z_{bh} \left[\ln^2 \frac{z_{bh}}{1 + z_{bh}} - 2 \ln \frac{z_{bh}}{1 + z_{bh}} + 2 \right] + 2 \tag{A1.4}$$

A1.2 TRANSFORMATION OF THE VERTICAL COORDINATES

The vertical σ coordinates for the three-dimensional stratified hydrodynamic model is obtained by letting

$$t' = t \tag{A1.5}$$

$$x' = x \tag{A1.6}$$

$$y' = y \tag{A1.7}$$

$$\sigma = \frac{z - \zeta(x, y, t)}{h(x, y) + \zeta(x, y, t)} = \frac{z - \zeta}{h + \zeta} = \frac{z - \zeta}{H} \tag{A1.8}$$

By using chain rule, the differential operators appearing in the gverning equations then become

$$\frac{\partial}{\partial t} = \frac{1}{\partial t'} - (\frac{1}{H} + \frac{\sigma}{H})\frac{\partial \zeta}{\partial t}\frac{\partial}{\partial \sigma} \tag{A1.9}$$

$$\frac{\partial}{\partial x} = \frac{1}{\partial x'} - (\frac{1}{H}\frac{\partial \zeta}{\partial x'} + \frac{\sigma}{H}\frac{\partial H}{\partial x'})\frac{\partial}{\partial \sigma} \tag{A1.10}$$

$$\frac{\partial}{\partial y} = \frac{1}{\partial y'} - (\frac{1}{H}\frac{\partial \zeta}{\partial y'} + \frac{\sigma}{H}\frac{\partial H}{\partial y'})\frac{\partial}{\partial \sigma} \tag{A1.11}$$

$$\frac{\partial}{\partial z} = \frac{1}{H}\frac{\partial}{\partial \sigma} \tag{A1.12}$$

The diffusion terms in the model equations involve the second-order derivatives which are:

$$\begin{aligned}\frac{\partial}{\partial x}\frac{\partial}{\partial x} = \frac{1}{H}[&\frac{\partial}{\partial x'}(H\frac{\partial}{\partial x'}) - \frac{\partial}{\partial \sigma}(\sigma\frac{\partial H}{\partial x'}\frac{\partial}{\partial x'}) - \sigma\frac{\partial}{\partial x'}(\frac{\partial H}{\partial x'}\frac{\partial}{\partial \sigma}) \\ &+ \frac{1}{H}(\frac{\partial H}{\partial x'})^2\frac{\partial}{\partial \sigma}(\sigma^2\frac{\partial}{\partial \sigma}) - \frac{\partial}{\partial x'}(\frac{\partial \zeta}{\partial x'}\frac{\partial}{\partial \sigma}) - \frac{\partial \zeta}{\partial x'}\frac{\partial^2}{\partial \sigma \partial x'} \\ &+ (\frac{\partial \zeta}{\partial x'})^2(\frac{1}{H}\frac{\partial^2}{\partial \sigma^2}) + \frac{z}{H}\frac{\partial \zeta}{\partial x'}\frac{\partial H}{\partial x'}\frac{\partial}{\partial \sigma}(\sigma\frac{\partial}{\partial \sigma})] \\ &= \frac{1}{H}\frac{\partial}{\partial x'}(H\frac{\partial}{\partial x'}) + \textit{higher order terms}\end{aligned} \tag{A1.13}$$

The vertical velocity in the (x,y,z) coordinates (w) and in the transformated coordinates ($\omega = \frac{d\sigma}{dt}$) are related from the following formula:

$$w = \frac{dz}{dt} = \frac{d}{dt}(\sigma H + \zeta) = H\omega + \sigma(u\frac{\partial h}{\partial x} + v\frac{\partial h}{\partial y}) + (1+\sigma)\frac{d\zeta}{dt} \tag{A1.14}$$

The hydrostatic equation

$$\frac{\partial P}{\partial z} = -\rho g \tag{A1.15}$$

becomes

$$-\partial P = \rho g\,\partial z = \rho g H\,\partial \sigma \tag{A1.16}$$

Integrating from the surface to any depth σ,

$$P(\sigma) = P_a - g H \int_0^\sigma \rho \, d\sigma = P_a + g H \eta \tag{A1.17}$$

where P_a is atomspheric pressure and

$$\eta = \int_\sigma^0 \rho d\sigma \tag{A1.18}$$

Therefore, ignoring atmospheric term, the horizontal pressure gradient term in the x-direction in the σ coordinates becomes:

$$\frac{\partial P}{\partial x} = g \frac{\partial H\eta}{\partial x} = g \frac{\partial H\eta}{\partial x'} - \frac{g}{H}\left(\frac{1}{H}\frac{\partial \zeta}{\partial x'} + \frac{\sigma}{H}\frac{\partial H}{\partial x'}\right)\frac{\partial H\eta}{\partial \sigma} \tag{A1.19}$$

A1.3 MONTE-CARLO RANDOM SIMULATION FOR TRAJECTORY MODEL

Diffusion of a solute or a cloud of partiles in uniform flow with homogenous turbulence is obviously similar to the classical case of molecular (or Fickian) diffusion in a quiescent medium. The well-known solution of Fickian diffusions is then applicable for the case under consideration when the molecular diffusivity is replaced by the eddy diffusivity. Only one-dimensional diffusion is considered here for simplicity. The analysis can easily be extended to two- and three- dimensional cases (Jin, 1993).

We first introduce a series of independent real random variables s (i) (i = 1, 2, ...). Each of these variables has a uniform distribution over the interval $[S_m - S_v, S_m + S_v]$, where S_m and S_v are two real numbers to be defined later. This distribution can be obtained by using a random floating-point number generator available on most computers. One can easily derive the mean (E_s) and standard deviation (σ_s) of s, the results being as follows:

$$E_s = \langle s \rangle = S_m \tag{A1.20}$$

$$\sigma_s^2 = < ss > - E_s^2 = \frac{S_v^2}{3} \tag{A1.21}$$

Suppose a particle is at $x = 0$ at time $t_0 = 0$. It undergoes for time $t = t_0, t_1, ..., t_n$ successive independent random displacements with step s (i) (i = 1, 2, ..., n). According to the central-limit theorem, the probability density distribution $P\ (x, t_n)$ of the particle location at time t_n approaches a Gaussian distribution as n increases:

$$P\ (x\ , t_n\ ) \approx \frac{1}{\sqrt{2\pi n\ \sigma_s^2}} \exp\left[- \frac{(x - n\ E_s)^2}{2 n\ \sigma_s^2} \right] \tag{A1.22}$$

The concentration distribution $c\ (x, t\ )$ of a solute of unit mass released instantaneously at $t = 0$, $x = 0$ in a uniform flow with a velocity u and diffusivity D_x is well known:

$$C\ (x\ , t_n\ ) = \frac{1}{\sqrt{4\pi D_x t_n}} \exp\left[- \frac{(x - u\ t_n)^2}{4 D_x\ t_n} \right] \tag{A1.23}$$

The analogy between equations (A1.22) and (A1.23)) is obvious. Since $t_n = n\ \Delta t$, the corresponding terms in both equations yields $E_s = u\ \Delta t$, $\sigma_s^2 = 2\ D_x\ \Delta t$, or, using Eqs. (A1.20) and (A1.21):

$$S_m = u\ \Delta t \tag{A1.24}$$

$$S_v = \sqrt{6 D_x \Delta t} \tag{A1.25}$$

As a result, the contribution due to the random movement can be added into the particle trajectory model as:

$$X^{n+1} = X^n + r_1 \sqrt{6\ D_x \Delta t} \tag{A1.26}$$

where, X^{n+1} is the partilce location at new time level, and X^n is the location at previous time level, r_1 is a pseudo-Gaussian random number with mean zero and a standard derivation of unity.

A1.4 NUMERICAL SCHEME OF ERROR FUNCTION

The function

$$EXF(A,B) = exp(A)\,erf(B) \tag{A1.27}$$

is calculated, where, $erf = 1 - erfc$ is the error function.

$$erfc(B) = \frac{2}{\sqrt{\pi}} \int_{B}^{\infty} exp(-\tau^2) d\tau \tag{A1.28}$$

Two different approximations are used for $EXF(A,B)$. For $0 \leq B \leq 3$:

$$EXF(A,B) = exp(A - B^2)(a_1\tau + a_2\tau^2 + a_3\tau^3 + a_4\tau^4 + a_5\tau^5) \tag{A1.29}$$

where

$$\tau = \frac{1}{1 + 0.3275911B} \tag{A1.30}$$

$$a_1 = .2548296 \;;\; a_2 = -.2844967 \;;\; a_3 = 1.421414 \;;\; a_4 = -1.453152 \;;\; a_5 = 1.061405 \;; \tag{A1.31}$$

and for $B > 3$

$$EXF(A,B) = \frac{1}{\sqrt{\pi}} exp(A - B^2)/(B + 0.5/(B + 1./(B + 1.5/(B + 2./(B + 2.5/(B + 1.)))))) \tag{A1.32}$$

For negative values of B, the following aditional relation is used:

$$EXF(A,B) = 2\,exp(A) - EXF(A,-B) \tag{A1.33}$$

The function $EXF(A,B)$ can not be used for very small or very large values of its arguments A, B.

The function returns zero for the following two conditions:

$$|A| > 170 \;\; B \leq 0 \qquad or \qquad |A - B^2| > 170 \;\; B < 0 \tag{A1.34}$$

APPENDIX 2

SPECTRAL ANALYSIS PROGRAM IN MATLAB

In MATLAB (*Signal Processing Toolbox User's Guide*, The MathWorks, Inc., 1992), there is a spectral analysis program (command) - *spectrum* (x, y, m), which was employed for the spectral analysis of water level, current and wind data during 1990 and 1991 field reason in Hamilton Harbour. P = *spectrum* (x, y, m) performs spectral analysis on the two sequences x and y using the Welch method of power spectrum estimation. The two sequences of length n points are divided into sections of m points each, where m must be a power of two. Successive sections are Hanning windowed, transformed with an m- point fast Fourier transform (FFT) and accumulated. 95 % confidence intervals are estimated. *spectrum* returns the $m/2$-by-8 array: P = $[P_{xx}\ P_{yy}\ P_{xy}\ T_{xy}\ C_{xy}\ P_{xxc}\ P_{yyc}\ P_{xyc}]$, that can be graphed using function *specplot* or ploted by users. The columns of P are P_{xx} = x power spectral density, P_{yy} = y power spectral density, P_{xy} = Cross spectral density, T_{xy} = Complex transfer function from x to y, C_{xy} = Coherence function between x and y, P_{xxc} = 95% confidence interval for P_{xx}, P_{yyc} = 95% confidence interval for P_{yy}, P_{xyc} = 95% confidence interval for P_{xy}.

P = *spectrum* $(x, y, m, noverlap)$ specifies that the m-point sections should overlap *noverlap* points.

P = *spectrum* (x, m) and *spectrum* $(x, m, noverlap)$ return the single sequence power spectrum. In these cases, spectrum returns the $m/2$- by-2 array P = $[P_{xx}\ P_{xxc}]$.

APPENDIX 3

PUBLICATIONS (JOURNAL, CONFERENCE PAPERS AND REPORTS)

[1]. Journal Articles

(1). Peer reviewed

Brissette F.P., Tsanis I.K., **Wu J.** (1993). "Wave directional spectra and current interaction in Lake St. Clair." *Journal of Great Lakes Research*, Vol. 19, No. 4, pp. 553-568.

Wu J. and Pu P. (1989). "Numerical simulations of the hydrodynamics of Lake Taihu using a irregular-grid finite difference model". *Memoirs of Nanjing Institute of Geography and Limnology, Academia Sinica*, Science Press, China, Vol. 6, pp. 1-13.

Wu J. (1989). "Numerical study of the seiche, wind-induced surges and currents in Lake Dianchi". *Nature, Society and Area Development*. ed. by Nanjing Institute of Geography and Limnology. Mapping Press, China, pp. 54-62.

Wu J., Kumigai M. and Y. Oonishi (1988). "A multi-layer model of hydrodynamics of Lake Tai and the southern basin of Lake Biwa" . *Transactions of Oceanography and Limnology*. No. 2, pp. 16-24.

Li Zihua, **Wu J.** and Shi Wenquan (1985). "Preliminary study on equations of growth and heat balance of conical hailstone". *Scientia Atmospherica Sinica*. Vol. 9, No. 4, pp. 428-433.

(2). Submitted for publication

Wu J. and Tsanis I. K. (1993). "Dye transport and residence time in a model basin" (*Journal of Hydraulic Research*, IAHR).

Tsanis I.K., **J. Wu** and J. Marsalek (1993). "Feasibility of modelling bacteria in the St. Clair River at Sarnia Bay" (*Journal of Great Lakes Research*).

Wu J. and Tsanis I. K. (1993). "Numerical study of wind-induced currents" (*Journal of Hydraulic Engineering*, ASCE).

Wu J. and Tsanis I. K. (1993). "VHI3D - An efficient three-dimensional wind-induced circulation model using the vertical/horizontal integrating (VHI) approach" (*Advances in Water Resources*, ASCE).

Wu J. and Tsanis I. K. (1993). "Verification of three-dimensional circulation models in Hamilton Harbour" (*Journal of Geophysic Research*).

I. K. Tsanis and Wu J. (1993). "LMS - an integrated lake modelling system" (*Advances in Water Resources*).

(3). In preparation

Tsanis I. K., F. Boyce and Wu J. (1993). "Current and water level in Hamilton Harbour, Canada" (*Journal of Great Lakes Research*).

Wu J. and Tsanis I. K. (1993). "Nested-grid modelling approach for the near-shore areas in the Great Lakes" (*Journal of Great Lakes Research*).

[2]. Refereed Conference Proceedings

Tsanis I.K. and Wu J. (1993). "Modelling bacteria in the St.Clair River in Sarnia". *Second International Conference on Water Pollution*. Milan, Italy, June 21-23.

Wu J. and I.K. Tsanis (1992). "A circulation and water quality modelling system for the Great Lakes and near-shore areas. *International Symposium on Hydraulic Research in Nature and Laboratory*. Wuhan, China, November, 1992.

Tsanis I.K. and Wu J. (1992). "Transport and dispersion of pollutants in a distorted model of the Windermere Basin". *12th CSCE Annual Conference*, Quebec City, Quebec, May 26-29, pp. 35-44.

Brissette F.P., Wu J. (1992). "Wave directional spectra and current interaction in Lake St. Clair". *Third International Workshop on Wave Hindcastting and Forcastting*, May 19-22, 1992, pp. 24-31

Wu J. and Tsanis I.K. (1991). "Quasi 3D hydrodynamic modelling for Lake St. Clair". *11th CSCE Annual Conference*, May 29-31, Vancouver, B.C., pp. 26-35.

Wu J. and Tsanis I.K. (1991). "A 2D Circulation model for the Great Lakes". *34th Congress of the International Association of Great Lakes Research*, June 2-6, Buffalo, N.Y.

Wu J., Han XiaoZhong, Jian Jiahu and Michio Kumigai. (1987). "A study of wind-wave

interaction at the platform and resuspension of the sediments in Lake Tai". *International Symposium on Lake Tai and Lake Biwa.* Sep. 21-25, 1987, Nanjing, China.

Wu J., Pu Peiming, Wang QianQian and Huang Qin (1987). "Features of current and horizontal diffusion fields at Dapu River mouth in Lake Tai". *International Symposium on Lake Tai and Lake Biwa.* Sep. 21-25, 1987, Nanjing, China.

Wu J., Cao Zuohao, Jiang Jiahu, Huanh Qin and Yasuaki Okumura. (1987). "Thermal regime and reflection feature of radiation at surface in Lake Tai". *International Symposium on Lake Tai and Lake Biwa.* Sep. 21-25, 1987, Nanjing, China.

Kumigai M., Y. Oonishi and J. Wu.(1987). "Predictive model for resuspension and deposition of bottom sediments". *International Symposium on Lake Tai and Lake Biwa.* Sep. 21-25, 1987, Nanjing, China.

[3]. Technical Reports - Government Publications

Tsanis I.K. and Wu J. (1993). "Modelling current movements in Hamilton Harbour". *Department of Fisheries and Oceans (DEFO) Report*, Phase I & II.

Tsanis I.K. and Wu J. and Charlton M. (1993). "Mixing, fate and transport of toxic chemicals in Hamilton Harbour." *GLURF Study 91-002*, NSSCC.

Tsanis I.K. and Wu J. (1992). "Remedial Measures for Sarnia Bay". *National Water Research Institute (NWRI) Report*, Rivers Research Branch, Environment Canada.

Tsanis I.K. and Wu J. (1991). "Modelling bacteria in the St.Clair River in Sarnia". *National Water Research Institute (NWRI) Report*, Rivers Research Branch, Environment Canada.

Tsanis I.K. and Wu J. (1991). "Study of water currents in the Canadian Great Lakes". *Atmospheric Environment Service (AES) Report.*

Tsanis I.K. and Wu J. (1990). "Hydrodynamic Simulation of Lake St.Clair". *Atmospheric Environment Service (AES) Report.*

[4]. Contributed Seminars

Wu J. (1991). "Hydrodynamic modelling of the Great Lakes", *Waves Seminar Series* at National Water Research Institute (NWRI).

Wu J. (1990). "Hydrodynamic/water quality modelling of the Great Lakes", *Graduate Seminar*, Department of Civil Engineering, McMaster University.